**Title**
Designing quantum dot solids for optoelectronic devices through matrix engineering

**Author**
Tolentino, Jason

**Publication Date**
2015

UNIVERSITY OF CALIFORNIA,
IRVINE

# Designing quantum dot solids for optoelectronic devices through matrix engineering

DISSERTATION

submitted in partial satisfaction of the requirements
for the degree of

DOCTOR OF PHILOSOPHY

in Material Science and Engineering

by

Jason Tolentino

Dissertation Committee:
Assistant Professor Matt Law, Chair
Assistant Professor Alon Gorodetsky
Associate Professor Regina Ragan

2015

# DEDICATION

To my loving fiancée, whose unconditional support, tenacity, and faith in my ability to complete this dissertation and then some…

To my parents and their significant others, whose words of encouragements, prayers, and financial support to provide me the means for an education which has led me to my career

To my sister, may this body of work continue to inspire and drive you to succeed and seek out what makes you happy.

# TABLE OF CONTENTS

PAGE

CHAPTER 6: INFRARED TRANSMISSION SPECTROSCOPY OF QUANTUM DOT THIN-FILM TRANSISTORS

CHAPTER 7: SUMMARY AND OUTLOOK

## LIST OF FIGURES

# LIST OF TABLES

# ACKNOWLEDGMENTS

I would first like to acknowledge my advisor, Matt Law for this incredible opportunity to work in his lab and support. I am truly grateful for his guidance and opportunities that he has afforded me. His incredible tenacity for scientific rigor has truly been an invaluable skill that will help shape my career as I move forward.

I would also like to thank my thesis committee members, Prof. Alon Gorodetsky, Prof. Regina, Ragan, and Prof. Allon Hochbaum for their contributions towards this work and advice towards advancing my technical speaking.

I would especially indebted to the *Law Lab* and its past and current members. Thanks to Dr. Yao Liu for his support when I first joined the lab. Without his guidance during my first two years in the lab, I would not have accomplished this much. Thanks also to the first *QDers* Mark Gibbs and Rachelle Ihly for being great lab members and teaching me the ropes within the lab. I especially want to point out Vineet Nair for his discipline, knowledge, and intuition, which have been an inspiration for me. Moreover, his friendship within the lab has made the commensuration of completing a PhD more enjoyable.

There are many other people who have helped me in large and small ways without the lab during my time at UCI (in no particular order of importance) – Moritz Limpinsel, Nick Berry, Sean Seefeld, Amanda Weber, Dr. Brandon Mercado, Juliette Micone, Nima Farhi, Sam Keene, Zhongyue Luan, Claire Cilpin, and Kan Fu.

The machine stop at UCI who help things run smoothly, people who are often overlooked, but who I would like to take the time to thank them now – Lee Moritz and Chris Peterson for their ingenuity, stories, and lessons when working in engineering and scientific teams. Without their craftsmen ship, many of my experimental setups would not have been up and running.

To those in the INRF and BION – Vu Phan, Lifeng Zhang, Jake Hes, Richard Chang, Dexter Humphrey, and Mo Kebali- thank you for your expertise and assistance during my development years while I was in the cleanroom. Thank you for your continued support and great conversations.

Personally, I would like to thank my new friends, colleagues, and professionals who are working on the Solar Decathlon while I was involved. Much respect to all of the people dedicated to building a sustainable home. Your dedication to a home that is sustainable, innovative, and more importantly livable has renewed my interests and goals towards enabling a more endurable future built upon the use of solar energy, innovative designs that are energy-efficient, and *green* materials.

I would also like to acknowledge the American Chemical Society and Nano Letters for their permission to reprint parts of "PbSe quantum dot field-effect transistors with air-stable electron mobilities above 7 $cm^2 V^{-1} s^{-1}$" in chapter 4.

Lastly, I would again like to thank my family – old and new – I truly could not have not done this without your love and support. *Mahalo* and salamat!

# CURRICULUM VITAE

## EDUCATION

**University of California, Irvine**
Ph.D. Candidate in Material Science & Engineering (2009-2015)
*Advisor*: Matt Law

**Boston University**, Boston, Massachusetts
B.S. in Aerospace Engineering (May 2009)

## RESEARCH & EXPERIENCE

**University of California, Irvine** **(May 2010 – 2015)**

- Matrix-engineering quantum dot thin films using atomic-layer deposition for improved carrier mobility, carrier diffusion lengths
- Characterized electronic structure in lead chalcogenide thin films using infrared transmission spectroscopy and photoluminescence spectroscopy
- Developed method to eliminate bias-stress effect in QD FET
- Long-term environmental testing of QD FETs
- Fundamental transport physics of QD optoelectronics
- Led maintenance of laboratory gloveboxes, cryostats, and thin film deposition systems with another graduate student.

**University of California, Irvine** **(January-April 2010)**
*Graduate student research lab rotation*
Material characterization and accelerated lifetime testing of thermal barrier coatings for use in turbine jet engines

**University of California, Irvine** **(June-December 2009)**
*Graduate student research lab rotation*
Characterized grain and grain boundaries in lithium-doped YSZ using Kelvin Probe Force Microscopy and Electron Backscatter Diffraction Analysis

**Boston University**, Boston Massachusetts **(March-May 2009)**
*Independent Study on turbomachinery blades*
Developed thermal-mechanical model to improve the lifetime of plasma barriercoating of turbomachinery blades.

**University of California, Irvine** **(June-August 2008)**
*Computational fluid dynamics (UCI AGEP Summer Fellow)*
Conducted comparative studies on land-based power generators using computational fluid dynamic solvers to determine the most efficient power generator

**Boston University**, Boston Massachusetts **(August 2006-May 2008)**
*Thermal and energy control in USAF satellite competition.*
Designed and developed a functional thermal control system to maintain a sustainable temperature environment for critical, temperature-sensitive components in a proposed USAF satellite.

**Tesoro Corporation**, Kapolei, Hawaii **(June-August 2006)**
*Determining effective solutions for increase product efficiency (Mech. Eng. Intern)*
Facilitated with senior scientists and engineers to enhance the efficiency of the refinery by 2% to separate crude oil through qualifying new material suppliers

## PRESENTATIONS

**Center for Advanced Solar Photophysics** **June 2013**
Talk: *Optical spectroscopy in PbSe quantum dot field-effect transistors*

**Center for Advanced Solar Photophysics** **August 2012**
Talk: *PbSe quantum dot films with high electron mobility > 7 cm$^{2}$V$^{-1}$s$^{-1}$*

**Center for Advanced Solar Photophysics** **August 2011**
Talk: *Charge transport in PbSe quantum dot films*

**University of California Irvine** **August 2009**
Talk: *Characterization of grains and grain boundaries of solid oxide fuel cell materials using Kelvin Probe Force Microscopy*

**Boston University** **April 2008**
Talk: *Thermal and Electrical Design for BUSAT Application:*
*Air Force Critical Design Review*

## PUBLICATIONS

[1] J. Tolentino, M. Law, Infrared transmission of PbSe quantum dot field-effect transistors, *In preparation* (2015).

[2] J. Tolentino, M. Law, Elimination of bias stress effect in ligand—free quantum dot field effect transistors, *In preparation* (2015).

[3] J. Zhang, J. Tolentino, R. Smith, J.Zhang, M. Beard, M. Law, A. J. Nozik, and J. C. Johnson, Carrier transport in PbS and PbSe QD films measured by photoluminescence quenching, *J. Phys. Chem. C*, **118**(2014) pp. 16228-16235.

[4] T. Otto, C. Miller, J. Tolentino, Y. Liu, M. Law, and D. Yu, Gate-dependent carrier diffusion length in PbSe quantum dot field-effect transistors, *Nano Lett.,* **13** (2013), pp. 3463-3469.

[5] Y. Liu$^{*}$, J. Tolentino$^{*}$, M. Gibbs, R. Ihly, C. L. Perkins, Y. Liu, N. Crawford, J. C. Hemminger, M. Law, PbSe quantum dot field-effect transistors with air stable electron mobilities above 7 cm$^{2}$V$^{-1}$s,$^{-1}$ *Nano Lett.,* **13** (2013), pp. 1578-1587.
*Authors contributed equally

[6] R. Ihly, J. Tolentino, Y. Liu, M. Gibbs, M. Law, The photothermal stability of PbS quantum dot solids, *ACS Nano* **5** (2011), pp. 8175-8186.

[7] Y. Liu, M. Gibbs, C. L. Perkins, J. Tolentino, M. H. Zarghami, J. Bustamante Jr, M. Law, Robust, functional nanocrystal devices using Atomic Layer Deposition, *Nano Lett.,* **11**, (2011), pp. 5349-5355.

## HONORS AND

National Science Foundation Graduate Research Fellowship (2010-2013)

AWARDS

Diversity Fellowship – University of California Irvine (2009)
UCI Alliance for Graduate Education and Competitive Edge Summer Fellowship (2009)
Boston University Dean's List (2005-2008)
Boston University CenSSIS Scholar Award (2005-2006)
International Baccalaureate Diploma

SKILLS

IGOR Pro, MATLAB, LabView
Solution-based thin film preparation
Quantum dot (Core, core-shell) synthesis
Cleanroom procedures
Photoluminescence spectroscopy
X-ray diffraction (powder, thin film)
Raman spectroscopy
Schlenk line techniques
TEM Cross Section Sample Preparation: Focused Ion Beam, Ion Milling
Solar cell and FET fabrication and characterization
Solidworks, AutoCAD, COMSOL
Glovebox use & maintenance
Atomic layer deposition & maintenance
Thermal evaporation
Fourier-transform spectroscopy
Microscopy (SEM, TEM, SKPM,AFM)
Electron Backscatter Diffraction
Visual C++, Absorption spectroscopy

# ABSTRACT OF THE DISSERTATION

Designing quantum solids for optoelectronic devices through matrix engineering

By

Jason Tolentino

Doctor of Philosophy in Material Science & Engineering

University of California, Irvine, 2015

Assistant Professor Matt Law, Chair

Colloidal quantum dot (CQD) solids represent a class of materials that allows one to control the optical and electronic properties due to their unique size-dependent properties with special electronic and optoelectronic device applications. Unfortunately, integration of these materials into high performing devices such as transistors and solar cells have been challenging due to: 1) uncontrolled environmental stability 2) lack of accurate control over charge carrier type and mobility 3) poor device operational stability and 4) limited experimental methods to probe the density of states in these materials in order to understand fundamental electronic and optical properties. In this thesis, we demonstrate the ability to stabilize and improve the environmental stability of these materials with amorphous $Al_2O_3$ (a-alumina). More importantly, we can accurately engineer the carrier type and mobility by varying the thickness of the alumina. Through a combination of small, compact inorganic ligands and the ability to passivate surface electronic traps, air-stable, high electron mobility PbSe QD field-effect transistors (FET) are obtained.

We then show that we can also improve transistor device operational stability through an *in-vacuo* ligand exchange with $H_2S$ gas introduced in an atomic layer deposition (ALD) chamber. We find that this method is universal when volatile ligands are used. Possible mechanisms for device instability will be discussed such as proton migration and trap passivation. Using an optimized film preparation, this work will be the first demonstration of a QD FET with an electron mobility greater than 10 $cm^2\ V^{-1}\ s^{-1}$ that is also operationally stable.

Finally, we introduce a unique transmission spectroscopy technique of field-effect transistors to electrostatically probe induced charge carriers in PbSe QD films. With this technique we resolve occupation of quantized states of the quantum dots rather than the matrix or interfacial states. This platform is used to test fundamental transport models as it relates to disordered semiconductors such as QDs. From this technique, we can draw important conclusions about charge transport at room temperature. This novel experimental method can be extended to other experimental setups such as photoluminescence and photoconductivity in order to understand how to rationally improve the electronic properties of QD films.

# CHAPTER 1

# INTRODUCTION: APPLICATIONS, ELECTRONICS, AND SURFACE CHEMISTRY

## 1.1 MOTIVATION

### 1.1.1 SEMICONDUCTORS AND NANOTECHNOLOGY

We currently live in a modern society where the use of semiconductors affects nearly all aspect of our lives. This large presence has changed the way in which we conduct business and research, acquire and store energy, as well as the way in which we communicate with each other across the globe. The advent of scientific understanding of semiconductors began with simple experiments on the electrical properties of materials which includes temperature dependent resistivity, rectification, and light-sensitivity which we now call the photolvatic effect. The earliest report of *semiconducting* behavior was in 1833 where Michael Faraday measured the resistance of “sulphurette of silver” (silver sulfide) as a function of temperature.[1] He found that by “applying a lamp” to the sample which increased the temperature of the material, the electrical conductivity increased. In the 19th century, this was contrary to what was known because for *metallic* samples such as copper, the opposite behavior is observed where the conductivity decreased as temperature is increased. A unified theory describing semiconducting behavior was not realized until Albert Einstein’s seminal publication on the photoelectric effect, which was later fortified by the subsequent work of Wilson, Mott, and Schottky.[2-5] Devices that benefited from semiconducting materials were developed based on empirical data before theory caught up with experiments. One of the most important discoveries, which led to a Nobel Prize in Physics, was the invention of the first transistor produced by Shockley, Bardeen, and Brattain at Bell Laboratories in 1947.[6] Today, transistors represent the fundamental building block for modern electronic devices and made its mark in allowing smaller radios, calculators, and most importantly computers. The drive for smaller electronic devices calls for even smaller transistors and thus driving the need for semiconducting materials that comprise of them. This driving force for developing hardware with increasing density of transistors was empirically described and predicated by Gordon Moore. This law, later popularized and termed as *Moore's Law* states that the number of transistors per processor will double every 12 months.[7] This prediction has proven to be accurate because as the capabilities and complexities of modern digital electronic devices continue to expand, the number and size of these transistors and processors must increase. Despite the success of this prediction, this *law* can be treated only as an observation and not a physical law that limits the performance and size of current and future transistor technology. With this in mind, the advancement of nanotechnology could spur the development of smaller processors and set back the date to which Moore's Law no longer applies; of course there will be a point where it is no longer to keep Moore's Law alive. At the forefront of increasing the density of transistors are low-dimensional semiconductors such as semiconducting nanowires and quantum dots. Colloidal semiconductor quantum dots are solution-processed semiconductors can be varied in size from 1-100 nm and could possibly be the next step towards the ever-shrinking semiconducting technology. These materials offer many opportunities with respect to technological applications, but there are many challenges that must be met to realize its utility in the semiconductor industry. In the next section, we must first understand semiconductors and the unique properties of these materials on the nanoscale.

### 1.1.2 SEMICONDUCTOR PROPERTIES FROM MOLECULAR ORBITAL THEORY

From a very basic definition, a semiconductor is a material that has an electrical conductivity that falls in between metals, which conduct heat and electricity, and insulators that do not conduct hear or electricity. The properties of semiconductors are dictated by the dispersion relationship (*E-k)* or band structure of the material, specifically the energy difference between the valence band and the conduction band. The valence band is constructed from occupied bonding orbitals and the conduction band is constructed from unoccupied anti-bonding orbitals. To understand this, we will take a simple molecule and use the guidelines set by the *linear combination of atomic orbitals* to construct the molecular diagram for a simple molecule $H_2$. According to molecular orbital theory, when two atoms are brought together, their *atomic* orbitals will overlap and form one that is spread between the two atoms. The mixing of these two atomic orbitals depends on the sign of the wave functions. In the case for $H_2$, each hydrogen atom will contribute one 1s atomic orbital. When two hydrogen atoms come together, each 1s hydrogen orbital interacts and produces two molecular orbitals: bonding and anti-bonding. If the electrons are in phase, they will have constructive interference resulting in a sigma bonding orbital (σ-bond) is the molecular orbital is symmetric with respect to the rotation around the bond axis. The bond formation stabilizes both atoms, which is lower in energy than their atomic orbitals as seen in figure 1.1 below. If the electrons are out of phase, they will have destructive interference and hence there will be a zero probability of finding an electron. This anti-bonding molecular orbital ($\sigma^*$-bond) energy is much higher than the original atomic orbitals as seen in Figure 1.1.

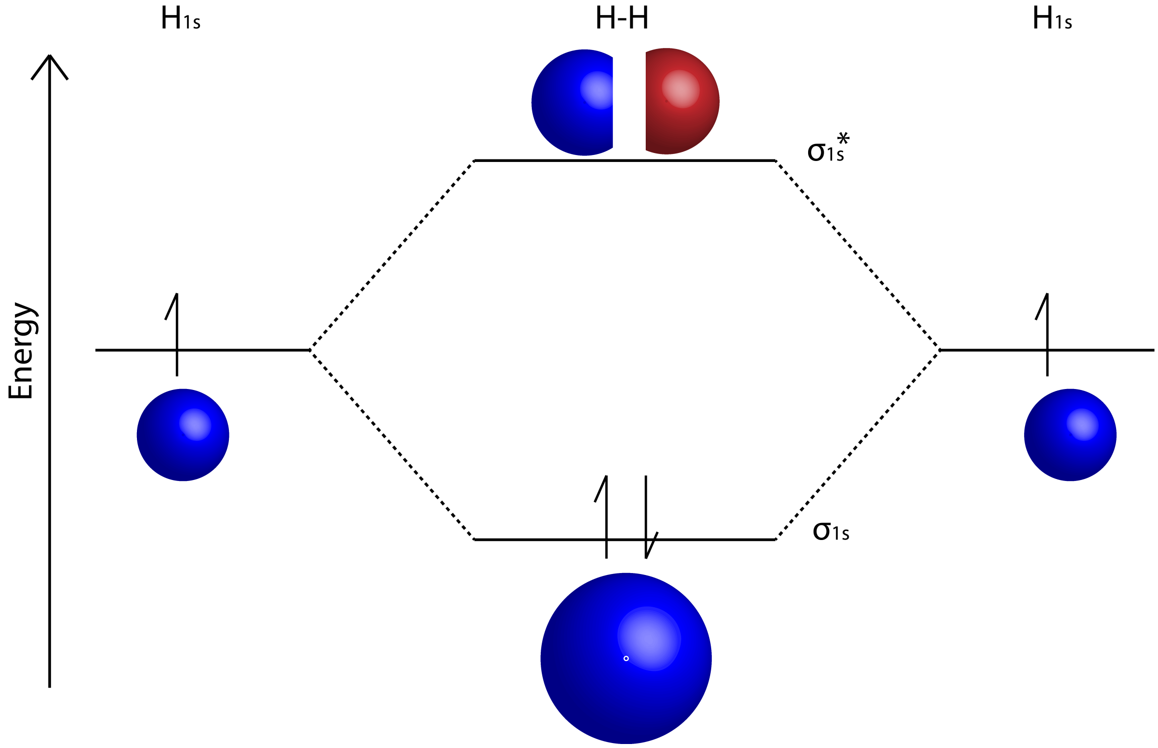

**Figure 1.1 Molecular orbital diagram for $H_2$**

From this simple molecule, we can imagine in an infinite lattice of atoms (e.g. bulk crystals), there will be an infinity number of bonding and anti-bonding orbitals that will be formed, and this infinite number of orbitals can be considered a *band* in simplest of terms. The difference in energy between the upper edge of the valence band and the lower edge of the conduction band is called the band gap and is analogous to the first electronic transition (HOMO-LUMO gap) in small molecular systems.

The band gap energy and the occupation of these bands controls many aspects of the optical and electronic properties of a material. Recalling our undergraduate electronic properties of materials, we can classify a material's electronic and optical properties as a metal, a semiconductor, or an insulator. Metals have a partially occupied band as the highest unoccupied band and conducts electrons without exciting a carrier to the conduction band. Insulators are described as having large band gaps that at room temperature, there is not enough thermal excitation to conduct electrons. Semiconductors fall in between these two regimes. Generally, semiconductors have band gaps from 0 eV (e.g. graphene) all the way through 4.0 eV (e.g. zinc sulfide). In general, the electronic properties of materials follow periodic table trends such as diamond (C, 5.5 eV), silicon (Si, 2.1 eV), selenium (Se, 1.74 eV), germanium (Ge, 0.67 eV), and tin (Sn, 0.1 eV). In this illustrative example, as you go across the periodic table the electronegativity increases exhibiting a stronger, directional covalent bonding, and thus having larger band gaps. The relative electronegativity values as you go across the periodic table are governed in party by the trends in the number of valence electrons that an atom holds. This illustrates the significance of the crystal structure and bonding when discussing semiconductors.

The importance of crystal structure emphasizes a key component in applying the molecular orbital theory to predict the electronic properties of materials, particularly when materials must have long-range order such that each atom is in the same bonding configuration and environment (e.g. oxidation state, bonding geometry). Highly disordered materials cannot be described as having bands comprised of orbitals with nearly all the same energies. Such discontinuity in the lattice due to differences in bonding geometries leads to variations in energies and prevent disordered materials from having continuous, degenerate band structures. In the absence of long-range order, boundaries between different crystal orientations and impurities such as interstitials and vacancies are found to have a drastic effect on the electronic properties of these materials. The scale in which these ordered domains come together is determined by the extent of delocalization (electron and hole) over the material, which is the most interesting component for semiconductor quantum dots. Unfortunately, these materials do not behave as *artificial atoms* as many have described them to be due to the inherent disorder of these materials. The effects of disorder will later be discussed in Chapter 6.

In the previous paragraph, while the periodic table can act as a guide for predicting the electronic properties of single element crystals, most semiconductors are composed of two or more elements. In binary systems, bonding occurs where a metal is oxidized by the more electronegative non-metal, which results in a cation (positively charged metal) and an anion (negatively charged non metal). In many cases, the highest occupied atomic orbital of the metal loses its electrons and becomes the conduction band. By similar arguments, the highest unoccupied atomic orbitals of the non-metal gains electrons during bonding and become the valence band. As such, the conduction band and valence band are made of metal-like and non-metal like orbitals (Figure 1.2). From this simple relationship, one can easily estimate the electronic properties of a bulk material based on the bonding between two elements. For example, compounds with ionic bonding tend to be insulators, while more covalent bonding leads to semiconducting properties. While crystal structure is important in determining the electronic structure and other physical properties, the band gap of binary semiconductors is mostly dominated by the electronegativity of the metal and non-metal. Such properties are of interest, with respect to lead selenide (PbSe) as this will be the primary focus for this work.

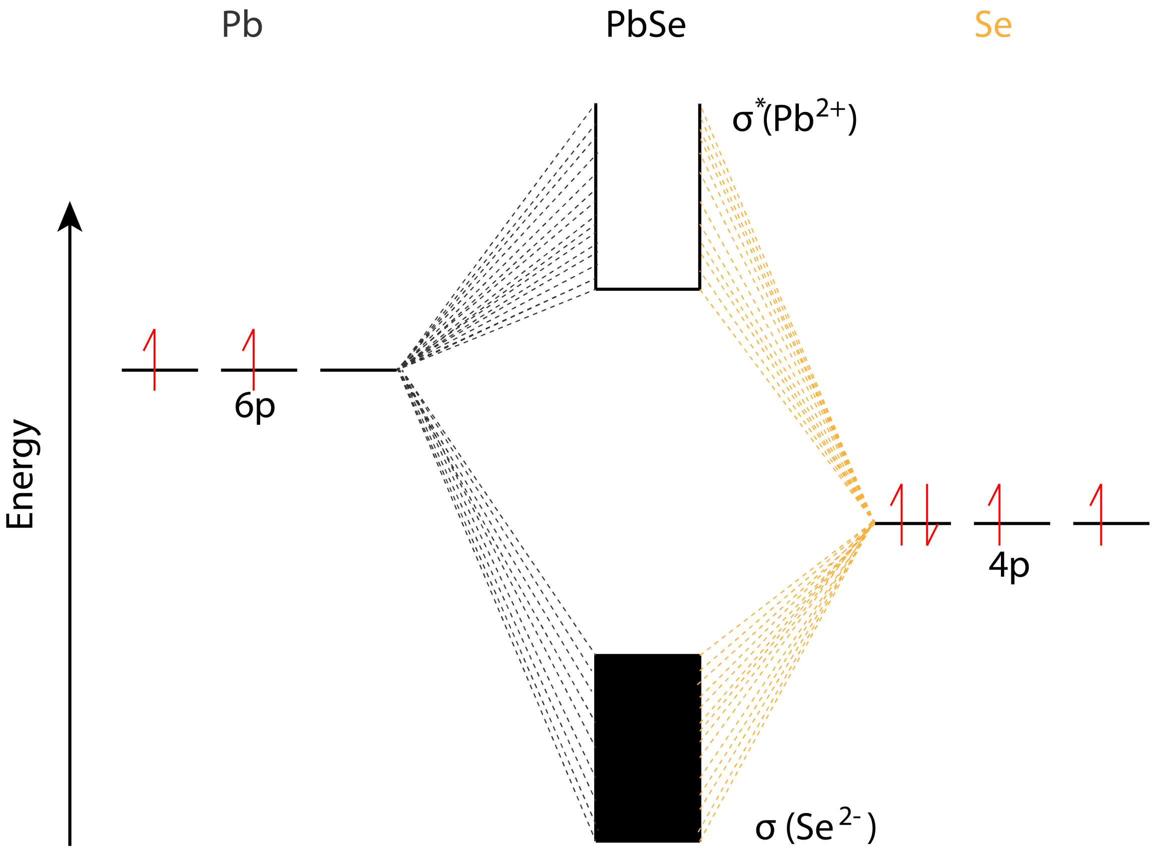

**Figure 1.2: Simplified molecular orbital diagram for bulk PbSe**

### 1.1.3 QUANTUM CONFINEMENT EFFECTS

The electronic structure of metal chalcogenide nanocrystals is similar to that of the same material in *3D*. The confined dimensions of nanocrystals lead to physical, optical, and electronic effects.[8-13] To understand the quantum size effect, the *particle-in-a-box* is a simple model used where the energy of a particle in an isolated potential is determined. The energy of a confined particle is then determined by the size of the box, the mass of the particle, and the principle quantum number.[14] As the size of box is decreased, the energy of the particle increases. In all semiconductors, when an electron is excited into the conduction band, it is electrostatically associated with the hole in the valence band. This *exciton* or bound electron-hold pair becomes delocalized over a given distance, which is defined as the *Bohr radius* because of it is analogy to the hydrogen Bohr model. In bulk semiconductors, the Bohr radius is significantly smaller the crystal lattice. However, if the material is made smaller than the Bohr radius, the energy of the exciton is affected by quantum confinement, which gives rise the size tunable band gap for nanocrystal materials.[15] For PbSe, the Bohr radius is approximately 47 nm, which means that nanocrystals must be smaller than 24 nm in diameter to be quantum confined. Figure 1 below shows several absorption spectra for different size PbSe quantum dots synthesized for this dissertation.

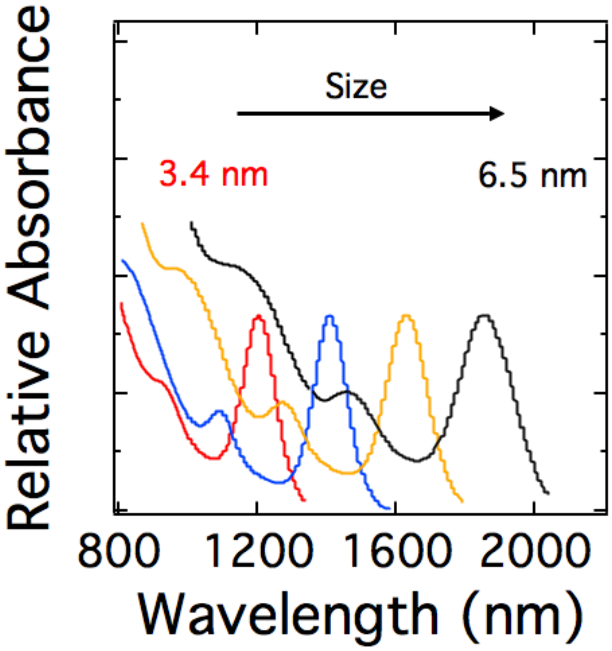

**Figure 1.3: Absorption spectra for four PbSe quantum dot sizes.** The black spectrum has a peak maximum at 1860nm corresponding to a quantum dot size of 6.5 nm. The orange spectrum has a peak maximum at 1630 nm corresponding to a size of 5.5 nm. The blue spectrum has a peak maximum at 1410 nm corresponding to a size of 4.4 nm. The red spectrum has a peak maximum at 1200 nm corresponding to a size of 3.4 nm.

Upon first inspection of figure 1.3, we see that the absorption spectra have a few features. Unlike bulk semiconductors where the bands are continuous, nanocrystals have discrete energy states because nanocrystals have fewer atoms results in fewer orbital overlaps, and less degeneracy at the band edge. As a result, there is enhanced absorption for some energies, but suppressed absorption at energies that are between state-to-state transitions (Figure 1.4). Moreover, due to the inhomogeneous nature of colloidal quantum dots, perturbations to the idealized artificial solid structure modifies the discreetness of the density of electronic states, thus broadening the excitonic absorption spectra as seen above. Further details concerning how variations in coupling and dot size affect the electrical properties of quantum dot arrays are provided in Chapter 6. For a detailed review refer to Hanrath's review paper.[16]

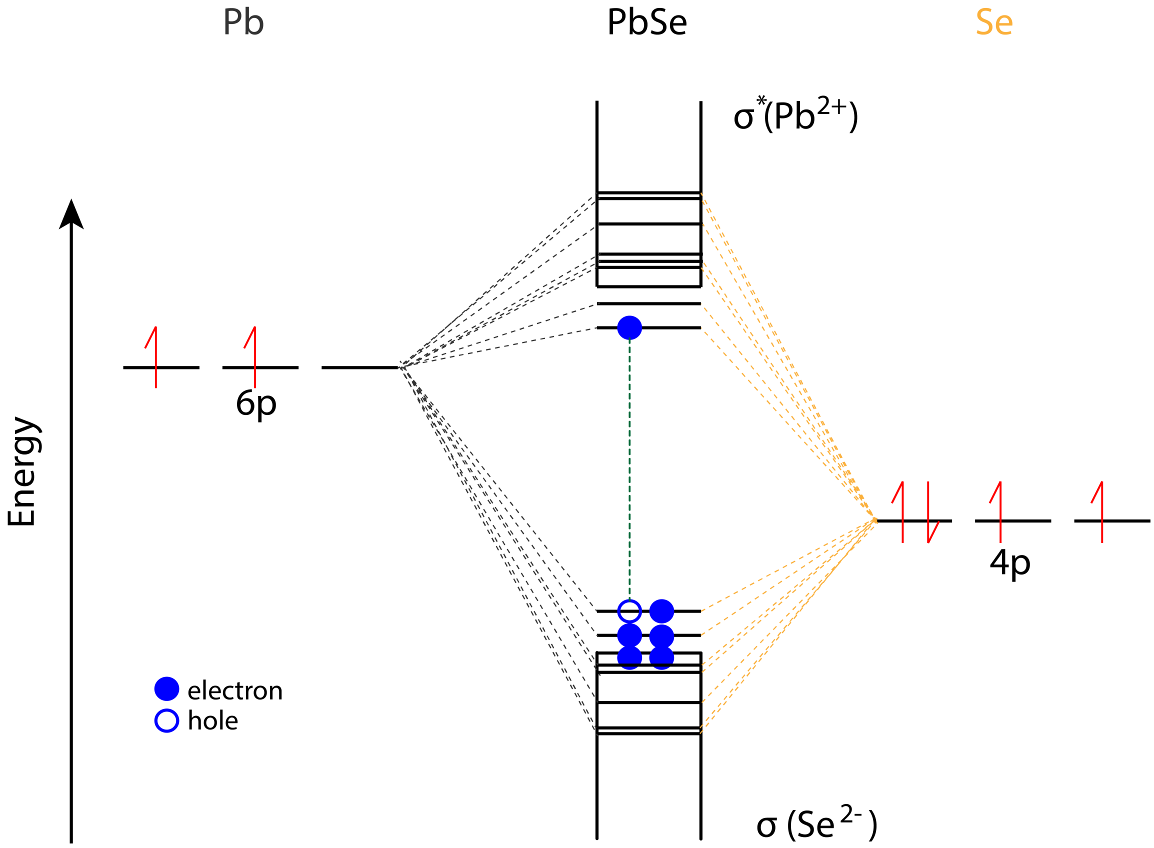

**Figure 1.4:** Simplified molecular orbital diagram for PbSe quantum dot

## 1.2 APPLICATIONS OF SEMICONDUCTOR QUANTUM DOTS

### 1.2.1 DEVICES UTILIZING THE PHOTOVOLTAIC EFFECT

The use of quantum dots in photovoltaics deserves its own in-depth coverage and as a result has been the subject of many review articles.[17-20] However, a short summary of the state-of-the-art will help motivate the specific research goals within this thesis. Leveraging on the ability to produce devices from a solution-processable ink of quantum dots, the possibilities to develop photovoltaic modules are endless. For example, demonstrations using roll-to-roll printing and spray coating of quantum dot inks have been demonstrated which would greatly impact production costs and allow wide-scale implementation of this renewable source of energy.[21,22] As such, the ease to fabricate devices from inks makes them ideal for three device architectures as is discussed below.

### 1.2.2 Grätzel cells

Many of the earlier devices utilizing quantum dots were Grätzel-like dye-sensitized solar cells. In a standard Grätzel cell, a light absorbing dye (i.e. Ru complex) sensitizes $TiO_2$ nanoparticles.[23,24] Light absorbed by the dye (typically $I^-/I_3^-$ redox couple) allows for photo induced charge separation in which the excited electrons are injected in the $TiO_2$. These injected electrons are then transported through the $TiO_2$ to a back contact and the electrons reach the counter electrode. Due to the oxidation of the dye, it will accept an electron from the $I^-$ redox mediator leading to the regeneration of the dye and oxidation of $I^-$ to $I^-_3$. This ion diffuses to the counter electrode and gets reduced by the injected electrons from the $TiO_{2,}$ which completes the circuit. The efficiency of this device depends on the energy levels of all components of the cell: the excited and ground state of the photosensitizer, Fermi level of the $TiO_2$, and the redox potential of the redox mediator ($I^-/I_3^-$).

As an alternative to the Ru complex photosensitizer, quantum dots such as CdS[24-26], PbS[27,28], and CdSe[29-31] have been used and much of the research focuses on the development of the appropriate surface chemistry that would like these quantum dots to porous $TiO_2$ electrodes. While this method has shown early success, it was found that the triiodide/iodide liquid electrolyte, which acted as a hole conductor, resulted in the chemical degradation of the QDs due to the iodide ions.[32] This electrolyte was then replaced with less corrosive liquid electrolytes such as polysulfide[33], cobalt complexes[34], or solid hole conductors.[35] Despite the improved chemical stability of quantum dot sensitized solar cells, these devices utilizing quantum dots suffer from the same problems *conventional* solar cells based on quantum dots: poor performance due to electronic disorder (i.e. charge trapping). Some of the approaches to reduce this effect have been using organic ligands or inorganic halide ligands[32,33] or by forming core/shell structures such as PbS/CdS[36,37] and PbS/$CH_3NH_3PbI_3$.[38]

### 1.2.3 Schottky Diodes

One of the simplest designs for quantum dot solar cells is the Schottky device in which a quantum dot film is sandwiched between two electrodes.[39,40] The driving force for carrier separation, as discussed by *Luther et. al*, is the work function difference between the two metal electrodes through which the field drives electrons and holes to their respective carrier selective electrode. There have been recent improvements in the open circuit voltage and overall device efficiency through the introduction of a blocking layer[41] and “careful” purification of the quantum dots[40], respectively. The resurgence of this design provides a simple architecture because of the reduction in the amount of interfaces to account for. In addition, it also allows one to study the transport properties in more detail in order to understand what is limiting device performance.[42] Unfortunately, despite the simplicity of the device architecture, the overall device performance is still behind that of p-n heterojunctions possibly due to Fermi level pinning.[43]

### 1.2.4 p-n heterojunction

In order to mitigate the effects of Fermi level pinning, which reduces the maximum attainable open-circuit voltage, a p-n heterojunction device is used in which two layers of dissimilar (or similar) semiconductors with different band gaps are brought together. The driving force for charge separation can include: i) gradient in work function, ii) gradient in electron affinity, iii) gradient in band gap, or iv) gradient in density of states. The most widely used method for establishing the charge-separating field is by varying the doping concentration within the active layer, which is what the quantum dot community has been doing with their variety of *surface passivation*[20,44-47] techniques and *quantum funneling*.[18,48]

### 1.2.5 Devices with enhanced performance utilizing multiple charge carriers

Due to quantum confinement effects, either in 1D (wires or rods) or in 0D (dots), novel photophysics appear especially when a quantum dot is excited with UV/visible light. In the previous discussion in Section 1.1.3, when a photon of sufficient energy is absorbed by a quantum dot, an electron-hole (e-h) pair is produced. The lowest absorbing states is generally termed the first exciton state, where excitons are e-h pairs that interact through a Coulomb potential. Compared to bulk semiconductors, the exciton binding energy is only present if the thermal energy, *kT*, is lower than the exciton binding energy which is only a few millielectron volts. In quantum confined materials, if the incident photon energy is larger than the band gap, then higher energy states absorb the photon to create a *hot exciton* with excess energy. This excess energy prior to cooling is converted to kinetic energy and if the excess kinetic energy is greater than twice the band gap of the semiconductor, it can produce one or more extra e-h pairs. In bulk semiconductors, this phenomenon is reduced because carriers cool to the band edge via phonon emission extremely quick, which will compete efficiently with hot carrier extraction. As such, due to quantum confinement effects in quantum dots, hot carrier cooling is slowed down so that multiple exciton generation (MEG) can compete more efficiently. While there is evidence for MEG in colloidal solutions of isolated quantum dots,[49-52] there has not been any experimental evidence for enhancement in devices due to MEG until 2011.[53] While this is a great accomplishment, the enhancement in current occurred at $E > 3$ eV which does not contribute much to the photocurrent if you compare the number of incident photon flux at $E \geq 3$ eV with that of $0.4 \text{ eV} < E < 3$ eV. In order to fully maximize the potential for MEG enhancement in devices, one would have to improve the carrier diffusion lengths in the *red* portion of the solar spectrum because of the poor photon to electron conversion efficiency for $E < 3$ eV for devices that demonstrated MEG. In this thesis, I will show how we can improve carrier mobility and thus carrier diffusion lengths with the goal to enhance solar cell performance.

### 1.2.6 Field-effect transistors

In addition to photovoltaic applications, the use of quantum dots in films for thin-film transistors offers enormous amount of potential due to the recent breakthroughs in performance (achievement of mobility greater than 30 $\mathrm{cm^2\ V^{-1}\ s^{-1}}$) as a result of properly choosing surface ligands and/or improved chemical treatment and device processing. Up until now, field-effect transistors (FETs) based on quantum dots have been more of a research tool in support of other devices such as solar cells. As such, these devices are the *workhorses* to evaluate charge transport within quantum dot solid films as a function of different processing such as chemical treatments[54-57], *doping*[58-60], and post-treatments.[61-6357-59] Despite the improved carrier mobilities for FETs based on quantum dots, there are still unanswered questions as to how these different chemical treatments improve carrier mobilities, particularly the chemical nature of these treatments and how it improves field-effect mobilities. Furthermore, since these methods in which the field-effect mobility is extracted relies heavily on the applied gate, it would be informative to determine if *trap filling* occurs. In addition, if true commercialization of quantum dots were to be realized, performance metrics such as hysteresis and the bias-stress effect must be addressed. In this thesis, I will address all of these issues in the appropriate chapters to follow.

### 1.2.7 Challenges

While the potential applications of quantum dots in photovoltaics and transistors have been the main motivation to study quantum dots, research in this area is stymied by the lack of accurate knowledge of the surface composition and the chemistry of these materials. Researchers are often times guided by the advancements in solar cell performance without designing complementary experiments to understand the reason for the improved performance. As it will become clear in the following section, understanding the nature of these ligands at the surface is essential for controlling their properties.

## 1.3 PERSPECTIVE - MOLECULAR ORBITAL THEORY AND SURFACE STATES

In this section, I provide a perspective on the concept of surface electronic trap states. While this thesis does not explicitly work through the problems, the experimental results relies on these ideas, which warrants this brief discussion. In order to tackle the problems inherent to using quantum dots in optoelectronic devices, we need to understand the complexities of both electronic structure and surface chemistry of these materials. This deep level of understanding of the electronic structure stands in contrast to the lack of knowledge concerning the surface states of quantum dots. Common ideas put forward are: i) high surface-area-to-volume ratio of these materials means there is larger proportion of atoms in the crystal lattice are surface atoms rather than bulk atoms, ii) excitons confined in the quantum dot is delocalized enough that it can interact with the surface of the quantum dot. Early studies using photoluminescence of cadmium chalcogenide quantum dots have seen differences in the quantum yield (ratio of the number of photons emitted to the number of photons absorbed) depending on the method of preparation.[9,64-66] Adding additional ligands to the solution can also control the intensity of the band-edge emission.[67]

While there is no concise theory on the nature of these surface states, the description that is provided here is consistent with the data that will be presented in this thesis and with theoretical and experimental work reported in literature. This description relies on a simplified molecular orbital theory with surface states. Often times, these states are referred to as *trap states*. In general, surface states can be considered a subset of *trap states* and it can be either on the surface or in the bulk. Surface states are a result of surface reconstructions due to dangling bonds, vacancies, and interstitials. These *trap states* are described as being localized, contrary to the diffuse nature of these low-lying states near the band edges. There are a few exceptions where these surface states are *delocalized,* but the effect on the optical properties and carrier mobility has not been considered.

In order to understand the nature of these states and how it modifies the electronic structure of a quantum dot, we will first consider a simplified molecular orbital diagram. It has been shown that the CBM is formed primarily by the Pb 6p orbital and the VBM is mostly from Se 4p orbital. Despite the valence electron configuration of a Pb atom of $6s^2 6p^2$, the Pb 6s electrons are found to be deep below the VBM, hence only two of the p electrons will participate in chemical bonding with the surrounding Se atoms (Figure 1.5).[68] To see how surface states affects this molecular orbital diagram, we have to consider the coordination environment for a PbSe crystal. Before I continue, I will define some basic nomenclature that will be used during this description. A surface is said to be *relaxed* if it displays the same symmetry as the bulk. A surface is *reconstructed* if it has a different symmetry from the bulk. When discussing mechanisms and driving forces for surface relaxations and reconstructions, I will refer to *dangling bonds* as surface derived *surface states* which has an excess charge density at the surface due to missing surface atoms. This dangling bond charge density is localized at the surface in *surface states*, which can be derived from surface cations or surface anions.

The crystal structure for PbSe can be described as having the rock-salt structure, which is an octahedrally coordinated crystal. As such, six Se or Pb atoms surround every Pb or Se atom. As discussed above, a Pb atom has two valence electrons available for bonding and Se has six. To form an octahedrally coordinated crystal, every Pb atom provides 2/6 electrons to each of its bonds.

For PbSe the atoms at the surface of a *rock salt* nanocrystal will have a different coordination environment than those within the core, either 5-fold coordinate on the {001} or {111} facet with each surface atom bonding to four neighbors in the surface plane and to one atom in the plane directly bellow the surface. These open coordination sites are often referred to as *dangling bonds*. In terms of crystal field theory, this means that the energy of surface lead atomic energy states would be pushed down in energy. In addition, the selenium states will be pushed up in energy. This simple picture qualifies the *mid-gap* energy levels of these surface atoms (Figure 1.5). In the case for lead atoms, the lead orbitals will be empty, while the surface selenium sites are filled. These empty lead orbitals will act as electron traps. Conversely, filled selenium orbitals act as hole traps by dropping electrons into the holes in the excited valence band.

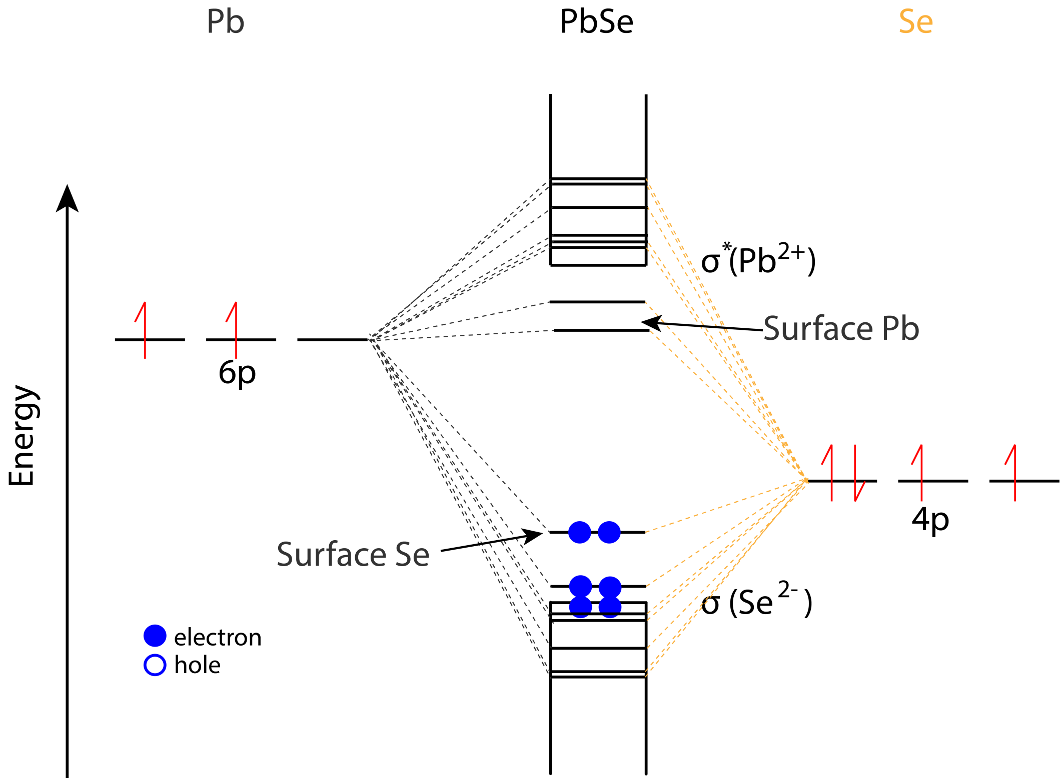

**Figure 1.5. Simplified molecular orbital diagram for PbSe quantum dot with surface states**

Furthermore, depending on the number of dangling bonds, the degree of *mid-gap states* can be tuned with quantum dot shape, stoichiometry, and electron-donating/electron accepting ligands. In a seminal paper, *Kim et. al* demonstrated that off stoichiometric dots results in the introduction of states (empty or filled) within the band gap of the semiconductor.[69] These states are highly localized on lead or sulfur/selenium atoms. Based on this important theoretical work, altering or removing ligands that bind to the quantum dots can affect the stoichiometry and more importantly affect the density and positional energy of the surface states. While the chemical nature of these ligands is important to understand in order to develop a robust method to process these quantum dots without compromising the electronic and optical properties, this thesis will establish a platform and technique to control and monitor the electronic properties as a function of different processing and ligand exchange chemistries.

This thesis is divided into chapters based on using transistors as a reliable platform to probe the electronic and optical properties of quantum dot films. In chapter 2 and 3, I describe the theory of field-effect transistors and how we process and manufacture quantum dots used in this thesis. By establishing the state-of-the-art in quantum dot film processing, I will then discuss how we can improve field effect mobility (Chapter 4), eliminate the bias-stress effect in quantum dot thin-film field-effect transistors (Chapter 5), and finally develop a platform to determine the role of these trap states using field-effect transistors (Chapter 6).

## 1.4 GENERAL EXPERIMENTAL DETAILS

### 1.4.1 Reagents

Lead oxide (PbO, 99.999%), selenium (99.99%), bis(trimethylsilyl)sulfide (TMS) oleic acid (OA, tech. grade, 90%), Diphenylphosphine (DPP, 98%), 1-octadecene (ODE, 90%), oxalic acid (anhydrous), trioctylphosphine (TOP, technical grade, >90%), 1,2-ethanedithiol (EDT,>98%), 1,4-benzenedithiol (BDT, 99%), formic acid (99+%), ammonium thiocyanate (SCN, >97.5%), 1,3,5-tricarboxylic acid (BTC, 95%), methanol (99.8%)

### 1.4.2 ALD precursors

Trimethylaluminum, elec. Gr. (TMA, 99.999%+), Dimethylcadmium (DMC, 97%), Diethylzinc (DEZ, min. 95%), Titanium (IV) chloride ($TiCl_4$, 99%), Deionized water (DI, min 50kOhm, freeze-pump-thaw 5 times using air-free techniques)

### 1.4.3 General preparation and materials characterization

All manipulations were performed under air-free conditions unless otherwise indicated using standard Schlenk line techniques or inside a glove box. Fourier-transform infrared spectra (FTIR) were obtained on a Thermo Scientific Nicolet 6700 spectrometer. UV-Vis absorption spectra were collected using a PerkinElmer Lambda 950 spectrometer. For air-free measurements, an airtight optical cell consisting of two 1.33" mated UHV ConFlat sapphire viewports were used. For structural characterization, x-ray diffraction were performed using a Rigaku Smartlab XRD using Cu Kα irradtion. For general film morphology a FEI Magellan 400 scanning electron microscope was used at 10 kV and 25 pA. To determine the size of the quantum dots, a Philips CM-20 transmission microscope operating at 200 kV was used.

For elemental analysis, multiple techniques were used. X-ray photoelectron spectroscopy (XPS) was used to determine sulfur concentration. XPS depth profiles were acquired using a modified Physical Electronics 5600 XPS with monochromatic Al Kα radiation (1486.6 eV) and a pass energy of 29 eV. Secondary ion mass spectrometry (SIMS) was performed by Evans Analytical Group using a Physical Electronics ADEPT-1010 dynamic SIMS instrument. Depending on film conditions and elements of interest, a 1 keV Cs ion beam for anions (S, O, H, C, P, Si, Al, Se), a 14.5 keV Cs ion beam was using for C,S, P, and Si, an 8 keV $O_2$ ion beam for cations (Na, Pb, Al, Zn, Ca, Fe, Ti). Estimated detection limits for elements in alumina overcoated films were 1 X $10^{19}$ atom $cm^{-3}$ for sulfur and hydrogen, 1 X $10^{18}$ atom $cm^{-3}$ for carbon, and 1 X $10^{17}$ atom $cm^{-3}$ for phosphorous and silicon. Estimated detection limits for the silicon substrate in which the films were prepared on were 1 X $10^{19}$ atom $cm^{-3}$ for hydrogen, 5 X $10^{17}$ atom $cm^{-3}$ for carbon and oxygen, and 1 X $10^{17}$ atom $cm^{-3}$ for sulfur and phosphorous. Atomic concentrations are accurate within 20% for the alumina layer using an $Al_2O_3$ standard and a factor of two in the PbSe/alumina layer using a ZnSe standard.

Estimates for interdot distance were calculated using density functional theory (DFT) provided by Dr. Nathan Crawford. Two PbSe slabs separated with $S^{2-}$ or $EDT^{2-}$ ligands were modeled using the RI-J method in the TURBOMOLE 6.4 software package. Two triangular slabs of $[Pb_{64}Se_{59}]^{10+}$ were aligned with their Pb {111} surface facing each other. Ten of either sulfide or ethandithiolate ligands were inserted in between the two slab and the neutral system was allowed to relax to an energy minimum. To estimate the interslab distance, interplane distances were taken as the difference between the average $z$-values of each plane.

Transistor measurements at room temperature were performed in a nitrogen-filled glovebox with a probe station using a Keithley 2636A dual-channel SourceMeter and Keithley 238 SourceMeter (for gated 4-point transistor measurements) driven by homemade LabView software. Low temperature transistor measurements were performed in a Janis ST-100 cryostat with a custom 5-probe sample mount. Liquid nitrogen was used to vary the sample temperature between 80 and 300K.

## REFERENCES

(1) Faraday, M. Experimental Researches in Electricity. Fourth Series. *Phil. Trans. R. Soc. Lond.* **2006**, 1–17.

(2) Einstein, A. On a Heuristic Viewpoint of the Creation and Modification of Light. *Ann d Phys* **1905**.

(3) Wilson, A. H.; Wilson. Semi-Conductors and Metals; Cambridge University Press, 2011.

(4) Mott, N. F. The Theory of Crystal Rectifiers. *Proc. R. Soc. Lond. A.* **1939**, *171*, 27–38.

(5) Schottky, W. Vereinfachte Und Erweiterte Theorie Der Randschicht-Gleichrichter. *Z. Physik* **1942**, *118*, 539–592.

(6) Shockley, W.; Bardeen, J.; Brattain, W. H. Shockley: the Electronic Theory of the Transistor - Google Scholar. *Science* **1948**.

(7) Moore, G. E. The Density of Transistors Assembled on a Microchip Doubles Every 12 Month! *Electronics* **1965**, *38*.

(8) Nirmal, M.; Dabbousi, B. O.; Bawendi, M. G.; Macklin, J. J.; Trautman, J. K.; Harris, T. D.; Brus, L. E. Fluorescence Intermittency in Single Cadmium Selenide Nanocrystals. *Nature* **1996**, *383*, 802–804.

(9) Bawendi, M. G.; Carroll, P. J.; Wilson, W. L.; Brus, L. E. Luminescence Properties of CdSe Quantum Crystallites: Resonance Between Interior and Surface Localized States. *J. Chem. Phys.* **1992**, *96*, 946.

(10) Nirmal, M.; Brus, L. Luminescence Photophysics in Semiconductor Nanocrystals.

*Accounts of Chemical Research* **1999**.

(11) Bawendi, M. G.; Steigerwald, M. L. The Quantum Mechanics of Larger Semiconductor Clusters (" Quantum Dots"). *Annu. Rev. Phys. Chem.* **1990**, *41*, 477–496.

(12) Krauss, T. D.; Brus, L. E. Charge, Polarizability, and Photoionization of Single Semiconductor Nanocrystals. *Physical Review Letters* **1999**, *83*, 4840–4843.

(13) Brus, L. Quantum Crystallites and Nonlinear Optics. *Appl. Phys. A* **1991**, *53*, 465–474.

(14) Schrodinger, E. An Undulatory Theory of the Mechanics of Atoms and Molecules. *Physical Review* **1926**, *28*, 1049–1070.

(15) Brus, L. E. Electron–Electron and Electron-Hole Interactions in Small Semiconductor Crystallites: the Size Dependence of the Lowest Excited Electronic State. *J. Chem. Phys.* **1984**, *80*, 4403.

(16) Hanrath, T. Colloidal Nanocrystal Quantum Dot Assemblies as Artificial Solids. *J. Vac. Sci. Technol. A* **2012**, *30*, 030802.

(17) Kamat, P. V. Boosting the Efficiency of Quantum Dot Sensitized Solar Cells Through Modulation of Interfacial Charge Transfer. *Accounts of Chemical Research* **2012**.

(18) Kramer, I. J.; Sargent, E. H. Colloidal Quantum Dot Photovoltaics: a Path Forward. *ACS Nano* **2011**.

(19) Talapin, D. V.; Lee, J. S.; Kovalenko, M. V. Prospects of Colloidal Nanocrystals for Electronic and Optoelectronic Applications. *Chem. Rev.* **2009**.

(20) Lan, X.; Masala, S.; Sargent, E. H. Charge-Extraction Strategies for Colloidal Quantum Dot Photovoltaics. *Nature Materials* **2014**, *13*, 233–240.

(21) Kamat, P. V. Quantum Dot Solar Cells. Semiconductor Nanocrystals as Light Harvesters. *Journal of Physical Chemistry C* **2008**, *112*, 18737–18753.

(22) Kramer, I. J.; Minor, J. C.; Moreno-Bautista, G.; Rollny, L.; Kanjanaboos, P.; Kopilovic, D.; Thon, S. M.; Carey, G. H.; Chou, K. W.; Zhitomirsky, D.; *et al.* Efficient Spray-Coated Colloidal Quantum Dot Solar Cells. *Adv. Mater.* **2014**, *27*, 116–121.

(23) O'Regan, B.; Gratzel, M. A Low-Cost, High-Efficiency Solar-Cell Based on Dye-Sensitized Colloidal Tio2 Films. *Nature* **1991**, *353*, 737–740.

(24) Hagfeldt, A.; Boschloo, G.; Sun, L.; Kloo, L.; Pettersson, H. Dye-Sensitized Solar Cells. *Chem. Rev.* **2010**, *110*, 6595–6663.

(25) Gerischer, H.; Lubke, M. A Particle Size Effect in the Sensitization of $TiO_2$ Electrodes by a CdS Deposit. *J. Electroannal. Chem.* **1986**, *204*, 225–227.

(26) Vogel, R.; Pohl, K.; Weller, H. Sensitization of Highly Porous, Polycrystalline TiO2 Electrodes by Quantum Sized CdS. *Chemical Physics Letters* **1990**.

(27) Vogel, R.; Hoyer, P.; Weller, H. Quantum-Sized PbS, CdS, Ag2S, Sb2S3, and Bi2S3 Particles as Sensitizers for Various Nanoporous Wide-Bandgap Semiconductors. *J. Phys. Chem.* **1994**, *98*, 3183–3188.

(28) Plass, R.; Pelet, S.; Krueger, J.; Gratzel, M.; Bach, U. Quantum Dot Sensitization of Organic-Inorganic Hybrid Solar Cells. *Journal of Physical Chemistry B* **2002**, *106*, 7578–7580.

(29) Liu, D.; Kamat, P. V. Photoelectrochemical Behavior of Thin Cadmium Selenide and Coupled Titania/Cadmium Selenide Semiconductor Films - the Journal of Physical Chemistry (ACS Publications). *J. Phys. Chem.* **1993**.

(30) Robel, I.; Subramanian, V.; Kuno, M.; Kamat, P. V. Quantum Dot Solar Cells. Harvesting Light Energy with CdSe Nanocrystals Molecularly Linked to Mesoscopic TiO2 Films. *J. Am. Chem. Soc.* **2006**, *128*, 2385–2393.

(31) Lee, H. J.; Yum, J.-H.; Leventis, H. C.; Zakeeruddin, S. M.; Haque, S. A.; Chen, P.; Seok, Il, S.; Grätzel, M.; Nazeeruddin, M. K. CdSe Quantum Dot-Sensitized Solar Cells Exceeding Efficiency 1% at Full-Sun Intensity. … *Physical Chemistry C* **2008**.

(32) Niu, G.; Wang, L.; Gao, R.; Ma, B.; Dong, H.; Qiu, Y. Inorganic Iodide Ligands in Ex Situ PbS Quantum Dot Sensitized Solar Cells with I-/I-3(-) Electrolytes. *Journal of Materials Chemistry* **2012**, *22*, 16914–16919.

(33) la Fuente, de, M. S.; Sánchez, R. S.; González-Pedro, V.; Boix, P. P.; Mhaisalkar, S. G.; Rincón, M. E.; Bisquert, J.; Mora-Seró, I. Effect of Organic and Inorganic Passivation in Quantum-Dot-Sensitized Solar Cells. *J. Phys. Chem. Lett.* **2013**.

(34) Comte, P.; Zakeeruddin, S. M.; Seok, S. I.; Gratzel, M. Regenerative PbS and CdS Quantum Dot Sensitized Solar Cells with a Cobalt Complex as Hole Mediator - Langmuir (ACS Publications). *Langmuir* **2009**.

(35) Im, S. H.; Kim, H.-J.; Kim, S. W.; Kim, S.-W.; Seok, S. I. All Solid State Multiply Layered PbS Colloidal Quantum-Dot-Sensitized Photovoltaic Cells. *Energy & Environmental Science* **2011**, *4*, 4181.

(36) Lai, L.-H.; Protesescu, L.; Kovalenko, M. V.; Loi, M. A. Sensitized Solar Cells with Colloidal PbS-CdS Core-Shell Quantum Dots. *Phys. Chem. Chem. Phys.* **2014**, *16*, 736–742.

(37) Shalom, M.; Buhbut, S.; Tirosh, S.; Zaban, A. Design Rules for High-Efficiency Quantum-Dot-Sensitized Solar Cells: a Multilayer Approach. *J. Phys. Chem. Lett.* **2012**, *3*, 2436–2441.

(38) Seo, G.; Seo, J.; Ryu, S.; Yin, W.; Ahn, T. K.; Seok, S. I. Enhancing the Performance of Sensitized Solar Cells with PbS/CH3NH3PbI3 Core/Shell Quantum Dots. *J. Phys. Chem. Lett.* **2014**, *5*, 2015–2020.

(39) Luther, J. M.; Law, M.; Beard, M. C.; Song, Q.; Reese, M. O. Schottky Solar Cells Based on Colloidal Nanocrystal Films - Nano Letters (ACS Publications). *Nano Lett.* **2008**.

(40) Piliego, C.; Protesescu, L.; Bisri, S. Z.; Kovalenko, M. V.; Loi, M. A. 5.2% Efficient PbS Nanocrystal Schottky Solar Cells. *Energy & Environmental Science* **2013**, *6*, 3054–3059.

(41) Yoon, W.; Boercker, J. E.; Lumb, M. P.; Placencia, D.; Foos, E. E.; Tischler, J. G. Enhanced Open-Circuit Voltage of PbS Nanocrystal Quantum Dot Solar Cells. *Sci. Rep.* **2013**, *3*.

(42) Bozyigit, D.; Lin, W. M. M.; Yazdani, N.; Yarema, O.; Wood, V. A Quantitative Model for Charge Carrier Transport, Trapping and Recombination in Nanocrystal-Based Solar Cells. *Nature Communications* **2015**, *6*, 6180–.

(43) Pattantyus-Abraham, A. G.; Kramer, I. J.; Barkhouse, A. R.; Wang, X.;

Konstantatos, G.; Debnath, R.; Levina, L.; Raabe, I.; Nazeeruddin, M. K.; Grätzel, M.; *et al.* Depleted-Heterojunction Colloidal Quantum Dot Solar Cells. *Nano Lett.* **2010**.

(44) Crisp, R. W.; Kroupa, D. M.; Marshall, A. R.; Miller, E. M.; Zhang, J.; Beard, M. C.; Luther, J. M. Metal Halide Solid-State Surface Treatment for High Efficiency PbS and PbSe QD Solar Cells. *Sci. Rep.* **2015**, *5*, 9945–.

(45) Kim, J. Y.; Adinolfi, V.; Sutherland, B. R.; Voznyy, O.; Kwon, S. J.; Kim, T. W.; Kim, J.; Ihee, H.; Kemp, K.; Adachi, M.; *et al.* Single-Step Fabrication of Quantum Funnels via Centrifugal Colloidal Casting of Nanoparticle Films. *Nature Communications* **2015**, *6*, 1–9.

(46) Chuang, C.; Brown, P. R.; Bulović, V.; Bawendi, M. G. Improved Performance and Stability in Quantum Dot Solar Cells Through Band Alignment Engineering. *Nature Materials* **2014**.

(47) Tang, J.; Kemp, K. W.; Hoogland, S.; Jeong, K. S.; Liu, H.; Levina, L.; Furukawa, M.; Wang, X.; Debnath, R.; Cha, D.; *et al.* Colloidal-Quantum-Dot Photovoltaics Using Atomic-Ligand Passivation. *Nature Materials* **2011**, *10*, 765–771.

(48) Kramer, I. J.; Levina, L.; Debnath, R.; Zhitomirsky, D.; Sargent, E. H. Solar Cells Using Quantum Funnels. *Nano Lett.* **2011**, *11*, 3701–3706.

(49) Schaller, R. D.; Klimov, V. I. High Efficiency Carrier Multiplication in PbSe Nanocrystals: Implications for Solar Energy Conversion. *Physical Review Letters* **2004**, *92*, 186601.

(50) Randy J Ellingson; Matthew C Beard; Justin C Johnson; Pingrong Yu; Olga I

Micic; Arthur J Nozik; Andrew Shabaev, A.; Alexander L Efros. Highly Efficient Multiple Exciton Generation in Colloidal PbSe and PbS Quantum Dots. *Nano Lett.* **2005**, *5*, 865–871.

(51) Beard, M. C.; Ellingson, R. J. Multiple Exciton Generation in Semiconductor Nanocrystals: Toward Efficient Solar Energy Conversion. *Laser & Photonics Reviews* **2008**, *2*, 377–399.

(52) Nair, G.; Bawendi, M. G. Carrier Multiplication Yields of CdSe and CdTe Nanocrystals by Transient Photoluminescence Spectroscopy. *Phys. Rev. B* **2007**, *76*, 081304.

(53) Semonin, O. E.; Luther, J. M.; Choi, S.; Chen, H. Y.; Gao, J.; Nozik, A. J.; Beard, M. C. Peak External Photocurrent Quantum Efficiency Exceeding 100% via MEG in a Quantum Dot Solar Cell. *Science* **2011**, *334*, 1530–1533.

(54) Law, M.; Luther, J. M.; Song, Q.; Hughes, B. K.; Perkins, C. L.; Nozik, A. J. Structural, Optical, and Electrical Properties of PbSe Nanocrystal Solids Treated Thermally or with Simple Amines. *J. Am. Chem. Soc.* **2008**, *130*, 5974–5985.

(55) Luther, J. M.; Law, M.; Song, Q.; Perkins, C. L.; Beard, M. C. Structural, Optical, and Electrical Properties of Self-Assembled Films of PbSe Nanocrystals Treated with 1,2-Ethanedithiol - ACS Nano (ACS Publications). *Nano Lett.* **2008**.

(56) Talapin, D. V. PbSe Nanocrystal Solids for N- and P-Channel Thin Film Field-Effect Transistors. *Science* **2005**, *310*, 86–89.

(57) Lee, J.-S.; Kovalenko, M. V.; Huang, J.; Chung, D. S.; Talapin, D. V. Band-Like Transport, High Electron Mobility and High Photoconductivity in All-Inorganic

Nanocrystal Arrays. *Nature Nanotechnology* **2011**, *6*, 348–352.

(58) Sahu, A.; Kang, M. S.; Kompch, A.; Notthoff, C.; Wills, A. W.; Deng, D.; Winterer, M.; Frisbie, C. D.; Norris, D. J. Electronic Impurity Doping in CdSe Nanocrystals. *Nano Lett.* **2012**, *2*, 2587–2594.

(59) Oh, S. J.; Berry, N. E.; Choi, J.-H.; Gaulding, E. A.; Paik, T.; Hong, S.-H.; Murray, C. B.; Kagan, C. R. Stoichiometric Control of Lead Chalcogenide Nanocrystal Solids to Enhance Their Electronic and Optoelectronic Device Performance. *ACS Nano* **2013**.

(60) Muramoto, S.; Gillen, J. G.; Murray, C. B.; Kagan, C. R. Bandlike Transport in Strongly Coupled and Doped Quantum Dot Solids: a Route to High-Performance Thin-Film Electronics - Nano Letters (ACS Publications). *Nano Lett.* **2012**.

(61) Liu, Y.; Tolentino, J.; Gibbs, M.; Ihly, R.; Perkins, C. L.; Liu, Y.; Crawford, N.; Hemminger, J. C.; Law, M. PbSe Quantum Dot Field-Effect Transistors with Air-Stable Electron Mobilities Above 7 Cm 2V −1s −1. *Nano Lett.* **2013**, 130307111258007.

(62) Kim, D. K.; Fafarman, A. T.; Diroll, B. T.; Chan, S. H.; Gordon, T. R.; Murray, C. B.; Kagan, C. R. Solution-Based Stoichiometric Control Over Charge Transport in Nanocrystalline CdSe Devices. *ACS Nano* **2013**, *7*, 8760–8770.

(63) Oh, S. J.; Berry, N. E.; Choi, J.-H.; Gaulding, E. A.; Lin, H.; Paik, T.; Diroll, B. T.; Muramoto, S.; Murray, C. B.; Kagan, C. R. Designing High-Performance PbS and PbSe Nanocrystal Electronic Devices Through Stepwise, Post-Synthesis, Colloidal Atomic Layer Deposition. *Nano Lett.* **2014**.

(64) Kuno, M.; Lee, J. K.; Dabbousi, B. O.; Mikulec, F. V.; Bawendi, M. G. The Band Edge Luminescence of Surface Modified CdSe Nanocrystallites: Probing the Luminescing State. *J. Chem. Phys.* **1997**, *106*, 9869.

(65) Murray, C. B.; Norris, D. J.; Bawendi, M. G. Synthesis and Characterization of Nearly Monodisperse CdE (E = Sulfur, Selenium, Tellurium) Semiconductor Nanocrystallites - Journal of the American Chemical Society (ACS Publications). *J. Am. Chem. Soc.* **1993**.

(66) Becerra, L. R.; Murray, C. B.; Griffin, R. G.; Bawendi, M. G. Investigation of the Surface Morphology of Capped CdSe Nanocrystallites by 31P Nuclear Magnetic Resonance. *J. Chem. Phys.* **1994**, *100*, 3297.

(67) and, G. K.; Murray, R. W. Ligand Effects on Optical Properties of CdSe Nanocrystals. *J. Phys. Chem. B* **2005**, *109*, 7012–7021.

(68) Allan, G.; Delerue, C. Confinement Effects in PbSe Quantum Wells and Nanocrystals. *Phys. Rev. B* **2004**, *70*, 245321.

(69) Kim, D.; Kim, D. H.; Lee, J. H.; Grossman, J. C. Impact of Stoichiometry on the Electronic Structure of PbS Quantum Dots. *Physical Review Letters* **2013**, *110*, 196802.

# CHAPTER 2

# THEORY OF THIN-FILM TRANSISTORS

## 2.1 INTRODUCING FIELD-EFFECT TRANSISTORS

Field effect transistors come in many flavors and can be characterized by four basic types: the junction FET (JFET); the metal-semiconductor FET (MESFET); the metal-oxide-semiconductor or the metal-insulator-semiconductor FET (MOS-FET/MIS-FET); and the thin-film transistor (TFT). Transistors based on quantum dot solids are predominately of the latter type. The main reason is that the materials are found to be of *low purity* and lack the intentional doping to create depletion or inversion regions due to the existence of donors or acceptors.

The electrical behavior of TFTs is remarkably similar to that of the MOS-FET. There are however subtle, yet important differences between the two types of transistors. The major difference is the dimensionality. In a MOS-FET, electrodes are connected laterally on the semiconductor side forming a three-dimensional device with a space charge and band bending which are the important to the workings of the device; a MOS-FET are often working in inversion and has a minimum thickness of about 100 nm. In contrast, TFTs can be made as thin as possible just as long as the channel is defect-free and there is a uniform coverage on the insulating layer. Thus, a TFT can in principle be made of a single monolayer[1,2] and any additional layers deposited on top can act as buffers for mechanical and chemical stability for the layer below that accommodates all of the current; however additional material can also serve as parasitic resistances and capacitances within the device which can reduce transistor performance such as an increase in off-current, thus decreasing the on-off ratios of the device; such parameters become especially important for applications in driving transistors of LEDs. For this same reason, the interface between the semiconductor and the insulator is of the utmost importance. It has been shown that surface treatments of the insulator layer[3-7] before deposition of the active layer increases carrier mobility and even improves the dynamic instability of the device[8-10]. In addition, traps at the interface or within the bulk can be found because of the layer discontinuities, which can have a severe effect on the device performance, reproducibility, and reliability.

Field-effect transistors are three-terminal devices consisting of a gate, drain, and source. Each of these terminals refers to their actual functions. The gate terminal can be considered as a physical gate that allows the flow of electrons or holes. The resistance of a semiconductor between the source and drain electrodes can be controlled by the electric field induced by the gate electrode (Figure 3.1). By applying a gate-source voltage, the current flowing through the semiconducting channel and between the source and drain electrodes can be modulated. The distance between the source and drain contact is measured as the channel length, $L$; the distance of the channel width, $W$, is determined by the width of the metal electrodes. In order to understand thin-film transistors, we will first discuss MOS-FETs as a starting point.

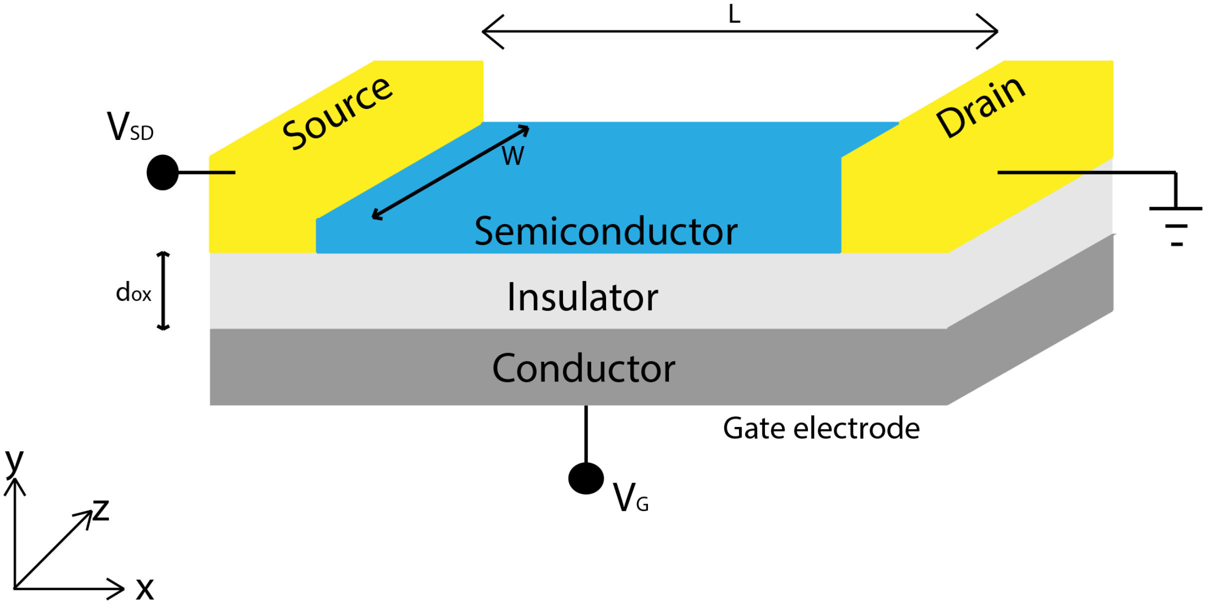

**Figure 2.1 Schematic diagram of a TFT device and its parameters.** This schematic demonstrates a thin-film transistor. The transistor consists of three terminals, the source, the drain, and the gate electrode. The resistance of the semiconducting channel is controlled by the electric potential that is applied to the gate electrodes which capacitively couples the gate and the channel.

## 2.2 BASIC TRANSISTOR MODEL AND TRANSISTOR EQUATIONS

In this section, a model to derive the basic transistor equations will be discussed and it is related to a single crystal silicon MOSFET and can be referenced and followed in *Sze's Physics of Semiconductors* book.[11]. The model, the surface charge density of a p-type semiconductor is calculated as a function of the surface potential. This derived formula will be modified according to Horowitz's description for disordered semiconductors[12], as is the case for quantum dot solids.

### 2.2.1 Metal-Insulator-Semiconductor Capacitor

MOS-FETs are essentially metal-insulator-semiconductor (MIS) diodes with electrodes connected on the sides of the semiconductor. In these devices, the applied bias to the gate electrode "writes" the charge in the semiconductor and the source and drain electrodes are used to measure the total free charge. In a simple model, we consider that the local electron and hole concentrations within the device depends on the energetic depth of the Fermi level and thus by the amount band bending $\varphi_S$ that is influenced by the magnitude of the applied gate voltage

$$n(\varphi_S, T) = n_0 \exp\left(\frac{q\varphi_S}{kT}\right)$$

$$p(\varphi_S, T) = p_0 \exp\left(-\frac{q\varphi_S}{kT}\right) \tag{2.1}$$

where $n_0$ and $p_0$ are the electron and hole densities in the material respectively. The band bending can then be solved for a p-type semiconductor:

$$\frac{d^2\varphi(x)}{dx^2} = -\frac{\rho(x)}{\varepsilon_{semiconductor}} = -\frac{q}{\varepsilon_{semiconductor}}(p - n + N_D(x) - N_A(x)) \tag{2.2}$$

where $x$ is the spatial coordinate perpendicular to the interface, $n$ and $p$ are the free electron and hole densities, respectively, and $N_D$ and $N_A$ are the ionized donor and acceptor densities. From eq. 2.2, it is clear that there is interdependence between free electrons, holes, and ionized donors and acceptors. Making the following assumptions and setting some boundary conditions, we can approximate the solution to this equation:

- Band bending is caused by ionized dopants and free charges do not contribute to the band bending (it is the result). For large doping densities, this is a good approximation but it does not illustrate how a MOS-FET can be placed under accumulation (it will be shown later how a simply TFT model can be used for a MOS-FET in accumulation)
- All acceptors are ionized ($N_A^- = N_A$)
- $N_D << N_A$ for a p-type material
- For $x<W$ (depletion width); $p(x) = 0$
- For $x>W$ (neutral region) ;$p(x) = N_A$

Thus, using the same formalism as that of Schottky and for MIS capacitors[13], one finds that the amount of band bending $V(x)$ from $x=0$ to $x=W$ follows a quadratic form

$$V(x) = \frac{qN_A}{2\varepsilon_{semiconductor}}(x-W)^2 \tag{2.3}$$

$$V(x) = 0 = \frac{qN_A}{2\varepsilon_{semiconductor}}(W)^2 \tag{2.4}$$

In addition, we can use the relationship between the band bending inside the semiconductor and the total external voltage, which includes the voltage drop across the oxide as

$$V_G = V_S + V_{ox} \tag{2.5}$$

We can calculate the potential drop across the oxide by using Maxwell's continuity of displacement equation ($D \equiv \varepsilon E$). Acknowledging that on the semiconductor side, the electric field is just determined by the derivative of the voltage $V(x)$, we find that

$$D_S(x = 0) = -\varepsilon_{semiconductor}\frac{dV(x)}{dx} = qN_AW \qquad (2.6)$$

On the oxide side, this displacement is the same and is therefore equal. Since we assume a perfect insulator, with no charges within the bulk of the material, the electric field in the oxide is $E_{ox} = D_{ox} / \varepsilon_{ox}$ and therefore the voltage drop across the oxide thickness $d_{ox}$ is

$$V_{ox} = D_{ox}d_{ox} / \varepsilon_{ox} \qquad (2.7)$$

$$= qN_AW\frac{d_{ox}}{\varepsilon_{ox}}$$

$$= \frac{\sqrt{2q\varepsilon_{semiconductor}N_AV_S}}{C_{ox}}$$

In order to derive Equation ( 2.7), we use the relationship between the band bending and the depletion width which is given by Equation (2.4) as well as the definition of the capacitance of a perfect parallel-plate capacitor ($C_{ox} = \varepsilon_{ox} / d_{ox}$). Combining Equations (2.5) and (2.7), we find that the total external voltage

$$V_G = V_S + \frac{\sqrt{2q\varepsilon_{se\ iconductor}N_AV_S}}{C_{ox}} \qquad (2.8)$$

From Equation (2.8), we find that depending on the static dielectric constant of the semiconductor, the acceptor carrier concentration, and the surface potential, for a typical MOS-FET, approximately half of the voltage is dropped across the oxide and other half within the semiconductor. A similar derivation can be done for a MOS-FET under accumulation or depletion by using different boundary conditions. What is most important is to consider the justifying claims that transistors are two-dimensional (it will be shown later (Chapter 6) whether this statement is true, especially for thin-film transistors based on quantum dots).

### 2.2.2 MOS-FET Current

When $V_G > V_T$, a conducting channel is established and further increases in the applied gate potential **does not** change the band bending because the density of states (DOS) in the conduction band is large enough that is can absorb additional space charges. This implies that at the interface, the current is proportional to the charge density at $x=0$ $(n=n(x=0)=(V_G - V_T)/C_{ox})$. Thus, the current is equal to the charge density in the channel, $qn = q(V_G - V_T)/C_{ox}$ multiplied by the electric field $E = V_{SD} / L$, and the electron (hole) mobility, scaled with the device dimensions of the channel length, $L$ and channel width $W$

$$I_{SD} = q\mu V_{SD} \frac{W}{L} \frac{(V_G - V_T)}{C_{ox}} \tag{2.9}$$

Note that this is current hold for small source-drain biases (linear regime in output characteristics) where a uniform, homogenous charge density between the source and drain is found.

Another way to solve for the total current is to follow the Drude's model for conductivity, where the current is proportional to the conductivity of the semiconductor, $\sigma$, and the applied voltage $V_{SD}$ between the source and drain electrodes.

$$I_{SD} \propto \sigma \cdot V_{SD} \tag{2.10}$$

with

$$\sigma = q \cdot p \cdot \mu_0 \tag{2.11}$$

where $q$ is the elementary charge, $p$ is the density of charge carriers in the semiconductor, and $\mu_0$ is the *trap-free* mobility since we assume that the semiconductor do not have traps and hence the mobility is not a function of electrostatic potential (as well as gate voltage). Based on this, the density of charge carriers is controlled by the gate voltage. In a p-type semiconductor, the density of holes in the valence band can be approximated as

$$p = N_V \cdot \frac{A}{n_D} \exp \frac{-(E_V - E_F)}{kT} \tag{2.12}$$

where $N_V$ is the effective density of states in the conduction band, $n_D$ and $n_A$ are the donor and acceptor densities, $E_C$ is the conduction band, $E_F$ is the Fermi level, $k$ is the Boltzmann constant, and $T$ is the temperature. The density of electrons in the semiconductor, as stated before, is influenced by the external potential ($\phi_S$). In addition, the potential is at its maximum at the interface and far away from the interface ($x > W$) such that there is no band banding and hence the surface potential beyond the depletion width can be neglected. Therefore the density of holes in the bulk can be described by Equation (2.12); however, the surface potential is strongly influenced by the magnitude of the gate potential, thus the density of holes depends on this potential. Depending on the sign and magnitude of the surface potential, $\phi_S$, the bands can bend either upwards or downwards so that either holes or electrons are accumulated. The density of holes as a function of potential can be expressed as

$$p(x) = p_0 \exp \left(-\frac{q\varphi_S(\ )}{kT}\right) \tag{2.13}$$

and for electrons

$$n(x) = n_0 \exp \left(\frac{q\varphi_S(x)}{kT}\right) \tag{2.14}$$

To calculate the charge density within the semiconductor, we can use Poisson's equation

$$\frac{d^2\varphi}{dx^2} = -\frac{\rho(x)}{\varepsilon_0\varepsilon_r} \tag{2.15}$$

where the total charge density within the material is given by the equation

$$\rho(x) = q[p(x) - p_0 - n(x) - n_0] \tag{2.16}$$

$\varepsilon_0$ is the vacuum permittivity, $\varepsilon_0$ is the relative permittivity of the semiconductor.

If we substituting (2.13) and (2.14) into (2.16) and integrate Equation (2.15) using the boundary conditions that at $x = 0;\ \varphi = 0$ and at $x \to \infty;\ \varphi = 0$:

$$\int_0^{\varphi_S} \frac{d^2\varphi}{dx^2} d\varphi = -\frac{q}{\varepsilon_{semi}} \int_0^{\varphi_S} \left\{ p_0 \left[ \exp\left( -\frac{q\ (x)}{kT} \right) - 1 \right] + n_0 \left[ \exp\left( \frac{q\varphi(x)}{kT} \right) - 1 \right] \right\} d\varphi$$

If we recall Gauss' Law for electric flux and rewriting it to solve for the charge density $Q_S = -\varepsilon_0\varepsilon_r E_S$, where $E_S$ is the electric field that is created by the charge density at the surface $Q_S$. Using the property of integrals

$$\frac{d^2y(x)}{dx^2} = f(y) \tag{2.17}$$

then

$$\left[\frac{dy(x)}{x}\right]^2 = 2\int f(y)dy \tag{2.18}$$

This will allow us to solve for $E^2$ as long as we have the boundary condition that $E=0$ when $\varphi = 0$. Setting $\beta = q/kT$ to make the integration easier to see

$$E(\varphi) = \sqrt{\frac{2qp_0}{\beta\varepsilon_{semi}}} F(\varphi, \frac{n_0}{p_0}) \tag{2.19}$$

where

$$F\left(\varphi, \frac{n_0}{p_0}\right) = \left\{ [\exp(-\beta\varphi) + \beta\varphi - 1] + \frac{n_0}{p_0}[\exp(\beta\varphi) - \beta\varphi - 1] \right\}^{1/2} \tag{2.20}$$

Now, we can determine the space charge density inside the device by using Gauss' Law

$$Q_S{}^2 = \left(\pm\sqrt{2\epsilon_{semi}kT}\right)^2 p_0 \left[\exp\left(-\frac{q\varphi_S}{kT}\right) + \frac{q\varphi_S}{kT} - 1\right] + \left(\pm\sqrt{2\epsilon_{semi}kT}\right)^2 n_0 \left[\exp\left(\frac{q\varphi_S}{kT}\right) - \frac{q\varphi_S}{kT} + 1\right]$$

(2.21)

Figure 2.2 gives a graphical representation of this space charge as a function of total band bending $\varphi_S$. The graph demonstrates four regions and describes the total charge density for a p-channel MOS-FET. Excess holes are accumulated at the dielectric/semiconductor surface if a negative surface potential is applied (**accumulation**). For zero surface potential, there is no band bending and no space charge in the semiconductor (**flat band)**. Deviations from zero are typically caused by differences in work functions between the gate material and the semiconductor layer. A small positive potential causes **depletion** of free holes (which only exists in the semiconductor since it is doped for this illustration) followed by a **weak inversion,** where the concentration of electrons becomes larger than the concentration of holes. For larger positive potentials, a region of **strong inversion** is reached where electrons are induced at the interface. We note that this solution does **not** apply for a MOS-FET in accumulation because the assumption that $N_A^- = N_A$ everywhere is **not** true. In accumulation the acceptors are neutralized in a region close to the interface. Note that for materials with deep levels such as organics and quantum dots, the assumption that all impurities are ionized is not valid. Moreover, for ambipolar materials with equal concentrations for electrons and holes, $p_0 = n_0 = n_i$

$$Q_S = \pm\sqrt{2\varepsilon_{semi}kT}\sqrt{n_i\left[\exp\left(-\frac{q\varphi_S}{kT}\right) - \exp\left(\frac{q\varphi_S}{kT}\right)\right]} \tag{2.22}$$

Based on this equation, depending on the sign of the surface potential, either electron or hole accumulation is possible or hence depletion or inversion is not possible, since this would require the existence of donors or acceptors. Note, it is currently not clear where the accumulated charge carriers are coming from, but it will be shown in this dissertation that it is coming from the source contact (which is at the same potential as the gate contact). As such, the energy barrier between the semiconductor and the metal contacts should be as small as possible to allow a large accumulation of carrier density in the semiconductor.

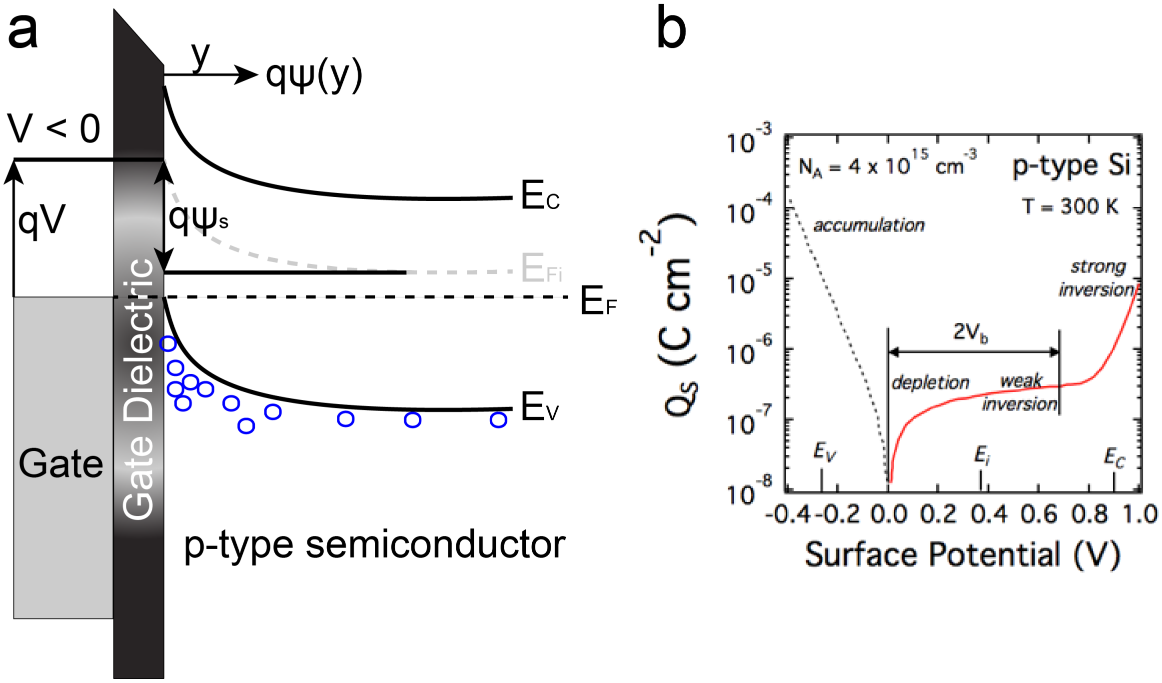

**Figure 2.2 Ideal metal-insulator-semiconductor capacitor energy diagram and surface charge density**. (a) The schematic shows the energy level alignment across the gate electrode/gate dielectric/p-type semiconductor capacitor. Under a negative potential to the gate electrode, the hole density in the semiconductor increases (accumulation). A positive potential to the gate electrode reduces the hole density (depletion) and a larger positive potential increases the electron density (inversion). $E_F$ is the Fermi level; $E_C$ is the conduction band; $E_V$ is the valence band; $E_{f,i}$ is the intrinsic Fermi level (if $E_F = E_{f,i}$ then $n=p=n_i$); $E_g$ is the optical band gap; $qV_G$ is the amount of band bending (note that it it's a negative sign of the electron charge); $qV_B$ flat band voltage of the bulk distance between the Fermi level and the intrinsic level. (b) Surface charge density as a function of total band bending in a typical silicon device (assuming the flat-band voltage is zero). This simulation is based on calculations by Garrett and Brattain[14]

### 2.2.3 Thin-film transistor current

Equation (2.21) describes the surface charge density in a transistor channel in general. This charge density is influenced by the gate voltage as well as the potential created by the source-drain voltage. As such, the potential becomes a two-dimensional function $\varphi(x, y) = \varphi(x) - V_{SD}(y)$. To derive an analytical expression for the drain current, several assumptions will be made:

- The derivation for the charge density for an ideal MIS capacitor will be used and it will be assumed that there are neither interface traps nor mobile oxide charges.
- There are no diffusion currents in the transistor and only drift currents
- The longitudinal electric field along the channel is much smaller than the transverse electric field across the gate dielectric (*Gradual-channel approximation*)

Using these assumptions, we can substitute $\varphi(x) = \varphi(x, y) = \varphi(x) - V_{SD}(y)$ and use the relationship that the current $I_{SD}$ *(x)* along the channel will be proportional to the local free charge, the electric field (*v=Eμ)*, and the carrier mobility.

$$I_{SD} = WQ_S(x)v(x) \tag{2.23}$$

Integrating Equation (2.23) since the current must be constant along the channel length *L*

$$I_{SD} = \frac{W}{L}\int_0^L Q_S(x)v(x)dx = \frac{\mu_0 W}{L}\int_0^L Q_S(x)E(x)dx \tag{2.24}$$

$$= \frac{\mu_O W}{L}\int_0^{V_{SD}} Q_S(x)\frac{dV_{SD}}{dx}dx \tag{2.25}$$

Following standard models[13,15], an assumption is made. The single assumption of this model is to treat the device as a simple plate capacitor. This means that all charges are immediately at the interface and there is no band banding or other ways to distribute charge. As such, the charge within the channel is directly proportional to the voltage drop at the insulator, like a classical capacitor (C=Q/V):

$$Q_S(x) = C_{OX}[V(x) - V_G] = C_{ox}[V_G - V_T - V_{SD}(x)] \tag{2.26}$$

where $Q_S(x)$ is the charge density at a position *x* along the channel (see Figure 2.1), $C_{ox}$ is the insulator capacitance density ($C_{ox} = \varepsilon_{ox} / d_{ox}$), *V(x)* is the local potential in the channel, and $V_G$ is the uniform potential at the gate electrode. It is noted that the units for the density of charge is *per square centimeter*, thus this treats the active layer as two-dimensional. Without considering traps, doping or other electronically active impurities, we assume that this charge is all free (later we will show that this assumption is not valid for quantum dot materials with traps). Therefore

$$I_{SD} = \frac{\mu_0 W}{L} \int_0^{V_{SD}} C_{ox}\, [V_G - V_T - V_{SD}(x)] dV_{SD} \tag{2.27}$$

To reiterate, the assumption for a field-independent mobility for quantum dot solids is not valid. Details on the field-dependent mobility will be discussed in section 4.6.5

For small source-drain voltages, $V_{SD} < V_G - V_T$, the voltage across the channel is considered uniform and Equation (2.27) becomes

$$I_{SD} \frac{\mu_0 W C_{ox}}{L} \left(V_G - V_T - \frac{V_{SD}}{2}\right) V_{SD}\ (linear\ region) \tag{2.28}$$

When the source-drain current increases and when its value is close to $V_G - V_T$ , the accumulated charge density is more and more reduced (or depleted) near the drain contact. For $V_{SD} = |V_G - V_T|$, the charge density near the drain contact is zero and the channel is said to be *pinched-off* such that any more increases in the source-drain voltage, shifts the point of pinch-off towards the source contact, resulting in the current to saturate (Figure 3.3). If we replace $V_{SD}$ with $V_G$ – $V_T$ in Equation (2.28) the source-drain current in the saturation region is obtained

$$I_{SD} = \frac{\mu_0 W C_{ox}}{2L}(V_G - V_T)^2 \quad (saturation\ region) \tag{2.29}$$

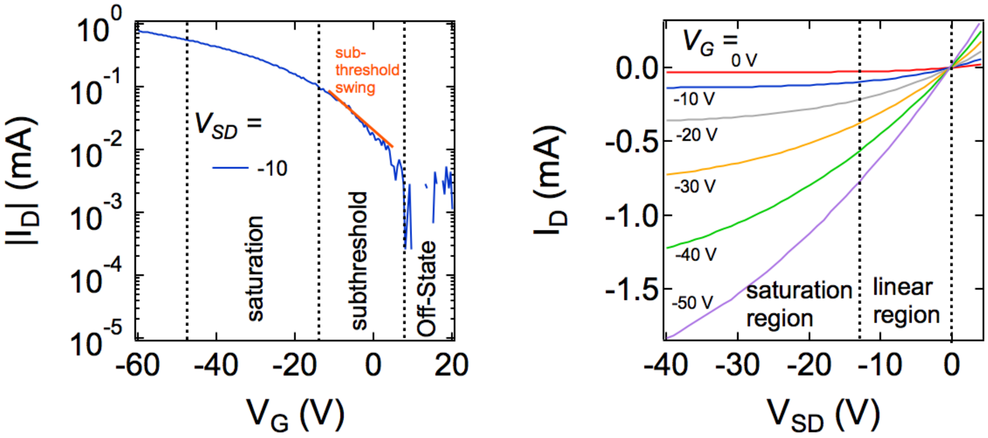

**Figure 2.3 Output and transfer characteristics of quantum dot thin film transistor under accumulation** (a) Left: transfer characteristics show the source-drain current at a constant source-drain voltage. By plotting on a logarithmic scale, we can distinguish the off-state, subthreshold, and saturation regions (b) Right : output characteristics illustrates the source-drain current as a function of applied source-drain voltage for several gate voltages. In an ideal case, the drain current increases linearly and then saturates when $V_{SD}$ > $V_G$ - $V_T$

The surface charge density within the **subthreshold region** depends non-linearly on the gate voltage, but it has been shown that the current within this region can depend exponentially on the gate voltage[13]

$$I_{SD} \sim \exp\left(-\frac{q\varphi_S}{kT}\right) \tag{2.29}$$

The slope within the region called the **subthreshold swing** can be described as [3]

$$S \equiv (\ln(10)\frac{kT}{q}\left(\frac{C_{ox}+qN_{traps}}{C_{ox}}\right) \tag{2.30}$$

where $N_{raps}$ is the trap density at the gate dielectric/semiconductor interface. It is clear that a steep subthreshold would be ideal which can occur either by eliminating the interfacial traps or increasing the capacitance of the dielectric layer. Note that the theoretical minimum for the subthreshold swing is 60 mV/decade.[13]

In the **off-state**, the drain current does not depend on the source-drain voltage, but strongly depends on the doping concentration in the semiconductor. In this region, the current can be approximated as

$$I_{SD} \sim \sqrt{\frac{N_V n_A}{n_D}}\sqrt{V_G}V_{SD} \tag{2.31}$$

Up to this point, we have neglected leakage currents within the gate dielectric during our derivation of the MIS capacitor and source-drain currents for a MOS-FET and TFT. In reality, there is a small gate leakage, which limits the on/off ratios and increases power consumption, which should be, avoided especially when it is used in active matrix displays such as drive transistors.

## 2.3 TRANSISTOR FIGURES OF MERIT

The current-voltage (*I-V)* characteristics of transistors are used to determine characteristic parameters such as transconductance, field-effect mobility, subthreshold swing, threshold voltage, on/off ratios, and contact resistance. These parameters are important especially for benchmarking transistors processed within different research facilities, industries, and universities.

The **transconductance** is defined as $g_m = \delta I_D/\delta V_G$ which describes the response of the source-drain current to changes in the gate voltage. One can normalize the transconductance to the channel width. Using Equations (2.28) and (2.29), one finds

$$g_m = \frac{\mu_0 W C_{ox}}{L} V_{SD} \quad (linear\ region) \tag{2.32}$$

$$g_m = \frac{\mu_0 W C_{ox}}{L} (V_G - V_T) \quad (saturation\ region)$$

One can see that the transconductance is inversely proportional to the channel length, so one can increase the transconductance by reducing the channel length of the transistor.

Similar to the derivation of the transconductance, the **field-effect mobility** can be extracted. From Equations (2.28) or (2.29), we can express the field-effect mobility in the linear regime or the saturation regime as

$$\mu_{lin} = \frac{\delta I_{SD}}{\delta V_G} \frac{1}{C_{ox} V_{SD}} \frac{L}{W} \tag{2.33}$$

$$\mu_{sat} = (\frac{\delta \sqrt{I_{SD}}}{\delta V_G})^2 \frac{2}{C_{ox}} \frac{L}{W} \tag{2.34}$$

Similar to MOS-FETs, the **threshold voltage** is defined as the voltage at the onset of inversion in the transistor. In transistors based on organic semiconductors and quantum dot solids, there is no inversion region (at lease currently) so this definition is not useful. Instead, we define the threshold voltage as the voltage where a small, conducting channel near the gate dielectric/semiconductor interface appears. For an intrinsic semiconductor, the threshold voltage can be described as[13]

$$V_T = \phi_{ms} - \frac{Q_f}{C_{ox}} \tag{2.35}$$

where $\phi_{ms}$ is the work function difference between the metal and semiconductor; $Q_f$ is the density of traps at the gate dielectric/semiconductor interface or within the bulk of the gate dielectric. Assuming there are no fixed charges and $\phi_{ms}$ is zero, the threshold voltage should be zero. However, the work function difference is usually non-zero and there is always a small presence of traps. Typical methods to estimate the threshold voltage are to extrapolate the source-drain current in the transfer characteristics to the intersection with the x-axis.

The ratio between the on-state current (usually at maximum $V_G$) and the off-state current at $V_G = 0$ is called the **on/off current ratio**. Typical values for transistors based on quantum dot solids are several orders of magnitude ($10^3$ to

## 2.4 CONTACT EFFECTS

Often times, nonlinearities are observed in the electrical characteristics in the output and transfer curves which deviate from the ideal cases such as shown in Figure 3.3. There is overwhelming evidence that the nonlinearities are a result of a barrier at the contact.

For instance, it was found that there was a change in the voltage drop at the contact depending on the choice of the metal by measuring the surface potential in a Kelvin-probe profilometer.[16,17] In quantum dot solids, the energy barrier at the interface between the contacts and the quantum dots often limits the source-drain current in transistors. This barrier is tuned by choosing an appropriate metal with the right work function that matches either the LUMO or HOMO energy of the quantum dot.[18] For example, in *Oh et al.* demonstrated the role of contacts on charge injection and transport. They found that by selecting different metals, changing the ligand exchange chemistry, and post deposition surface passivation, they were able to control the polarity and magnitude of the device currents in PbSe TFT's.

From the ideal Mott-Schottky theory, choosing metal electrodes for controlling charge injection, the barrier height for electron injection is assumed to be the difference between the metal work function and the electron affinity of the semiconductor. If partial Fermi-level pinning occurs, there will be a small or favorable electron (hole) injection for a low (high) work function metal. Often times, this can reproduce non-linearities with contact barriers and even result in a field-dependent mobility, which the authors have not discussed nor cared to show their *I-V* characteristics (output curves). Further discussion will be presented in 4.6.5.1.

## REFERENCES

(1) Schön, J. H.; Meng, H.; Bao, Z. Self-Assembled Monolayer Organic Field-Effect Transistors. *Nature* **2001**, *413*, 713–716.

(2) Park, B.-N.; Seo, S.; Evans, P. G. Channel Formation in Single-Monolayer Pentacene Thin Film Transistors. *J. Phys. D: Appl. Phys.* **2007**, *40*, 3506–3511.

(3) Islam, M. M.; Pola, S.; Tao, Y.-T. Effect of Interfacial Structure on the Transistor Properties: Probing the Role of Surface Modification of Gate Dielectrics with Self-Assembled Monolayer Using Organic Single-Crystal Field-Effect Transistors. *ACS Applied Materials and Interfaces* **2011**, *3*, 2136–2141.

(4) Ito, Y.; Virkar, A. A.; Mannsfeld, S.; Oh, J. H.; Toney, M.; Locklin, J.; Bao, Z. Crystalline Ultrasmooth Self-Assembled Monolayers of Alkylsilanes for Organic Field-Effect Transistors. *J. Am. Chem. Soc.* **2009**, *131*, 9396–9404.

(5) Pernstich, K. P.; Haas, S.; Oberhoff, D.; Goldmann, C.; Gundlach, D. J.; Batlogg, B.; Rashid, A. N.; Schitter, G. Threshold Voltage Shift in Organic Field Effect Transistors by Dipole Monolayers on the Gate Insulator. *J. Appl. Phys.* **2004**, *96*, 6431–6438.

(6) Acton, O.; Dubey, M.; Weidner, T.; O'Malley, K. M.; Kim, T.-W.; Ting, G. G.; Hutchins, D.; Baio, J. E.; Lovejoy, T. C.; Gage, A. H.; *et al.* Simultaneous Modification of Bottom-Contact Electrode and Dielectric Surfaces for Organic Thin-Film Transistors Through Single-Component Spin-Cast Monolayers. *Advanced Functional Materials* **2011**, *21*, 1476–1488.

(7) Kobayashi, S.; Nishikawa, T.; Takenobu, T.; Mori, S.; Shimoda, T.; Mitani, T.;

Shimotani, H.; Yoshimoto, N.; Ogawa, S.; Iwasa, Y. Control of Carrier Density by Self-Assembled Monolayers in Organic Field-Effect Transistors. *Nature Materials* **2004**, *3*, 317–322.

(8) Gleskova, H.; Gupta, S.; Sutta, P. Structural Changes in Vapour-Assembled N-Octylphosphonic Acid Monolayer with Post-Deposition Annealing: Correlation with Bias-Induced Transistor Instability. *Organic Electronics* **2013**, *14*, 3000–3006.

(9) Chua, L.-L.; Zaumseil, J.; Chang, J.-F.; Ou, E. C. W.; Ho, P. K. H.; Sirringhaus, H.; Friend, R. H. General Observation of N-Type Field-Effect Behaviour in Organic Semiconductors. *Nature* **2005**, *434*, 194–199.

(10) Yuan, Y.; Giri, G.; Ayzner, A. L.; Zoombelt, A. P.; Mannsfeld, S. C. B.; Chen, J.; Nordlund, D.; Toney, M. F.; Huang, J.; Bao, Z. Ultra-High Mobility Transparent Organic Thin Film Transistors Grown by an Off-Centre Spin-Coating Method. *Nature Communications* **2014**, *5*.

(11) Sze, S. M.; Ng, K. K. Physics of Semiconductor Devices - Simon M. Sze, Kwok K. Ng - Google Books. **2006**.

(12) Horowitz, G. Organic Field-Effect Transistors. *Adv. Mater.* **1998**, *10*, 1–13.

(13) Sze, S. M.; Ng, K. K. Physics of Semiconductor Devices, 3rd Ed; John Wiley & Sons, 2008.

(14) Garrett, C.; Brattain, W. H. Physical Theory of Semiconductor Surfaces. *Physical Review* **1955**, *99*, 376–387.

(15) Colinge, J. P.; Colinge, C. A. Physics of Semiconductor Devices; Springer Science

& Business Media, 2007.

(16) Puntambekar, K. P.; Pesavento, P. V.; Frisbie, C. D. Surface Potential Profiling and Contact Resistance Measurements on Operating Pentacene Thin-Film Transistors by Kelvin Probe Force Microscopy. *Appl. Phys. Lett.* **2003**, *83*, 5539.

(17) Nichols, J. A.; Gundlach, D. J.; Jackson, T. N. Potential Imaging of Pentacene Organic Thin-Film Transistors. *Appl. Phys. Lett.* **2003**, *83*, 2366.

(18) Oh, S. J.; Wang, Z.; Berry, N. E.; Choi, J.-H.; Zhao, T.; Gaulding, E. A.; Paik, T.; Lai, Y.; Murray, C. B.; Kagan, C. R. Engineering Charge Injection and Charge Transport for High Performance PbSe Nanocrystal Thin Film Devices and Circuits. *Nano Lett.* **2014**, *14*, 6210–6216.

# CHAPTER 3

# MANUFACTURING PROCESS: THIN-FILM TRANSISTOR FABRICATION, QUANTUM DOT SYNTHESIS, AND THIN-FILM DEVELOPMENT

Quantum dot (QD) TFTs are thin-film transistors in which the conducting channel is made of a few QD layers thick. Such materials include PbX (X=S, Se, Te) and CdX(X=S, Se, Te). One of the basic requirements for these thin films is that it must be of good quality with very little cracks, smooth surface roughness, and high packing density. Unfortunately, common deposition methods involve a solid-state ligand exchange, which prevents periodic arrangement of quantum dots, an idealized goal to take advantage of the collective properties of these individual nanocrystals.

As for the other materials and interfaces within the transistor, it can be manufactured from other organic or inorganic materials. For instance, the gate electrode can be a metal (Al, Cr, Mo, or Au) or an inherently conducting substrate (e.g. chemically doped or highly degenerate Si or a conjugated polymer like PEDOT:PSS). The gate dielectric layer commonly employs insulating metal oxide or nitride (e.g. $AlO_x$, $SiN_x$, $SiO_2$). Alternatively, using high-κ dielectrics such as hafnia or alumina benefit from accumulating larger carrier densities, larger on/off ratios, and lower power consumption since the voltage required to operate the voltage is reduced due to the higher capacitance of the dielectric layer. For details on these methods, with particular application towards quantum dot solids, one can refer to the following literature.[1-5]

The source-drain contacts for QD-TFTs are usually prepared by photolithography or by thermal evaporation of metals through a shadow mask. Using these lithography techniques, TFTs with channel lengths as small as 5μm are easily realized. For the fabrication of QD-TFTs, there are two configurations that are commonly used (Figure 3.1b and 3.1d).

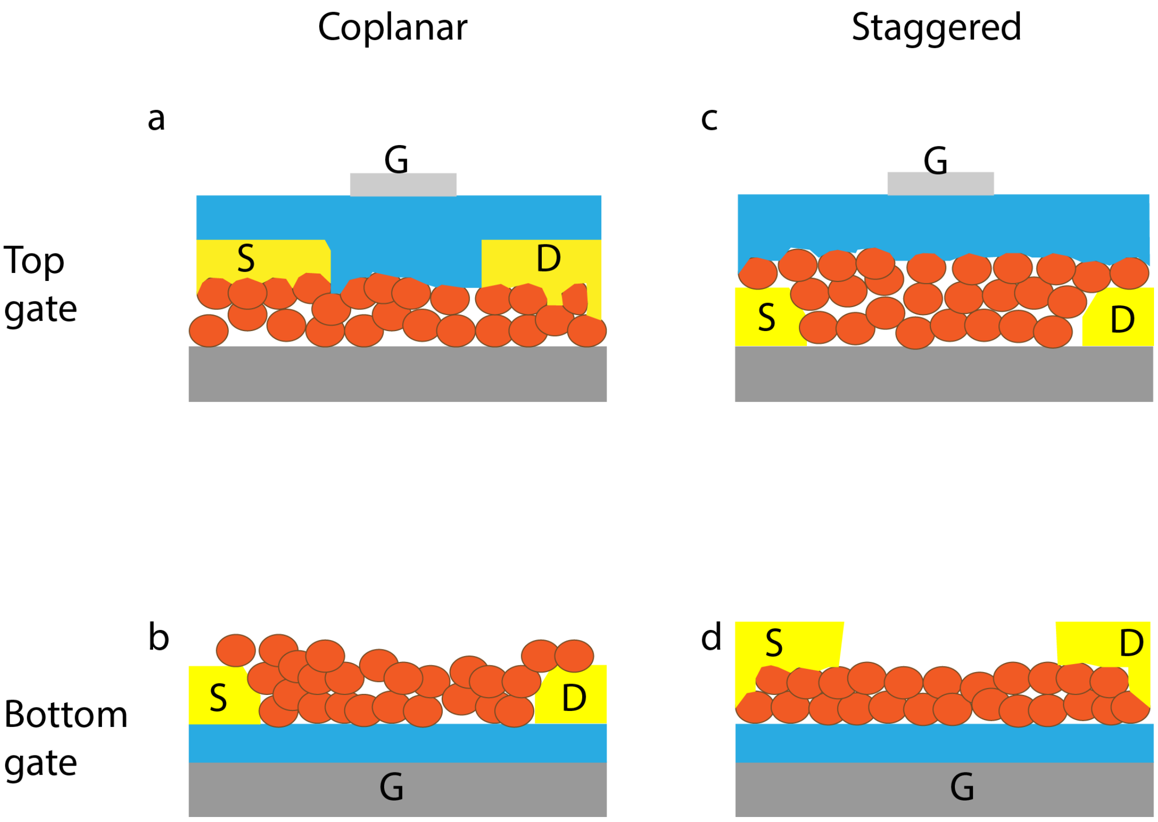

**Figure 3.1 Schematic of common thin-film transistor geometries** (a) Top-gate coplanar with source-drain contacts (b) Bottom-gate coplanar with source-drain contacts (c) Top-gate (inverted) staggered geometry with respect to the source-drain contacts (d) Bottom-gate (inverted) staggered geometry with respect to the source-drain contacts

For the bottom-gate device geometry, it is common to use a highly degenerate p++ or n++ silicon wafer as a handle wafer and gate electrode where then a gate material such as $SiO_2$ is used to electrically isolated the QD film from the metallic-like handle wafer. To prepare the source-drain contacts, they are either pre-patterned using photolithography and electron-beam or thermal evaporation or post-patterned via shadow mask evaporation. Following the device preparation, the QD film can be deposited by a variety of methods such as drop casting[6-10] , spin coating[11-14], dip coating[15-18] and more recently centrifugal casting[19] . For top-gate configurations, following the deposition of the source and drain contacts and the QD films, a dielectric layer such as $SiO_2$[1,15,16,20-22] , $Al_2O_3$ [23,24], PMMA[22,24] [, Cytop[5,25], or an ion gel[26-29] is formed on the top. To reiterate, this dielectric layer separates the top gate from the QD film.

When considering which geometry to use, we have to consider the following factors: morphology, contact resistance, and interfaces (semiconductor/gate, semiconductor/metal). Using a bottom-gate coplanar with the source-drain contacts or the top-gate (inverted) staggered geometry with respect to the source-drain contacts, one would expect that having abrupt and sharp interfaces with different heights and surface roughness would lead to non-uniform films and domains of low densely packed QDs. Currently, there are no reports on the differences in QD TFT performance with regard to these two different geometries. The only advantage is process time, which is much less for pre-patterned substrates with a bottom-gate configuration. In contrast, using top-gate coplanar geometries with respect to the source-drain contacts or a bottom-gate (inverted) staggered geometry with respect to the source-drain contacts has the advantage of producing high-quality films because of the smooth surface of the handle wafer (top-gate coplanar) or the dielectric material (bottom-gate staggered). However, there have been reports demonstrating the effects of evaporating metals (especially reactive metals such as

Ag) on top of quantum dots. *Swisher* et al found that by evaporating metal electrodes on top of QDs when fabricating solar cells, this can lead to electrical shorts because of the often rough and even discontinuous films.[30] In addition, it has been shown that by thermal evaporation of certain metals on top of QDs (e.g. Pb, Se, and In), the conductivity and dominant carrier type within the TFT channel; this could be a highly undesired effect especially if this is not the intent of the process development.

## 3.1 THIN-FILM TRANSISTOR PROCESS DEVELOPMENT

In this thesis, a bottom-gate coplanar device geometry will be used, unless otherwise stated. Top-contact (inverted) staggered geometries will be used to study the effects of a Schottky barrier formation with films (section 4.6.5.1). For the development of TFTs, standard photolithography was used. The basic procedure is as follows:

1. Cleaning Si/$SiO_2$ wafers in 3:1 $H_2SO_4$ : $H_2O_2$ bath for 15 minutes followed by a thorough rinsing with DI water. This step is required to remove organic contaminants
2. Dehydration of wafers at 120°C for 15 minutes. This step is required to drive off any moisture and to prepare the surface for self-assembled monolayer treatment
3. Vapor deposition of hexamtheyldisilizane (HMDS) in a YES oven to improve adhesion of the photoresist to the oxide wafer
4. Spin coat Shipley 1827 (S1827) to produce a 500nm thick polymer film. Check the relative humidity because it will change the thickness of the polymer film. For higher RH% (>60%), use faster spin speeds.

5. Soft bake at 90°C for 10 minutes (12 minutes total to account for some heat loss when the wafers are placed in the oven) to drive off solvents used in the resist
6. UV-flood lamp exposure of photoresist coated wafers for 30 seconds using a Chrome photo mask provided by Photo Sciences, Inc.
7. Hard bake at 120°C for 5 minutes (7 minutes total to account for heat loss when wafers are placed in oven)
8. Develop with MF-319 at room temperature for 30 seconds (no more than 1 minute) to prevent over developing and swelling of patterns
9. Hard bake at 120°C for 10 minutes (12 minutes total) to drive off excess water and tetramethylammonium hydroxide from the developer
10. Electron-beam evaporation of 3 nm titanium (used as an adhesion layer) followed by 40 nm of gold

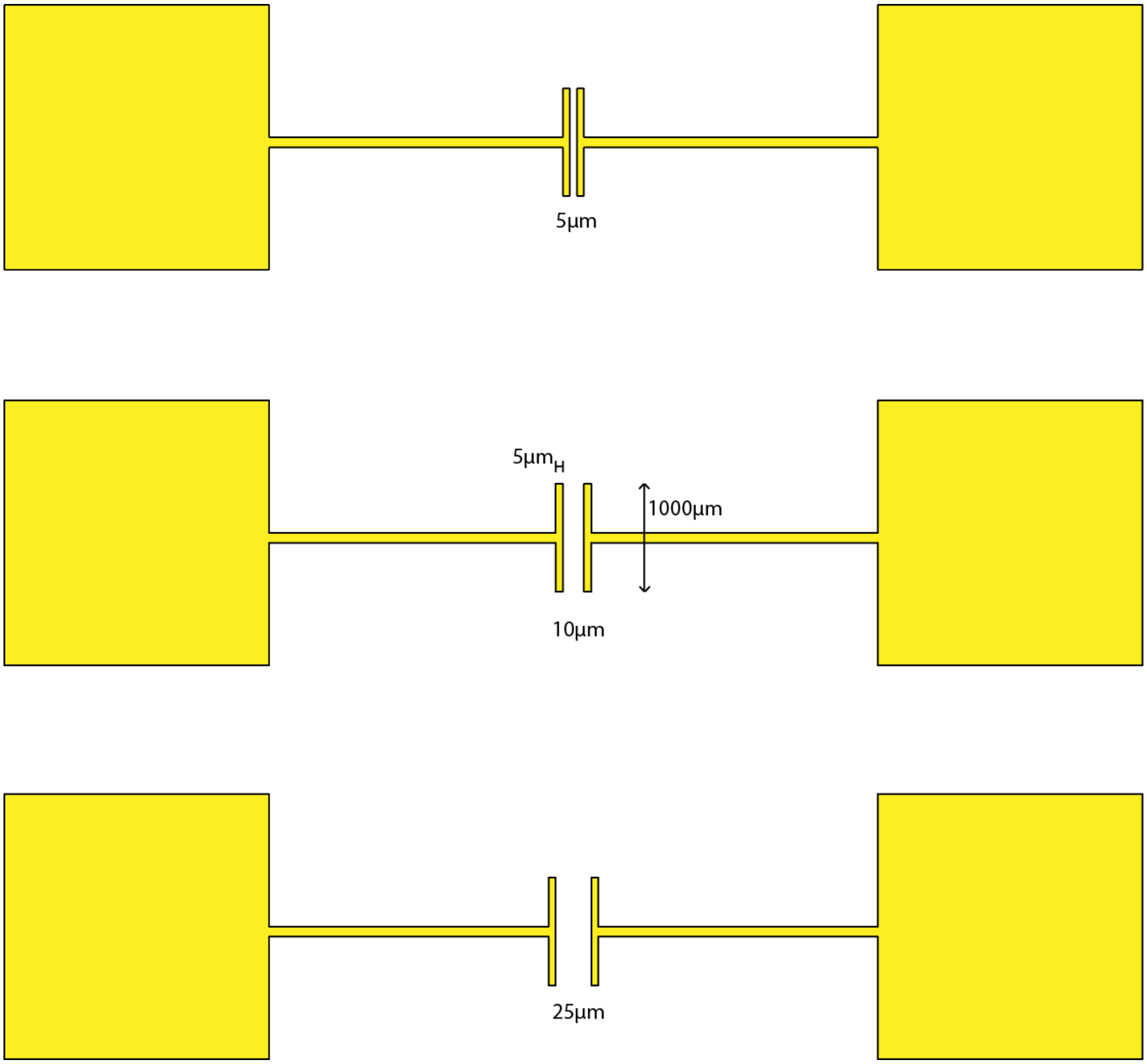

**Figure 3.2 Schematic of TFT electrode design for bottom-gate coplanar with source-drain contacts.** As illustrated, there are three different channel lengths of 5 µm, 10 µm, and 25 µm. Then channel width is 1000µm and the smallest feature size defining the electrode width is 5 µm

## 3.2 QUANTUM DOT SYNTHESIS

Since quantum dot emission is size dependent as featured in Figure 3.3a, colloidal growth must be carefully controlled to achieve the target average radius with a narrow particle size distribution. A variety of methods have been developed including hydrothermal[31] , hot injection[32], sol-gel[33], microemulsions[34], and even arrested precipitation in water.[35] The most common method is the hot injection route which was pioneered[32] and modified to produce superior crystallinity and higher photoluminescence quantum yield as a result of higher temperature reactions, and to provide better size control and surface passivation due to the growth of quantum dots in trioctylphosphine oxide (TOPO) rather than water.[36] Many studies have been performed to optimize quantum dot performance by varying synthesis parameters such as reaction solvent composition, precursor concentration, types of precursor, and temperature; all of which affect the reaction kinetics.

In the majority of all published literature regarding the synthesis of quantum dots, either the hot injection organometallic synthesis or arrested precipitation is used. The success of these methods relies heavily on the behavior of the ligands. These ligands keep the particles isolated and prevent agglomeration as well as help in a more homogenous growth during synthesis. Nanocrystal size variations are reduced and even shape controlled when ligands control the growth rate of particles[37-40]. These ligands passivate the surface since it binds to the surface during synthesis. Furthermore, it protects the surface from oxidation and minimizes the electronic trapping properties of surface defects, both of which help maintain high photoluminescence quantum yield

(PLQY)[8,9,41,42]. In addition, it is found that depending on the isolation and purification of the quantum dots to remove the by products of the reaction, the PLQY is drastically reduced due to the removal of metal carboxylate complexes ( L-M($O_2CR$)$_2$ , L=oleyl, tetradecyl, M= Pb, Cd). In comparison, there are several factors favor arrested precipitation including fewer environmental and safety hazards. However, the reaction is typically in an aqueous solution, limiting the temperature of the reaction to no greater than 100°C. This places the limit for mobility and diffusion of adatoms on the surface of growing nanocrystals, resulting in defects in the material. These defects can act as nonradiative recombination sites for electron-hole pairs produced by incident excitation light, thus reducing the PLQY of the quantum dots. In order reconcile this limitation, nanocrystals formed by arrested precipitation were subjected to a post-processing heat treatment.[43,44]

While the formation of nanocrystals have been found to follow several mechanisms such as autocatalytic and aggregative processes, most metal chalcogenide nanocrystal synthesis appears to follow nucleation and growth pathways in which soluble monomers diffuse and add to growing crystals or dissociate during Ostwald ripening. In this case, one can view the synthesis of nanocrystals as follows (Scheme 1):

1) a reaction between precursors supplies the reaction with monomers ([ME]$_i$)
2) followed by subsequent crystallization and growth or dissociation of nanocrystals during Ostwald ripening

$$MX_2 + ER_2 \rightarrow [ME]_i + 2RX \underset{\xleftarrow[\phantom{dissocation}]{}}{\overset{\xrightarrow{\phantom{growth}}}{\overset{growth}{\underset{dissocation}{\rule{5em}{0.4pt}}}}} [ME]_n \qquad \text{Scheme 1}$$

M= Cd, Pb, etc

E = S, Se, Te

X = $O_2CR$, Cl, SR, etc

L = $PR_3$, $NH_2R$, etc

$MX_2$ = $Cd(O_2CR)_2$, $Pb(O_2CR)_2$, $CdCl_2$, $PbCl_2$, $Pb(SCN)_2$

### 3.2.1 Thermodynamically controlled – hot injection synthesis

In context of the hot injection method, the conversion kinetics/thermodynamics and nanocrystal nucleation and growth has to be considered. As such, the combined influence of energy barriers, driving forces, material availability, and diffusion affects the formation of nanocrystals. The thermodynamics for any process explains which final state is preferred at equilibrium because it is more stable. If the net change in the Gibbs free energy, $\Delta G$, is *negative*, this provides a strong driving force towards equilibrium. Kinetics, on the other hand, will describe a nonequilibrium rate in which a process transitions towards equilibrium. In the case of the growth rate of nanocrystals, there will be some finite probability that random thermal energy will enable $M$ and $E$ components to overcome some kind of barrier, which is characterized by some activation energy in order to increase the size of the nanocrystal. The growth rate often exhibits Arrhenius temperature dependence. A simple expression for the growth rate can be expressed as such

$$v = r \cdot \exp\left(-\frac{Q}{kT}\right) \tag{3.1}$$

where $r$ is the rate coefficient which is a function of time, particle size, precursor concentration, $Q$, is the activation energy, $k$ is the Boltzmann constant, and $T$ is temperature.

Colloidal quantum dot formation can be divided into three stages: *nucleation, growth, and ripening.* During nucleation, the concentration of liquid monomer (reactants or precursors) is partially depleted by the formation of many nuclei of approximately the same size. Next particles begin to grow by consuming these monomers. Finally, as the monomers is finally consumed, the average size increases by competitive growth or ripening, when larger particles grow while smaller particles shrink and disappear in order to reduce the net surface energy of the system (i.e. Oswald ripening). During the synthesis of monodisperse quantum dots, rapid nucleation is typically far from equilibrium. However, the final ripening stage is closer to equilibrium because the time scales are long and the reactant concentrations are low.

To understand nucleation and growth of nanocrystals, there are several models that have been invoked to explain particle size distributions during nucleation, growth, and ripening of nanocrystals. Based on purely thermodynamics, the *Gibbs-Thomson* relation is used. This theory was originally developed to quantify the thermal equilibrium between liquid droplets and the surrounding vapor, but it was soon adapted to describe solid spherical nanocrystals with a radius $R$, in equilibrium with the surrounding reaction solution with a monomer concentration $C_{eq}$. It was shown by *Sugimoto et al.* that one can derive an expression for the surface energy.[45] In this derivation, they relate the concentration of monomer $C_{eq}$ that would be in equilibrium with a flat bulk solid and $\Omega_{solid}$ which is the molecular volume of the solid material.

$$C_{eq(R)} = C_{eq,\infty} \exp\left(\frac{2\Omega_{solid}\gamma}{R k_B T}\right) \tag{3.2}$$

In the Gibbs-Thomson treatment, the 1/R increase in the chemical potential of a nanocrystal compared to the chemical potential of a bulk semiconductor originated from the increase in surface energy from dangling bonds on the surface of the nanocrystal. At equilibrium, the chemical potential of the particle is the same as the chemical potential of the reaction. As such, smaller particles would be at equilibrium with higher precursor concentrations. As described by the authors, the specific surface energy does not depend on the particle's radius, but rather than the properties of the interface. Sugimoto derived an expression for this surface energy without adsorption for solid particles in a liquid

$$\gamma = -\frac{k_B T \ln\{\Omega_{liquid} C_{eq,\infty}\}}{(36\pi\Omega_{solid}^2)^{1/3}} \tag{3.3}$$

This equation provides a starting point for concepts of nucleation, growth, and ripening in nanocrystals when considering thermodynamics only. The first concept is that nucleation occurs during initial high monomer concentrations (immediately during the precursor injection for a hot injection synthesis). If nuclei were to form randomly with a size larger than some critical radius $r^*$ these radii will be energetically stable and can grow, while smaller radii would spontaneously dissociate or redissolve to lower the Gibbs free energy. This critical size can be estimated using thermodynamics. The free energy of formation, $\Delta G$, is the sum of volume energy and surface energy as shown in the equation below, where $\rho$ is the density, $\mu_{solid}$ and $\mu_{liquid}$ are the chemical potentials of the bulk solid and liquid monomer, respectively.

$$\Delta G = \frac{4}{3}\pi R^3 \rho(\mu_{solid} - \mu_{liquid}) + 4\pi R^2 \gamma \qquad (3.4)$$

$$= \frac{4}{3}\pi R^3 \Delta G_V + 4\pi R^2 \gamma$$

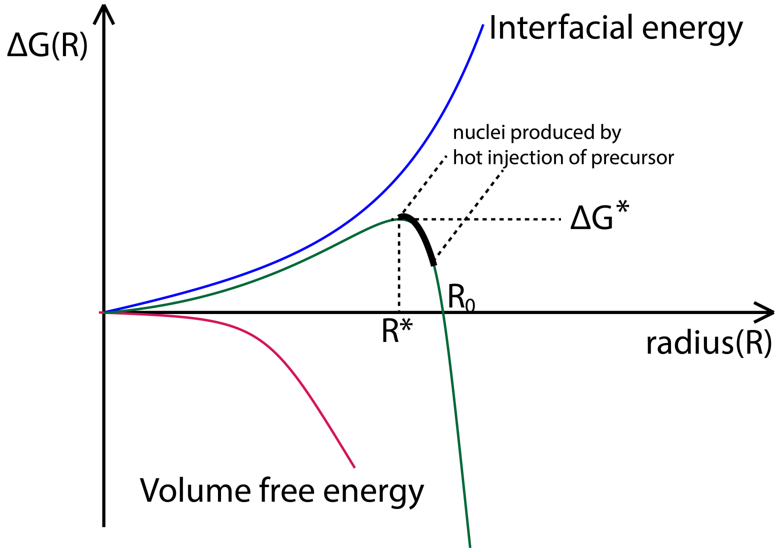

**Figure 3.3 Sketch of the free energy of formation of a cluster according to classical nucleation theory for homogenous nucleation**

For particle formation, the free energy change, $\Delta G(R)$, is balanced by two competing factors, the volume free energy and the interfacial energy due to the formation of solid phase, just as depicted in Figure 3.3 above. If $(\mu_{solid} - \mu_{liquid}) < 0$, then $\Delta G_V < 0$. As R increases, initially for small radii particles, $R^3 > R^2$, so $\Delta G(R) > 0$; for large $R$, $R^3 < R^2$, then $\Delta G(R) < 0$. As a result, $\Delta G(R)$ must go through a maximum as illustrated in the figure above. At the maximum

$$\frac{d\Delta G(R)}{dr} = 0 = 4\pi R^2 \Delta G_V + 8\pi R\gamma$$

$$R^* = -\frac{2\gamma}{\Delta G_V}$$

substituting the critical radius $R^*$ into Eqn 3.4

$$\Delta G^* = \Delta G(R^*) = \frac{4}{3}\pi R^{*3}\Delta G_V + 4\pi R^{*2}\gamma$$

$$= \frac{4}{3}\pi\left(-\frac{8R^3}{\Delta G_V^3}\right)\Delta G_V + 4\pi\left(\frac{4\gamma^2}{\Delta G_V^2}\right)$$

$$= \frac{16\pi\gamma^3}{3\Delta G_V^2}$$

Looking at Eqn 3.4 and Figure 3.3, we see that beyond this critical radius, $\Delta G(R)$ decreases with increasing $R$, and at $R_0$, $\Delta G(R) = 0$. Thus,

$$0 = \Delta G(R) = -\frac{4}{3}\pi R_0^3 \Delta G_V + 4\pi R_0^2\gamma$$

$$R_0 = -\frac{3\gamma}{\Delta G_V}$$

From these derivations, we can make several observations. When a particle grows to $R_0$, the nucleation barrier decreases to zero. However, it is noted that $\Delta G(R_0)$ is not a minimum. At this point, nucleation continues as the $\Delta G(R)$ will become negative (<0) and becomes thermodynamically favorable.

### 3.2.2 Kinetically controlled – heat up synthesis

While the "*hot-injection method*" synthesis mentioned above yields size distributions of $\sigma \sim 5\%$ experimentally for II-VI, III-V, and IV-VI semiconductor nanocrystals , goals towards increasing the monodispersity, that is, having nanocrystals of nearly all the same size. With respect to photovoltaic applications, having a better monodispersity lessens the energy landscape through which carriers have to travel resulting in a better charge extraction.[46]. Additionally, simulations suggest that having narrow size distribution can result in larger open-circuit voltages in solar cell devices.[46,47] Furthermore, discussions and efforts are now being made towards the formation of nanocrystal superlattices, including our lab. Such ordered arrangements can leverage off the collective properties and novel photophysics of these materials. For instance, increasing the packing fraction can increase light absorption per unit volume as well enhance electronic coupling between dots with the potential for extended states or *band-like* transport. [14,46] With respect to photodetectors, one can also imagine well-controlled absorption and emission line widths that allows for better spectral tuning.

To effectively improve the size distributions of nanocrystals, unlike the *hot-injection* method described in the previous section, the reaction has to be *diffusion-controlled* or diffusion-limited, kinetically. While it is beyond the scope of this thesis, I will briefly discuss diffusion and a reaction rate controlled synthesis. Following the notion outlined in *Talapin et. al*'s publication[48], the evolution of a single nanocrystal in a colloidal solution can be described as a thermally activated process. We consider a single particle in an infinite solution with a constant volume of solution with a constant monomer concentration. This monomer can react with the surface adding a new unit to the nanocrystal or can leave the surface. These monomers, at the beginning of all syntheses, are either bound to ligands at either prohibit or lower their reactivity, or are present in a larger complex that requires some thermal decomposition before the monomer is chemically available. In a reaction, the precursor, defined as a ligand-monomer complex, dissociates from its ligands or reacts to form free monomer with a rate constant:

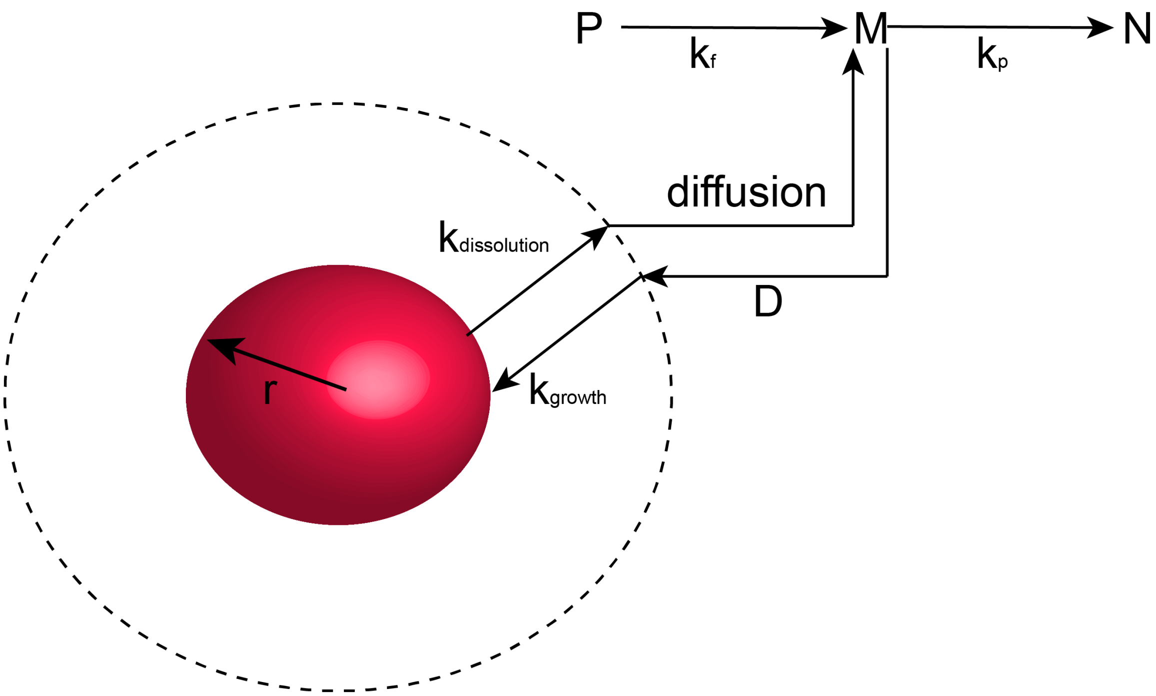

**Figure 3.4 Schematic outlining mechanism of NC nucleation and growth.** First, precursors (P) dissociate into monomers (M), followed by the formation of nuclei (N). The nuclei grows as monomers continue to diffuse to the particle/solution interface and then reacts and becomes incorporated into the nanocrystal lattice.

$$k_f = \frac{d[M]}{dt} = -\frac{d[P]}{dt} A exp\left\{-\frac{E_A}{RT}\right\}[P] \tag{3.5}$$

Here, $A$ is a prefactor, $E_A$ is the activation energy for precursor decomposition or dissociation, which is related to the magnitude of the ligand binding energy, and $T$ is the temperature of the nanocrystals. Upon heating, the precursor is transformed into monomers dictated by the rate $k_f$ based on the monomer formation reaction:

$$P \overset{k_f}{\rightarrow} M$$

The monomer aids in the formation of stable nuclei by reacting with metastable nuclei by diffusion of the monomers to the particle/solution interface at a rate $D$ (see figure 3.4) and is then incorporated into the particle at a rate governed by the relative magnitudes of the growth and dissolution rate constants ($k_g$ and $k_d$). The ratio of these rates gives the equilibrium constant for the dissociation of the bulk material

$$K_{eq} = {}^{k_d}\!/_{k_g} = C_o \tag{3.6}$$

Diffusion of these monomers from the bulk of the solution towards the particle surface/interface is described using Fick's first law (see reference). Under steady-state conditions, the number of monomers added and removed from the surface must be equal to those diffusing towards the particle from the bulk. Following the reference, the concentration of monomer near the interface is:

$$[M]_r = \frac{D[M]_{bulk} + rk_d \exp\left(\beta \frac{2\gamma V_m}{rRT}\right)}{rk_g \exp\left(-\alpha \frac{2\gamma V_m}{rRT}\right) + D} \tag{3.7}$$

The reference continues to simplify to obtain an important expression for the size dependent rate of the particle radius relating the total flux of monomers towards the particle surface to yield:

$$\frac{dr^*}{d\tau} = \frac{S - \exp(\frac{1}{r^*})}{r^* + Kexp(\frac{\alpha}{r^*})}$$

$$r^* = \frac{RT}{2\gamma V_m} \qquad \tau = \frac{R^2T^2DC^0}{4\gamma^2 V_m}t \qquad K = \frac{RT}{2\gamma V_m}\frac{D}{k_g} \qquad S = \frac{[M]_{bulk}}{C^0}$$

(3.8)

Here, $K$ is a dimensionless parameter describing the type control of the process (ratio between diffusion controlled or reaction rate controlled); $S$ is the parameter describing oversaturation of the monomer of the monomer in solution. When D << $k_g$ (K approaches 0) and $r^*$ >> 1 which is considered the diffusion controlled process. Others have called this as the *focusing and defocusing* of the size distribution of growing II-VI, III-V, and more recently IV-VI semiconductor nanocrystals. From the expression 3.8, there remains doubt on how one can determine nanocrystal growth is diffusion or reaction limited. An argument for diffusion-limited growth has been focused on experimental observation of ensemble narrowing, which is easily simulated as K approaches zero. Experimentally, this can be achieved for low reaction temperatures and low monomer diffusion to the particle surface. Often times, a *heat-up synthesis* tends to be the preferred method. If we analyze this issue further, to expect the growth rate to be purely diffusion controlled or diffusion limited, the rate of nanocrystal growth has to equal the rate of surface reaction, $k_r$ ($k_r >> D$). This reduces equation 3.8 to

$$\frac{dr}{d\tau} = \frac{D}{V_m}[M]_{bulk} \tag{3.8}$$

If we estimate things such as a diffusion coefficient for monomers of about D ~ $10^{-9}$ $m^2s^{-1}$, a molar volume of $V_m$ ~ $10^{-5}$ $m^3$ $mol^{-1}$, and a monomer concentration *[M]* of 100 mol $m^{-3}$ (0.1M), the approximate growth rate for a nanometer sized nuclei is $10^{-3}$ $ms^{-1}$, which is several orders of magnitude faster than what is typically observed in nanocrystals (~$10^{-10}$ to $10^{-9}$ m $s^{-1}$)![49,50]

For PbSe, diffusion controlled synthesis has been recently been achieved in efforts to improve monodispersity[51-53] and incorporate halides[54,55] for improved device performance. Due to the ability to tune the band gap of quantum dots, these materials make them useful for applications such as photovoltaics, photodetectors, and infrared light emission. In many of these applications, it would be desirable to have monodisperse quantum dots, which means having nanocrystals of nearly all the same size. This monodispersity should reduce the energetic landscape introduced due to inhomogeneity of current quantum dot films, which should maximize the rate of charge extraction and increase open-circuit voltage. The work by Weidman *et al.* demonstrated size dispersions as low as 3%. Such improvements could lead to more ordered arrangements of nanocrystals which can increase light absorption per unit volume and enhance inter-dot coupling.

In light of these recent reactions and by approximating values for monomer concentration, it is surprising that in the diffusion limit, surface chemistries and differences in the lead halide precursor played a large role in the growth rate of the PbSe nanocrystals.[54]Given the amounts that were used in the paper, it seems more likely that the growth was limited by the rate at which the precursor is converted into monomer or at the nanocrystal surface. One would expect that the precursor conversion rate and the surface reaction rate would be similar. Rather than the chemical nature of the ligand chemistry controlling diffusion of monomers to the particle surface, others have shown that by controlling the viscosity of the reaction[56] and the ratios of the precursor in a viscous solution[51], one can obtain nanocrystals with excellent monodispersity that can be considered truly diffusion-controlled.

### 3.3 Thin-film development

For the entire thesis, PbSe quantum dots are prepared using the *hot-injection* method based on previously published methods.[16] For film formation, a layer-by-layer procedure is adopted using a mechanical dip coater mounted inside a glovebox (DC Multi-4, Nima Technology). For all substrates (glass, double sided polish silicon, quartz, prepatterned FETs, or sapphire substrates), three 15 minutes sonication in Hellmanex® III solution (20% v/v), Millipore water, and isopropyl alcohol, and then dried under $N_2$ flow. For films, a 5 mg $mL^{-1}$ solution of quantum dots in dry hexane were alternately dipped at a speed of 200 mm/s in a ligand treatment solution (2 mM for 1,2-ethanedithiol (EDT), 2 mM for formic acid (FA), 2 mM for 1,4-benzenedithiol (BDT), 0.5 mM sodium sulfide ($Na_2S$), 4 mM ammonium thiocyante ($NH_4SCN$)). Films of various thicknesses range from 16 nm to 350 nm (thin for FETs and XPS, thicker for XPS, UV-Vis, FTIR, SIMS, and XRD studies). For IR studies, films of oleate-capped QDs were made by spin coating a 100 mg $mL^{-1}$ solution of quantum dots in dry octane.

## REFERENCES

(1) Talapin, D. V.; Lee, J. S.; Kovalenko, M. V. Prospects of Colloidal Nanocrystals for Electronic and Optoelectronic Applications. *Chem. Rev.* **2009**.

(2) Hetsch, F.; Zhao, N.; Kershaw, S. V.; Rogach, A. L. Quantum Dot Field Effect Transistors. *Materials Today* **2013**, *16*, 312–325.

(3) Klimov, V. I. Nanocrystal Quantum Dots, Second Edition; CRC Press, 2010.

(4) Nozik, A. J.; Beard, M. C.; Luther, J. M.; Law, M. Semiconductor Quantum Dots and Quantum Dot Arrays and Applications of Multiple Exciton Generation to Third-Generation Photovoltaic Solar Cells. *Chem. Rev.* **2010**, *110*, 6873–6890.

(5) Chung, D. S.; Lee, J.-S.; Huang, J.; Nag, A.; Ithurria, S.; Talapin, D. V. Low Voltage, Hysteresis Free, and High Mobility Transistors From All-Inorganic Colloidal Nanocrystals. *Nano Lett.* **2012**, *12*, 1813–1820.

(6) Gao, J.; Johnson, J. C. Charge Trapping in Bright and Dark States of Coupled PbS Quantum Dot Films. *ACS Nano* **2012**, *6*, 3292–3303.

(7) Gao, J.; Zhang, J.; van de Lagemaat, J.; Johnson, J. C.; Beard, M. C. Charge Generation in PbS Quantum Dot Solar Cells Characterized by Temperature-Dependent Steady-State Photoluminescence. *ACS Nano* **2014**, *8*, 12814–12825.

(8) Hughes, B. K.; Ruddy, D. A.; Blackburn, J. L.; Smith, D. K.; Bergren, M. R.; Nozik, A. J.; Johnson, J. C.; Beard, M. C. Control of PbSe Quantum Dot Surface Chemistry and Photophysics Using an Alkylselenide Ligand. *ACS Nano* **2012**, *6*, 5498–5506.

(9) Chappell, H. E.; Hughes, B. K.; Beard, M. C.; Nozik, A. J.; Johnson, J. C. Emission

Quenching in PbSe Quantum Dot Arrays by Short-Term Air Exposure. *J. Phys. Chem. Lett.* **2011**, *2*, 889–893.

(10) Blackburn, J. L.; Chappell, H.; Luther, J. M.; Nozik, A. J.; Johnson, J. C. Correlation Between Photooxidation and the Appearance of Raman Scattering Bands in Lead Chalcogenide Quantum Dots. *J. Phys. Chem. Lett.* **2011**, *2*, 599–603.

(11) Liu, C.-Y.; Kortshagen, U. R. A Silicon Nanocrystal Schottky Junction Solar Cell Produced From Colloidal Silicon Nanocrystals. *Nanoscale Research Letters* **2010**, *5*, 1253–1256.

(12) Anwar, S. Handbook of Research on Solar Energy Systems and Technologies; IGI Global, 2012.

(13) Sun, L.; Choi, J. J.; Stachnik, D.; Bartnik, A. C.; Hyun, B.-R.; Malliaras, G. G.; Hanrath, T.; Wise, F. W. Bright Infrared Quantum-Dot Light-Emitting Diodes Through Inter-Dot Spacing Control. *Nature Nanotechnology* **2012**, *7*, 369–373.

(14) Hanrath, T. Colloidal Nanocrystal Quantum Dot Assemblies as Artificial Solids. *J. Vac. Sci. Technol. A* **2012**, *30*, 030802.

(15) Liu, Y.; Gibbs, M.; Puthussery, J.; Gaik, S.; Ihly, R.; Hillhouse, H. W.; Law, M. Dependence of Carrier Mobility on Nanocrystal Size and Ligand Length in PbSe Nanocrystal Solids. *Nano Lett.* **2010**.

(16) Law, M.; Luther, J. M.; Song, Q.; Hughes, B. K.; Perkins, C. L.; Nozik, A. J. Structural, Optical, and Electrical Properties of PbSe Nanocrystal Solids Treated Thermally or with Simple Amines. *J. Am. Chem. Soc.* **2008**, *130*, 5974–5985.

(17) Luther, J. M.; Law, M.; Beard, M. C.; Song, Q.; Reese, M. O. Schottky Solar Cells Based on Colloidal Nanocrystal Films - Nano Letters (ACS Publications). *Nano Lett.* **2008**.

(18) Gaulding, E. A.; Diroll, B. T.; Goodwin, E. D.; Vrtis, Z. J.; Kagan, C. R.; Murray, C. B. Deposition of Wafer-Scale Single-Component and Binary Nanocrystal Superlattice Thin Films via Dip-Coating. *Advanced Materials* **2015**, *27*, 2846–.

(19) Kim, J. Y.; Adinolfi, V.; Sutherland, B. R.; Voznyy, O.; Kwon, S. J.; Kim, T. W.; Kim, J.; Ihee, H.; Kemp, K.; Adachi, M.; *et al.* Single-Step Fabrication of Quantum Funnels via Centrifugal Colloidal Casting of Nanoparticle Films. *Nature Communications* **2015**, *6*, 1–9.

(20) Talapin, D. V. PbSe Nanocrystal Solids for N- and P-Channel Thin Film Field-Effect Transistors. *Science* **2005**, *310*, 86–89.

(21) Nag, A.; Kovalenko, M. V.; Lee, J.-S.; Liu, W.; Spokoyny, B.; Talapin, D. V. Metal-Free Inorganic Ligands for Colloidal Nanocrystals: S2–, HS–, Se2–, HSe–, Te2–, HTe–, TeS32–, OH–, and NH2– as Surface Ligands. *J. Am. Chem. Soc.* **2011**.

(22) Osedach, T. P.; Zhao, N.; Andrew, T. L.; Brown, P. R. Bias-Stress Effect in 1,2-Ethanedithiol-Treated PbS Quantum Dot Field-Effect Transistors - ACS Nano (ACS Publications). *ACS Nano* **2012**.

(23) Choi, J.-H.; Oh, S. J.; Lai, Y.; Kim, D. K.; Zhao, T.; Fafarman, A. T.; Diroll, B. T.; Murray, C. B.; Kagan, C. R. In Situ Repair of High-Performance, Flexible Nanocrystal Electronics for Large-Area Fabrication and Operation in Air. *ACS Nano* **2013**, *7*, 8275–8283.

(24) Kim, D. K.; Lai, Y.; Vemulkar, T. R.; Kagan, C. R. Flexible, Low-Voltage, and Low-Hysteresis PbSe Nanowire Field-Effect Transistors. *ACS Nano* **2011**, *5*, 10074–10083.

(25) Nugraha, M. I.; Haeusermann, R.; Bisri, S. Z.; Matsui, H.; Sytnyk, M.; Heiss, W.; Takeya, J.; Loi, M. A. High Mobility and Low Density of Trap States in Dual-Solid-Gated PbS Nanocrystal Field-Effect Transistors. *Advanced Materials* **2015**, *27*, 2107–2112.

(26) Lokteva, I.; Thiemann, S.; Gannott, F.; Zaumseil, J. Ambipolar, Low-Voltage and Low-Hysteresis PbSe Nanowire Field-Effect Transistors by Electrolyte Gating. *Nanoscale* **2013**, *5*, 4230–4235.

(27) Kang, M. S.; Sahu, A.; Norris, D. J.; Frisbie, C. D. Size- and Temperature-Dependent Charge Transport in PbSe Nanocrystal Thin Films. *Nano Lett.* **2011**.

(28) Kang, M. S.; Sahu, A.; Norris, D. J.; Frisbie, C. D. Size-Dependent Electrical Transport in CdSe Nanocrystal Thin Films. *Nano Lett.* **2010**, *10*, 3727–3732.

(29) Sahu, A.; Kang, M. S.; Kompch, A.; Notthoff, C.; Wills, A. W.; Deng, D.; Winterer, M.; Frisbie, C. D.; Norris, D. J. Electronic Impurity Doping in CdSe Nanocrystals. *Nano Lett.* **2012**, *2*, 2587–2594.

(30) Swisher, S. L. Transfer-Printed Electrodes for Colloidal Nanocrystal Solar Cells Utilizing “Soft” Polydimethylsiloxane Stamps. *Master of Science, Plan II* **2012**, 1–21.

(31) Xie, Y.; Qian, Y. T.; Wang, W. Z.; Zhang, S. Y.; Zhang, Y. H. A Benzene-Thermal Synthetic Route to Nanocrystalline GaN. *Science* **1996**, *272*, 1926–1927.

(32) Murray, C. B.; Norris, D. J.; Bawendi, M. G. Synthesis and Characterization of Nearly Monodisperse CdE (E = Sulfur, Selenium, Tellurium) Semiconductor Nanocrystallites - Journal of the American Chemical Society (ACS Publications). *J. Am. Chem. Soc.* **1993**.

(33) Lifshitz, E.; Dag, I.; Litvin, I.; Hodes, G.; Gorer, S. Optical Properties of CdSe Nanoparticle Films Prepared by Chemical Deposition and Sol–Gel Methods. *Chemical Physics Letters* **1998**, *288*, 188–196.

(34) Chen, D. H.; Wu, S. H. Synthesis of Nickel Nanoparticles in Water-in-Oil Microemulsions. *Chem. Mater.* **2000**, *12*, 1354–1360.

(35) Merkoci, A.; Marin, S.; Castaneda, M. T.; Pumera, M.; Ros, J.; Alegret, S. Crystal and Electrochemical Properties of Water Dispersed CdS Nanocrystals Obtained via Reverse Micelles and Arrested Precipitation. *Nanotechnology* **2006**, *17*, 2553–2559.

(36) Peng, Z. A.; Peng, X. G. Formation of High-Quality CdTe, CdSe, and CdS Nanocrystals Using CdO as Precursor. *J. Am. Chem. Soc.* **2001**, *123*, 183–184.

(37) Koh, W.-K.; Bartnik, A. C.; Wise, F. W.; Murray, C. B. Synthesis of Monodisperse PbSe Nanorods: a Case for Oriented Attachment. *J. Am. Chem. Soc.* **2010**, *132*, 3909–3913.

(38) Zhang, J.; Crisp, R. W.; Gao, J.; Kroupa, D. M.; Beard, M. C.; Luther, J. M. Synthetic Conditions for High-Accuracy Size Control of PbS Quantum Dots. *J. Phys. Chem. Lett.* **2015**, *6*, 1830–1833.

(39) Arjan J Houtepen; Rolf Koole; Daniël Vanmaekelbergh; Johannes Meeldijk, A.;

Stephen G Hickey. The Hidden Role of Acetate in the PbSe Nanocrystal Synthesis. *J. Am. Chem. Soc.* **2006**, *128*, 6792–6793.

(40) Cho, K. S.; Talapin, D. V.; Gaschler, W. Designing PbSe Nanowires and Nanorings Through Oriented Attachment of Nanoparticles - Journal of the American Chemical Society (ACS Publications). *Journal of the American …* **2005**, *127*, 7140–7147.

(41) Nag, A.; Chung, D. S.; Dolzhnikov, D. S.; Dimitrijevic, N. M.; Chattopadhyay, S.; Shibata, T.; Talapin, D. V. Effect of Metal Ions on Photoluminescence, Charge Transport, Magnetic and Catalytic Properties of All-Inorganic Colloidal Nanocrystals and Nanocrystal Solids. *J. Am. Chem. Soc.* **2012**.

(42) Anderson, N. C.; Hendricks, M. P.; Choi, J. J.; Owen, J. S. Ligand Exchange and the Stoichiometry of Metal Chalcogenide Nanocrystals: Spectroscopic Observation of Facile Metal-Carboxylate Displacement and Binding. *J. Am. Chem. Soc.* **2013**, *135*, 18536–18548.

(43) Kershaw, S. V.; Harrison, M. T.; Burt, M. G. Putting Nanocrystals to Work: From Solutions to Devices. *Philosophical Transactions of the Royal Society A: Mathematical, Physical and Engineering Sciences* **2003**, *361*, 331–343.

(44) Gaponik, N.; Talapin, D. V.; Rogach, A. L.; Eychmüller, A.; Weller, H. Efficient Phase Transfer of Luminescent Thiol-Capped Nanocrystals:  From Water to Nonpolar Organic Solvents. *Nano Lett.* **2002**, *2*, 803–806.

(45) Sugimoto, T.; Shiba, F. A New Approach to Interfacial Energy. 3. Formulation of the Absolute Value of the Solid–Liquid Interfacial Energy and Experimental

Collation to Silver Halide Systems †. *J. Phys. Chem. B* **1999**, *103*, 3607–3615.

(46) Guyot-Sionnest, P. Electrical Transport in Colloidal Quantum Dot Films. *J. Phys. Chem. Lett.* **2012**.

(47) Zhitomirsky, D.; Kramer, I. J.; Labelle, A. J.; Fischer, A.; Debnath, R.; Pan, J.; Bakr, O. M.; Sargent, E. H. Colloidal Quantum Dot Photovoltaics: the Effect of Polydispersity. *Nano Lett.* **2012**, *12*, 1007–1012.

(48) Talapin, D. V.; Rogach, A. L.; Haase, M.; Weller, H. Evolution of an Ensemble of Nanoparticles in a Colloidal Solution: Theoretical Study. *J. Phys. Chem. B* **2001**, *105*, 12278–12285.

(49) Shevchenko, E. V.; Talapin, D. V. Study of Nucleation and Growth in the Organometallic Synthesis of Magnetic Alloy Nanocrystals: the Role of Nucleation Rate in Size Control of CoPt3 Nanocrystals - Journal of the American Chemical Society (ACS Publications). *J. Am. Chem. Soc.* **2003**.

(50) Owen, J. S.; Chan, E. M.; Liu, H.; Alivisatos, A. P. Precursor Conversion Kinetics and the Nucleation of Cadmium Selenide Nanocrystals. *Journal of the American …* **2010**.

(51) Weidman, M. C.; Beck, M. E.; Hoffman, R. S.; Prins, F.; Tisdale, W. A. Monodisperse, Air-Stable PbS Nanocrystals viaPrecursor Stoichiometry Control. *ACS Nano* **2014**, *8*, 6363–6371.

(52) Kim, J. Y.; Chou, K. W.; Amassian, A.; Sargent, E. H. High-Performance Quantum-Dot Solids via Elemental Sulfur Synthesis - Yuan - 2014 - Advanced Materials - Wiley Online Library. *Adv. Mater.* **2014**.

(53) Ma, W.; Swisher, S. L.; Ewers, T.; Engel, J.; Ferry, V. E.; Atwater, H. A.; Alivisatos, A. P. Photovoltaic Performance of Ultrasmall PbSe Quantum Dots. *ACS Nano* **2011**, *5*, 8140–8147.

(54) Zhang, J.; Gao, J.; Miller, E. M.; Luther, J. M.; Beard, M. C. Diffusion-Controlled Synthesis of PbS and PbSe Quantum Dots with in Situ Halide Passivation for Quantum Dot Solar Cells. *ACS Nano* **2013**.

(55) Zhang, J.; Gao, J.; Church, C. P.; Miller, E. M.; Luther, J. M.; Klimov, V. I.; Beard, M. C. PbSe Quantum Dot Solar Cells with More Than 6% Efficiency Fabricated in Ambient Atmosphere. *Nano Lett.* **2014**, *14*, 6010–6015.

(56) Cademartiri, L.; Bertolotti, J.; Sapienza, R.; Wiersma, D. S.; Freymann, von, G.; Ozin, G. A. Multigram Scale, Solventless, and Diffusion-Controlled Route to Highly Monodisperse PbS Nanocrystals. *Journal of Physical Chemistry B* **2006**, *110*, 671–673.

# CHAPTER 4

# HIGH MOBILITY QD FIELD-EFFECT TRANSISTOR WITH AN AIR STABLE ELECTRON MOBILITY ABOVE 7 CM$^2$ V$^{-1}$ S$^{-1}$

## 4.1 Context

Attempts to utilize lead chalcogenide quantum dots in light-emitting diodes, field-effect transistors, and photovoltaics have consistently demonstrated poor device performance. Reports claim that organic ligands bound to the quantum dots are the root of the problem because they inhibit efficient charge transport.[1] In films based on quantum dots, they are usually separated by a surfactant molecule, which plays an important role in electrical transport. Most of these surfactants, classified according to the polar head group, are long hydrocarbon chains, which act as dielectric tunneling barriers. In the regime of weak coupling, the electronic structure can be described as discrete wavefunctions localized on individual particles.[2] When two or more semiconducting quantum dots are brought in close proximity to each other, these wavefunctions can interact (and couple), forming *molecular orbitals* delocalized over several particles or even throughout the entire array of quantum dots. The quantum mechanical coupling between the energy levels can be expressed in terms of the coupling energy $\beta \approx h\Gamma$, where $h$ is Planck's constant and $\Gamma$ is the tunneling rate between two orbitals of quantum dots. The tunneling rate is approximated as:

$$\Gamma \approx \exp\{-2(\frac{2m^*\Delta E}{h^2})^{1/2}\Delta x$$

where $m^*$ is the electron effective mass, $\Delta E$ is the height of the tunnel barrier, and $\Delta x$ is the distance between the quantum dots. It is clear that the tunneling rate decreases exponentially with increasing separation between the quantum dots and weakly dependent on the barrier height and the carrier effective mass. Hence, by reducing $\Delta x$ and $\Delta E$ by properly designing the inter-quantum dot medium or replacing the long hydrocarbon chains with smaller, more compact ligands, the strength of electronic coupling can be controlled.

## 4.2 Previous ligand exchange reactions

There are enormous amounts of reports claiming removal of the long hydrocarbon chains with other surfactants. If the surfactant has no charge groups on its head, it is a *non-ionic surfactant*. If the head of the surfactant has a negative (positive) charge, the surfactant is more *anionic (cationic)*. While both of these organic surfactants can bind to the quantum dot, anionic ligands *must* be present in order to balance the charge of the excess metal at the surface of the quantum dot based on elemental analysis demonstrating metal excess ranging from 28 to 37% depending on the size of the quantum dot and purification.[3] Some exchange reactions include pyridine or other amines, which is not effective in displacing X-type surfactants (anionic surfactant, i.e. carboxylates and phosphonates) alone without accumulating charge at the nanocrystal surface. Furthermore, these reactions do not achieve complete exchange.[4-6] As such methods to remove these X-type ligands are necessary. The most common method relies on salt metathesis, where the salt of the desired anion is added to exchange the native X-type ligand. These reactions rely on mass action in which a large excess of the desired anion (along with the charge balancing counter cation) are added in a supersaturated solution to insure full exchange of the quantum dot ligand shell. Common X-type ligands include halide[7,8], sulfide[9,10], thiocyanate[11], and metal chalcogenide anions[12].

The work described in this chapter is based on prior studies where PbSe quantum dots with anionic alkylcarboxylate (oleic acid) were exchanged with thiolates (EDT) to develop thin films.[13] These films are further processed by depositing a conformal coating of amorphous $Al_2O_3$ or thin layer of amorphous $Al_2O_3$ followed by crystalline ZnO via atomic-layer deposition (ALD). This method allows for the development of robust inorganic nanocomposites in which the quantum dots are protected against oxidative and photothermal damage. In addition, infilling QD transistors and solar cells yielded stable devices with improved device performance.

In this chapter, the focus will be on developing a process in which the electronic coupling can be improved by using small inorganic ligands which favors high-mobility transport. In addition, the work here will demonstrate the ability to tune the carrier concentration and passivate surface acceptor states by infilling the QDs with amorphous alumina. This combined approach is important because although the use of small ligands can potentially yield higher carrier mobility and better transport in quantum dot films, it does not guarantee that it passivate the density of states within the band gap. Often times, mobility in quantum dot solids and in other disordered semiconductor FETs such as a-Si[14] and organic semiconductors[15,16] usually increase with increasing magnitude of the gate voltage (larger gate-induced carrier densities). When a bias is applied to the gate, a surface potential $\varphi_S$ develops at the semiconductor-interface, which results in shifting the

Fermi level at the surface towards the band edge, thus partially filling the density of states within the gap. Accordingly, any additional charge carriers have its energy closer to the band edge, so its thermal release becomes easier and the *effective mobility* increases. Utilizing four-point gated FETs, we can distinguish between a *trap-filled* field-effect mobility, which overestimates the intrinsic mobility of the film and a field-effect mobility that does not depend on carrier density. As a result, this chapter will demonstrate electron mobilities above 7 cm$^2$ V$^{-1}$ s$^{-1}$ in PbSe QD FETs by using ALD infilling of amorphous alumina (a-$Al_2O_3$) to reduce the density of surface trap states and to tune the carrier concentration in QD films prepared by dip coating with sodium sulfide ($Na_2S$).

### 4.3 Characterization of sulfide-exchanged, alumina infilled PbSe QD thin film

To prepare sulfide-exchanged, alumina infilled PbSe QD thin films, a layer-by-layer dip coating process of alternating deposition of QDs in 2 mg/ml hexane solution and a 0.5 mM $Na_2S$ ligand exchange in methanol was adopted (Fig 4.1a).

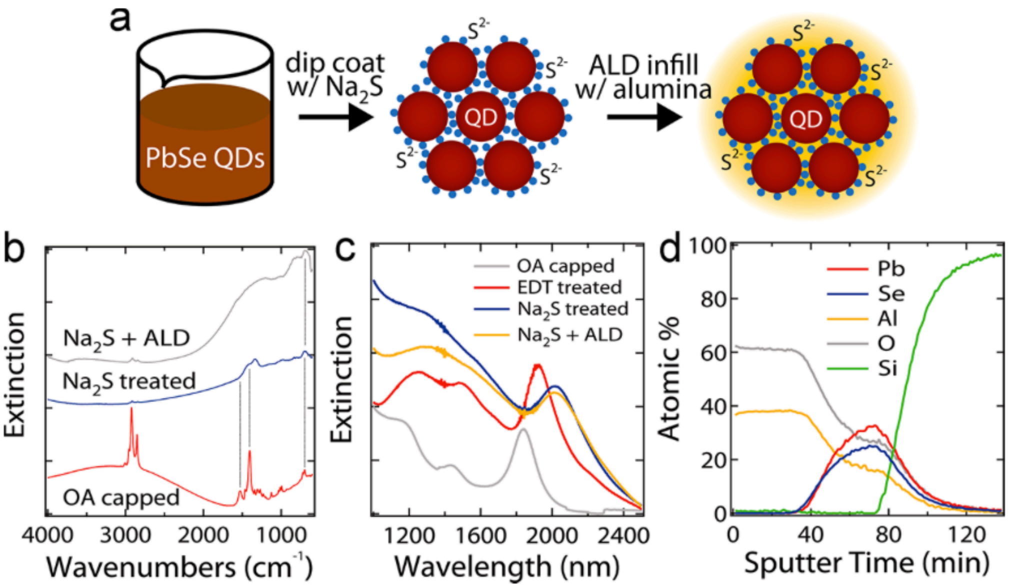

**Figure 4.1 Basic characterization of sulfide-exchanged, alumina infilled PbSe QD film** (a) Fabrication process via a layer-by-layer dip coating with sodium sulfide ligand exchange to yield sulfide-capped films. These films are further processed with alumina ALD (b) FTIR spectra of oleate-capped PbSe, sulfide-capped PbSe before and after alumina ALD (c) Comparative optical extinction spectra of oleate-capped (grey), EDT-capped (red), sulfide-capped (blue), and sulfide-capped and alumina infilled (orange) (d) XPS depth profile of a 150 nm thick sulfide-capped, alumina infilled PbSe film

FTIR spectra of sulfide-exchanged, 6.3 nm PbSe QD films before and after ALD infilling at 54°C were compared to spectrum of oleate-capped QD films prepared by spin coating to quantify the extent of oleate removal. This X-type ligand exchange with sodium sulfide results in more than 97.5% reduction of the integrated C-H stretch signal at 3300 $cm^{-1}$, consistent with quantitative removal of oleate by sulfide, as expected from an earlier report with solid-state sulfide ligand exchange of CdX, PbX, and CdX/PbX core-shell QDs.[12] Alumina infilling of sulfide-exchanged films causes no additional changes to the integrate C-H signal.

UV-Vis-IR extinction spectra of these same films on glass are compared to a common organic ligand, 1,2-ethanedithiol (EDT). For a spin-coated, oleate-capped PbSe film, the first exciton absorption peak is at 1840nm. When treated with EDT, the peak shifts to 1933 nm. Compared to sulfide-exchanged and sulfide-exchanged and alumina infilled, the peak is at 2020 nm. The corresponding redshifts are 32, 60, and 60 meV respectively. The corresponding peak widths are 62, 59, 80, and 88 meV. It is clear that the exchange with sulfide when compared to EDT results in larger redshift combined with a substantial peak broadening. This is attributed to the small interdot distance in the sulfide-exchanged films resulting in 1) enhanced dielectric screening, 2) stronger electronic coupling, and 3) partial QD necking, all of which can decrease the confinement energy (redshift) and increase the spread in confinement energies (broadening).

To illustrate this effect, structural models were simulated using a Pb-terminated PbSe {111} slabs bridged by a monolayer of the ligand. The interdot distance, defined as the average distance between surface Pb atoms, are 3.76 ± 0.006 Å and 6.4 ± 0.19 Å with sulfide and EDT ligands respectively. It is expected that the small interdot distance when using sulfide ligands will encourage necking and fusion of dots at low temperature. It is noted that additional processing of these sulfide-exchanged films do not cause additional peak shifting but there is some additional broadening which is not understood at this time.

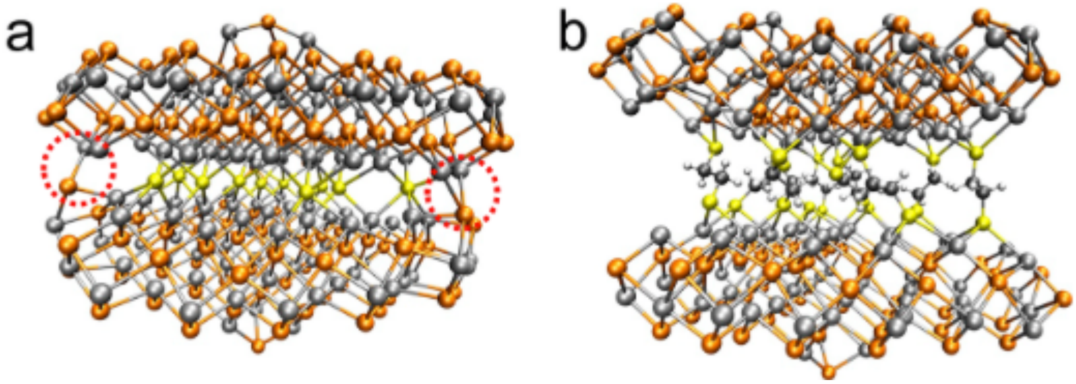

**Figure 4.2 DFT structural models of ligand-bridged Pb-terminated PbSe {111} slabs**

(a) Sulfide ligands (b) EDT ligands. Grey sphere = Pb, Orange sphere = Se, Yellow sphere = S, Black sphere = C, White sphere = H

To further demonstrate the changes in interdot distance, transmission electron microscopy was used. As expected, oleate-capped PbSe QDs have an interdot distance of about 33 Å which is twice the distance of oleic acid. It is possible this interdot distance can be overestimated or underestimated depending on the degree of interlocking of the hydrophilic hydrocarbon chains. Comparing the images of PbSe QDs treated with EDT and sodium sulfide, it is also clear that there is necking and/or fusion of the dots as a result of the very small sulfide ligand confirming the DFT structural models.

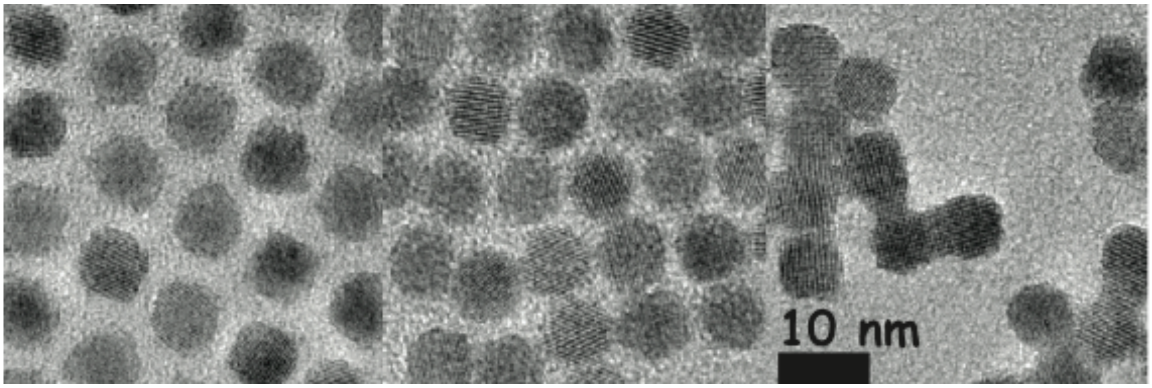

**Figure 4.3 Transmission electron microscopy of PbSe QDs** (a) oleate-capped (b) EDT-treated (c) sulfide-capped

### 4.4 Elemental analysis of sulfide-exchanged, alumina infilled PbSe QD films

To characterize the elemental composition of the infilled QD films, X-ray photoelectron spectroscopy (XPS) and secondary ion mass spectrometry (SIMS) depth profiling was used.

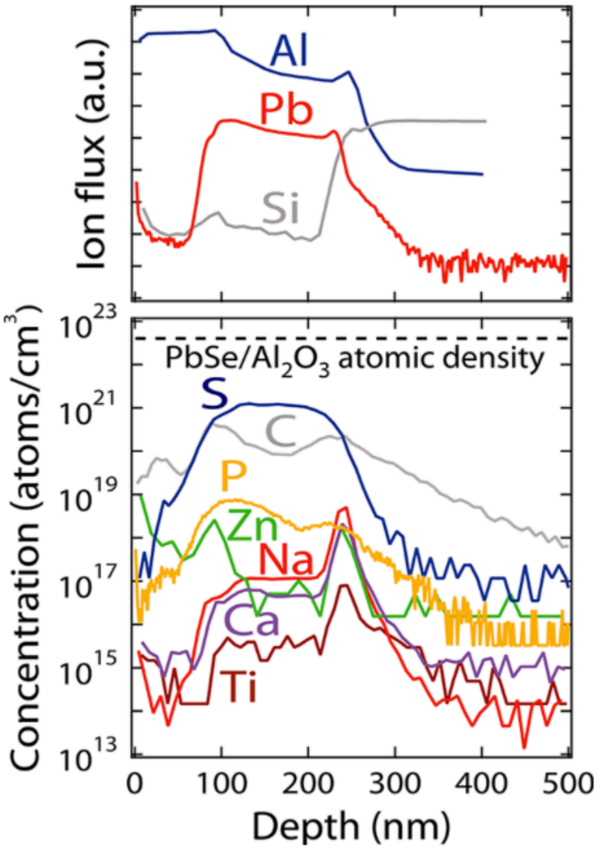

**Figure 4.4 SIMS depth profiles for 270 nm thick sulfide-treated and ALD overcoated PbSe QD film on a silicon substrate.** The top panel are the matrix elements. The bottom panel are the atomic density of the PbSe/$S^{2-}$/$Al_2O_3$ nanocomposites calculated using a 50:50 mixture with a 20% void fraction

Based on DFT structural models and TEM images, the factor of 2 decrease in the interdot distance compared to a PbSe QD thin film treated with EDT, one would expect that it would be difficult for the trimethylaluminum molecule to diffuse towards the entire thickness of the film since the available *pore* space (free space not occupied by QDs) is reduced. In order to determine if the TMA molecule can indeed fill these small pore sizes, structural models of the two most common forms found can be determined.

Thermodynamic calculations based on the free-energy minimization was used to determine the nature and relative amounts of equilibrium product species following thermal decomposition of trimethylaluminum.[17] The results demonstrated that at high temperatures and low pressures, the dominant product species is the monomeric form (Fig 4.5a) and at low temperatures and high pressures, the dimer form is dominant (Fig 4.5b)

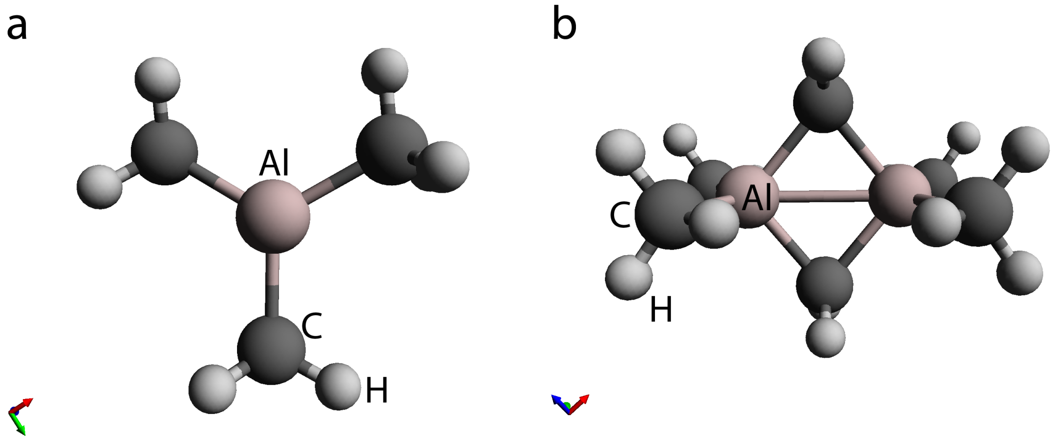

**Figure 4.5 Ball and stick model of trimethylaluminum** (a) monomer form (b) dimer form

From the ball and stick model, the monomer species can be described as an aluminum atom bonded to three methyl ($CH_3$) bonds. The symmetry is trigonal planar (three fold). The dimer species can be described as two shared methyl groups bridging two aluminum atoms. The Al-C (bridging) and Al-C (terminal) distances are reported to be 2.14 Å and 1.97 Å respectively. This is consistent with those values obtained from DFT structural models (Table 4.1).

| **Monomer** | | **Dimer** | |
|---|---|---|---|
| | **Avg. Distance** | | **Avg. Distance** |
| Al-C (terminal) | 1.979 | Al-C (terminal) | 2.017 |
| C-H | 1.114 | C-H | 1.114 |
| Al-C (bridging) | - | Al-C (bridging) | 2.074 |
| Internuclear distance | 3.424 x 3.455 x 4.259 | Internuclear distance | 7.4 x 7.4 x 4.2 |

**Table 4.1 Average atomic distances determined from structural model** (Fig 4.5)

Based on the ALD deposition conditions, the dominant species of the TMA is the dimer form. From this, we see that despite the reduced interdot distance from 6.4 Å to 3.7 Å when going from EDT-treated to sulfide-capped PbSe QD films, the dimer form of TMA is small enough to reach the bulk of the film. To confirm this, an XPS depth profile was conducted. A typical XPS depth profile for a 6.3 nm PbSe QD film sulfide-capped, infilled and overcoated with amorphous alumina deposited at 54°C is shown Fig 4.1d. Indeed, we see that the aluminum reaches the bottom of the substrate, further confirming that the alumina indeed infills the interstitial spaces within the QD film, consistent with the previous report for films treated with EDT.[13]

In addition to the confirmation that alumina infills and overcoats the QD film, concentrations of S, Na, C, P, Zn, Ca, Ti, and Fe was measured as a function of depth (bottom panel of Fig 3). Carbon and phosphorous was selected because it used in the reagents to synthesize the QDs. Sulfur and sodium was selected because it was used for the ligand exchange process. Impurities (Zn, Ca, Ti, and Fe) was selected because it is found is some trace amounts in the Pb(II) oxide precursor material for QD synthesis. Sulfur is found in concentrations of $10^{21}$ atoms/cm$^3$, which is nearly equal to the calculated concentration of Pb surface atoms in a randomly packed 6.3 nm PbSe QD film (3 X $10^{21}$ atom/cm$^3$); sulfur exists as a monolayer on the QD surface. Based on previous electrical conductivity reports on impurities and alkali metals on PbSe single crystals[18], we find that for the concentration of sodium (1 X $10^{17}$ atoms/cm$^3$) is negligible and does not contribute to the electronic transport. The concentration of carbon of about 0.1 to 0.5 atomic % is consistent with the removal of oleate as well as unavoidable due to the wet chemistry used to make these films. Phosphorous is also found in about 20-90 ppm due to the use of TOP and DPP in the QD synthesis. At this time, the role of phosphorous in electronic transport has not been extensively studied. In one report, it was found that an improvement in solar cell devices when DPP was not introduced during the synthesis.[19]

While the authors propose a difference in Fermi level position due to doping, since the $V_{OC}$ increased when using no DPP, the incorporation of phosphorous within the bulk or on the surface of the QD is not known. Based on XPS depth profiles shown here, we cannot distinguish between the surface and the bulk and we can only confirm that it exists in small amounts. There have been proposed reaction mechanisms when using secondary (DPP) and tertiary (TOP) phosphines in the synthesis of QDs. The authors propose that the secondary phosphine (DPP = $PPh_2$) when bridged between two selenium atoms increases the reactivity to yield MX (M = Pb, Cd, X = S, Se) nanocrystals in larger quantities due to a decrease in activation energy barrier.[20] More importantly, based on their structural calculations for the bonding configuration of $PPh_2$ to Se, the "ligand" bound to the nanocrystal surface is neutral. From this, the idea of doping with phosphorous and changing the Fermi level may not be correct. Instead, based on the non-stoichiometric model presented by Kim et al., it seems more likely that the number of Pb and Se exposed surfaces during the nanocrystal purification and EDT ligand exchange could have resulted in the change in Fermi level when DPP was not used.[21] The measured trace impurities for Zn, Ca, Ti, and Fe are 10 ppm, 650 ppb, 40 ppb, and < 100 ppb. In sum, the elemental analysis illustrates that PbSe QD films that are treated with $Na_2S$ and infilled with alumina contains <100 ppm phosphorus and trace amounts of Na, Zn, Ti, Ca, and Fe.

## 4.5 Field-effect transistor characteristics of sulfide-exchanged, alumina infilled PbSe films

QD FETs were made using 6.3 nm PbSe QD FETs treated with $Na_2S$ by dip coating films on prepatterned source/drain electrodes (Section 3.1) on $Si/SiO_2$ substrates.

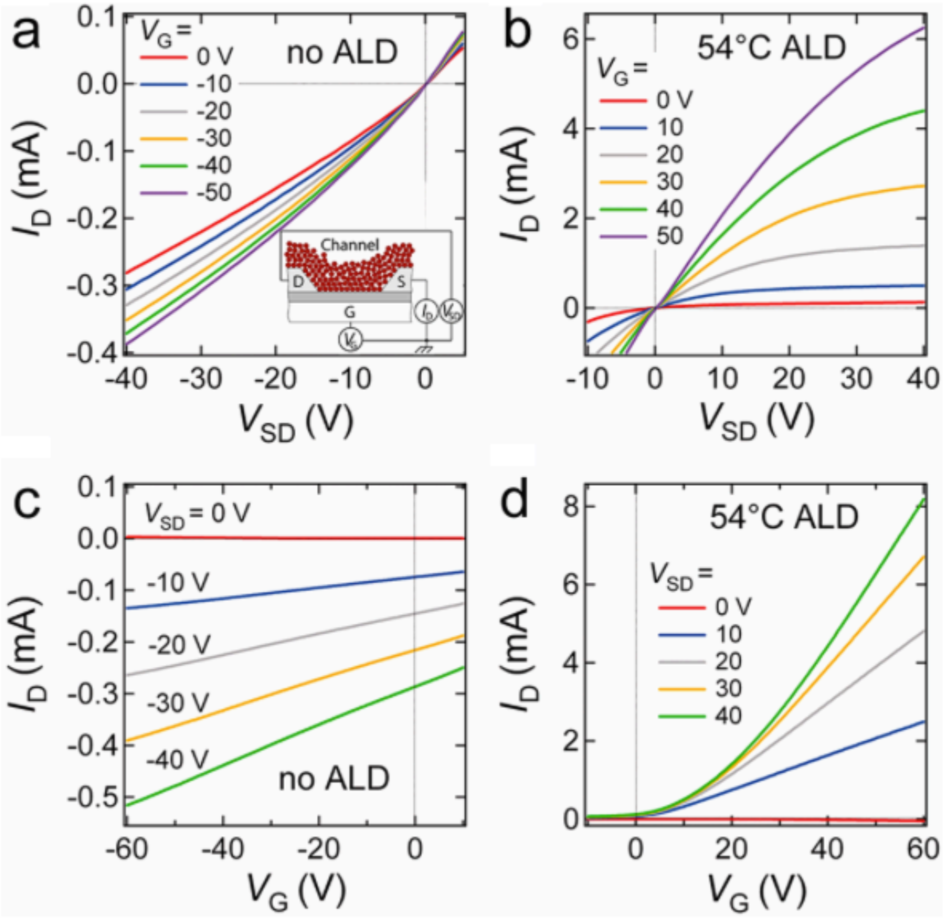

**Figure 4.6 *I*-*V* characteristics of 6.3 nm PbSe QDs treated with $Na_2S$ before and after ALD deposition at 54°C** (a,b) Output characteristics (c,d) Transfer characteristics. Data acquisition was performed at room temperature using a sweep rate of 50 $Vs^{-1}$.

Figure 4.6 demonstrates a typical FET performance for PbSe QD films treated with $Na_2S$. Before ALD, the device shows a high p-channel conductance (Fig 4.6a,c) with a quasi-linear *I-Vs* with high off currents consistent with a high concentration of holes in the film that cannot be modulated by the applied gate (normally on transistor in depletion mode). The calculated linear field-effect mobility measured at a source-drain voltage of -10V is about 0.1-0.15 $cm^2\ V^{-1}\ s^{-1}$. This larger mobility can be explained due to increased electronic coupling due to the smaller interdot distance.[2] After alumina deposition, the FET is ambipolar with a dominant n-channel and a weak p-channel (Fig 4.6b,d) The calculated linear field-effect mobility for electrons and holes measured at a source-drain voltage of +/-10 V is about 4.5-6.1 and 0.07-0.2 $cm^2\ V^{-1}\ s^{-1}$ respectively. This field-effect mobility at the time was the highest electron mobility reported.

Since this mobility was the highest ever reported during data collection, efforts to increase the mobility even further were pursued by increasing the deposition temperature.

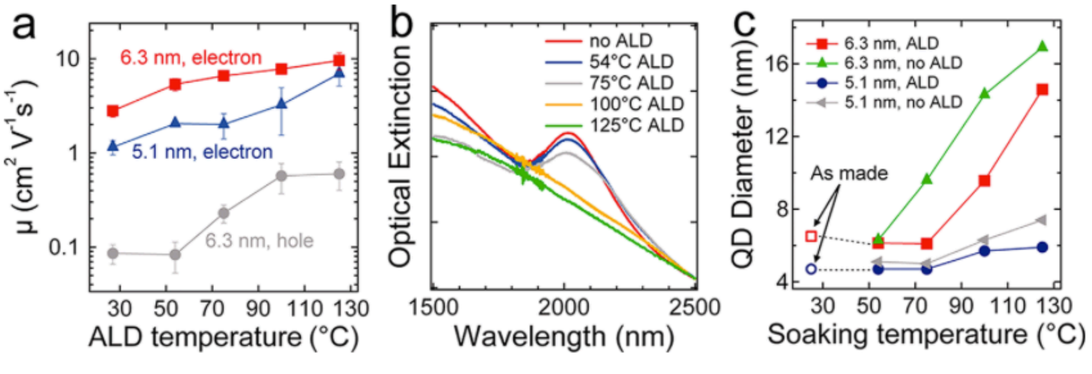

**Figure 4.7 Effect of ALD processing temperature on field-effect mobility**(a) Electron and hole field-effect mobility of alumina-infilled, sulfide-capped PbSe QDs FETs as a function of ALD deposition temperature (b) Optical extinction of PbSe QD films before

and after ALD infilling at 54, 75, 100, and 125°C (c) Average QD diameter versus ALD infilling temperature

In figure 4.7a, the electron and hole mobilities increase with ALD infilling temperature; an average of 6-10 devices were used. The average electron mobility using 6.3 nm PbSe QDs increases from 2.8 $cm^2 V^{-1} s^{-1}$ at 27°C to 9.6 $cm^2 V^{-1} s^{-1}$ at 125°C, while the average hole mobility increases from 0.086 to 0.6 $cm^2 V^{-1} s^{-1}$ over the same temperature range. A similar trend is found when using 5.1 nm QDs, but with smaller mobilities due to competing effects of 1) charging energy (larger energy required to add an electron to a small QD)[22] 2) size-dependent trap level (ratio of $N_{trap} / N_{free}$ is larger for smaller dots)[23] and 3) number of geometric hops required to reach a charge collecting electrode.[22]

Since PbX QDs are sensitive to temperatures, these QDs can neck, ripen and sinter[24,25] during ALD deposition, the size and size distribution was measured using optical extinction spectra and X-ray diffraction (XRD). The optical spectra show that the first exciton of 6.3 nm PbSe QD films is featureless when the QD films are processed in the ALD at temperature $\geq$100°C due to Ostwald ripening resulting in a increase in QD sizes and optical band gap (Fig 4.7b). Using the Scherrer size broadening equation to calculate the average QD size, the diameter of the PbSe QD remains the same for ALD infilling temperatures $\leq$75°C (red and blue data in Fig 4.7c) At temperatures of 100°C and 125°C, the average QD size increases from 6.3 nm to 9.6 nm and 14.6 nm respectively. This is indicative that the QDs are fusing together above 75°C. As such, the increase in electron and hole mobility above 75°C is due to the reduction of interdot energy barriers to charge transport. To avoid these sintering effects, the rest of the focus in this temperature will be for PbSe QD films process at ≤75°C.

In addition to higher field-effect mobilities for PbSe QDs treated with $Na_2S$, these devices are also stable indefinitely in air (Fig 4.8). The variability in values is due to a slight increase in contact resistance due repeated contact with tungsten needle required for device measurement resulting in the possible degradation of the gold contact. As previously demonstrated, the ALD overcoating process inhibits gas diffusion of $O_2$ which is detrimental to performance for PbX QD optoelectronics.[13,24]

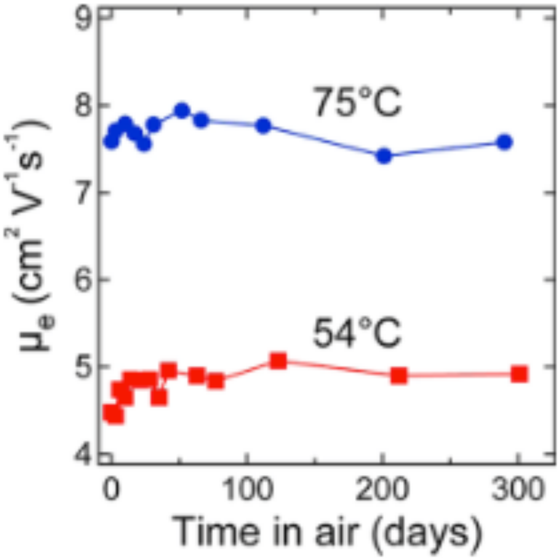

**Figure 4.8 Electron field-effect mobility of PbSe QDs treated with $Na_2S$ and infilled and overcoated at 54°C and 75°C.** Films were stored in the dark at room temperature in a cool drawer outside of the glovebox.

## 4.6 Design of experiments to explain the increase in field-effect mobility

In order to understand the role of the alumina in increasing the field-effect mobility in PbSe QDs treated with $Na_2S$, a few control experiments were conducted.

### 4.6.1 Gate insulator passivation

The first control experiment was to test the hypothesis that the alumina layer is modifying the $SiO_2$ gate oxide. It is well documented that surface-bound water that hydrogen bonds to the silanol groups on the $SiO_2$ dielectric is responsible for a variety of device-related failure mechanisms such as hysteresis[26], charge trapping[27], and the bias-stress effect[28], all of which can result in a decrease in the calculated field-effect mobility. To improve this interface, modifications to surface is often pursued through the use of self-assembled monolayers (SAM)[29], depositing a high-κ dielectric material such as $HfO_2$ or $Al_2O_3$[30], or depositing hydroxyl-free hydrophilic SiN[31] or CYTOP[32,33]. While the effects of these modifications warrant its own discussion, it will be saved for Chapter 5.

To test if the change in the gate oxide were responsible for the increase mobility, 2-3 nm alumina was deposit on the normal 200 nm $SiO_2$ gate oxide.

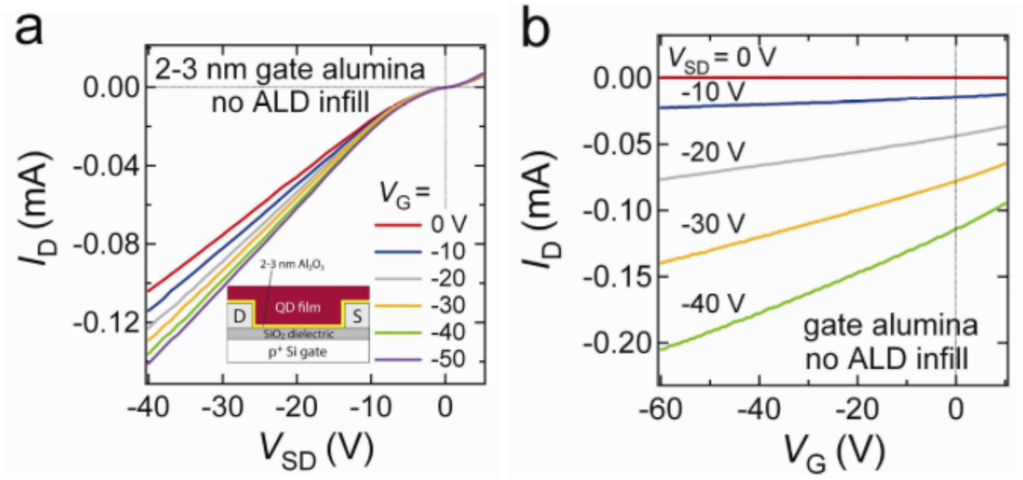

**Figure 4.9 Effect of $Al_2O_3$ on gate oxide surface** *I-V* characteristics (a) output and (b) transfer for 6.3 nm PbSe QD FET treated with $Na_2S$ with a 2-3 nm thick alumina layer deposited on the oxide and source-drain electrodes.

It is clear from figure 4.9 that modifying the gate dielectric before QD film deposition does not cause the improvement in the FET performance. It is noted that there is non-linear region near zero due to the increase contact resistance due to the deposited alumina on the source-drain electrodes

### 4.6.2 Extended heating

The next control experiment was to consider the impact of only film heating. As previously shown in figure 4.7, sintering the QDs can increase electronic coupling and increase mobility.

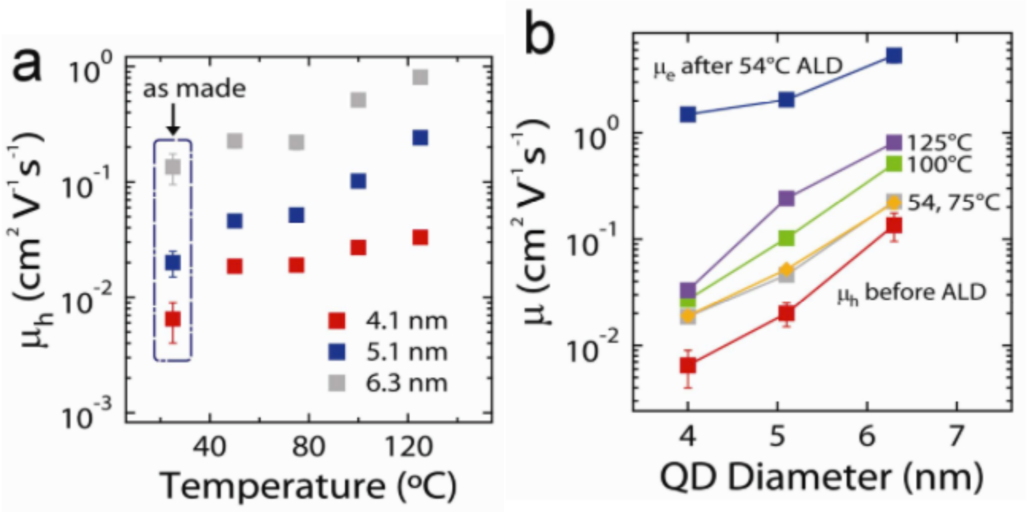

**Figure 4.10 Control experiments to examine the effect of film heating on field-effect mobility** (a) Hole field effect mobility as a function of soaking temperature. FET devices were held at the desired temperature for 9 hours to simulate the ALD growth conditions but no alumina infilling (b) Hole field-effect mobility versus QD diameter size

From figure 4.10, it is clear that despite the increase amount of QD necking and film densification, there are no changes to the FET characteristics (p-channel to dominant n-channel) nor was there a similar order of magnitude increase in field-effect mobility.

### 4.6.3 Current transients

As another control experiment, it was hypothesized that the changes to the FET characteristics after ALD infilling is caused due to the current transients.[22,34-36] (current vs. time, threshold voltage vs. time). For FETs without alumina ALD, changing the gate voltage increases the source-drain current, but it is followed by an anomalous stretched exponential decay of the current (also called bias-stress effect). Such behavior is attributed to the screening of the applied electric field possibly due to trapping. The transients are a thermally activated behavior. Current transients for typical FETs before and after infilling are shown in figure 4.11 and 4.12 respectively.

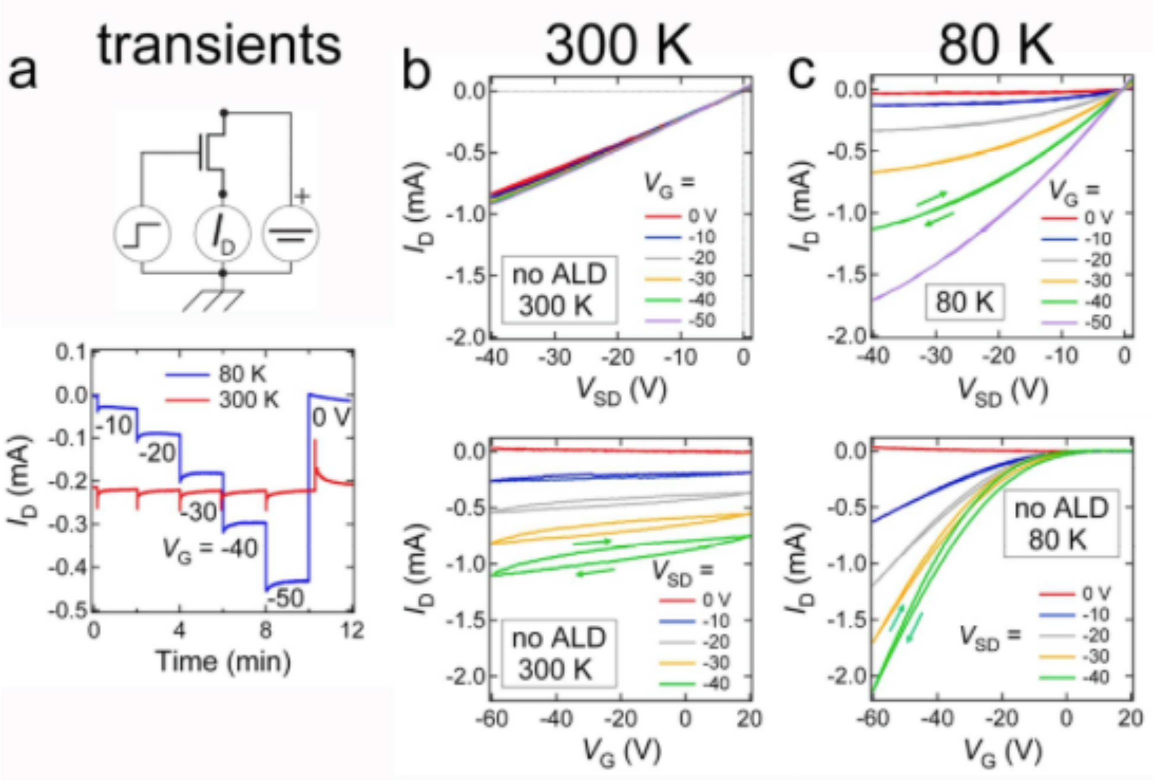

**Figure 4.11 *I-V* characteristics for a PbSe QD treated with $Na_2S$ before ALD** (a) Schematic of the measurements circuit and the source-drain current versus time for a device at 80 and 300 K. Bias conditions: $V_{SD}$ = - 5 V, $V_G$ is stepped from 0 V to -50 V in -10 V increments (b,c) Output and transfer characteristics for the FET at 300K and 80K respectively.

It is often reported that the transients is a thermally activated behavior due to a thermally activated barrier to trapping[35] or thermally activated ligand rearrangements or

QD motion.[36] This thermally activated behavior is confirmed in figure 4.11. Below 150K, the transients were suppressed for FETs without the ALD infilling and often completely eliminated for infilled FETs (Fig 4.12).

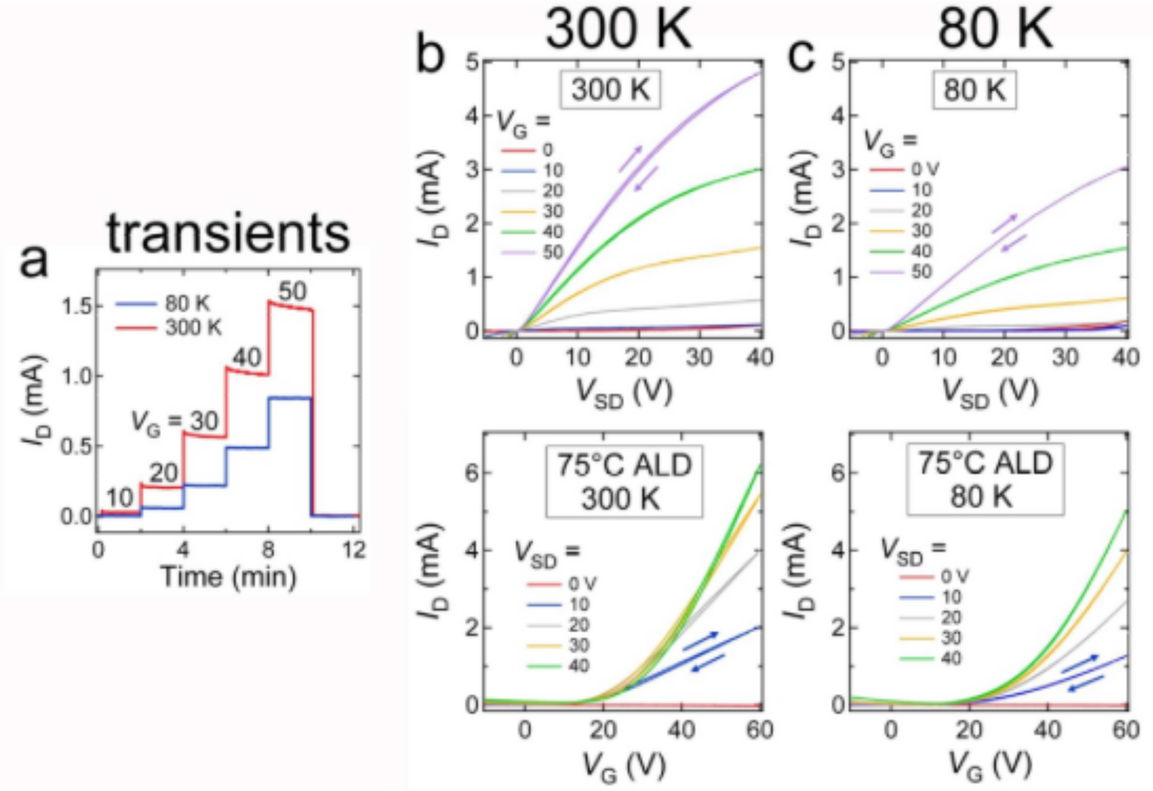

**Figure 4.12 *I-V* characteristics for a PbSe QD treated with $Na_2S$ after ALD** (a) Schematic of the measurements circuit and the source-drain current versus time for a device at 80 and 300 K. Bias conditions: $V_{SD}$ = + 5 V, $V_G$ is stepped from 0 V to +50 V in +10 V increments (b,c) Output and transfer characteristics for the FET at 300K and 80K respectively.

Moreover, the elimination of the current transients at low temperatures did not result in changes in the carrier mobility or carrier type: FETs without the alumina ALD remained p-channel with no sign of a n-channel conductivity, while the infilled FETs remained dominantly n-channel at all temperatures. Through these sets of experiments, the suppression of the current transients as a result of the ALD infilling is not the reason for the change in carrier type and the high electron mobility observed in these devices.

### 4.6.4 Sweep rate dependent mobility

As a final control experiment, the dependence on carrier mobility on the gate voltage sweep rate was tested. The hypothesis was that the high electron mobility is an artifact of fast sweeping. If we think about what is the mobility a measure of, it determines how fast charge carriers in a semiconductor drift due to an applied external electric field. While this definition of mobility seems to be independent of device parameters, its experimental determination is not straightforward and it often depends on how it is measured. In FETs, charge carriers are induced by the application of the gate voltage. By monitoring the changes in the channel conductivity as a function of gate voltage, the mobility can be extracted. The assumption in this statement is that electrical transport is *not* time dependent during the time in which the gate voltage is swept. This implies that the mobility is a steady-state value and can be well defined within the time span of the measurement. Unfortunately, this condition is not always satisfied, particularly for disordered semiconductors such as organic semiconductors.[37-39] These studies demonstrated that the mobility can decrease a few orders of magnitude within minutes which prevents the assignment of a single field-effect mobility.

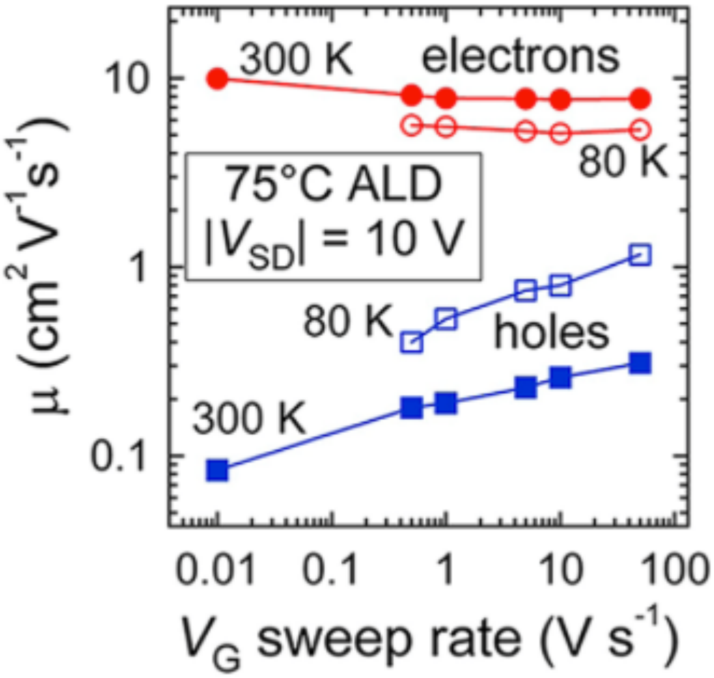

**Figure 4.13 Scan rate dependent field-effect mobility for a PbSe QD FET treated with $Na_2S$ and infilled with alumina at 75°C**. Closed symbols = 300 K. Open symbols = 80 K.

To rule out the scan rate dependence of the mobility as the explanation for the observed high electron mobility, field-effect mobility was measured for scan rates ranging from 0.01 to 50 $Vs^{-1}$ . For a typical device infilled at 75°C, the electron and mobility at 300 K and 80 K show no dependence in the sweep rates (Fig 4.13). For devices without the ALD infilling, the electron and hold mobility increases by a factor of 4 over the same range of sweep rates. From these experiments, we confidently establish that the change in the dominant carrier type and improvement in mobility is a consequence of the alumina infilling of the sulfide-capped QD films: it is a consequence of the film and not due to the modifications of the gate dielectric, film heating, film annealing, or artifacts from device measuring (time-dependent current/mobility)

### 4.6.5 Surface acceptor trap passivation

#### 4.6.5.1 Contact resistance and four-point gated FETs

To explain how the change in FET characteristics and increase in field-effect mobility is due to the alumina infilling Figure 4.14 demonstrates the evolution of the FET characteristics as a function of number of ALD cycles. In fig 4.14a, there is a systematic change from a dominant p-channel transport to n-channel dominated ambipolar transport from 0 to 40 cycles of alumina. The transfer characteristics no longer change after 40 cycles implying an effective alumina thickness.

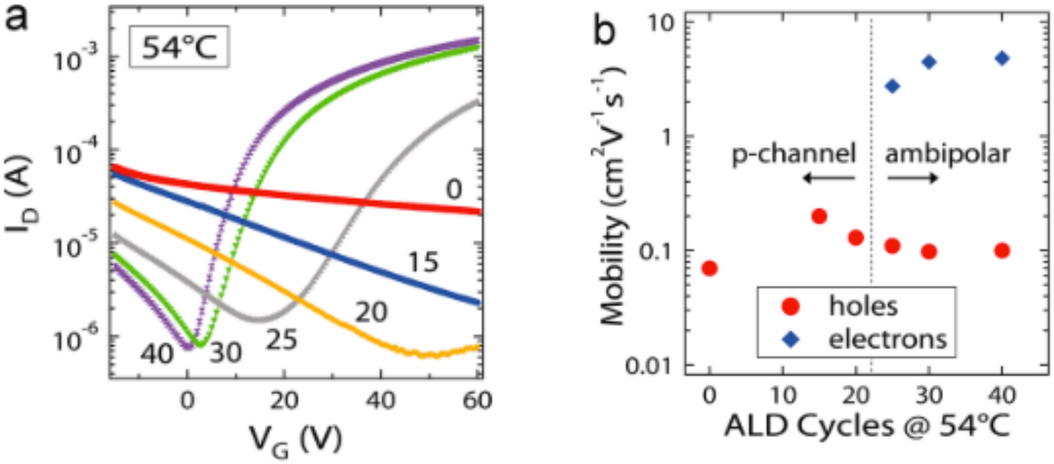

**Figure 4.14 Evolution of FET behavior with the number of ALD cycles** (a) Transfer characteristics for six devices measured at $V_{SD}$ = +10V at room temperature (b) Linear field-effect mobility for these six devices

In addition, the hole current decreases as the electron current increases, and the threshold voltage shifts from a large positive value to about 0 V. We believe the changes in the FET behavior are due to the passivation of acceptor states and electron traps on the QD surfaces. We assume that the sulfide ions act as acceptor dopants and cause the moderately high hole concentration in these devices. Unpassivated chalcogenide ions on the surface of nonstoichiometric CdX and PbX are believed to be the acceptors.[40-43] In light of more recent work, the non-stoichiometry also controls the dominant carrier type and hence the Fermi level position.[21,44] This high hole concentration is the reason for the high p-channel conductance with a weak gate modulation; large doping prevents these devices from turning off. It is only until the hole concentration is reduced by reducing the temperature can the non-infilled FETs be modulated by the gate (Fig 4.11).

To recap, the alumina deposition decreases the hole concentration due to the high carrier concentration of surface acceptors, causing the FETs to evolve from unipolar p-channel transport before ALD to ambipolar transport after 20-25 cycles of alumina. For ALD cycles >30, the transport is predominately n-channel. This decrease in the hole concentration as a function of ALD cycles is the reason for the shift in the threshold voltage from a large positive value to a threshold voltage of about 0V, as well as the change in the dominant carrier type.

Secondly, the increase in the electron mobility after the alumina infilling is due to passivating electron surface traps within the band gap. Trap passivation can explain the observed increase in mobility with both increasing number of ALD cycles (having a more complete alumina coating resulting in better passivation) and increasing ALD temperature (higher temperature increases precursor activity and more complete surface reactions). Comparing the mobility dependence on gate bias for devices before and after ALD infilling can test the idea of trap filling.

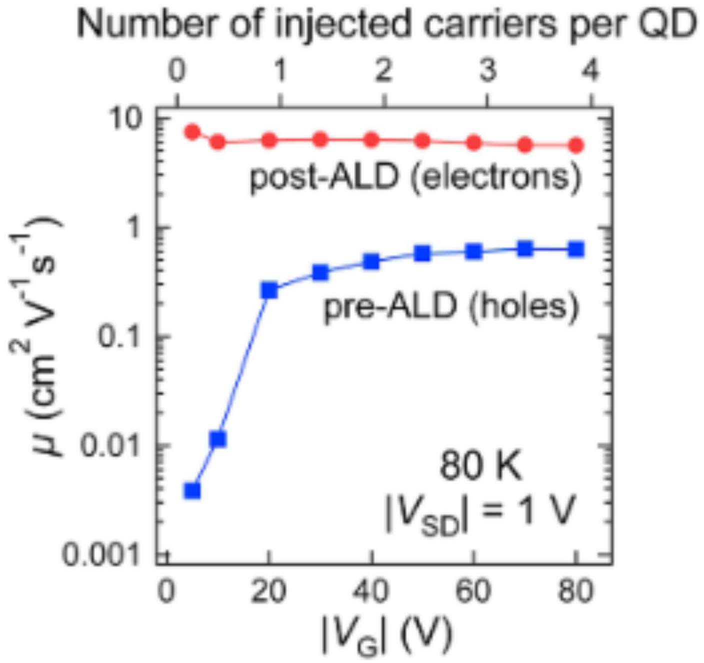

**Figure 4.15 Field-effect mobility as a function of carrier density for sulfide-capped PbSe QD FETs before and after ALD infilling at 75°C**. The devices were measured at 80 K in a gated 4-point FET geometry to eliminate effects due to contact resistances

Evidence for trap passivation can be seen in figure 4.15. In order to accurately measure field effect mobility, a 4-point FET geometry with a thinner (~1 nm) Ti adhesion layer was used to eliminate contact resistance effects and the non-linear *I-V* characteristics in our normal devices at small source-drain voltages, which we believe is caused by an injection barrier between the QDs and titanium. As previously stated in section 2.4, contact effects must be considered especially in the mobility extraction. One can imagine that a device with a large contact resistance will tend to limit the available current out of the device. With that said, we first sought out to prove that the origin of the *quasi*-linear *IVs* was due to potential barrier that exists with the intimate contact of the low work-function metal (Ti) with the nanocrystals near the metal/semiconductor interface.[45] In order to demonstrate this, we compared the *IV* characteristics of devices made with sulfide-capped films that have been alumina infilled with two different processing: 1) 40 nm of Au on top of a self-assembled monolayer (3-mercaptopropyl trimethoxysilane (3-MPTMS) to promote gold adhesion to the oxide surface and 2) 5 nm of Ti metal adhesion layer followed by 35 nm of Au

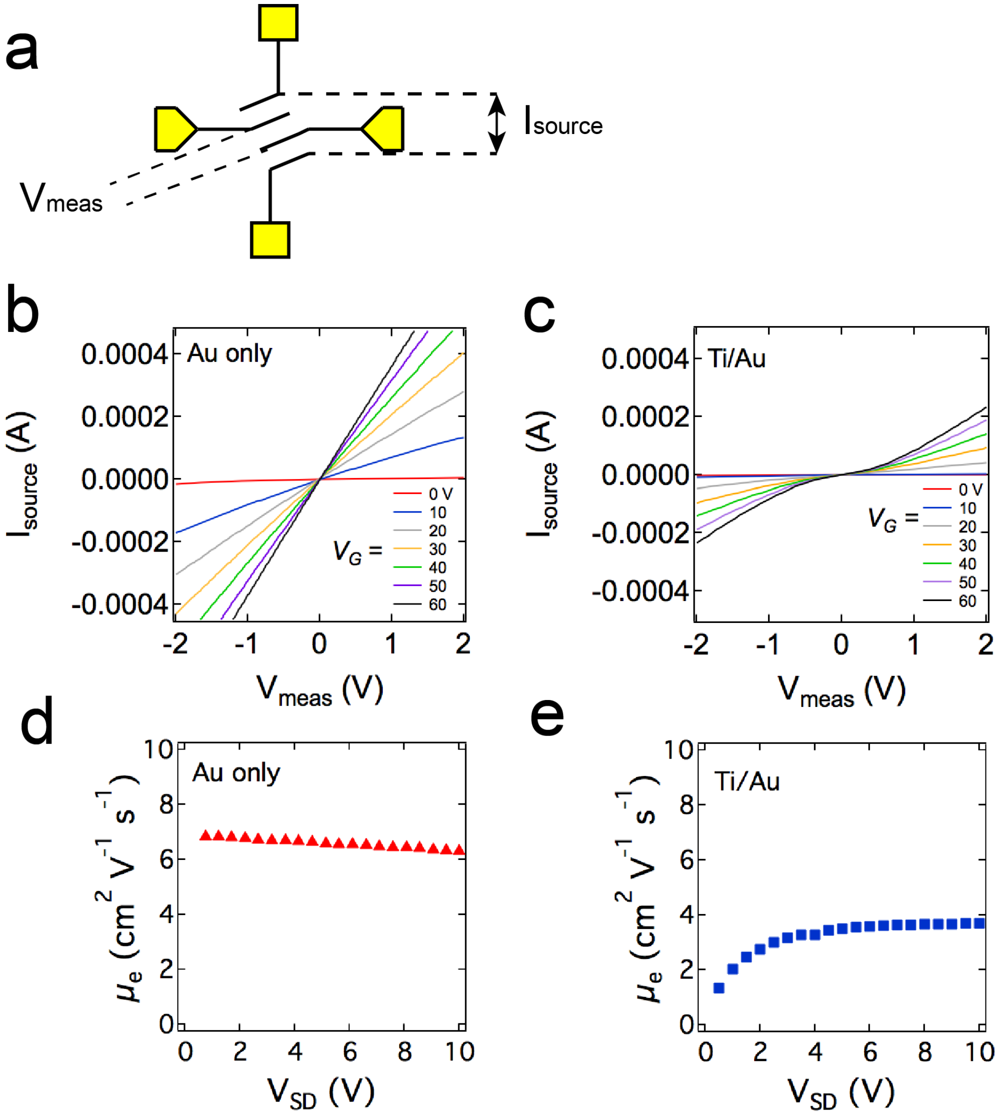

**Figure 4.16 Gated four-terminal field-effect transistor** (a) Device architecture for the gated four-probe field-effect transistor measurement configuration. Channel dimensions W = 1000 μm, L = 25 μm. (b) Bottom-contact geometry with gold electrodes using 3-mercaptopropyl trimethoxysilane (3-MPTMS) adhesion for gold deposition (c) Bottom-contact geometry with a 5 nm Ti adhesion layer followed by 35 nm of gold. During the gate four-probe probe measurements, the gate voltage is held constant while the current is swept while sensing the potential difference between the two inner electrodes

Plotted on the same scales, it is clear that the large contact resistance is due to the low work function metal which is the primary reason for the *quasi*-linear *IV*s in most of the data collected in this chapter. This has important implications especially when developing, interpreting, and extracting performance metrics from transistors that do not have ideal *IV* characteristics. This is nicely demonstrated in Fig 4.16d and 4.16e where there is an electric field dependence on the field-effect mobility. In section 2.2.2 and 2.3, the derivation and expression for the field-effect mobility illustrates that the mobility is inversely proportional to the electric field because a larger electric field would increase the transit time of carriers to the current collecting electrodes, thus decreasing mobility. Instead, the opposite is observed for devices with high contact resistance. If we examine 4.16c, with increasing magnitude or electric field with the applied source-drain bias, the potential barrier is lowered, causing the increase in current (V > 2 V). Concomitantly, the mobility also increases from 0 to 2 V after which the mobility is no longer dependent on the source-drain bias with increasing biases. Based on this experiment and process, we can now confidently rule out contact resistance effects in interpreting and quantifying the field effect mobility.

To further prove our quantified mobility, we also studied the gate-dependent mobility using the new processing established above. The data in figure 4.15 were acquired at 80 K in order to eliminate current transient affects and to simplify the comparisons between devices before and after ALD because of the weak modulation for pre-ALD sulfide-capped films. As illustrated in figure 4.15, for films without alumina

ALD, the mobility increases approximately an order of magnitude from 0 V to -40 V. This gate dependent mobility in disordered semiconductors is common in amorphous Si[46], organic semiconductors[39,47], and nanocrystalline $TiO_2$[48] where an increase in carrier density results in trap filling, leading to an apparent increase in performance.[16,49]

The average hole density induced in the accumulation layer by the applied gate bias can be estimated using $p = C_{ox}(V_G - \frac{V_{SD}}{2} - V_T)/e$ which corresponds to about 1.9 holes per QD at a gate bias of about -40 V. At this large gate bias, the Fermi level is close to the $1S_h$ (HOMO) level such that most of the traps are filled (including mid-gap and band tail states). Above this gate bias, the induced carriers transport through the $1S_h$ quantized states. In contrast, films with ALD infilling, which show high electron mobilities, the mobility does not increase with the gate voltage because the trap density is low due to the ALD processing. With fewer traps (more free charge carriers), the induced carriers can readily access the $1S_e$ (LUMO) quantized states of the QDs even at low applied fields. These statements will be later qualified in Chapter 6 to determine if charges truly access quantized states and whether or not we truly have trap filling. From this experiment, we find that our ALD infilling greatly reduces the concentration of localized gap states in the sulfide-capped PbSe QD FETs resulting in a change in the FET characteristics and an increase in electron mobility.

### 4.7 Discussion and outlook

Alternative explanations for the increase in mobility is that it lowers the tunneling barrier height, reducing of the QD charging energy, or an increase in effective dielectric constant of the films. Each of these cannot account for the main observations including the change in dominant carrier type. Although, an increase in electron mobility due to an increase in dielectric constant is because scattering from Coulombic impurities/dopants can be strongly dampened. Through this screening weakening effect, the damping of Coulombic scattering is much larger which can result in improved carrier mobilities. We can also rule out the tunneling barrier because alumina is a wide bang gap ($E_G > 7$eV). We can also rule out the changes in charging energy because PbSe QD films without ALD already have charging energy of less then 10-15 meV[25], making the impact of reducing the effective dielectric constant when the interstitial voids are infilled with alumina relatively unimportant.

In light of this trap filling effect in QD FETs, we now consider whether these QD FET mobilities are relevant to QD solar cells. There are several distinctions between field-effect mobility and field-free mobility of carriers in a QD film when used in a solar cell (difference between trap free and trap filled). First, consider the geometry of transistors. Based on classical semiconductor theory, the accumulation of charge at the interface between the semiconductor and dielectric will depend on the application of a gate voltage.[50] As such, charge transport from source to drain electrodes occurs solely in this thin sheet of carriers buried within the transistor structure. Indeed, transport in FETs is essentially two-dimensional with more than 90% of the induced charge is concentrated to within the first 10 nm or so under most bias conditions. By plotting the carrier density as a function of distance away from the oxide, we can determine how far the electric field penetrates the semiconductor, and more importantly the assumption in treating the induced charge as a two-dimensional sheet. Using reasonable values for the dielectric constant, surface potential, and bulk donor density, we can solve for the spatial charge density.

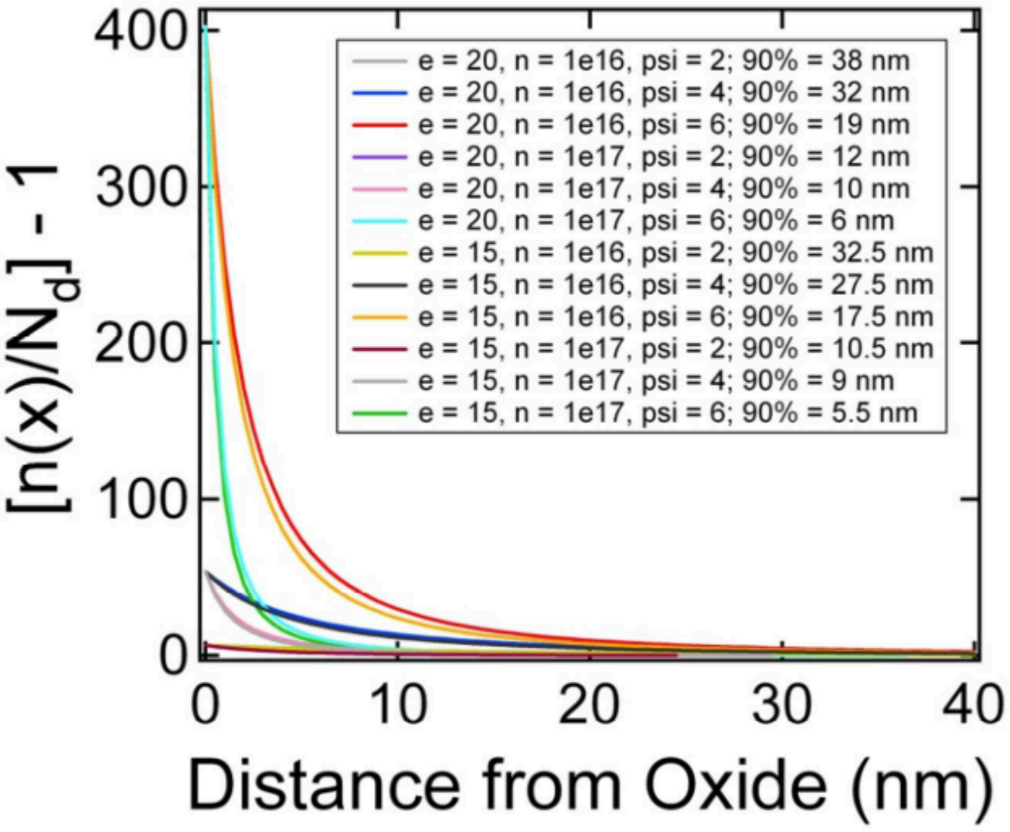

**Figure 4.17** Normalized excess electron density in the accumulation layer for a PbSe QD FET at room temperature. The thickness of the accumulation layer that contains 90% of the induced charge

While it appears that the charge distribution in FETs is two-dimensional, experiments designed to prove this will be demonstrated in Chapter 6. One can imagine this theory does not hold for a number of reasons: 1) different dielectric properties 2) difference in mobilities indicating a barrier to carrier transport along the dielectric interface 3) random dipoles in the dielectrics with higher dielectric constant or polar surfaces. These bottlenecks along the dielectric surface can force charge carriers further away from the dielectric interface resulting in less of a two-dimensional carrier distribution and more three-dimensional.

Secondly, in our FETs, information is based on the majority carrier, but in solar cells, the most important parameter is the minority carrier mobility in the p(n) active layer. Thirdly, as we have seen in figure 4.15, FET mobility values are usually measured under high-injected carrier density and under trap-filled conditions, resulting in larger mobilities than mobility in QD films under equilibrium conditions (no external bias or illumination). One can also imagine that even under the applied electric field, the Fermi level in the QD FET is changing because of different gap state occupancy and changes in the surface potential, resulting in a different charge transport mechanism in FETs compared to solar cells. As such, we advocate caution in translating field-effect mobility to solar cells. Although, if QD FETs are shown to have fewer gap states and weak dependence on the gate voltage, like the QD FETs demonstrated in this chapter, the field-effect mobility should in principle be comparable to a field-free mobility which can be used to describe solar cells based on similarly prepared QD films. On the other hand, if QD FETs have a large concentration of gap states and a strong dependence of mobility on gate bias, we question is solar illumination mimic this behavior. It has been shown in nanocrystalline $TiO_2$ films, the carrier mobility increases by an order of magnitude under ~1 sun illumination as a result of trap filling.[48,51] A similar effect should occur in illuminated PbX QD films and it has actually been demonstrated that depending on the excitation density and energy, one can populate and depopulate shallow and trap states.[52] Although, QD FET mobilities can **never** be applied in a quantitative way to illuminated QD solar cells due to the fact that in transistors, the mobility measured is the *majority* carrier type. The transistor action typically involves the majority carriers of the source and drain regions, but these carriers that move across the channel do have carrier of the opposite type (minority carriers). However, the carriers in the transverse direction drastically outnumbers the opposite type since they are removed by the electric field that creates the inversion region, so FETs are indeed "majority carrier" devices. In solar cells, the *minority* carrier mobility is more important for a solar absorbing material rather than the majority carrier mobility. In a typical *p-n* junction, majority carriers will diffuse across the depletion region. These carriers reaching the junction will become minority carriers, which are then swept across the depletion region due to drift. The total number of minority carriers, under applied bias and illumination will determine the efficiency of the device and hence why minority carrier diffusion length (and minority carrier lifetime) is important in solar cells; hence FET mobilities cannot be directly translated to carrier mobilities in solar cells.

# REFERENCES

(1) Talapin, D. V.; Lee, J. S.; Kovalenko, M. V. Prospects of Colloidal Nanocrystals for Electronic and Optoelectronic Applications. *Chem. Rev.* **2009**.

(2) Remacle, F.; Levine, R. D. Quantum Dots as Chemical Building Blocks: Elementary Theoretical Considerations. *ChemPhysChem* **2001**, *2*, 20–36.

(3) Moreels, I.; Lambert, K.; Smeets, D.; De Muynck, D.; Nollet, T.; Martins, J. C.; Vanhaecke, F.; Vantomme, A.; Delerue, C.; Allan, G.; *et al.* Size-Dependent Optical Properties of Colloidal PbS Quantum Dots. *ACS Nano* **2009**, *3*, 3023–3030.

(4) Hanrath, T.; Veldman, D.; Choi, J. J.; Christova, C. G.; Wienk, M. M.; Janssen, R. A. J. PbSe Nanocrystal Network Formation During Pyridine Ligand Displacement. *ACS Applied Materials and Interfaces* **2009**, *1*, 244–250.

(5) Murray, C. B.; Norris, D. J.; Bawendi, M. G. Synthesis and Characterization of Nearly Monodisperse CdE (E = Sulfur, Selenium, Tellurium) Semiconductor Nanocrystallites - Journal of the American Chemical Society (ACS Publications). *J. Am. Chem. Soc.* **1993**.

(6) Lokteva, I.; Radychev, N.; Witt, F.; Borchert, H.; Parisi, J.; Kolny-Olesiak, J. Surface Treatment of CdSe Nanoparticles for Application in Hybrid Solar Cells: the Effect of Multiple Ligand Exchange with Pyridine. *J. Phys. Chem. C* **2010**.

(7) Tang, J.; Kemp, K. W.; Hoogland, S.; Jeong, K. S.; Liu, H.; Levina, L.; Furukawa, M.; Wang, X.; Debnath, R.; Cha, D.; *et al.* Colloidal-Quantum-Dot Photovoltaics

Using Atomic-Ligand Passivation. *Nature Materials* **2011**, *10*, 765–771.

(8) Kim, S.; Noh, J.; Choi, H.; Ha, H.; Song, J. H.; Shim, H. C.; Jang, J.; Beard, M. C.; Jeong, S. One-Step Deposition of Photovoltaic Layers Using Iodide Terminated PbS Quantum Dots. *J. Phys. Chem. Lett.* **2014**, *5*, 4002–4007.

(9) Zhang, H.; Hu, B.; Sun, L.; Hovden, R.; Wise, F. W. Surfactant Ligand Removal and Rational Fabrication of Inorganically Connected Quantum Dots - Nano Letters (ACS Publications). *Nano Lett.* **2011**.

(10) Nag, A.; Kovalenko, M. V.; Lee, J.-S.; Liu, W.; Spokoyny, B.; Talapin, D. V. Metal-Free Inorganic Ligands for Colloidal Nanocrystals: S2–, HS–, Se2–, HSe–, Te2–, HTe–, TeS32–, OH–, and NH2– as Surface Ligands. *J. Am. Chem. Soc.* **2011**.

(11) Fafarman, A. T.; Koh, W.-K.; Diroll, B. T.; Kim, D. K.; Ko, D.-K.; Oh, S. J.; Ye, X.; Doan-Nguyen, V.; Crump, M. R.; Reifsnyder, D. C.; *et al.* Thiocyanate-Capped Nanocrystal Colloids: Vibrational Reporter of Surface Chemistry and Solution-Based Route to Enhanced Coupling in Nanocrystal Solids. *J. Am. Chem. Soc.* **2011**.

(12) Lee, J.-S.; Kovalenko, M. V.; Huang, J.; Chung, D. S.; Talapin, D. V. Band-Like Transport, High Electron Mobility and High Photoconductivity in All-Inorganic Nanocrystal Arrays. *Nature Nanotechnology* **2011**, *6*, 348–352.

(13) Liu, Y.; Gibbs, M.; Perkins, C. L.; Tolentino, J.; Zarghami, M. H.; Jorge Bustamante, J.; Law, M. Robust, Functional Nanocrystal Solids by Infilling with Atomic Layer Deposition. *Nano …* **2011**.

(14) Kakinuma, H. Fermi-Level-Dependent Mobility-Lifetime Product in a-Si:H.

*Phys. Rev. B* **1989**, *39*, 10473–10476.

(15) Horowitz, G.; Hajlaoui, R.; Fichou, D.; Kassmi, El, A. Gate Voltage Dependent Mobility of Oligothiophene Field-Effect Transistors. *J. Appl. Phys.* **1999**, *85*, 3202–3206.

(16) Dimitrakopoulos, C. D.; Purushothaman, S.; Kymissis, J. Low-Voltage Organic Transistors on Plastic Comprising High-Dielectric Constant Gate Insulators. *Science* **1999**.

(17) Carlsson, J. O. Thermodynamics of the Homogeneous and Heterogeneous Decomposition of Trimethylaluminum, Monomethylaluminum, and Dimethylaluminumhydride: Effects of Scavengers and Ultraviolet-Laser Photolysis. *J. Vac. Sci. Technol. B* **1991**, *9*, 2759.

(18) Peng, H.; Song, J. H.; Kanatzidis, M. G.; Freeman, A. J. Electronic Structure and Transport Properties of Doped PbSe. *Phys. Rev. B* **2011**, *84*, 125207–112520.

(19) Leschkies, K. S.; Beatty, T. J.; Kang, M. S.; Norris, D. J.; Aydil, E. S. Solar Cells Based on Junctions Between Colloidal PbSe Nanocrystals and Thin ZnO Films. *ACS Nano* **2009**, *3*, 3638–3648.

(20) Yu, K.; Liu, X.; Zeng, Q.; Leek, D. M.; Ouyang, J.; Whitmore, K. M.; Ripmeester, J. A.; Tao, Y.; Yang, M. Effect of Tertiary and Secondary Phosphines on Low-Temperature Formation of Quantum Dots. *Angew. Chem.* **2013**, *125*, 4923–4928.

(21) Kim, D.; Kim, D. H.; Lee, J. H.; Grossman, J. C. Impact of Stoichiometry on the Electronic Structure of PbS Quantum Dots. *Physical Review Letters* **2013**, *110*, 196802.

(22) Liu, Y.; Gibbs, M.; Puthussery, J.; Gaik, S.; Ihly, R.; Hillhouse, H. W.; Law, M. Dependence of Carrier Mobility on Nanocrystal Size and Ligand Length in PbSe Nanocrystal Solids. *Nano Lett.* **2010**.

(23) Bozyigit, D.; Lin, W. M. M.; Yazdani, N.; Yarema, O.; Wood, V. A Quantitative Model for Charge Carrier Transport, Trapping and Recombination in Nanocrystal-Based Solar Cells. *Nature Communications* **2015**, *6*, 6180–.

(24) Ihly, R.; Tolentino, J.; Liu, Y.; Gibbs, M.; Law, M. The Photothermal Stability of PbS Quantum Dot Solids - ACS Nano (ACS Publications). *ACS Nano* **2011**.

(25) van Huis, M. A.; Kunneman, L. T.; Overgaag, K.; Xu, Q.; Pandraud, G.; Zandbergen, H. W.; Vanmaekelbergh, D. Low-Temperature Nanocrystal Unification Through Rotations and Relaxations Probed by in Situ Transmission Electron Microscopy. *Nano Lett.* **2008**, *8*, 3959–3963.

(26) Bauer, S.; Schwödiauer, R.; Neugebauer, H. Current Versus Gate Voltage Hysteresis in Organic Field Effect Transistors - Springer. *Monatshefte für Chemie- …* **2009**.

(27) Gu, G.; Kane, M. G. Moisture Induced Electron Traps and Hysteresis in Pentacene-Based Organic Thin-Film Transistors. *Appl. Phys. Lett.* **2008**, *92*, 053305.

(28) Bobbert, P. A.; Sharma, A.; Mathijssen, S. Operational Stability of Organic Field-Effect Transistors - Bobbert - 2012 - Advanced Materials - Wiley Online Library. *Adv. Mater.* **2012**.

(29) McDowell, M.; Hill, I. G.; McDermott, J. E.; Bernasek, S. L.; Schwartz, J.

Improved Organic Thin-Film Transistor Performance Using Novel Self-Assembled Monolayers. *Appl. Phys. Lett.* **2006**, *88*, 073505.

(30) Kim, D. K.; Lai, Y.; Vemulkar, T. R.; Kagan, C. R. Flexible, Low-Voltage, and Low-Hysteresis PbSe Nanowire Field-Effect Transistors. *ACS Nano* **2011**, *5*, 10074–10083.

(31) Li, F. M.; Nathan, A.; Wu, Y.; Ong, B. S. Organic Thin-Film Transistor Integration Using Silicon Nitride Gate Dielectric. *Appl. Phys. Lett.* **2007**, *90*, 133514.

(32) Kalb, W. L.; Mathis, T.; Haas, S.; Stassen, A. F.; Batlogg, B. Organic Small Molecule Field-Effect Transistors with Cytop™ Gate Dielectric: Eliminating Gate Bias Stress Effects. *Appl. Phys. Lett.* **2007**, *90*, 092104.

(33) Häusermann, R.; Batlogg, B. Gate Bias Stress in Pentacene Field-Effect-Transistors: Charge Trapping in the Dielectric or Semiconductor. *Appl. Phys. Lett.* **2011**, *99*, 083303.

(34) Luther, J. M.; Law, M.; Song, Q.; Perkins, C. L.; Beard, M. C. Structural, Optical, and Electrical Properties of Self-Assembled Films of PbSe Nanocrystals Treated with 1,2-Ethanedithiol - ACS Nano (ACS Publications). *Nano Lett.* **2008**.

(35) Kang, M. S.; Sahu, A.; Norris, D. J.; Frisbie, C. D. Size- and Temperature-Dependent Charge Transport in PbSe Nanocrystal Thin Films. *Nano Lett.* **2011**.

(36) Osedach, T. P.; Zhao, N.; Andrew, T. L.; Brown, P. R. Bias-Stress Effect in 1,2-Ethanedithiol-Treated PbS Quantum Dot Field-Effect Transistors - ACS Nano (ACS Publications). *ACS Nano* **2012**.

(37) Sirringhaus, H. Reliability of Organic Field-Effect Transistors. *Advanced Materials* **2009**.

(38) Zilker, S. J.; Detcheverry, C.; Cantatore, E.; de Leeuw, D. M. Bias Stress in Organic Thin-Film Transistors and Logic Gates. *Appl. Phys. Lett.* **2001**, *79*, 1124.

(39) Chen, Y.; Lee, B.; Yi, H. T.; Lee, S. S.; Payne, M. M.; Pola, S.; Kuo, C. H.; Loo, Y. L.; Anthony, J. E.; Tao, Y. T.; *et al.* Dynamic Character of Charge Transport Parameters in Disordered Organic Semiconductor Field-Effect Transistors. *Phys. Chem. Chem. Phys.* **2012**, *14*, 14142.

(40) Gómez-Campos, F. M.; Califano, M. Hole Surface Trapping in CdSe Nanocrystals: Dynamics, Rate Fluctuations, and Implications for Blinking. *Nano Lett.* **2012**.

(41) Franceschetti, A. Structural and Electronic Properties of PbSe Nanocrystals From First Principles. *Phys. Rev. B* **2008**, *78*, 075418–075424.

(42) Bryant, G. W.; Jaskolski, W. Surface Effects on Capped and Uncapped Nanocrystals. *J. Phys. Chem. B* **2005**, *109*, 19650–19656.

(43) Gai, Y.; Peng, H.; Li, J. Electronic Properties of Nonstoichiometric PbSe Quantum Dots From First Principles - the Journal of Physical Chemistry C (ACS Publications). *J. Phys. Chem. C* **2009**.

(44) Oh, S. J.; Berry, N. E.; Choi, J.-H.; Gaulding, E. A.; Paik, T.; Hong, S.-H.; Murray, C. B.; Kagan, C. R. Stoichiometric Control of Lead Chalcogenide Nanocrystal Solids to Enhance Their Electronic and Optoelectronic Device Performance. *ACS Nano* **2013**.

(45) Pesavento, P. V.; Chesterfield, R. J.; Newman, C. R.; Frisbie, C. D. Gated Four-Probe Measurements on Pentacene Thin-Film Transistors: Contact Resistance as a Function of Gate Voltage and Temperature. *J. Appl. Phys.* **2004**, *96*, 7312.

(46) Shur, M.; Hack, M.; Shaw, J. G. A New Analytic Model for Amorphous Silicon Thin-Film Transistors. *J. Appl. Phys.* **1989**, *66*, 3371.

(47) Pesavento, P. V.; Puntambekar, K. P.; Frisbie, C. D.; McKeen, J. C.; Ruden, P. P. Film and Contact Resistance in Pentacene Thin-Film Transistors: Dependence on Film Thickness, Electrode Geometry, and Correlation with Hole Mobility. *J. Appl. Phys.* **2006**, *99*, 094504.

(48) Fisher, A. C.; Peter, L. M.; Ponomarev, E. A.; Walker, AB; Wijayantha, K. Intensity Dependence of the Back Reaction and Transport of Electrons in Dye-Sensitized Nanacrystalline TiO2 Solar Cells. *Journal of Physical Chemistry B* **2000**, *104*, 949–958.

(49) Horowitz, G. Organic Field-Effect Transistors. *Adv. Mater.* **1998**, *10*, 1–13.

(50) Colinge, J. P.; Colinge, C. A. Physics of Semiconductor Devices; Springer Science & Business Media, 2007.

(51) Kopidakis, N.; Schiff, E. A.; Park, N. G.; van de Lagemaat, J.; Frank, A. J. Ambipolar Diffusion of Photocarriers in Electrolyte-Filled, Nanoporous TiO2. *Journal of Physical Chemistry B* **2000**, *104*, 3930–3936.

(52) Bakulin, A. A.; Neutzner, S.; Bakker, H. J.; Ottaviani, L.; Barakel, D.; Chen, Z. Charge Trapping Dynamics in PbS Colloidal Quantum Dot Photovoltaic Devices. *ACS Nano* **2013**, *7*, 8771–8779.

# CHAPTER 5

# ELIMINATING BIAS-STRESS EFFECT IN QUANTUM DOT THIN-FILM TRANSISTORS

## 5.1 Context

Much of the research QD FETs has traditionally focused on the semiconducting layer by controlling the majority carrier type[1-3] and increasing field-effect mobility[2-7] through remote doping[5], stoichiometric control[1,2], and using compact inorganic ligands.[3,6,7]For a more in-depth review of the state-of-the-art QD FET please refer to the review by Hetsch et. al.[8] Despite these remarkable improvements in the field-effect mobility, the operational stability (current transients) has yet to be scrutinized in order to improve the instability. There have been reports that have observed these current transients in PbX QD FETs, which presents itself as a pronounced hysteresis in the I-V characteristics, a shift in the threshold voltage, and an anomalous stretched exponential decay in current.[4,9-12] In one report attempting to understand the current transients (also referred to as the bias-stress effect) have concluded that a charge induced ionization of the organic ligands when the gate voltage is applied, resulting in a screening of the applied electric field.[12] Another more common explanation is charge trapping at the semiconductor-insulator interface. These traps have been assigned to ligand-mediated traps in which the ligand changes phase resulting in a liquid Pb metallic surface, which is proposed to have an excess of surface states.[13] These traps have also been classified as dynamic where it is a charging-activated trap formation in which Pb-Pb dimers are formed upon charging.[14,15]

In this chapter, we will review the bias-stress effect in QD FETs because it has been annoyance and a curiosity because of its anomalous behavior. These current transients can potentially complicate measurements of transport physics particularly mechanisms of transport and most importantly prevent a reliable calculation of extracted field-effect mobility. This behavior can also inhibit potential use of these QD films in practical applications such as drive transistors for LED technology.

### 5.2 Introduction to the bias-stress effect

In the context of bias-stress effect, some fraction of the carriers induced by the applied gate bias becomes trapped in states near or at the interface with the gate dielectric. As a result, there is a build-up of a sheet of trapped charge that screens the applied field. These trap states can be found in the gate dielectric, in the semiconductor channel, or at the semiconductor/dielectric interface and may be pre-existent or formed by the channel carriers as a result of the bias stress (e.g. via ionization of charged defects at the interface or in the semiconducting channel).[16] Progressive screening of the gate electric field results in a decay in the source-drain current and increases the magnitude of the gate voltage needed to induce a conducting channel (threshold voltage). These current transients and shifts in the threshold voltage under applied gate bias are signatures of the bias stress effect (Fig 5.1).

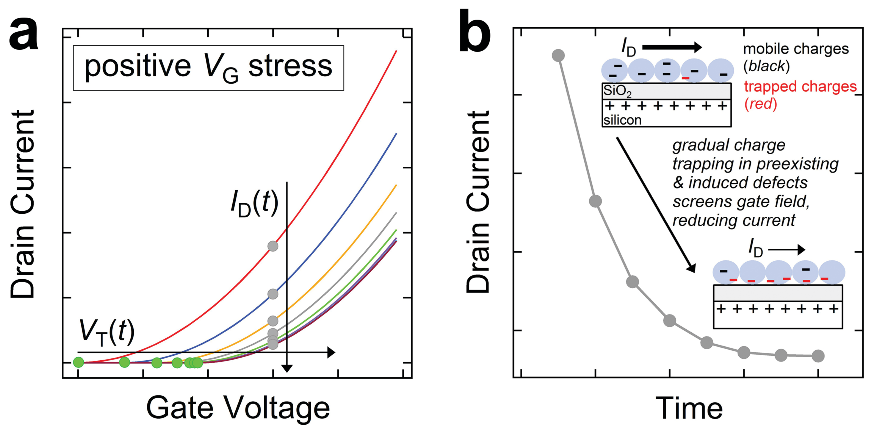

**Figure 5.1 The gate bias-stress effect in QD FETs** (a) Time evolution of the transfer characteristics for a n-channel FET subjected to a constant positive gate bias stress. Electron trapping near the dielectric/QD interface results in a shift in the threshold voltage for longer stressing times (b) The source-drain current shows a stretched exponential decay due to the screening of the electric field by trapped charges.

### 5.3 Design for eliminating gate-bias stress effect in QD FETs

Figure 5.2 below shows the process used to fabricate PbSe QD FETs that are free of the bias-stress effect. In the first step, we deposit conductive PbSe QDs onto prepatterned FET substrates using a layer-by-layer dip coating technique[9,10]in which the native oleate ligands are replaced with a smaller ligand that has a high vapor pressure in its neutral form (not bound to the QDs) such as 1,2-ethanedithiolate (EDT), formate, or thiocyanate. In the second step, the QD film is exposed to a single pulse of $H_2S$ gas in an ALD chamber to protonate the small ligand, which quantitatively desorbs and escapes into the gas phase as a neutral molecule, leaving behind a QD film capped with approximately a monolayer of $HS^-$ species. In the final step, the film is then infilled and overcoated with amorphous alumina[17,18] in the same chamber which results in an all-inorganic, ligand-free QD nanocomposite FET which is not affected by the bias-stress effect at room temperature.

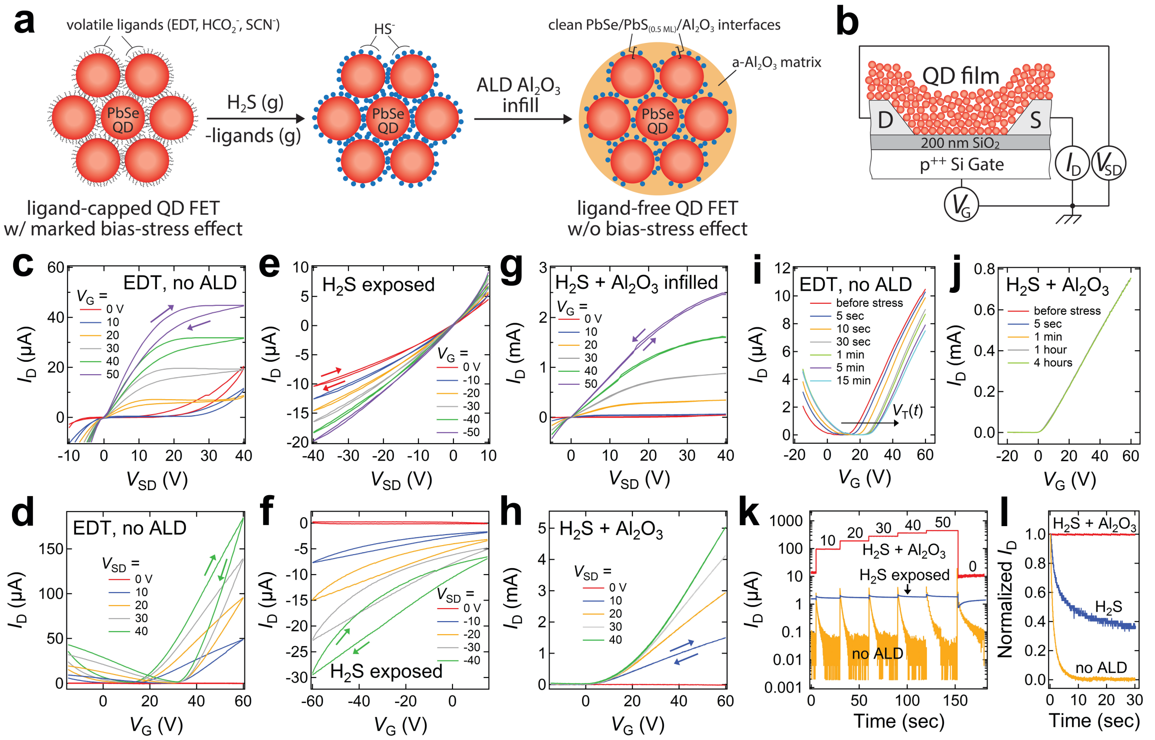

**Figure 5.2 Designing QD FETs with zero bias-stress effect** (a) the fabrication process. A single pulse of $H_2S$ gas (~3 X $10^6$ L) is used to protonate and remove volatile ligands from the surface of the QDs (b) Cartoon of the device schematic (c) Output *I-V* characteristics of an EDT-capped PbSe QD FET. The output curves after (e) one pulse of $H_2S$ gas followed by (g) infilling and overcoating with alumina ALD. (d) Transfer characteristics of an EDT-capped PbSe QD FET. The transfer curve after (f) one pulse of $H_2S$ gas followed by (h) infilling and overcoating with alumina ALD. Typical stressing experiments of (i) EDT-capped PbSe QD FET followed by (j) infilling and overcoating with alumina. (k) Log-linear plot of $I_D$ versus time for EDT-capped PbSe QD, after $H_2S$ exposure, followed by alumina ALD. (l) Comparison of the $I_D$ transient during the fabrication process.

The key step to eliminating the bias-stress effect in these QD FETs is to remove the organic ligands and to produce atomically-clean and abrupt PbSe/PbS/$Al_2O_3$ interface using the ALD chamber. The $H_2S$ exposed and alumina-infilled QD FETs show nearly identical performance characteristics – including high electron mobility, perfect long-term air stability, and zero drain current transients – regardless of the volatile ligand used in the fabrication.

Before the ALD treatments, QD films fabricated with ethanedithiol result in ambipolar transistors with low field-effect mobilities, large hysteresis, and suffer from the bias-stress effect (Fig 5c and 5d). Exposing the same FET to a pulse of $H_2S$ at temperatures < 75°C causes a dramatic change in their output characteristics. The FETs become p-channel transistors with a higher conductivity and faster, more severe transients that causes quasi-linear output plots (Fig 5c). These $H_2S$ exposed FETs behave in a similar fashion to sulfide-capped QD FETs recently prepared in our laboratory using a solid-state ligand exchange with $Na_2S$.[17] The similarity in FET behavior is likely due to the abundance of electronically-active sulfides adsorbed on the surface of the QDs in both types of films. To our surprise, upon infilling the $H_2S$-exposed devices with amorphous alumina using low-temperature ALD, the FETs become *n*-channel transistors with high electron mobilities, negligible hysteresis, and negligible bias-stress transients. We characterized the bias-stress effect in two fashions. The first is monitoring the shifts in the threshold voltage as a function of stressing times. Fig 5i illustrates that the threshold voltage shifts as much as 20 V within 15 minutes. This positive shift in the voltage onset of a conducting channel indicates that somehow there is an immobile charge at the semiconductor interface which results in the screening in the electric field. Secondly, we characterized the drain current transients of the EDT-capped, $H_2S$-exposed, and infilled devices by measuring the $I_D$ at a constant source-drain voltage ($V_{SD}$) while stepping the gate voltage ($V_G$) from 0 V to $\pm$50 V in 10 V increments. Figure 5e shows a log-linear plot of $|I_D|$ versus time comparing the different steps in our processing measured at room temperature. It is clear that EDT-capped device and the $H_2S$ exposed device exhibit quasi-exponential current transients after a step change in $V_G$, whereas the infilled device shows no such transients. The absence of the bias-stress effect in these devices is more obvious when the data are plotted on a linear scale, revealing a staircase-like shape that is expected for a well-behaved FET that responds to changes in $V_G$ with sudden and stable changes in the source-drain current (Fig 5k). This ALD chemistry involving $H_2S$ and alumina produces the first example of a PbX QD FET that is free of bias-stress effect at room temperature.

### 5.4 Attempts to modify the gate oxide surface

Initial attempts to determine the effects of the $H_2S/Al_2O_3$ combination were to monitor modifications to the gate oxide surface. Currently, the organic semiconductor community have established that modifying the native oxide with a self-assembled monolayer or a buffer layer that has no hydroxyls improves the current transients due to the omnipresent protons on the surface of many oxide based gate dielectrics.[19-23]. To test this hypothesis, before QD film deposition on the prepatterned FET substrate, the substrate was dosed with ~$3 \times 10^6$ L of $H_2S$ followed by ~ 4nm of $Al_2O_3$ ALD deposition.

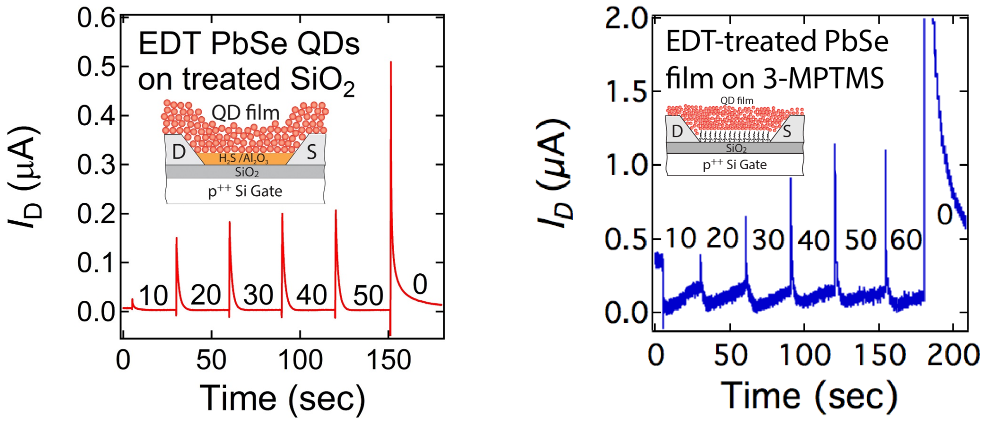

**Figure 5.3 Control experiments to isolate gate oxide surface modification** (a) with $H_2S$ dose and $Al_2O_3$ deposition and (b) a self-assembled monolayer (3-mercaptopropyl trimethoxy silane). 6.2 nm PbSe QDs EDT-treated film was deposited after surface modification. Current transients were measured at room temperature immediately after oxide treatment

As illustrated in fig 5.3, contrary to what has been established about the role of surface modifications to the gate oxide surface, FET devices that have been processed with a gate modification do not result in an improved operational stability. One can reason that for organic semiconductors having a modified surface with various organic molecules with different geometries and polarities of the terminating head groups can lead to changes in the microstructure and growth of the organic semiconductor during the film development.[24] These changes are found to improve the operational stability of organic field-effect transistors due to improvements in molecular ordering and packing.[20,25-28] No changes in QD morphology on the oxide surface was observed.

### 5.5 Universal method to fabricate transient-free FETs using volatile ligands

Having established that this process does not modify the gate dielectric surface, we now explore different surface chemistries to develop these PbSe QD thin films. We find that this processing method results in bias-stress free transistors only when volatile ligands are used initially. For example, the vapor pressure of formic acid[29,30] (HCOOH) and hydrocyanic acid[31,32] (HSCN) are relatively high and readily evaporate at the temperatures we use for the $H_2S$ exposure (30-75°C). FTIR spectroscopy shows that exposing formate-capped or thiocyanate-capped QD films to an $H_2S$ pulse results in the complete loss of the characteristic IR signatures. The carboxylate peaks of the adsorbed formate at 1554 and 1327 $cm^{-1}$ disappears after the $H_2S$ exposure, as does the characteristic -C≡N stretch of thiocyanate at 2021 $cm^{-1}$. This is consistent with the idea that protonation and evaporation of the ligands by the $H_2S$ gas exposure.

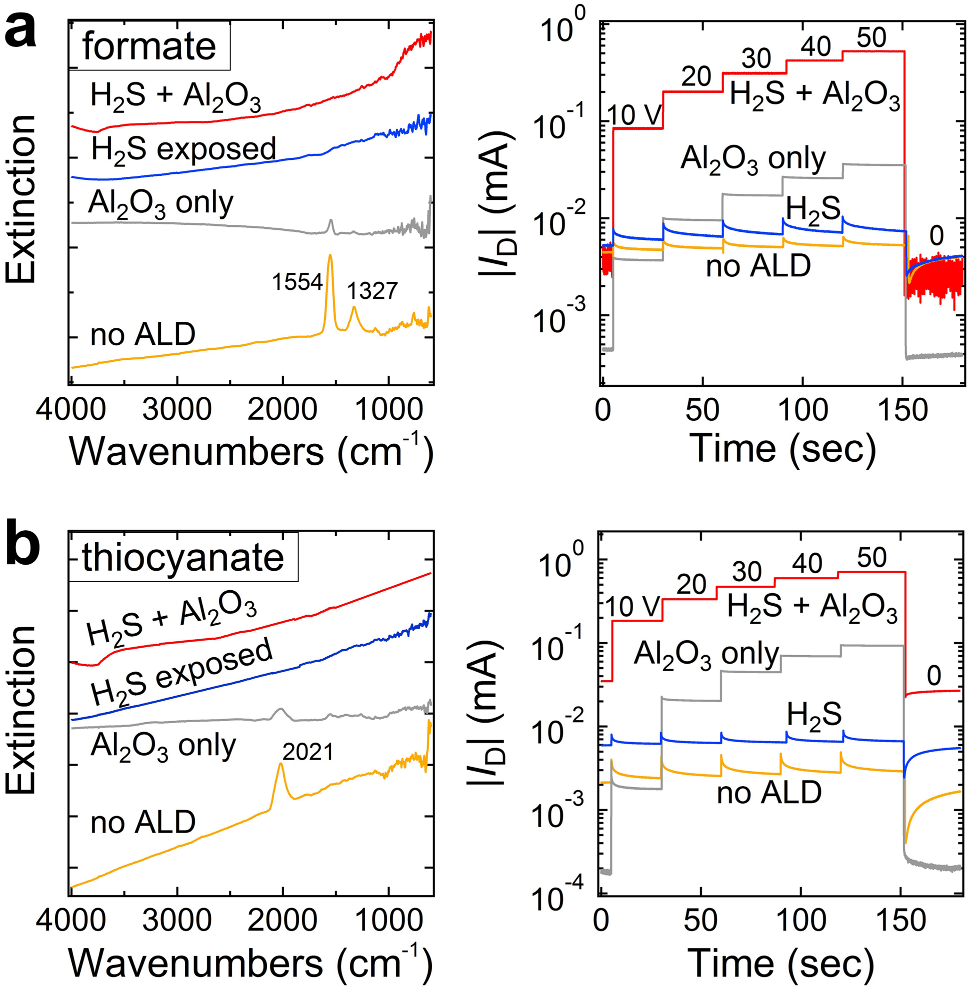

**Figure 5.4 Volatile ligands produce stable FETs.** FTIR spectra and current transients for films made from (a) formate-capped and (b) thiocyanate-capped PbSe QDs. The spectra show the complete loss of the ligand upon exposure of the as-made films (yellow traces) to $H_2S$ (blue traces). Alumina deposition results in little changes to the spectra (red traces) as expected. The $H_2S$ exposed, alumina-infilled FETs display negligible bias-stress effect

Subsequent infilling with alumina ALD causes little additional change to the IR spectra. However, after infilling the FETs they are free of the current transients and show *I-V* plots that are essentially identical to those of $H_2S$-exposed and infilled FETs made from EDT-capped QD films. Similar to the EDT-capped films, both $H_2S$-induced ligand exchange and alumina infilling are required to eliminate the transients of formate- and thiocyanate-capped films; $H_2S$ exposure alone removes the ligands but not the transients (Fig 5.2l). Meanwhile, the optical absorption spectra indicate that a similar amount of redshifting and broadening of the first exciton peak occurs for the EDT-, formate-, and thiocyanate-capped films upon $H_2S$ exchange and again upon infilling. The excitonic peak remains narrow for all films, indicating that the $H_2S$ and the alumina infilling steps do not result in the increase in polydispersity of the QDs by processes such as etching, necking, sintering, or ripening.

### 4.8 Nonvolatile ligands result in persistent current transients

In order to understand this process, we verified that the current transients persist if nonvolatile ligands are used to prepare QD films. Figure 5.5 shows that FTIR and current transients for films capped with oxalate, trimesate, and 1,4-benzenedithiolate (BDT) ligands; each ligand in its neutral form have very low vapor pressures.[32,33] As expected, $H_2S$ exposure does not remove these ligands from the films because the ligands do not evaporate when protonated. Indeed, the absence of C=O and S-H peaks in the IR spectra of $H_2S$ exposed films suggests that these three ligands are not protonated by $H_2S$. Since the neutral ligands are trapped on the surface of the QD surface in the absence of any solvent, any protonated ligands are likely to back repel the $H_2S$ exposure. Subsequent alumina infilling also has little impact on the ligand loading. Indeed, all FETs made using nonvolatile ligands show marked bias-stress transients, with a magnitude and decay constants of the transients varying differently for the ligands.

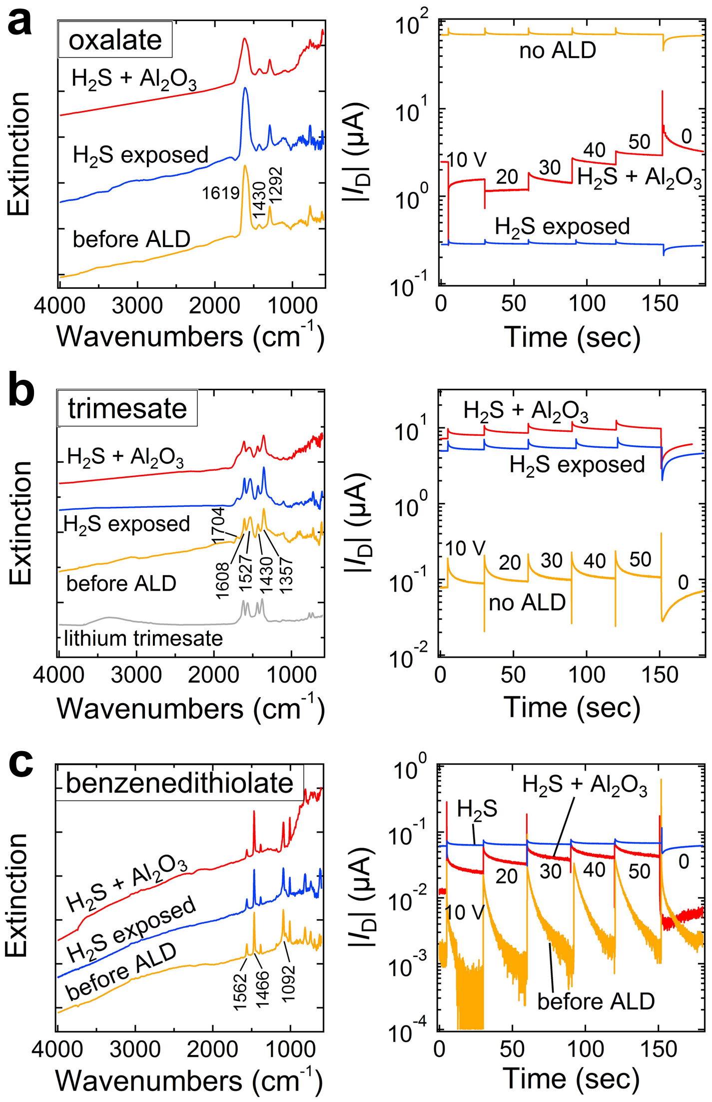

**Figure 5.5 Nonvolatile ligands yield QD FETs that retain significant bias-stress effect**

FTIR spectra and current transients for films made from (a) oxalate-capped (b) trimesate-capped, and (c) 1,4-benzenedithiolate-capped PbSe QDs. Before (yellow traces) and after

$H_2S$ exposure (blue traces) show that the ligands still remain. Alumina infilling following the $H_2S$ exposure show significant current transients.

From figure 5.5 above, we can infer that ligand removal is a necessary, but not a sufficient condition for eliminating the bias-stress effect. Complete elimination of this anomalous behavior requires ligand removal *and* overcoating of the QDs with alumina. The strong correlation between the chemical state of the QD surface and the presence of the transients suggests that the bias-stress effect in PbSe QD FETs is caused by charging and/or field screening by species on the surface of the QDs. It is likely that the QDs with poorly-passivated surfaces suffer the most extreme bias-stress effect.

### 4.9 Elemental analysis of ligand-free QD films

We measured the elemental composition of the infilled films by secondary ion mass spectrometry (SIMS) in order to understand the nature of the interface produced by the $H_2S$ exposure and alumina infilling process. To set a baseline for the SIMS studies of films, we first determined the amount of sulfur and other impurities in a bulk powder of oleate-capped PbSe QDs using glow discharge mass spectrometry (GDMS). The GDMS data complied in table 5.1 shows fifteen elements above the limit of detection out of 74 total elements. Matrix elements (Pb, Se, and C), gas-forming elements (H, N, O, and noble gases), and radioactive elements were not quantified in this experiment. Elements above 1 ppm at.% (which is about $5 \text{ X } 10^{16}$ atoms $\text{cm}^{-3}$ in an idealized QD solid) are phosphorous (2040 ppm), silicon (31 ppm), chlorine (25 ppm), sulfur (6 ppm), boron (3.1

ppm), calcium (1.3 ppm), aluminum (1.0 ppm), sodium (1.0 ppm), and bismuth (0.94 ppm). For the purpose of this experiment, most of the important conclusions from the GDMS data are that the sulfur content in our as-made QDs is low (<10 ppm). However, the GDMS data is also worth a brief discussion. First, the high level of phosphorus (equivalent to 15% of a monolayer on the QD surface) is reasonable based on the use of trioctylphosphine selenide (TOP-Se) and diphenylphosphine (DPP) in the QD synthesis. The phosphorus is presumably present as adsorbed molecular species derived from DPP and TOP-Se rather than point defects in the PbSe lattice. Secondly, the total impurity content of only ~70 ppm is surprising because the QDs are surprisingly pure despite a lack of effort to ensure high-purity conditions but, on the other hand, several of the impurities are in sufficiently high concentrations to act as dopants, traps, and recombination centers in QD films (particularly Si, Cl, B, Al, Na). Due to kinetics and thermodynamics of growing nanocrystals with impurities, it is often found that impurity doping nanocrystals results in adsorption of the impurity atom on the surface. Recent theoretical efforts has shown that a dopant introduced into a growing nanocrystal can be incorporated into the interior of the QD by using ligands that preferentially binds to the impurity atom.[34] Depending on the size of the dopants, smaller impurity dopants will adsorb on the surface whereas larger dopants will incorporate into the bulk. While the electronic behavior of these impurity atoms have not been rigorously studied, it is well known that many of the elements shown in Table 5.1 are electronically active in bulk PbSe in order to control the thermoelectric properties.[35] A better understanding of the location and electronic behavior of these impurities is needed to determine whether they may cause the deep traps that are thought to limit the efficiency of QD solar cells.

**Table 5.1** GDMS Elemental Analysis of As-Made Oleate-Capped PbSe QD Powders

| element | ppm wt. | ppm at. | atoms/cm$^3$ |
|---|---|---|---|
| P | 3000 | 2040 | $1 \times 10^{20}$ |
| Si | 41 | 31 | $1.5 \times 10^{18}$ |
| Cl | 40 | 25 | $1.2 \times 10^{18}$ |
| Bi | 9.2 | 0.94 | $4.6 \times 10^{16}$ |
| S | 9 | 6 | $3 \times 10^{17}$ |
| Ca | 2.4 | 1.3 | $6.2 \times 10^{16}$ |
| B | 1.6 | 3.1 | $1.5 \times 10^{17}$ |
| Al | 1.3 | 1.0 | $5.0 \times 10^{16}$ |
| Na | 1.1 | 1.0 | $5.0 \times 10^{16}$ |
| Zn | 0.57 | 0.18 | $9.0 \times 10^{15}$ |
| Ni | 0.28 | 0.10 | $4.9 \times 10^{15}$ |
| Fe | 0.15 | 0.057 | $2.8 \times 10^{15}$ |
| V | 0.1 | 0.04 | $2 \times 10^{15}$ |
| Ti | 0.07 | 0.03 | $2 \times 10^{15}$ |
| Mn | 0.02 | 0.008 | $4 \times 10^{14}$ |

We also used SIMS mainly to quantify the amount of sulfur present at the PbSe/$Al_2O_3$ interface for out transient-free FETs. We initially thought that the sulfur adsorbed on the QDs during $H_2S$ exchange would be removed by $H_2O$ during the subsequent ALD of $Al_2O_3$ resulting in a truly clean PbSe/$Al_2O_3$ interface. However, SIMS showed that about 0.4 monolayer of sulfur (1.5 X $10^{21}$ atoms cm$^{-3}$) remained on the surface of the QDs when formate-capped films were exposed to $H_2S$ and then infilled with alumina in the usual way. This sulfur content is quantitatively similar to that of sulfide-capped, $Al_2O_3$ infilled PbSe QD films reported in Chapter 4. As control experiments on a formate-capped film infilled with alumina without the $H_2S$ exposure (or any other sources of sulfur) showed a sulfur concentration about 20 times lower (8 X $10^{19}$ atoms cm$^{-3}$ = 1740 ppm or about 2%

of a sulfur monolayer on the QD surface), confirming that the sulfur observed in our transient-free films is inherent to the $H_2S$ exposure rather than some uncontrolled background source. We comment that we cannot account for the larger sulfur concentration in our sulfur-free infilled films compared to that of as-made QD powder measured by GDMS (1740 ppm vs. 6 ppm), but adventitious adsorption of thiols from the atmosphere of our glove box during the fabrication of the films may be responsible. Additional control experiments on a benzenedithiolate-capped film infilled with alumina without any exposure to $H_2S$ showed tenfold higher sulfur and carbon levels and fourfold higher hydrogen levels than the transient-free film, consistent with the retention of the BDT ligand on the surface of the QD after ALD as seen in the IR spectra (Fig 5.5c). All three films had very similar amounts of phosphorus (6-10 X $10^{18}$ atoms $cm^{-3}$). Our SIMS results suggest that the structure of the QD/alumina interface in the transient-free FETs is $PbSe/PbS_{(0.5\ ML)}/Al_2O_3$ rather than a $PbSe/Al_2O_3$ interface.

## 4.10 Role of $H_2O$ versus $H_2S$ in removal of volatile ligands and transient-free FETs

So far we have shown that *in vacuo* exposure to $H_2S$ is an effective way to protonate and desorb volatile anionic ligands from the surface of the QD films. We find that $H_2O$ works in a similar fashion as well, but larger doses of $H_2O$ are needed for full ligand exchange because $H_2O$ is a significantly weaker acid than $H_2S$ since the conjugate bases of $HS^-$ is weaker than $HO^-$ because sulfur has a larger atomic radius concentrating less charge. The IR spectra in Fig 5.6 shows the degree of ligand removal for formate-capped QD films exposed to different doses of $H_2S$ and $H_2O$ vapor. As seen from the spectra, one

$H_2S$ of 3 X $10^6$ Langmuir (L) is sufficient to remove all formate from the film surface. In our ALD system, this dose is obtained either by a single large pulse ($P_{max} \sim 1$ *Torr*) or seven smaller pulses ($P_{max} \sim 0.12$ *Torr*) of $H_2S$ (see Fig 5.5). The same dose of $H_2O$ removes only 60-70% of the formate but we can achieve quantitative removal of formate by using approximately ten times larger dosage of $H_2O$ (~3 X $10^7$ L). If the formate is removed by $H_2S$, subsequent infilling with alumina completely eliminates the current transients, as shown in Fig 5.2. If a large dose of $H_2O$ is used instead, the transients of the alumina infilled, ligand-free films are suppressed by not rigorously eliminated (Fig 5.6 b and c). We infer that is seems that a small amount of sulfur at the PbSe/$Al_2O_3$ interface is beneficial for complete elimination of the transients. Further studies is necessary to understand the interface between the QD surface and the first few nanometers of the ALD coating.

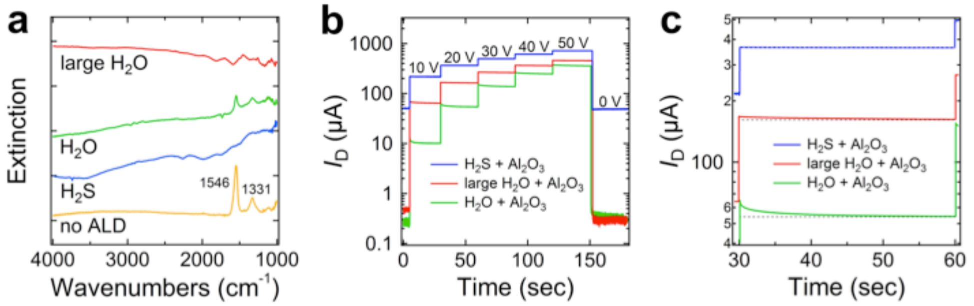

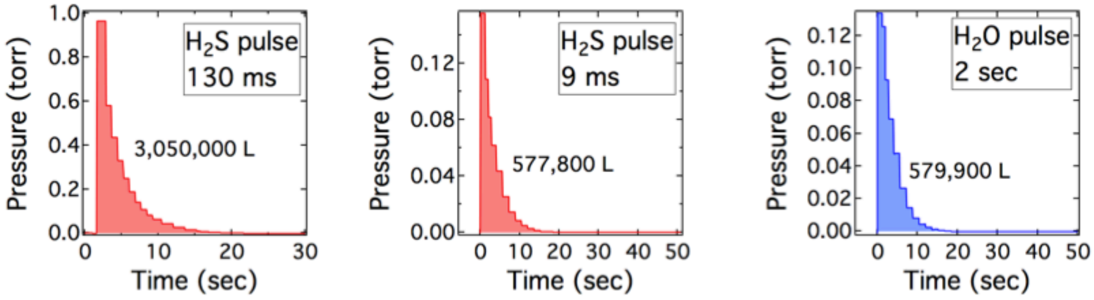

**Figure 5.6 Large doses of $H_2O$ remove basic ligands to yield nearly transient-free FETs after alumina infilling** (a) FTIR spectra of formate-capped QD films before ALD (yellow trace), after 3 X $10^6$ L exposure to $H_2S$ (blue trace) or $H_2O$ (green trace), and after a 3 X $10^6$ L exposure to $H_2O$ (red trace). $H_2S$ exposure results in complete ligand exchange, while the same does of $H_2O$ removes about 60-70% of the formate. Large doses of $H_2O$ is sufficient to exchange all the formate (b) $I_D$ time traces of the resulting infilled FETs. The transients are absent in the $H_2S$-exchanged devices, very weak in the device made by complete ligand exchange with a large $H_2O$ dose, and substantial transients in the device made by partial ligand exchange with $H_2O$. (c) Magnified view of the time trace in (b) at $V_G = 50$ V on a log-linear plot.

Having the sulfur at the interface is also responsible for the higher conductivity for the $H_2S$-exchanged films (Fig 5.6b). This larger current in the $H_2S$-treated FETs at $V_G = 0$ *V* is due to a larger, more negative threshold voltage compared to the $H_2O$-exchange FETs, which is not indicative of a lower on/off ratio.

## 4.11 Mechanism to elucidate the effects of $H_2S$ exposure and alumina infilling in eliminating the transients in QD FETs

In order to understand the mechanism for this process, we can review what is known about the bias-stress effect: (i) it is thermally activated (ii) they are associated with the surface of the QDs rather than the gate dielectric or the FET contacts (iii) they are eliminated by ligand exchange with $H_2S$ followed by coating the QDs with amorphous alumina to form PbSe/$PbS_{(0.5\ ML)}/Al_2O_3$ interface (iv) they are suppressed, but not eliminated by surface treatments that combine the removal of the volatile ligands followed by a conformal coating of the QDs by ALD. It was clear that the transients seem to depend on the chemistry of the QD surface, so we tested how the transients respond to changing (a) the pulse sequence for alumina deposition and (b) alumina thickness

### 5.9.1 Effect of first pulse for alumina deposition on current transients

We find that the transient is eliminated only if alumina is deposited by the initiation of a pulse of $H_2O$. Starting instead with a pulse of trimethylaluminum (TMA) after $H_2S$ exchange results in FETs with sizable bias-stress transients and lower conductivity, regardless of which ligand exchange process is used.

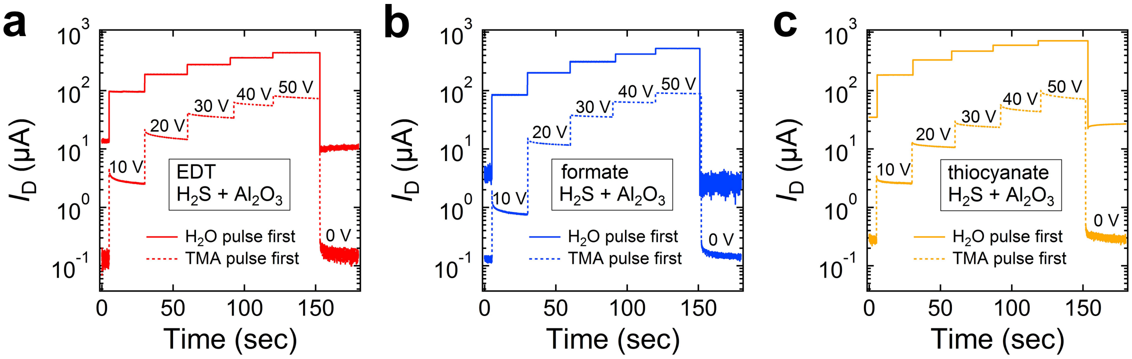

**Figure 5.7 Initiating alumina deposition with $H_2O$ eliminate the transient, but starting with TMA does not**. $I_D$ time traces for $H_2S$-exchanged alumina infilled FETs made from (a) EDT-, (b) formate-, and (c) thiocyanate-capped QDs. Solid traces correspond to devices in which the alumina deposition was initiated with a pulse of $H_2O$ first. Dashed traces correspond to devices when the alumina deposition was initiated with a pulse of TMA

This suggests that the transients is caused by electronic states or mobile species on the PbSe surface that are better passivated by starting the alumina ALD sequence with $H_2O$ instead of TMA. Starting with $H_2O$ may passivate surface Pb ions that may not be already coordinated with $SH^-$; thereby eliminating surface states while also providing a more hydroxylated QD surface for better alumina nucleation and growth. In contrast, starting with TMA likely creates $Pb\text{-}S\text{-}Al(Me)_2$ species on the surface that may sterically block the coordination of unpassivated Pb ions by $H_2O$ and lead to a patchier and lower-quality coating as a result.

### 5.9.2 Effect of alumina thickness on current transients

Not only is the ALD pulse sequence is important, but also the thickness of the alumina coating. In order to test the quality of the ALD coating,  we measured a series of FETs and TEM grids made by infilling $H_2S$-exchanged QD films with different amounts of alumina (0, 10, 20, 30, 40, and 120 ALD cycles). Figure 5.8 shows that the transients are severe in devices prior to ALD (0 cycles) and become gradually weaker with increasing number of ALD cycles and completely disappear for devices made with at least 40 cycles (the number needed to fully infill the QD films and suppress the current transients)

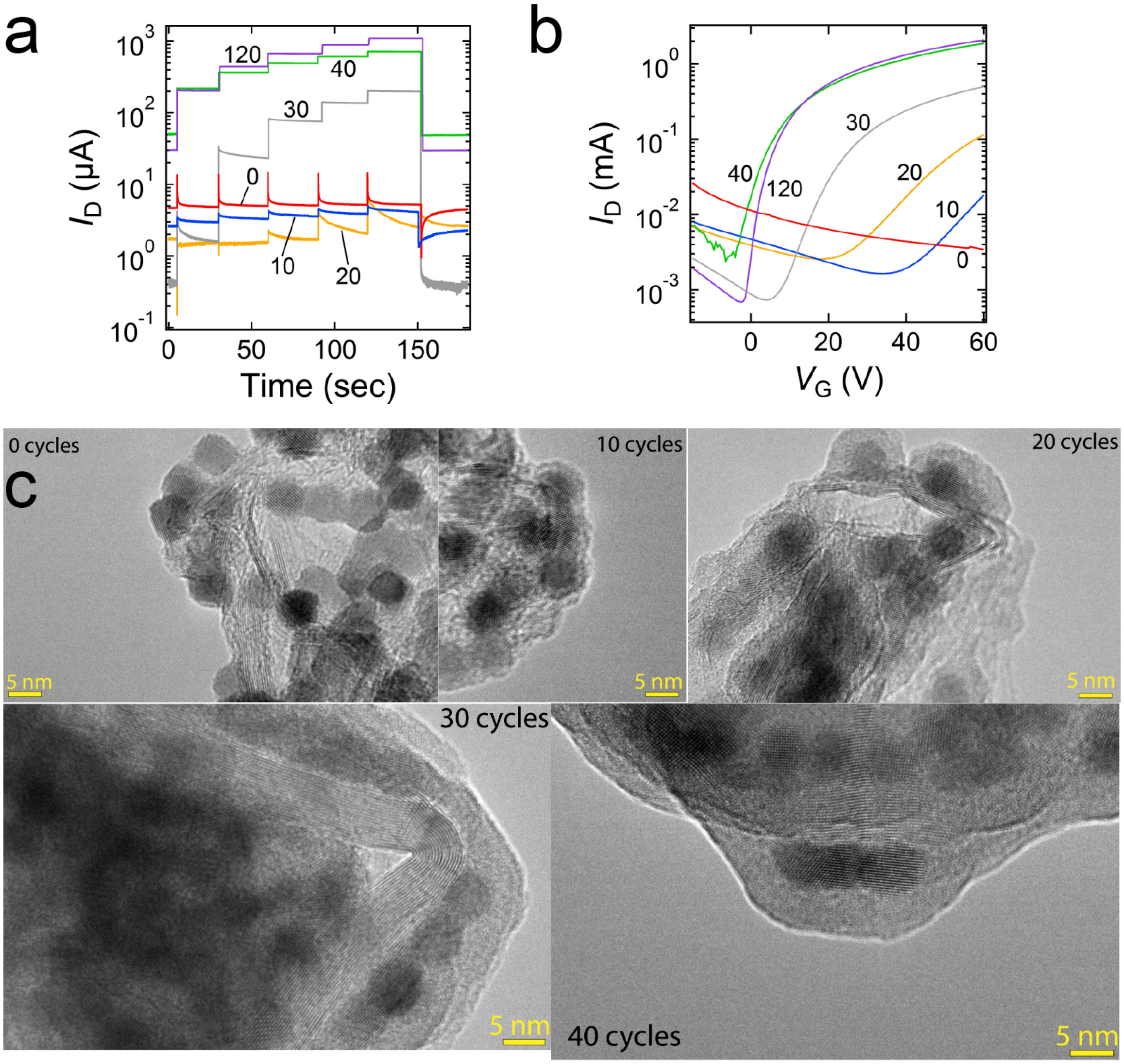

**Figure 5.8. $Al_2O_3$ infilling thickness dependence on $I_D$ transients and morphology.** (a) $I_D$ time traces for different thicknesses of alumina – 0 cycles (red), 10 cycles (blue), 20 cycles (yellow), 30 cycles (grey), 40 cycles (green), 120 cycles (purple) (b) Transfer characteristics for different thickness. With continuing evolution of ALD cycles, the threshold voltage shifts from >60 V to -4V.

The *I-V* characteristics of these devices also show a continuous evolution with the number of ALD cycles; the threshold voltage shifts from >60 V (0 cycles) to -4 ± 1 V (≥ 40 cycles), and *n*-channel appears and gradually dominates the device behavior (Fig 5.7b). Similar changes were recently observed during alumina infilling of $Na_2S$-treated QD FETs (Chapter 4). The fact that the transients disappear gradually over ~40 ALD cycles rather than suddenly after the first few ALD cycles provides critical information about their origin. Our first initial thought was that the alumina initially grows as islands on the QD surface (Volmer-Weber growth) rather than a continuous film. This would make sense due to the low growth temperature we use for the ALD process, which favors nucleation of alumina at high-energy surfaces rather than a continuous layer-by-layer growth. Thus, we believe that the transients are due to charging of electronic states (or ionic motion) on the QD surface. The ALD alumina stops the transients by passivating the PbSe/PbS surface electronically and/or preventing ionic motion/rearrangements on the QD surface. From the TEM images, it is clear that even after 10 cycles of alumina ALD, the growth is uniform and conformal around the QDs, ruling out the hypothesis that island growth was limiting the minimum amount of alumina required to suppress the bias-stress effect.

We can also rule out charging surface states on the QD surface because it cannot account for the magnitude or $V_G$ dependence of the observed transients. Many of the transients correspond to a charge of approximately 1-10μC, which is much larger than the total charge that can be accommodated in QD surface states (~0.01 μC assuming one trapped charge for each surface atom. From this simple approximation, there are simply not enough surface states to store this much charge on each QD. However, charging plus screening of the applied gate field by charges or dipoles can account for most features of the transients.

### 5.9.3 Surface proton migration mechanism

### 5.9.3.1 Proton mobility in solids

It is general knowledge (in physical chemistry) that protons and hydroxide ions diffuse fairly quickly especially in ice and in liquid water, with protons diffusing twice as fast as hydroxide ions.[36,37]. These measured diffusivities were measured using solid state NMR techniques and under an applied field.[38] We note that the diffusion mechanism that will be discussed below will be lower because these protons under consideration will be attached to hydrogen-bonded water and accompanied typically by counter ions.

This topic of proton conduction is of scientific and technological significance with special applications in ion-exchange materials such as Nafion™ used as proton pumps and membrane in fuel cells[39,40] and polymer members used in hydrogen fuel cells.[41] For instance, in hydrogen fuel cells, a proton-conducting separator like Nafion is used and it typically has high ionic conductivity. Controlling the bulk material properties of these membranes requires fundamental understanding of the mechanisms for proton migration in order to further improve the performance of these applications. The two most widely referenced mechanisms are the *Grotthuss mechanism* and the *vehicle mechanism*.

### 5.9.3.2 Grotthuss mechanism (lone hydrogen migration)

The Grotthuss mechanism is the simplest model to consider in which a protons tunnels from one water molecule to the next through hydrogen bonds.[42] This process is a thermally activated behavior and has been seen to quench at temperatures $\leq$ 190 K, particularly for ice.[43]. This translational process is an incoherent process in which a $H^+$ is displaced along a hydrogen bond and then transported through this hydrogen bond to a neighbor hydrogen bond. This mechanism can only occur on the presence of defects. Hydrogen defects can be present in metal oxides in the form of protons, neutral hydrogen (H), or $H^-$ hydride ions. It is generally assumed that there are protons present at room temperature and atmospheric oxygen pressure. These hydrogens are typically bounded to electronegative species such as oxygen. In order for these ions to migrate long distances, the ions must be associated with strong hydrogen bonding clusters such as that found in ice. Stronger hydrogen bonding results in shorter O-O distances. These short distances afford for the ease in migration such that the bond breaking energy of hydrogen bonds is the smallest. Furthermore, for continued proton migration, a reorientation of the hydrogen bonding is required for long-range $H^+$ conduction to occur.

### 5.9.3.3 Vehicle mechanism (proton-carrying mechanism)

In contrast to the *lone proton migration* mechanism, another mechanism that has also been invoked is the vehicle mechanism. It is similar to the Grotthuss mechanism but it differs, however, in that the proton migrates in one direction as $OH_3^+$ bonded to a *vehicle* such as $H_2O$ whereas the *unburdened* chemical species move in the opposite direction. This mechanism of cooperative motion in which the counter-flow of protons and its *vehicles* is essential, voids or defects are created through thermal activation as described in defect chemistry and free volume theory where charge neutrality and mass balance must be preserved for diffusion to occur.[44]

Whether is it through the *Grotthuss mechanism* or the *vehicle mechanism* that can explain proton migration, it is this author's opinion that it is a matter of semantics. In the end, we have to consider what the final state looks like. If we consider the mobility of protons versus hydroniums (vehicle), protons will always have a larger mobility via the traditional Brownian diffusion since the proton can easily hop off a hydronium and just transport as a proton instead of requiring the large hydronium to diffuse.

#### 5.9.3.4 Ion-exchange on PbSe QD films infilled with amorphous alumina

Having ruled out morphology effects in the alumina layer during deposition, we now entertain the idea that perhaps surface proton migration could be the cause of the current transients. In contrast to the commonly invoked mechanism for proton motion in organic semiconductors[19,23,45] where in the presence of water, the holes in the semiconductor are in equilibrium with protons in the oxide surface, the protons stem from the hydroxylated alumina surface (hydroxyls). It is not unconceivable that our alumina layers possesses these chemical species because it has been reported that hydroxyl content for $Al_2O_3$ ALD increases with decreasing temperature.[46-48] The rationale behind the large measured hydrogen content for alumina films grown at lower temperatures is because at lower temperatures, the TMA reaction with the $Al\text{-}OH^*$

surface species was found to be incomplete. As such, during the deposition of $Al_2O_3$ via ALD, the hydroxyl species can build up in the growing $Al_2O_3$ film. In these vibrational infrared studies, they found that annealing up to 1000K could reduce the hydroxyl accumulation. Based on these results and the relatively low temperatures ($\leq$ 75°C), it is reasonable to find surface protons within the bulk of alumina film.

Assuming protons can migrate on the hydroxylated alumina surface, one would expect that if we could exchange these protons with larger cations, the diffusion of these metal cations would weaken. To test this hypothesis, we tested partially-infilled QD FETs such that surface protons can still migrate ($Al_2O_3$ thicknesses ~ 2.5 nm). The film is then soaked for 3 hours in an ion exchange solution of potassium nitrate ($KNO_3$); 0.1M in DMSO at room temperature.

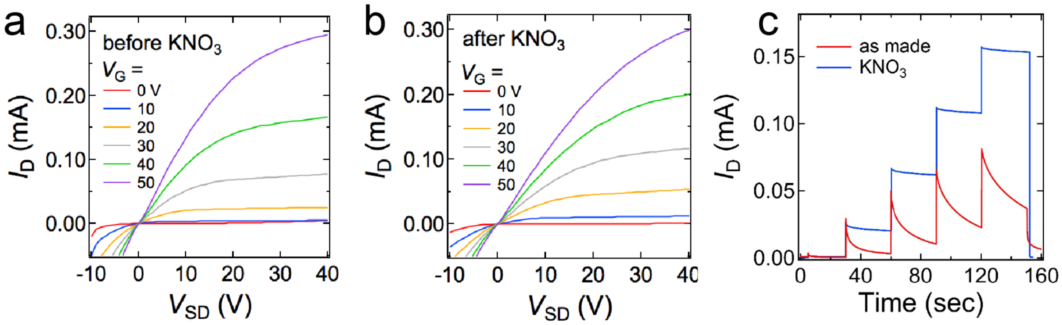

**Figure 5.9 Ion-exchange with $K^+$** Output characteristics (a) PbSe SCN-capped, $H_2S$-exposed and infilled with ~2.5 nm alumina ALD (b) same FET as (a) but treated with 0.1M $KNO_3$ for 3 hours in DMSO. The *IV*s are unaffected because the exchange does not affect the surface charge (c) $I_D$ time traces before and after the ion exchange process.

Referring to fig 5.9 above, we can comment on several, yet important aspects of the ion exchange process. First, the current values in fig 5.9a and 5.9b are essentially the same because the ion exchange process **should not** affect the surface charge of the alumina surface ($H^+/K^+$). Secondly, we observe a dramatic improvement in the current transients during this exchange process qualifying the idea that surface proton migration could be one of the causes for the bias-stress effect in QD FETs at least for QD films that has a thin layer of aluminum oxide.

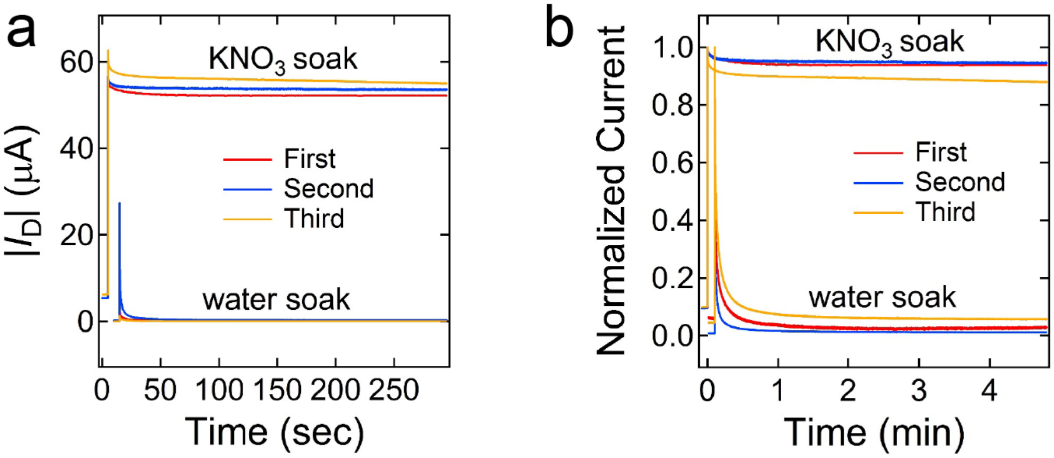

**Figure 5.10. Reversibility of $H^+/K^+$ exchange for three rounds of sequential soaks in $KNO_3$ and pure water** (a) Raw current transients (b) normalized current transients. Bias conditions: $V_{SD}$ = + 5V, $V_G$ stepped from 0 to 40 V. All measurements performed at room temperature inside a glove box.

Furthermore, this exchange process is reversible to an extent. To test the dynamic reversibility of this ion exchange process, three rounds of sequential soaks in 0.1M $KNO_3$ in DMSO followed by pure water (pH = 5.5; freeze, pump, thawed five times) were performed. In figure 5.10, a sequential soak in water after the potassium exchange restores the current transients back to its original behavior. This sequence was performed on the same device to demonstrate that this process is indeed reversible.

In addition, we also pursued the concept of the dependence on the size of the alkali cation. We hypothesized that the current transients would weaken for larger cations.

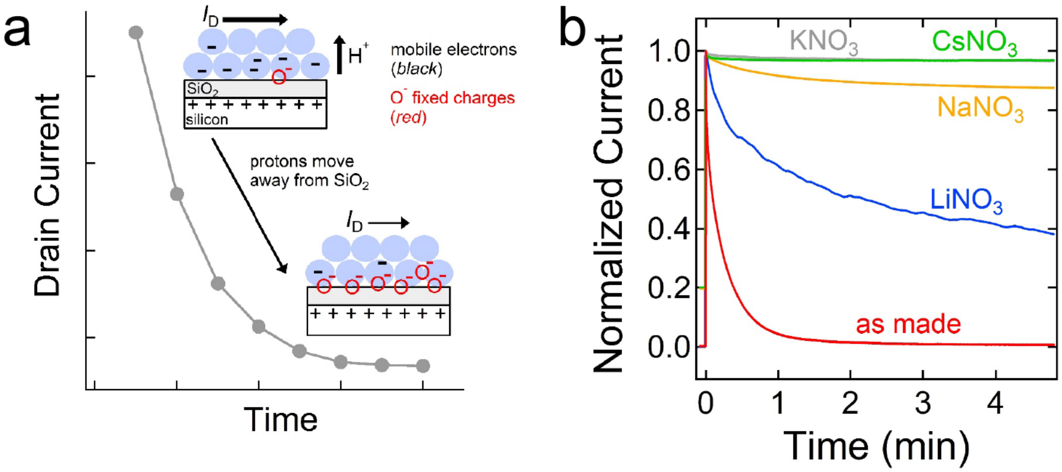

**Figure 5.11 Surface proton migration mechanism for bias-stress effect in QD FETs infilled with alumina**. (a) Charge screening due to proton migration (b) Alkali cation dependence on current transients.

In figure 5.11b, it is clear that the current transient progressively becomes weaker with increasing size of the alkali cation during the ion exchange process. Possible explanations could be that for larger cations, the diffusion of these ions is slower. This phenomenon is commonly seen in $SiO_2$ MOS capacitors in which they have shown that accumulated charge during capacitance-voltage measurements increases with time due to migration of an alkali cation (Na[49], Ca and Mg[50]). The authors proposed that the mechanism for diffusion under an applied bias was either due to a columbic bonding force present in the oxide or by an interfacial chemical bond. In light of our results, we can explain the mechanism for proton migration and the ion exchange process by simply considering the surface species of the surface of our alumina layer.

It is documented that the isoelectric point (IEP) for amorphous alumina is about 8-9 when there is no other ions on the surface except ($H^+$/$OH^-$ ). This value is more or less the point in which the total concentration of surface anionic sites is equal to total concentration of surface cationic sites; in other words, it is the pH in which the oxide surface carriers no net electrical charge.[51] Since this IEP, which is essentially the point-of-zero charge (PZC) is high (more acidic than that of $SiO_2$), it would be easier for the alumina surface to carry negative surface charge which results in the tendency to adsorb cations especially at $pH > PZC_{alumina}$. As such, one should expect that the adsorption of the larger alkali cations becomes weaker on an oxide surface due to electrostatics. It has been shown that adsorption coefficients for different alkali metals on an alumina surface is constant except for lithium.[52]. From this we can infer at most that the weakening of transients with increasing radius and weight of the alkali cation is not due to a more efficient ion exchange processes. Instead we argue that improvement in the current transients is due to slower diffusion coefficients for these alkalis on alumina surfaces and not electric field-assisted diffusional processes.[53]. To recap, surface proton migration in a hydroxylated alumina (in the presence of water) surface occurs when an electric field is present during the application of the gate bias. This proton diffuses up through the film through negatively charged surfaces[54] ($O^-$, fixed negative charges). Simultaneously electrons injected at the metal contact (grounded to the gate electrode) are also swept through the source-drain bias resulting in both ionic and electronic migration within the device. As the proton moves away from the surface, it leaves a negative charge to maintain charge balance in the alumina layer, which effectively screens the gate electric field, resulting in the current transients (bias-stress effect) (see fig 5.11a inset for cartoon of operation). If proton migration screens the electric field, this can also explain recent results establishing the lack of electric fields in heterojunction solar cells based on quantum dots (results unpublished).

## 4.12 High performing field-effect transistors with high mobility, zero bias-stress effect and low density of trap states

Having established one of the causes for the bias-stress effect, we can now optimize our device processing to slightly higher ALD temperatures. As previously shown in chapter 4, processing our films at 75°C yields better devices most likely due to increased electronic coupling (slight sintering) and higher density of alumina. Using our previous processing, we obtain QD FETs with a large electron mobility of about 13 $cm^2 V^{-1} s^{-1}$.

Furthermore, these devices, when processed with $H_2S$, these FETs are also operationally stable.

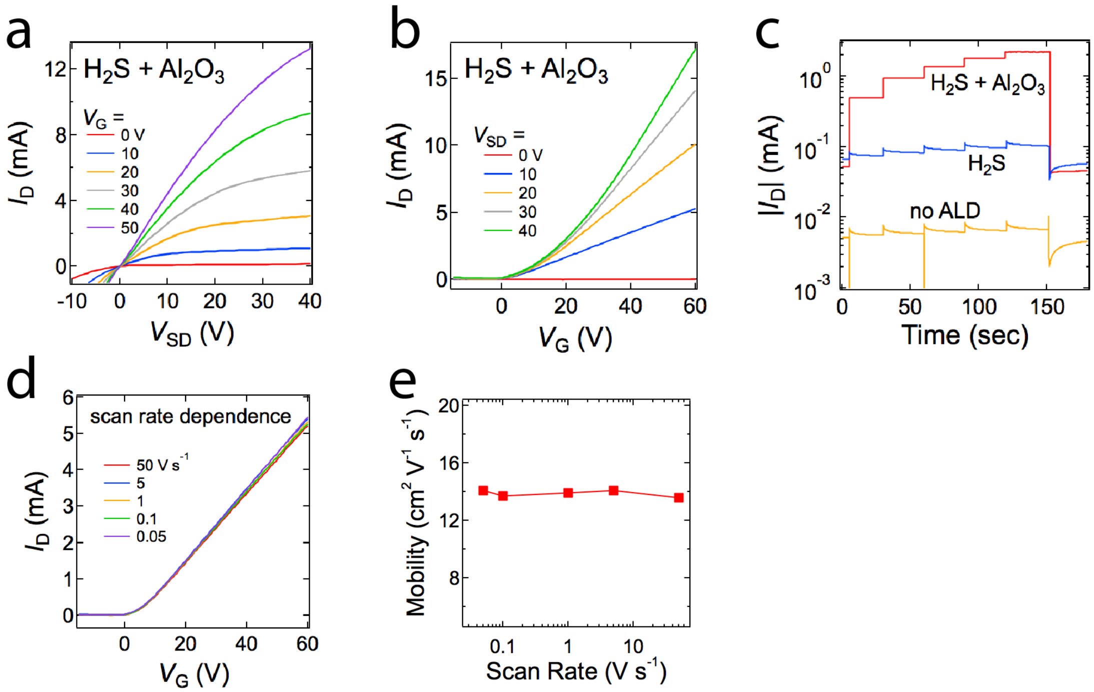

**Figure 5.12 High mobility, zero bias-stress effect PbSe QD SCN-treated FET** (a) Output characteristics (b) Transfer characteristics (c) $I_D$ vs. time traces for PbSe SCN-treated films before ALD (orange), after $H_2S$ (blue), and then infilled with alumina ALD at 75°C (red) (d) Transfer characteristics at $V_{SD}$ = + 10 V at different scan rates (e) Scan rate independent mobility extracted from (c)

To determine the reason for the increase in mobility at this temperature, we easily rule out heating effects by measuring the grain size via XRD as well as monitoring the optical absorption. There is no significant narrowing in the XRD pattern, nor is there significant broadening or "washing" of the 1st exciton transition as previously seen for sulfide-capped films when processed at temperatures above 100°C.

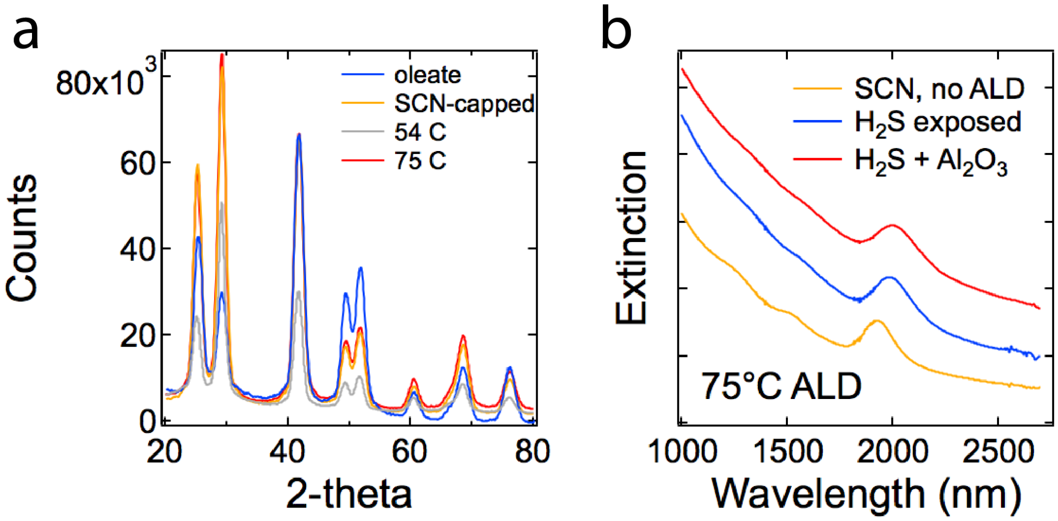

**Figure 5.13 XRD and optical extinction comparison for PbSe QD films processed at 75°C**. Films processed at a slightly lower temperature are also used for comparison

From figure 5.13a, we can calculate the QD diameter using the Scherrer equation. Table 5.2 below summarizes the data. Inferring from table 5.2 and figure 5.13, we can definitively rule out changes in dot morphology due to extended or higher processing temperatures. If heating did play a role, one would expect that it would occur at much larger temperatures as we have seen in chapter 4

| **Processing/Film** | **{111}** | **{200}** | **{220}** |
|---|---|---|---|
| Oleate | 6.18 | 5.45 | 5.88 |
| SCN-capped | 6.21 | 6.32 | 6.14 |
| SCN/$H_2S/Al_2O_3$ (75°C) | 6.31 | 6.55 | 6.18 |

**Table 5.2 Grain size analyses comparing different film processing**

Having ruled out changes in dot morphology, we now entertain the idea that perhaps small improvements in packing or domains of order as one of the reasons for the improved mobility. In disordered semiconductors, the density of states near the conduction band or near the valence band is often described as having an exponential tail of states. This disorder can easily imagined: 1) variations in quantum dot coupling during the ligand exchange process 2) QDs are faceted with different ligand binding configurations 3) size distributions, despite recent success, is still on the order of 5% 3) films are not highly packed 4) QD cores are sub-stoichiometric which can lead to a broadening in states. Each of these descriptions can lead to an exponentially decreasing density of states characterized by $N(E) = N_0 \exp(-\frac{\Delta E}{E_U})$ where $\Delta E$ is the energy difference measured from the conduction (valence) band for a n-type (p-type) semiconductor and $E_U$ is a characteristic energy describing the exponential distribution from the band edge known as the *Urbach tail.* This width as previously studied in organic semiconductors[55,56], a-Si[57], and quantum dots[58]can be a result of physical disorder such as grain boundaries and atomic defects or even energetic disorder such as differences in stoichiometry or variations in coupling. In order to estimate the amount of disorder using field-effect transistors, while there are many methods in which the density of states is extracted in field-effect transistors, the most popular method is measuring the field-effect conductance as a function of temperature[57,59-61]. These *temperature* methods reduce the problem to one dimension, zero-temperature statistics to make the integrals easy, and assume the interface trap density is negligible. In addition, using these approaches, the relevant energy scale is derived from the activation energy $E_A = \Delta E\ (V_G)$ of the current (i.e. the field-effect conductivity) which is obtained from temperature dependent measurements. If however, the electrical characteristics change on the time scale of the temperature dependent measurement (*bias-stress effect*), these approaches would not be suitable.

Using the *temperature method* introduced by *Fortunato et al.*, they suggest an extraction scheme for high accuracy of the density of trap states in amorphous silicon thin-film transistors. The following simplifying assumptions include:

1. Charge density is homogenous along the transistor channel ($V_{SD} << V_G$ (linear regime)
2. The semiconductor is homogenous and perpendicular to the insulator-semiconductor interface
3. Negligible interface-state density (i.e. no fixed charges)

To determine the density of states, the authors use the abrupt approximation : all charge is assumed to reside in the region close to the dielectric-semiconductor interface. The authors also assume that the film thickness (grain size) is much smaller than the Debye length ($L_D$) which reduces the problem to one dimension (x-direction – perpendicular to the insulator-semiconductor surface). Again, by neglecting the free charge density and transistor operation in the subthreshold regime, where the free-charge density is negligible compared to the density of trapped charge), the volume density of charge (for an undoped material) can be expressed as

$$n(\psi) = -q\int_{E_V}^{E_C} N_g(E)f(E-E_F-q\psi)dE + q\int_{E_V}^{E_C} N_g(E)f(E-E_F)dE \tag{5.1}$$

which flow sufficiently low temperatures, (zero temperature approximation – negligible interface density of states and delta function of Fermi level)

$$n(\psi) = -q\int_{E_F}^{E_F+q\psi} N_g(E)dE \tag{5.2}$$

by multiplying $2\delta\psi/\delta x$ and integrating from x = 0(oxide-semiconductor interface) to x = d (flat band)

$$\left(\frac{d\psi}{dx}\right)^2_{x=0} = \frac{2q}{\varepsilon_{semicondcutor}}\int_0^{\phi_s} d\psi \int_{E_F}^{E_F+q\phi} N_g\,(E)dE \tag{5.3}$$

From this expression, the gap-state density is given by

$$N_g(E_F+\psi_s) = \frac{\varepsilon_{semi}}{2q}\frac{\delta^2}{\delta\psi_s^2}\left(\frac{d\psi}{dx}\right)^2_{x=0} \tag{5.4}$$

In the absence of surface states, the electric field at the semiconductor interface is given by

$$\frac{d\psi(x)}{dx}_{x=0} = -\frac{\varepsilon_{0x}}{\varepsilon_{semi}}\frac{V_{0,ox}}{t_{ox}} = -\frac{\varepsilon_{0x}}{\varepsilon_{semi}}\frac{V_G-V_{FB}-\psi_s}{t_{ox}} \tag{5.5}$$

where $\varepsilon_{0x}$ is the dielectric constant, $t_{0x}$ is the thickness of the oxide layer, $V_{FB}$ is the flat band voltage, $V_G$ is the gate voltage, and $V_{0x}$ is the voltage drop across the oxide.

The interface potential (surface potential) *ψ(x)* in equation 5.4 and 5.5 are obtained as described in the paper. First, transport is assumed to be by electrons only and is defined as

$$G = G_0 - \frac{G_0}{d}\int_0^{\psi_s} \frac{\exp\,({}^{q\psi}/_{kT})-1}{{}^{d\psi}/_{dx}}\, d\psi \tag{5.6}$$

$G_0$ is the flat band conductance given by

$$G_0 = G_{00}\exp((E_F - E_c)\,/kT) \tag{5.7}$$

Differentiating 5.6

$$\frac{dG}{d\psi_s} = -\frac{G_0}{d}\frac{\exp\,({}^{q\psi}/_{kT})-1}{{}^{d\psi}/_{dx}}) \tag{5.8}$$

From equation 5.5 and 5.8 and the following relations:

$$\frac{dG}{dV_G} = G_{00}\frac{\varepsilon_{0x}}{dt_{0x}}\frac{\exp\,[\frac{E_F-E_C+q\psi_S}{kT}]}{n(\psi_S)} \tag{5.9}$$

From this derivation, we can quickly validate these assumptions, especially in light of transistors based on disordered semiconductors. For instance, as will be illustrated in the next chapter, a model for transport based on disordered semiconductors based on percolation theory states that carriers will dive downwards in energy and transport around unoccupied states around the Fermi level. The population or concentration of these states around the Fermi level will be dependent on the applied gate bias. This gate bias will influence the surface potential (electric field) at the semiconductor interface and will determine the amount of band bending at the semiconductor-insulator interface. The amount of band banding (potential shift) from the Fermi level is determined by this surface potential, and hence applied gate field. By doing a temperature dependent conductivity measurement, one can determine the gap density of states if the relationship $V_G(\psi_s)$ and the bulk Fermi level. From fitting the temperature dependent conductivity measurements at different applied gate voltages, one can determine the activation energy in equation 5.9, which is the difference between the Fermi level and the conduction band edge at the semiconductor-dielectric interface

$$\Delta E \ \approx E_F - E_C + q\psi_s \tag{5.10}$$

Once the activation energy is known, the surface (interface) potential $\psi_s$ $(V_G)$ can be calculated from equation 5.10 above, assuming *a priori* a value for the difference between $E_F$ – $E_{C.}$ Then the electric field with equation 5.5 can be calculated and the final result in introduced into equation 5.4 and the numerical differentiation with respect to the surface potential will yield the trap density of states as a function of energy $E \ = \Delta E \ \approx E_F - E_C + q\psi_s$. The results of this analysis is summarized below and compared to different processing.

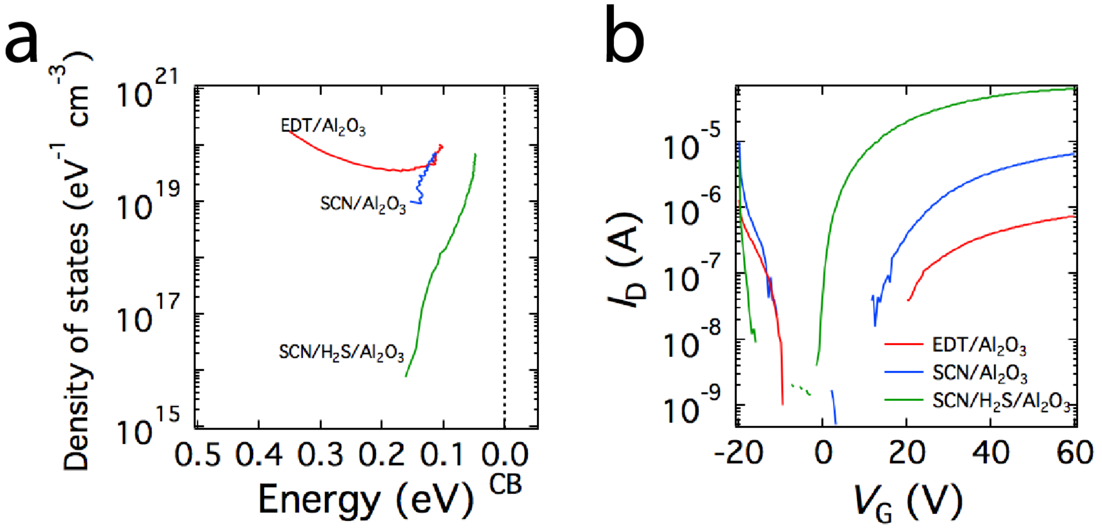

**Figure 5.14 Density of states extracted using the temperature method**[57] (a) A comparison between (a) density of states and (b) subthreshold swing (transfer characteristics) between FET devices with different mobilities : EDT/$Al_2O_3$ (0.2 cm$^2$ V$^{-1}$ s$^{-1}$), SCN/$Al_2O_3$ (5.2 cm$^2$ V$^{-1}$ s$^{-1}$), SCN/$Al_2O_3$ (13 cm$^2$ V$^{-1}$ s$^{-1}$)

Fitting the extracted density of states to an exponential function $N(E) = N_0 \exp\left(-\frac{\Delta E}{E_U}\right)$ we can estimate a band tail width of 35 meV, 100 meV, and 226 meV from the slope. At face value, it is clear that that the tail in the density of states extracted from field-effect conductivity measurements narrows (larger slope, smaller tail width) improves with FET devices that have shown higher mobility. We are aware that these values must be check with other complementary techniques such as photothermal deflection spectroscopy (PDS) and perhaps intensity modulated photocurrent spectroscopy based on NRELs data. Neglecting the absolute values of the Urbach tail, we can speculate that the improvement in device performance when using SCN-capped films versus EDT-capped films, especially at higher processing temperatures could be due to structural improvement of the packing of the NCs (figure 5.15) as previously suggested.[62-64]. An example of the morphology for SCN-capped PbSe quantum dots is illustrated below.

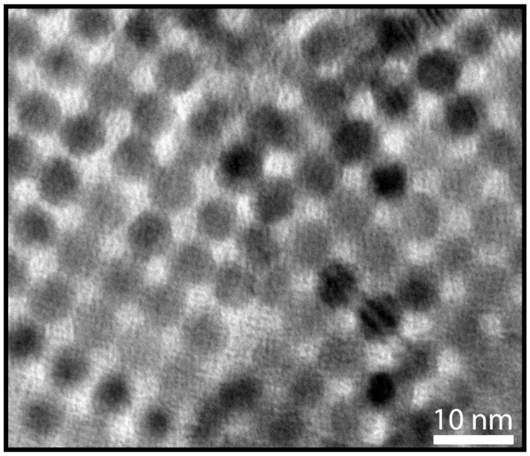

**Figure 5.15 Transmission electron microscope of SCN-capped PbSe films**.

Further work is needed to deconvolute the role of order in these films and whether it is truly an improvement in order or a reduction in interfacial states which leads to reduction in trap density of states near the semiconductor interface and an improved subthreshold swing (fig 5.14b) as outlined in *Powell et al.*[65]. Nonetheless, this approach in approximating the trap density of states can be extended to determine the position of the Fermi level and typical transport energy $E^*$ as a function of charge density (gate voltage) which is important to understand charge transport in quantum dot films using field-effect transistors. This will idea will be discussed in next chapter.

## REFERENCES

(1) Oh, S. J.; Berry, N. E.; Choi, J.-H.; Gaulding, E. A.; Paik, T.; Hong, S.-H.; Murray, C. B.; Kagan, C. R. Stoichiometric Control of Lead Chalcogenide Nanocrystal Solids to Enhance Their Electronic and Optoelectronic Device Performance. *ACS Nano* **2013**, *7*, 2413–2421.

(2) Kim, D. K.; Fafarman, A. T.; Diroll, B. T.; Chan, S. H.; Gordon, T. R.; Murray, C. B.; Kagan, C. R. Solution-Based Stoichiometric Control Over Charge Transport in Nanocrystalline CdSe Devices. *ACS Nano* **2013**, *7*, 8760–8770.

(3) Nag, A.; Chung, D. S.; Dolzhnikov, D. S.; Dimitrijevic, N. M.; Chattopadhyay, S.; Shibata, T.; Talapin, D. V. Effect of Metal Ions on Photoluminescence, Charge Transport, Magnetic and Catalytic Properties of All-Inorganic Colloidal Nanocrystals and Nanocrystal Solids. *J. Am. Chem. Soc.* **2012**, *134*, 13604–13615.

(4) Oh, S. J.; Berry, N. E.; Choi, J.-H.; Gaulding, E. A.; Lin, H.; Paik, T.; Diroll, B. T.; Muramoto, S.; Murray, C. B.; Kagan, C. R. Designing High-Performance PbS and PbSe Nanocrystal Electronic Devices Through Stepwise, Post-Synthesis, Colloidal Atomic Layer Deposition. *Nano Lett.* **2014**, *14*, 1559–1566.

(5) Muramoto, S.; Gillen, J. G.; Murray, C. B.; Kagan, C. R. Bandlike Transport in Strongly Coupled and Doped Quantum Dot Solids: a Route to High-Performance Thin-Film Electronics - Nano Letters (ACS Publications). *Nano Lett.* **2012**, *12*, 2631–2638.

(6) Nag, A.; Kovalenko, M. V.; Lee, J.-S.; Liu, W.; Spokoyny, B.; Talapin, D. V. Metal-

Free Inorganic Ligands for Colloidal Nanocrystals: S2−, HS−, Se2−, HSe−, Te2−, HTe−, TeS32−, OH−, and NH2− as Surface Ligands. *J. Am. Chem. Soc.* **2011**, *133*, 10612–10620.

(7) Lee, J.-S.; Kovalenko, M. V.; Huang, J.; Chung, D. S.; Talapin, D. V. Band-Like Transport, High Electron Mobility and High Photoconductivity in All-Inorganic Nanocrystal Arrays. *Nature Nanotechnology* **2011**, *6*, 348–352.

(8) Hetsch, F.; Zhao, N.; Kershaw, S. V.; Rogach, A. L. Quantum Dot Field Effect Transistors. *Materials Today* **2013**, *16*, 312–325.

(9) Luther, J. M.; Law, M.; Beard, M. C.; Song, Q.; Reese, M. O. Schottky Solar Cells Based on Colloidal Nanocrystal Films - Nano Letters (ACS Publications). *Nano Lett.* **2008**, *8*, 3488–3492.

(10) Liu, Y.; Gibbs, M.; Puthussery, J.; Gaik, S.; Ihly, R.; Hillhouse, H. W.; Law, M. Dependence of Carrier Mobility on Nanocrystal Size and Ligand Length in PbSe Nanocrystal Solids. *Nano Lett.* **2010**, *10*, 1960–1969.

(11) Rosen, E. L.; Sawvel, A. M.; Milliron, D. J.; Helms, B. A. Influence of Surface Composition on Electronic Transport Through Naked Nanocrystal Networks. *Chem. Mater.* **2014**, *26*, 2214–2217.

(12) Osedach, T. P.; Zhao, N.; Andrew, T. L.; Brown, P. R. Bias-Stress Effect in 1,2-Ethanedithiol-Treated PbS Quantum Dot Field-Effect Transistors - ACS Nano (ACS Publications). *ACS Nano* **2012**, *6*, 3121–3127.

(13) Nelson, C. A.; Zhu, X. Y. Reversible Surface Electronic Traps in PbS Quantum Dot Solids Induced by an Order–Disorder Phase Transition in Capping

Molecules. *J. Am. Chem. Soc.* **2012**, *134*, 7592–7595.

(14) Voznyy, O.; Thon, S. M.; Ip, A. H.; Sargent, E. H. Dynamic Trap Formation and Elimination in Colloidal Quantum Dots. *J. Phys. Chem. Lett.* **2013**, *4*, 987–992.

(15) Thon, S. M.; Ip, A. H.; Voznyy, O.; Levina, L.; Kemp, K. W.; Carey, G. H.; Masala, S.; Sargent, E. H. Role of Bond Adaptability in the Passivation of Colloidal Quantum Dot Solids. *ACS Nano* **2013**, *7*, 7680–7688.

(16) Aleksić, S.; Pantić, D. The Influence of Interface and Semiconductor Bulk Traps Generated Under HEFS on MOSFETs Electrical Characteristics. *Proceedings of the 5th Small Systems Simulation Symposium 2014* 59–64.

(17) Liu, Y.; Tolentino, J.; Gibbs, M.; Ihly, R.; Perkins, C. L.; Liu, Y.; Crawford, N.; Hemminger, J. C.; Law, M. PbSe Quantum Dot Field-Effect Transistors with Air-Stable Electron Mobilities Above 7 Cm 2V −1s −1. *Nano Lett.* **2013**, *13*, 1578–1587.

(18) Liu, Y.; Gibbs, M.; Perkins, C. L.; Tolentino, J.; Zarghami, M. H.; Jorge Bustamante, J.; Law, M. Robust, Functional Nanocrystal Solids by Infilling with Atomic Layer Deposition. *Nano Lett.* **2011**, *11*, 5349–5355.

(19) Bobbert, P. A.; Sharma, A.; Mathijssen, S. Operational Stability of Organic Field-Effect Transistors - Bobbert - 2012 - Advanced Materials - Wiley Online Library. *Adv. Mater.* **2012**, *24*, 1146–1158.

(20) Sirringhaus, H. Reliability of Organic Field-Effect Transistors. *Advanced Materials* **2009**, *21*, 3859–3873.

(21) Chua, L.-L.; Zaumseil, J.; Chang, J.-F.; Ou, E. C. W.; Ho, P. K. H.; Sirringhaus, H.;

Friend, R. H. General Observation of N-Type Field-Effect Behaviour in Organic Semiconductors. *Nature* **2005**, *434*, 194–199.

(22) Yuan, Y.; Giri, G.; Ayzner, A. L.; Zoombelt, A. P.; Mannsfeld, S. C. B.; Chen, J.; Nordlund, D.; Toney, M. F.; Huang, J.; Bao, Z. Ultra-High Mobility Transparent Organic Thin Film Transistors Grown by an Off-Centre Spin-Coating Method. *Nature Communications* **2014**, *5*, 3005.

(23) Sharma, A.; Mathijssen, S. G. J.; Kemerink, M.; de Leeuw, D. M.; Bobbert, P. A. Proton Migration Mechanism for the Instability of Organic Field-Effect Transistors. *Appl. Phys. Lett.* **2009**, *95*, 253305.

(24) Lee, W. H.; Choi, H. H.; Kim, D. H.; Cho, K. 25th Anniversary Article: Microstructure Dependent Bias Stability of Organic Transistors. *Advanced Materials* **2014**, *26*, 1660–1680.

(25) Cho, S.-H.; Lee, Y.-U.; Lee, J.-S.; Jo, K.-M.; Kim, B. S.; Kong, H.-S.; Kwon, J.-Y.; Han, M.-K. Effect of Self-Assembled Monolayer (SAM) on the Oxide Semiconductor Thin Film Transistor. *Display Technology, Journal of* **2012**, *8*, 35–40.

(26) Minari, T.; Kano, M.; Miyadera, T.; Wang, S.-D.; Aoyagi, Y.; Seto, M.; Nemoto, T.; Isoda, S.; Tsukagoshi, K. Selective Organization of Solution-Processed Organic Field-Effect Transistors. *Appl. Phys. Lett.* **2008**, *92*, 173301–173304.

(27) Islam, M. M.; Pola, S.; Tao, Y.-T. Effect of Interfacial Structure on the Transistor Properties: Probing the Role of Surface Modification of Gate Dielectrics with Self-Assembled Monolayer Using Organic Single-Crystal Field-Effect

Transistors. *ACS Applied Materials and Interfaces* **2011**, *3*, 2136–2141.

(28) Zhang, X.-H.; Tiwari, S. P.; Kippelen, B. Pentacene Organic Field-Effect Transistors with Polymeric Dielectric Interfaces: Performance and Stability. *Organic Electronics* **2009**, *10*, 1133–1140.

(29) Coolidge, A. S. The Vapor Pressure and Heats of Fusion and Vaporization of Formic Acid. *J. Am. Chem. Soc.* **1930**, *52*, 1874–1887.

(30) Coolidge, A. S. The Vapor Density and Some Other Properties of Formic Acid. *J. Am. Chem. Soc.* **1928**, *50*, 2166–2178.

(31) Giauque, W. F.; Ruehrwein, R. A. The Entropy of Hydrogen Cyanide. Heat Capacity, Heat of Vaporization and Vapor Pressure. Hydrogen Bond Polymerization of the Gas in Chains of Indefinite Length. *J. Am. Chem. Soc.* **1939**, *61*, 2626–2633.

(32) Yaws, C. L. *Handbook of Vapor Pressure: Volume 4: Inorganic Compounts and Elements*; 1995; Vol. 4.

(33) Yaws, C. L. *The Yaws Handbook of Vapor Pressure*; 2015.

(34) Erwin, S. C. Doping PbSe Nanocrystals: Predictions Based on a Trapped-Dopant Model. *Phys. Rev. B* **2010**.

(35) Peng, H.; Song, J. H.; Kanatzidis, M. G.; Freeman, A. J. Electronic Structure and Transport Properties of Doped PbSe. *Phys. Rev. B* **2011**, *84*, 125207–112520.

(36) Agmon, N. Mechanism of Hydroxide Mobility. *Chemical Physics Letters* **2000**, *319*, 247–252.

(37) Agmon, N. Proton Solvation and Proton Mobility. *Israel Journal of Chemistry*

**1999**, *39*, 493–502.

(38) Simpson, J. H.; Carr, H. Y. Diffusion and Nuclear Spin Relaxation in Water. *Physical Review* **1958**, *111*, 1201–1202.

(39) Huth, A.; Schaar, B.; Oekermann, T. A “Proton Pump” Concept for the Investigation of Proton Transport and Anode Kinetics in Proton Exchange Membrane Fuel Cells. *Electrochimica Acta* **2009**, *54*, 2774–2780.

(40) Luo, Z.; Chang, Z.; Zhang, Y.; Liu, Z.; Li, J. Electro-Osmotic Drag Coefficient and Proton Conductivity in Nafion® Membrane for PEMFC. *International Journal of Hydrogen Energy* **2010**, *35*, 3120–3124.

(41) Kreuer, K. D. On the Development of Proton Conducting Polymer Membranes for Hydrogen and Methanol Fuel Cells. *Journal of Membrane Science* **2001**, *185*, 29–39.

(42) Agmon, N. The Grotthuss Mechanism. *Chemical Physics Letters* **1995**, *244*, 456–462.

(43) Cowin, J. P.; Tsekouras, A. A.; Iedema, M. J.; Wu, K.; Ellison, G. B. Immobility of Protons in Ice From 30 to 190|[Thinsp]|K. *Nature* **1999**, *398*, 405–407.

(44) Kofstad, P. *Nonstoichiometry, Diffusion, and Electrical Conductivity in Binary Metal Oxides*; 1972.

(45) Lee, B.; Wan, A.; Mastrogiovanni, D.; Anthony, J. E.; Garfunkel, E.; Podzorov, V. Origin of the Bias Stress Instability in Single-Crystal Organic Field-Effect Transistors. *Phys. Rev. B* **2010**, *82*, 085302.

(46) M D Groner; F H Fabreguette; J W Elam, A.; S M George. Low-Temperature

Al2O3 Atomic Layer Deposition. *Chem. Mater.* **2004**, *16*, 639–645.

(47) Ott, A. W.; Klaus, J. W.; Johnson, J. M.; George, S. M. Al3O3 Thin Film Growth on Si(100) Using Binary Reaction Sequence Chemistry. *Thin Solid Films* **1997**, *292*, 135–144.

(48) Dillon, A. C.; Ott, A. W.; Way, J. D.; George, S. M. Surface Chemistry of Al2O3 Deposition Using Al(CH3)3 and H2O in a Binary Reaction Sequence. *Surface Science* **1995**, *322*, 230–242.

(49) Snow, E. H.; Grove, A. S.; Deal, B. E.; Sah, C. T. Ion Transport Phenomena in Insulating Films. *J. Appl. Phys.* **1965**, *36*, 1664–11.

(50) Williams, C. K.; Hamaker, R. W.; Ganesan, S. G.; Kuehn, R. T.; Swartzel, K. R.; OSullivan, J. Low Temperature Diffusion of Alkali Earth Cationsin Thin, Vitreous SiO2 Films. *J. Electrochem. Soc.* **2015**, *142*, 303–311.

(51) Gulicovski, J. J.; Čerović, L. S.; Milonjić, S. K. Point of Zero Charge and Isoelectric Point of Alumina. *Materials and Manufacturing Processes* **2008**, *23*, 615–619.

(52) Piasecki, W.; Zarzycki, P.; Charmas, R. Adsorption of Alkali Metal Cations and Halide Anions on Metal Oxides: Prediction of Hofmeister Series Using 1-pK Triple Layer Model. *Adsorption-Journal of the International Adsorption Society* **2010**, *16*, 295–303.

(53) Gubbels-Elzas, A.; Thijsse, B. J. Ionic Motion During Field-Assisted Oxidation of Aluminium Studied by Molecular Dynamics Simulations. *Computational Materials Science* **2014**, *90*, 196–202.

(54) Hattori, S.; Kalia, R. K.; Nakano, A.; Nomura, K.-I.; Vashishta, P. Ion Dynamics at Porous Alumina Surfaces. *Appl. Phys. Lett.* **2012**, *101*, 063106–5.

(55) Venkateshvaran, D.; Nikolka, M.; Sadhanala, A.; Lemaur, V.; Zelazny, M.; Kepa, M.; Hurhangee, M.; Kronemeijer, A. J.; Pecunia, V.; Nasrallah, I.; *et al.* Approaching Disorder-Free Transport in High-Mobility Conjugated Polymers. *Nature* **2014**, *515*, 384–388.

(56) Puigdollers, J.; Marsal, A.; Cheylan, S.; Voz, C.; Alcubilla, R. Density-of-States in Pentacene From the Electrical Characteristics of Thin-Film Transistors. *Organic Electronics* **2010**, *11*, 1333–1337.

(57) Fortunato, G.; Meakin, D. B.; Migliorato, P.; Le Combers, P. G. Field-Effect Analysis for the Determination of Gap-State Density and Fermi-Level Temperature Dependence in Polycrystalline Silicon. *Philosophical Magazine B* **2006**, *57*, 573–586.

(58) Erslev, P. T.; Chen, H.-Y.; Gao, J.; Beard, M. C.; Frank, A. J.; van de Lagemaat, J.; Johnson, J. C.; Luther, J. M. Sharp Exponential Band Tails in Highly Disordered Lead Sulfide Quantum Dot Arrays. *Phys. Rev. B* **2012**, *86*, 155313.

(59) Fortunato, G.; Migliorato, P. Determination of Gap State Density in Polycrystalline Silicon by Field-Effect Conductance. *Appl. Phys. Lett.* **1986**, *49*, 1025–4.

(60) Lang, D. V.; Chi, X.; Siegrist, T.; Sergent, A. M.; Ramirez, A. P. Amorphouslike Density of Gap States in Single-Crystal Pentacene. *Physical Review Letters* **2004**, *93*, 086802.

(61) Roelofs, W. S. C.; Mathijssen, S. G. J.; Janssen, R. A. J.; de Leeuw, D. M.; Kemerink, M. Accurate Description of Charge Transport in Organic Field Effect Transistors Using an Experimentally Extracted Density of States. *Phys. Rev. B* **2012**, *85*, 085202–085206.

(62) Weidman, M. C.; Beck, M. E.; Hoffman, R. S.; Prins, F.; Tisdale, W. A. Monodisperse, Air-Stable PbS Nanocrystals viaPrecursor Stoichiometry Control. *ACS Nano* **2014**, *8*, 6363–6371.

(63) Guyot-Sionnest, P. Electrical Transport in Colloidal Quantum Dot Films. *J. Phys. Chem. Lett.* **2012**, *3*, 1169–1175.

(64) Rivnay, J.; Noriega, R.; Northrup, J. E.; Kline, R. J.; Toney, M. F.; Salleo, A. Structural Origin of Gap States in Semicrystalline Polymers and the Implications for Charge Transport. *Phys. Rev. B* **2011**, *83*, 121306.

(65) Powell, M. J.; Pritchard, J. The Effect of Surface States and Fixed Charge on the Field Effect Conductance of Amorphous Silicon. *J. Appl. Phys.* **1983**, *54*, 3244–3246.

# CHAPTER 6

# INFRARED TRANSMISSION SPECTROSCOPY OF QUANTUM DOT FIELD-EFFECT TRANSISTORS

## 6.1 Context

The use of colloidal quantum dot solids offer an interesting alternative to top down approaches for the realization of low cost solar cells with the potential for high power conversion efficiencies beyond the thermodynamic limit outlined by Shockley et al.[1] Traditionally, solar cells can only harvest a set amount of energy from the solar spectrum. The band gap of the semiconductor determines how much solar energy can be converted. In Shockley and Queisser's seminal paper, they determined the theoretical limit of a single junction solar cell is about 33% for a semiconductor with a band gap of 1.4 eV. Photons below the band gap that do not get absorbed do not generate electrical current, while photons with energy greater than the band gap are lost unnecessarily through the emission of phonons (thermalization). Due to quantum confinement effects, it is expected that that the coupling between carriers and phonons is reduced, thus slowing down the relaxation process. This slow cooling offers the opportunity to extract these "hot-carriers" instead of lost as heat. This phenomenon is called *multiple exciton generation (MEG)* and is akin to *impact ionization* for bulk semiconductors. MEG has recently been demonstrated with EQE peaking at 114%[2]. Unfortunately, the MEG solar cell only contributed to about 1 mA/ cm$^2$ at 3.2 eV and a champion device with a power conversion efficiency (PCE) of 4.4%. In order to improve the collection of multiple free charge carriers and hence improve device efficiency, understanding and eliminating the most damaging disorder that plague QD solids – surface electronic states – is required.

Currently, advancements in synthetic protocols[1-3] and processing[4-8] have led to improvements in quantum dot (QD) solar cell performance, each claiming to control stoichiometry, tune the Fermi level, and tune the surface state concentration. However, there is a lack in understanding of the role of surface states and how each of these different processing alter or eliminate these electronic defects. While there have been attempts and models[9-14] trying to explain the non-trivial trends in charge transport as a function of nanocrystal size, the origins of the trade-offs facing the optimization of nanocrystal-based optoelectronic devices is still lacking. Different explanations have been put forward as to why surface treatments improve performance. For example, reports propose that surface treatments passivate trap states which are expected to reduce conductivity and serve as recombination centers.[7,8,11] Recent reports, which have led to high performing QD solar cells, determine that the role of surface treatments is to align the energy levels of the semiconductor through surface dipoles on the surface of the QDs.[7,15-17] By changing the energy levels of the semiconductor with surface dipoles, changes in the Fermi level can also occur which can also lead to trap passivation if the Fermi level is more positive (negative) of the electron (hole) trap. While it is clear that surface treatments impact device performance, there is no consistent explanation on which physical process limits the performance and how trap states are involved.[9,12-14,18-20]

To rationally assess the impact of different fabrication techniques, it is necessary to develop new experimental platforms coupled with fundamental transport studies. Such platforms can be conveniently accessed with field-effect transistors. The ability to control carrier density and move the Fermi level of the QD film at the surface (near the semiconductor/dielectric interface) can provide direct insight into the charge transport, trapping, and recombination processes that can play an important role in understanding how to improve devices based on QD solids. Such understanding of the physical processes that determine field-effect mobility, threshold voltage, sub-threshold swing, etc. would enable us to assess the origins of performance limitations in these devices and develop guidelines for achieving higher performance.

Early studies of the role of trap states of QD based transistors presented photocurrent measurements in PbS QD FETs where they postulated the existence of a nearly full, metallic midgap band 0.4 eV below the conduction band for a 1.3 eV band gap. They argue that conduction in the dark is related to low mobility carriers moving in the metallic mid gap band, while high mobility carriers in the conduction or valence band mediate photoconduction. With evidence provided from spectrally resolved photocurrent, the authors imply a delocalized band-like transport mediated by a large density of trap states. This concept was extended with a recent report illustrating charge percolation pathways through an in-gap state.[14] The authors argue that electrons hop to empty gap states (unlike the previous report above) resulting in higher electron mobility because of a partially delocalized mid gap band. The data was supported by scanning tunneling spectroscopy (STS) and kelvin probe force microscopy (KPFM) claiming that transport is conducted through oxygen related species for films treated with ethanedithiol (EDT). Without varying the temperature and relying on STS and KPFM data, the mechanism of transport can only be inferred. It cannot distinguish nor resolve trap states from quantum-confined states.

In this chapter, we carry out a systematic investigation of charge orbital occupation of PbSe QD FETs using infrared transmission spectroscopy. Using a field-effect transistor geometry, we can measure optical transitions under the influence of an applied electric field to uniquely identify charge occupation in QD thin films.

## 6.2 Design of transmission field-effect transistors based on quantum dot solids

We fabricated large-area PbSe QD FETs on silicon substrates specifically designed for infrared transmission spectroscopy. Conventional FETs typically utilize degenerately doped silicon as a combined substrate and gate electrode, but such substrates are opaque in the infrared region due to strong free carrier absorption. To fabricate infrared-transparent FETs, we used boron ion implantation to generate a thin (1 μm), heavily doped ($p^{++}$) gate electrode on the surface of an intrinsic, double-sided polished float zone silicon wafer (ρ ~ 8,000-10,000 ohm-cm), followed by plasma-enhanced chemical vapor deposition of 200 nm $SiO_2$ to serve as the gate oxide. Large-area (~0.8 $cm^2$) interdigitated electrode sets with narrow finger electrodes (5 μm width; 5 nm Ti, 35 nm Au) were photolithographically patterned onto the oxide. The resulting substrates are highly transparent to excitation in the range of 0.02-1.2 eV. The large-area electrodes provide for an active area convenient and necessary for transmission spectroscopy. PbSe QD films are then deposited on these substrates by dip coating with ethanedithiol (EDT) ligands. The films were then coated with ~20 nm of amorphous alumina by atomic layer deposition

(ALD) to yield environmentally stable devices suitable for long-term infrared transmission measurements. (Fig 6.1a).

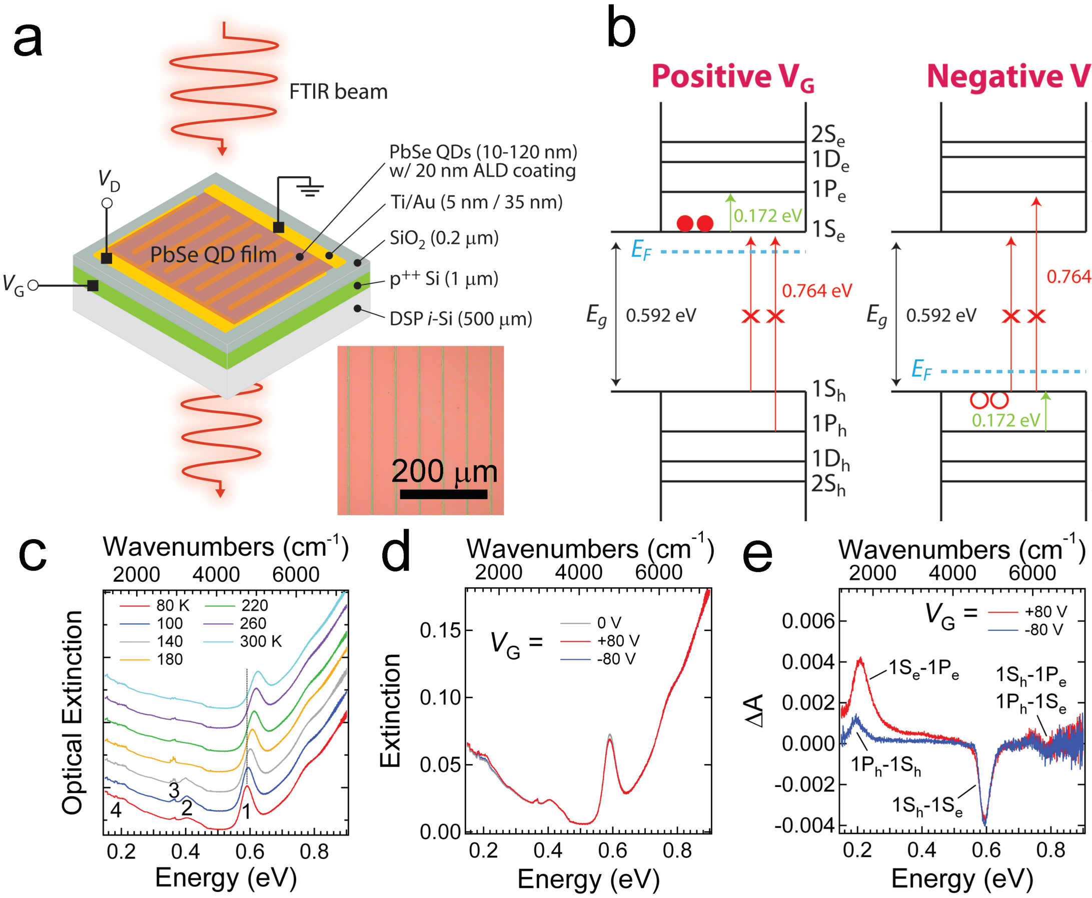

**Figure 6.1 Large-area PbSe QD FETs for transmission electroabsorption spectroscopy.** (a) Device architecture and experimental design (b) Single-particle energy level diagrams for 6.2 nm diameter, EDT-capped PbSe QDs, illustrating spectral bleaches (red transitions) and induced absorptions (green transitions) expected for a positive $V_G$ (electron accumulation) and negative $V_G$ (hole accumulation). (c) Raw extinction spectra for a 6.2 nm PbSe EDT-treated, ALD overcoated as a function of temperature from 80-300 K under equilibrium condition (zero applied biases). Feature **1** is the first exciton transition, which blueshifts, broadens, and weakens with increasing temperature. Feature

**2** (3100-3600 cm$^{-1}$) is assigned to adsorbed water and ice formation on the sample at low temperatures. Features **3** (2850-2980 cm$^{-1}$) and **4** (1200-1700 cm$^{-1}$) represent the C-H stretch and fingerprint absorption regions of EDT and organic molecules adsorbed on the surfaces in the beam path. (d) Raw extinction spectra of a device at $V_G$ = 0, +80, and -80 V. $V_{SD}$ = 0V. T = 80 K. (e) Difference spectra calculated from the raw data in (d). Positive changes (induced absorption) and negative changes (bleaches) are assigned using energy level diagrams in (b).

To date, the study of delocalized charges in QDs has been limited only to electrochemical methods. In a few reports studying PbSe and CdSe QDs, successful injection of electrons and holes into quantum confined states were observed in a reflection measurement implementing an electrochemical cell.[21-24] However, conducting ions such as $LiClO_4$ or strong reducing agents like sodium biphenyl were used and mixed in an anhydrous alkane solution of the QDs. While spectroscopic observation of these solutions or working electrodes utilizing QDs demonstrated all the features associated with the presence of electrons or holes in the QDs, one cannot rule out effects such as surface reactions that may occur when using strongly reducing agents, electrochemical stability which can lead to loss of injected carriers due to surface redox reactions, and the role of the diffusion of redox species when the measurement is done at low temperatures (T < 200K). By modulating the QD electrode in these experiments, more than 1 carrier/dot is observed and complete bleaching of the first exciton transition is observed.[21,22] Despite these observations, this experiment has its disadvantages: (i) limited to low temperatures due to electrochemical instability of the injected carriers (ii) required the use of conductive ions to inject carriers uniformly throughout electrode. To overcome these limitations, we use field-effect transistor geometries to inject carriers in coupled QD films.

Upon injection of charge carriers using the applied gate bias, the optical properties of the QD film changes remarkably. Fig 6.d illustrates the raw extinction spectra of 6.2 nm PbSe QDs EDT-treated and $Al_2O_3$ overcoated under zero applied potential and after a positive or negative gate bias of ± 80 V. Taking the difference between equilibrium and non-equilibrium conditions, fig 6.e illustrates a negative change (bleach) and a positive change in absorbance (induced absorption). Under positive gate bias, electrons accumulate at the QD/gate oxide interface, which leads to a bleach in the first exciton transition at 80 K (0.59 eV) and an induced absorption at 0.23 eV. Under negative gate bias, holes accumulate at the QD/gate oxide interface, leading to similar bleach at 0.59 eV and an induced absorption at 0.21 eV. The slight differences in the intraband (1S-1P) transition energy under electron and hole injection is assigned to anisotropic differences in the electron and hole *P* states splitting into $P_t$ and $P_l$ and the fact that the second transition is of the $P_{||}$- $P_{||}$ type despite the widely accepted similar effective masses of electrons and holes for PbSe calculated using effective mass theory; in other words, transitions occur between states of the same symmetry but with opposite parity.[25] A third feature is also observed upon electron and hole accumulation at ~0.76 eV consistent with the bleach of the second exciton transition.

## 6.3 Control experiments to determine origin of changes in absorption

In order to understand the origin of the changes in absorption demonstrated in the difference spectra in fig 6.1e, we designed several experiments by changing the electrode configurations. Figure 6.2 below summarizes the results of these control experiments.

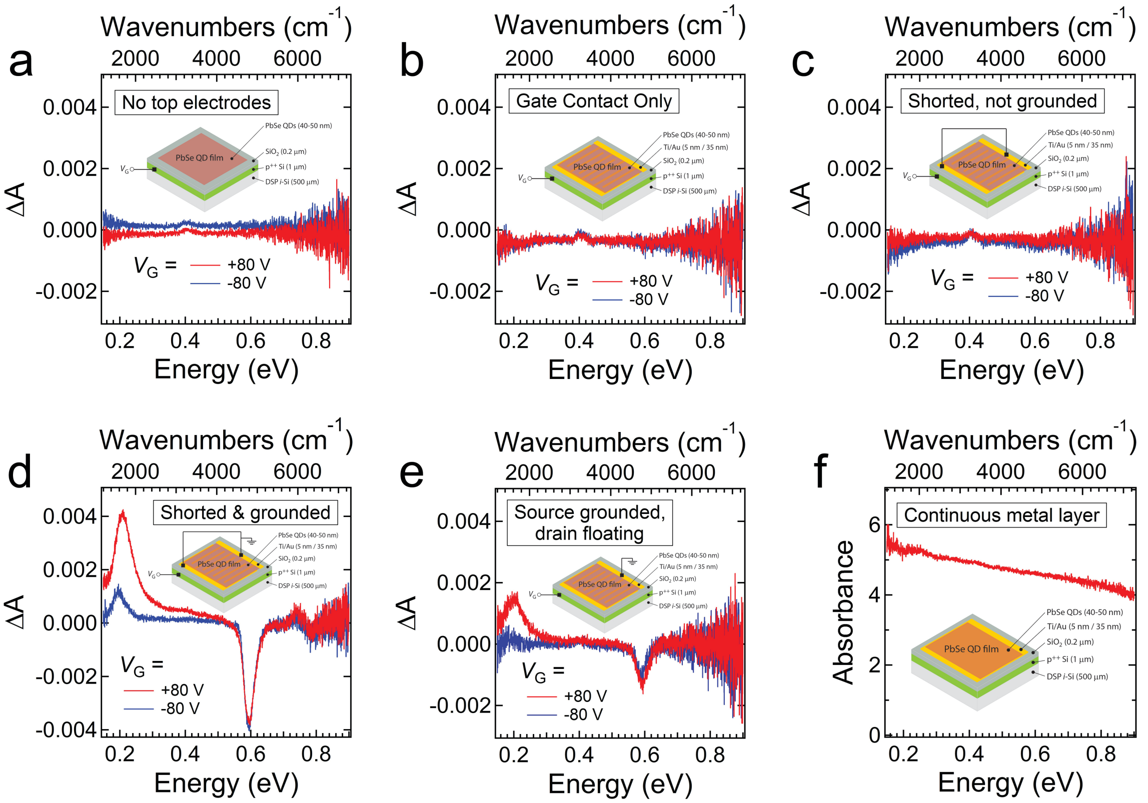

**Figure 6.2. Results of control experiments designed to determine the origin of injected carriers. Difference spectra obtained at 80 K for several electrode configurations.** (a) device with no source/drain electrodes (b) source and drain electrodes are floating (not wired) (c) source and drain electrodes are shorted together but floating (d) source and drain electrodes are shorted together and grounded in the circuit (e) source is floating

and drain is grounded (f) Extinction spectrum of a sample with a continuous metal film (5 nm Cr/35 nm Au) in place of interdigitated electrode set

All difference spectra were acquired at 80 K and under the same biasing conditions of $V_G = \pm 80$ V, $V_{SD} = 0$ V. The difference spectra for a device configuration with no metal electrodes and PbSe QDs on the gate dielectric, fig 6.2a shows that carriers are not injected into the device upon biasing the gate. By changing the measurement circuit and keeping the source and drain electrodes at open circuit, the injected carriers are once again not detected in the film when the device is biases with a gate voltage (see Fig 6.2b). When the device is shorted, but not grounded to the gate electrode, no carriers are injected into the film (see Fig 6.2c). Finally, when the source and drain electrodes are shorted, but grounded to the gate electrode to complete the circuit, carriers are injected into the device upon biasing the gate. Based on this control, we can infer that a properly grounded, complete measurement circuit is needed to inject carriers. If instead of completing the circuit by shorting the source and drain electrodes, but held one electrode floating, the amplitude of the bleach and induced absorption are smaller (fig 6.2e). The reduced amplitude of about a factor of two can be explained because with one electrode grounded (floating ground), the source and drain electrodes are not at the same potential. With one electrode floating and not grounded, the voltage that is applied is not referenced to ground and has no reference, thus there is no sink for the injected carriers to complete the circuit. For one electrode that is grounded, there is a proper sink for the injected carriers, but it does not prove the source of the injected carriers. As a final control experiment, a continuous metal film was used in place of the interdigitated electrodes. On top of this metal layer, QDs were deposited. In fig 6.2f, it is clear that the sample remains completely opaque indicating that the injected carriers are from the QDs in the channel and do not come originate from the QDs located on top of the metal electrodes.

## 6.4 Magnitude in the changes in absorption dependence on the number of injected carriers

Through the control experiments for different device architectures, we prove that the changes in absorption are clearly from the QDs that act as the FET conducting channel. For a properly completed measurement circuit, we can control the amount of carriers that are injected in the channel with the gate voltage as well as the source-drain voltage. To make the interpretations easier, all measurements were done at 80 K to remove the effects of current transients. At a constant gate voltage of $V_G$ = + 80 V, increasing the source-drain bias $V_{SD}$ results in an increasingly pronounced derivative line shape for the $1S_h - 1S_e$ bleach in the difference plots (Fig 6.3b). The initial hypothesis for the first-derivative line shape was the Stark effect, which is the spectral splitting of molecules and atoms due to the presence of an electric field. For large molecules on the order of a single QD, we can estimate the potential drop and thus the electric field in a single QD. Accounting for the randomly packed arrangement of QDs on the gate oxide surface, the potential drop across a single QD < 0.5 V. Based on this estimate, we can rule out the Stark effect which results in a blue-shift and decrease in intensity, because typical electric field values that demonstrate the Stark effect is on the order of $10^5$ V $cm^{-1}$.

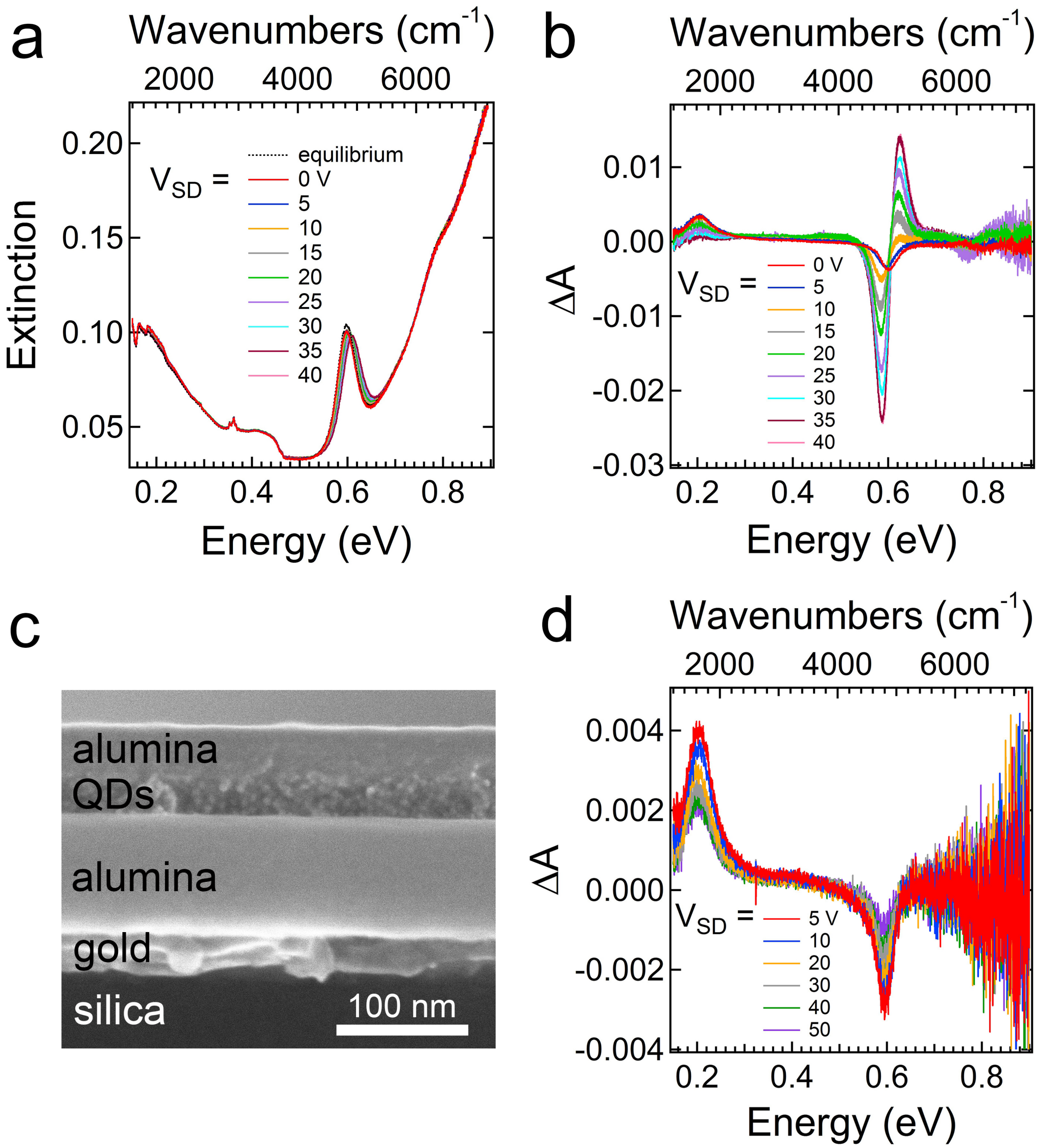

**Figure 6.3 Source-drain dependence and joule heating effects.** (a) Raw extinction spectra and (b) difference spectra as a function of $V_{SD}$. (c) Cross-sectional SEM image of a different FET fabricated on interdigitated electrodes coated with 93 nm of ALD alumina in order to reduce $I_{SD}$ to a negligible value (< 1 nA). (d) Difference spectra as a function of $V_{SD}$ for the insulating FET, showing a normal bleach line shape.

As another hypothesis, we considered joule-heating effects. From the *I-V* characteristics for the same FET device measured for transmission changes, we can estimate the expected peak shifts in the first energy transition of the QD film at 80 K. Assuming uniform heating and no other heat losses through the film such that all the current is converted to heat, we can calculate the energy $Q = I^2R$; the resistance in this equation is extracted from the *I-V* characteristics measured at 80 K. From the calculated heat energy, $Q$, we can estimate the temperature change due to joule-heating from the expression

$$h = \frac{Q}{A\Delta T} \tag{6.1}$$

$h$ is the heat transfer coefficient (250 W $m^{2}$ $K^{-1}$ for bulk PbSe); $A$ is the surface area of the QD film

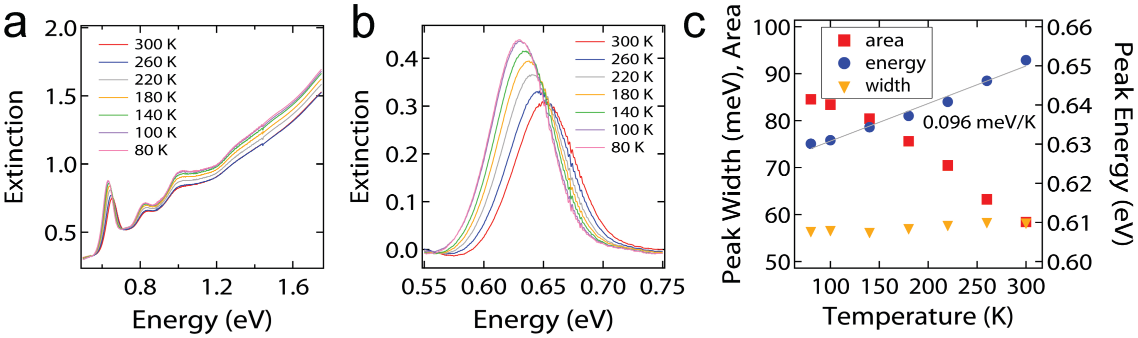

**Figure 6.4 Variable-temperature optical extinction spectra of films of 6.2 nm OA-capped PbSe QDs** (a) Extinction spectra of a film as a function of temperature from 80 – 300K. (b) Comparison of the first exciton transition versus temperature. Spectra were baseline corrected to determine peak width, area, and position (c) Plots of the first

exciton peak energy, width, and area versus temperature. The fit shows a positive band gap temperature coefficient of 0.096 meV/K

Using the temperature dependent band gap relationship for the same film of 0.096 meV/K (fig 6.4), we can estimate the peak energy position from the calculated temperature difference due to joule heating. The measured and calculated peak position as a function of $I_{SD}$ is illustrated in fig 6.5a and 6.5b, respectively. The close correspondence to the trend and behavior of the peak position as a function of source-drain current confirms the joule heating hypothesis and rules of the Stark effect.

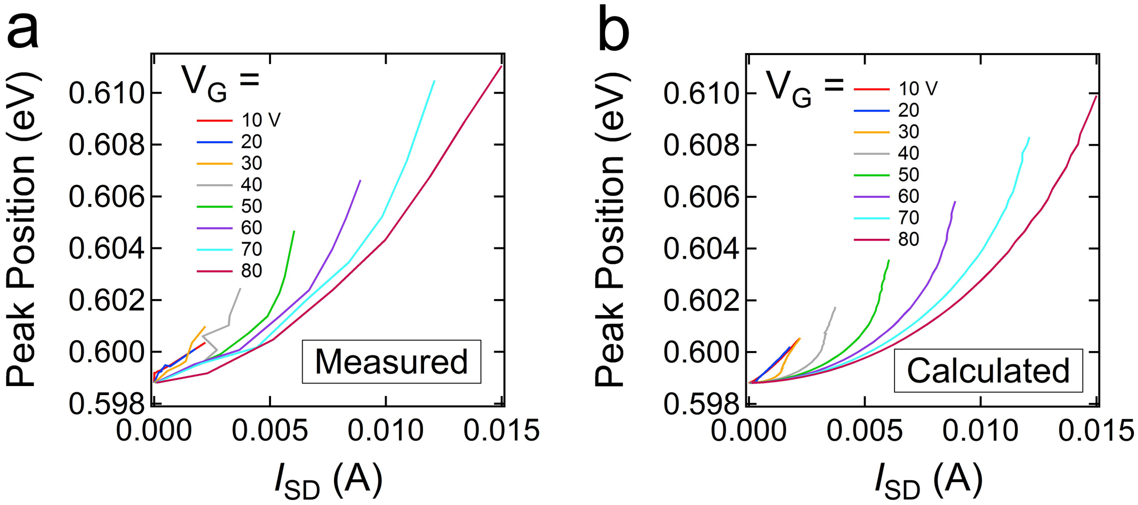

**Figure 6.5 Evaluating the joule-heating hypothesis** (a) Measured and (b) calculated peak position on source-drain current ($I_{SD}$) for several gate voltages

Furthermore, to illustrate the joule-heating effect as the dominant mechanism for the peak shift, we deposited 93 nm of ALD alumina on top of the interdigitated electrodes. Following the alumina deposition, 32 nm of PbSe QDs, infilled and overcoated with ALD alumina was deposited on top of the alumina (fig 6.3c). To confirm the insulating nature of the alumina coated metal electrodes, *I-V* characteristics were measured at 80 K to ensure negligibly low current values (fig 6.6c). For the same device, the difference spectra were measured and no derivative-line shape was observed (fig 6.3d) in contrast to devices with normal Ti/Au contacts (fig 6.3b). With increasing electric field (source-drain bias), the intensities actually decrease. We explain this by looking at the time dependence of the difference spectra after stepping the gate voltage from $V_G$ = + 80 V to 0 V and comparing it to devices with normal Ti/Au contacts. For conductive devices, the injected charges are mobile enough to escape very quickly, probably in a small fraction of a second (fig 6.6a). However, injected charges slowly leak from the insulating device over a period of 10-15 seconds (fig 6.6b). This suggests that due to the imperfect ALD coating, there is a slow charge migration into the semi-isolated channel resulting in a slower decay of charges. Furthermore, when the semi-isolated channel is biased with increasing source-drain magnitude, there are fewer carriers in the channel.

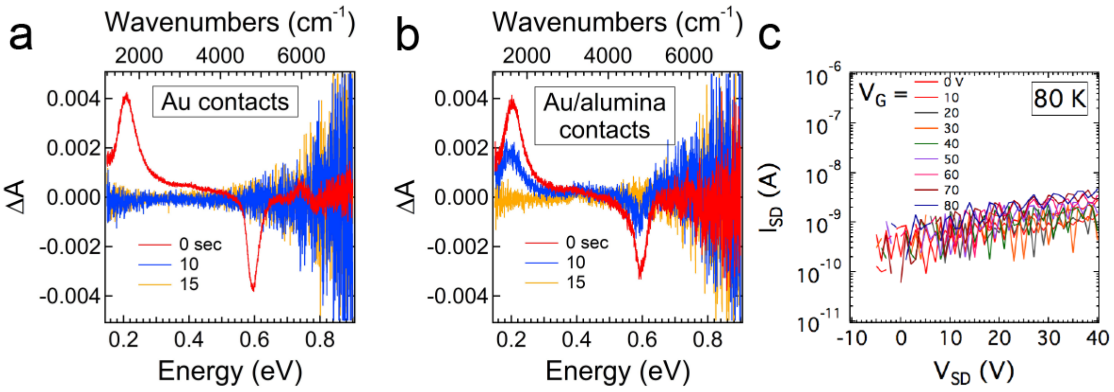

**Figure 6.6 Difference spectra as a function of time** (a) FET device with normal Ti/Au contacts (b) Ti/Au contacts coated with 93 nm ALD alumina (c) Output characteristics of 5 nm Ti / 35 nm Au / 93 nm $Al_2O_3$ ALD

### 6.5 Thickness dependent transmission spectra

Having demonstrated that the origin of the changes in absorption spectra was due to the QDs in the FET channel, the next set of experiments sought out to determine what percentage of the film is being affected with the applied gate bias. As previously discussed in chapter 4, classical semiconductor theory predicts that the induced charge in a FET channel can be considered to be a sheet of charge that accumulates at the semiconductor/insulator interface. Assuming no effects due to surface electronic states and Fermi level pinning, the penetration of the electric field due to the applied gate bias extends no more than 10-15 nm of the film (~1-2 QD layers). If this were true, the magnitude in the changes in absorption as a function of gate bias should not change for varying film thicknesses.

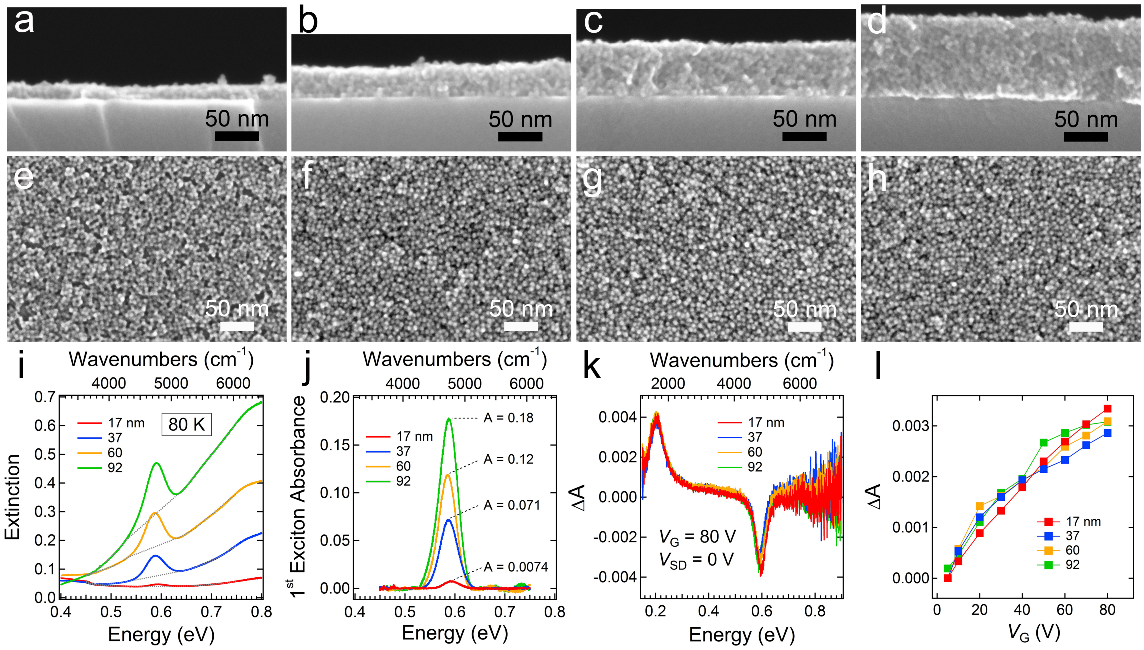

**Figure 6.7 Thickness dependent electrical state filling.** (a-d) Top down and (e-h) cross-section scanning electron microscope (SEM) images of 6.2 nm, EDT-treated, alumina infilled PbSe QDs for film for film thickness of 17, 37, 60, and 92 nm (i) Raw extinction spectra for different film thickness measured at 80 K (j) Normalized extinction spectra showing a quasi-linear dependent absorption as a function of thickness (k) Difference spectra for 17 nm, 37 nm, 60 nm, and 92 nm thick 6.2 nm QD films, showing a thickness-independent ΔA. Biasing conditions were $V_{SD}$ = 0 V and $V_G$ = +80 V. Temperature = 80 K. (l) First exciton bleach (ΔA) versus $V_G$ showing a thickness-independent changes for all applied biases.

To ensure proper comparisons, similar film density and morphology was needed across all film thicknesses As seen from the top down SEM images in fig 6.7e-h, a randomly packed film is observed, as previously seen in other reports from our group.[26,27] For different film thicknesses, the absolute absorption increases quasi-linearly perhaps due to non-uniformity in thinner films (<20 nm). SEM images for 17 nm shows 90% dense, but continuous film morphology compared to thicker films. To exclude current transient effects at temperatures higher than 180 K, all data were acquired at 80 K. For applied biases of $V_G$ = +80 V, the difference spectra for all film thicknesses show similar magnitude changes in the first exciton bleach and induced absorption. Furthermore, fitting the first exciton bleach ($\Delta A$) for different gate voltages, demonstrates a bleach thickness-independence confirming that all changes in the extinction spectra under applied bias is attributed to the first few QD layers. This is first experimental evidence demonstrating that the charge density in thin-film transistors based on QDs is truly two-dimensional.

## 6.6 Transmission spectra for varying mixtures of QD sizes – effects of disorder

Having established this platform, experiments were then performed to test fundamental charge transport properties. Based on fig 6.1, we demonstrated for the first time that carriers do indeed access quantized states of the QDs. Under this assumption, any site energy disorder such as size heterogeneity would produce a tortuous energetic landscape because of the variation in energy levels due to differences in size and coupling. In previous reports, it has been shown that due to lower-energy sub-assemblies of QDs due to size heterogeneity, the site energy disorder enhances auger recombination[28] and incoherent exciton diffusion.[29-31] This efficient auger recombination is a concern for devices that work at charge carrier densities in excess of ~$10^{-3}$ charge carriers per QD such as QD LEDs or QD solar cells under concentrated sunlight.

It is well known that energetic disorder due to variations in coupling and dot size can reduce the mobility of charge carriers, particularly in QD solids.[32] The effect of energy disorder on the charge carrier mobility in a Gaussian density of states has been studied in length for a variety of disordered materials, similar to QDs.[33-35] This energy disorder causes charge carriers to diffuse to lower energy sites and slow down carrier diffusion.

### 6.6.1 Percolation approach to hopping in disordered semiconductors

In order to understand this, we will briefly discuss the principle of percolation and how it relates to charge transport in disordered semiconductors and how it can be extended to describe physical mechanisms of transport within quantum dot solids. Due to the inherent energetic and spatial disorder found in quantum dots, charge transport is described as incoherent hoping of carriers via randomly distributed localized states. The rate for a carrier to hop from an occupied site *i* to an empty site *j*, separated by the distance $r_{ij}$ is assumed to be described by the popular Miller-Abrahams expression:[36]

$$v_{ij} = v_0 \exp\left(-\frac{2r_{ij}}{\alpha} - \frac{\epsilon_j - \epsilon_i + |\epsilon_i - \epsilon_j|}{2kT}\right) \tag{6.2}$$

α is the localization length of charge carriers in the localized states usually on the order of $10^{-8}$ cm, $\varepsilon_i$, $\varepsilon_j$, are the carrier energies on sites *i* and *j*, respectively, *k* is the Boltzmann constant, and *T* is the temperature. Upon immediate inspection on the equation, the energy difference between states *i* and *j* should be compensated by absorption or emission of phonons but is ignored. The prefactor $v_0$ is the attempt-to-escape frequency, which usually depends on interactions. Equation 6.2 above is valid only in the case if the starting site *i* is occupied by the carrier and the final states *j* is empty. In most cases, especially in when we discuss mobility and conductivity measured in field-effect transistors, the transition rate for a pair of sites *i*, *j* should also depend on the position of the Fermi level $\varepsilon_F$ :

$$v_{ij} = v_0 \exp\left(-\frac{2r_{ij}}{\alpha} - \frac{\epsilon_j - \epsilon \ + |\epsilon_i - \epsilon_F| + |\epsilon_j - \epsilon_F|}{2kT}\right) \tag{6.3}$$

As such, if both sites *i* and *j* have energies far above the Fermi level, these sites are mostly unoccupied hence no charge carrier on these pair of sites will provide transport, regardless of how close in space and in energy they may be. Conversely, if both energies are far below the Fermi level, both sites are mostly occupied and thus there would be no site to hop into. Hence, the contribution of any pair of sites depends on the carrier concentration dictated by the Fermi level. Also, note that in this equation, we do not account for the density of states, so it could be high at certain energies such that the distance to a site in that energy range would be small enough to favor it over sites at other energies. As such, it is assumed the density of states is uniform and hoping is around the Fermi level ($|\varepsilon_j - E_F|$; $|\varepsilon_i - E_F|$; $||\varepsilon_j - \varepsilon_i| > kT$).

The essence of this expression and approach to charge transport in disordered semiconductors is that hopping transport is determined by the rate of these hops that is the most difficult but still relevant for long range transport. In fact, hopping is a percolation process in which the slowest transitions still need to provide a connected path through the system. The easiest analogy is assume we have a grid paper and a pen

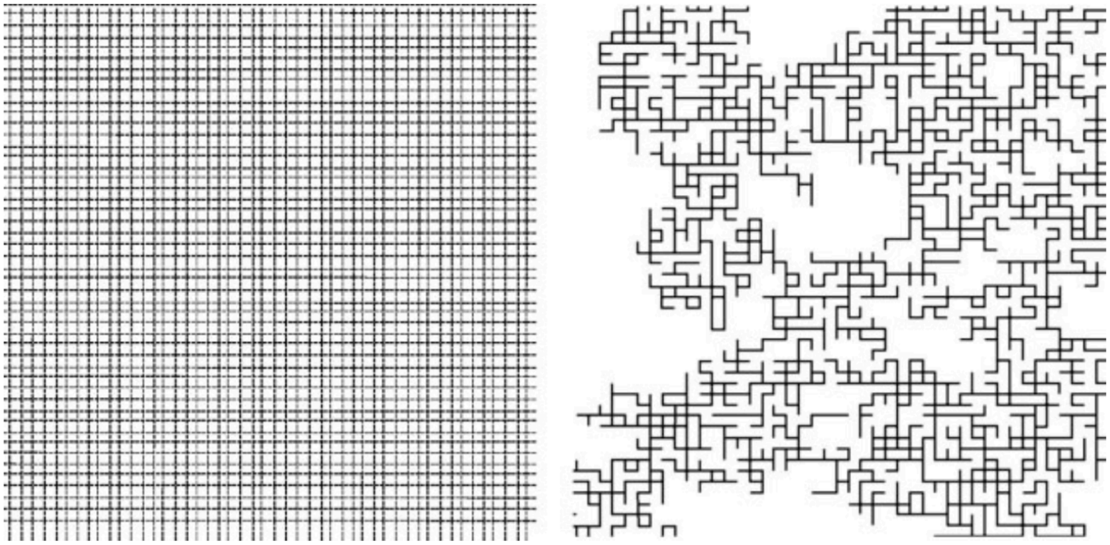

**Figure 6.8 Definition of conductance in a random resistor network** (left) square grid (right) example of bond percolation made by marking only one side of small square at a time

Now let us pick a random square (left most figure) and randomly mark one of its sides. At first there would be disconnected lines (called bonds) and eventually we would start to see a network of lines starting to form. At some critical point, we would identify clusters of lines that can be marked that form a continuous path going from the top to the bottom of the page. In percolation theory, this phenomenon is said to have connectivity and the percolation threshold has been reached. The extension of this percolation theory to conductivity problems for a random resistor network has been applied for different types of structures such as randomly close packed mixtures of hard spheres. [37,38] Universal to all percolation problems is the idea of connectivity.

The first stage in casting the hopping problem onto a percolation problem is typically done by going from a hopping system to a resistor network by turning the hopping rates into equivalent resistors.[39-41] Following the authors formalism, the current between two sites *i* and *j* is approximated as

$$I_{ij} \approx G_{ij}(E_{Fj} - E_{Fi}) \tag{6.4}$$

where

$$G_{ij} \approx \frac{qv_0}{kT} \exp\left(-2\alpha R_{ij}\right) \exp\left(-\frac{\epsilon_j - \epsilon_i + |\epsilon_i - \epsilon_F| + |\epsilon_j - \epsilon_F|}{2kT}\right) \tag{6.5}$$

This conductance $G_{ij}$ is essentially the hopping rate expressed in the Miller-Abrahams equation (6.3). In order to compute the conductivity of the system, we can use percolation theory to find a critical conductance $G_C$ that governs the conductivity of the system. The motivation here is that the conductance path that is the path with least resistance will be taken. Moreover, to go from one side to another, we only need conductance paths of values equal or larger than this critical conductance. This is only valid if the system is said to be *dilute* meaning the spread of resistance values is large and that the critical conductance is significant different.

If we now consider a resistor network and arrange it based on their conductivity or resistivity and add them to a network starting from highest value, there will be a critical point where a continuous path is formed across the sample. This is the classical critical-path problem. Extending this a little bit further, in equation 6.5, the critical conductance will be met when either the distance $R_{ij}$ is maximized or $\varepsilon_{ij}$ is maximized.

This system is considered to be non-correlated where the critical conductance does not depend on both distance (spatial disorder) and energy (energetic disorder).

Values for critical probability in this classical percolation problem depends on various factors packing density[42] and geometry.[37,42]. Depending on the packing fraction and hence the number of nearest neighbors, the critical percolation probability can range from 20% for a diamond cubic structure to 50% for a face-centered cubic lattice.[37].

### 6.6.2 Percolation pathways in PbSe QD films

In light of this theory, we wanted to use our newly developed platform to look at energetic disorder effects on state filling and mobility. In a previously published paper within the group, the authors postulated that since quantum dots are characterized by some size-dependent energy levels due to a distribution in sizes and coupling, charge transport *should* be inhibited if the energetic disorder defined as $\Delta\alpha \geq kT$. In this paper, they estimated the values as the width in energy of the first exciton peak attributing the disorder only due to size distributions. One has to consider that there are other forms of energetic disorder that dictates transport within these highly disordered quantum dot films such as states below the gap. Moreover, correlations between energetic and spatial disorder can also complicate this picture of hopping using percolation theory as a unified theory.[39,43,44]

To test the role of energetic disorder to variations in dot size, we control the number percentage of 6.2 nm QDs in a matrix of 5.7 nm QDs unlike the previous publication in the group, which was based on mass. To accurately calculate the number of

6.2 nm PbSe QDs for a given volume and concentration, we have to make the few simple assumptions. First, an accurate determination of the two sizes for the QDs was required. From the size of the QD, we can estimate the surface area and the volume of the QD to determine the mass of the PbSe dot knowing the density. Using the surface area, we can calculate the number of surface atoms and number of lead surface atoms (assuming Pb-rich surfaces) per QD. Assuming 50% coverage of oleic acid on the QDs, we can determine the number of surface lead atoms *with* oleate on the surface. We can then calculate the mass of oleic acid on a QD in grams and the total mass of the QD. Finally, knowing the percent of QD mass that is OA and total mass of the QD, we can calculate the number of QDs in 1 gram.

To quantify the amount added in solutions used to fabricate QD thin films, we use small angle x-ray scattering (SAXS). Using a software package (NANO solver), the scattering intensity is converted to a volume distribution function using a Fourier transform technique. Initial parameters for the fit include density, initial guesses for mixture percentages and particle size.

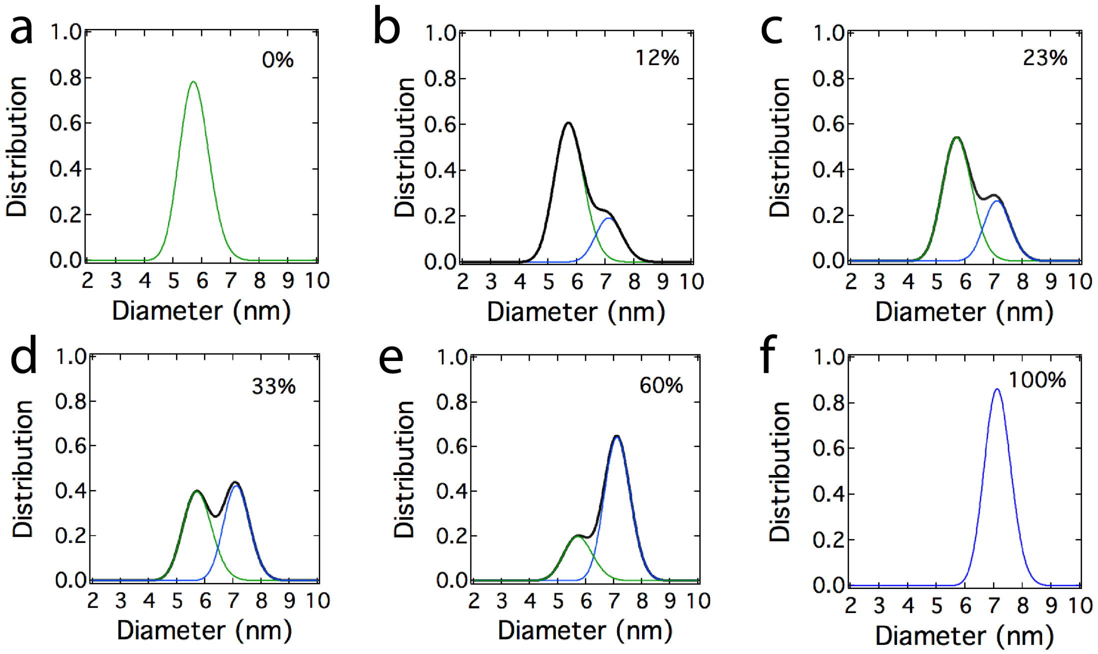

**Figure 6.9 Small angle x-ray scattering volume distributions of mixed solutions used to make QD films for FETs.** From the volume distribution, the number percentage of large 6.4 nm dots in a matrix of small 5.4 nm dots. The annotation in each subfigure is the measured number percentage calculated using the fitted peaks. The intended number percentage is as follows (a) 0% (b) 10% (c) 20% (d) 30% (e) 50% (f) 100%. Green fits : small dots (5.4 nm). Blue fits: large dots (6.5 nm)

In figure 6.9, using SAXS, the particle size for the parents solutions before mixing were measured to be 5.6 nm and 7.1 nm. TEM size analysis of the same dots measures 5.4 nm and 6.5 nm. Given the close correspondence in measured particle size, we continue further using SAXS to measure the distribution of large dots in a matrix of small dots. Based on the intended number percentage of large dots, we find that SAXS quantitatively matches the expected value to about ± 10%.

Having established the number percentages, we can then use the large-area absorption FET platform to look at the role of order on the statistics of state filling.

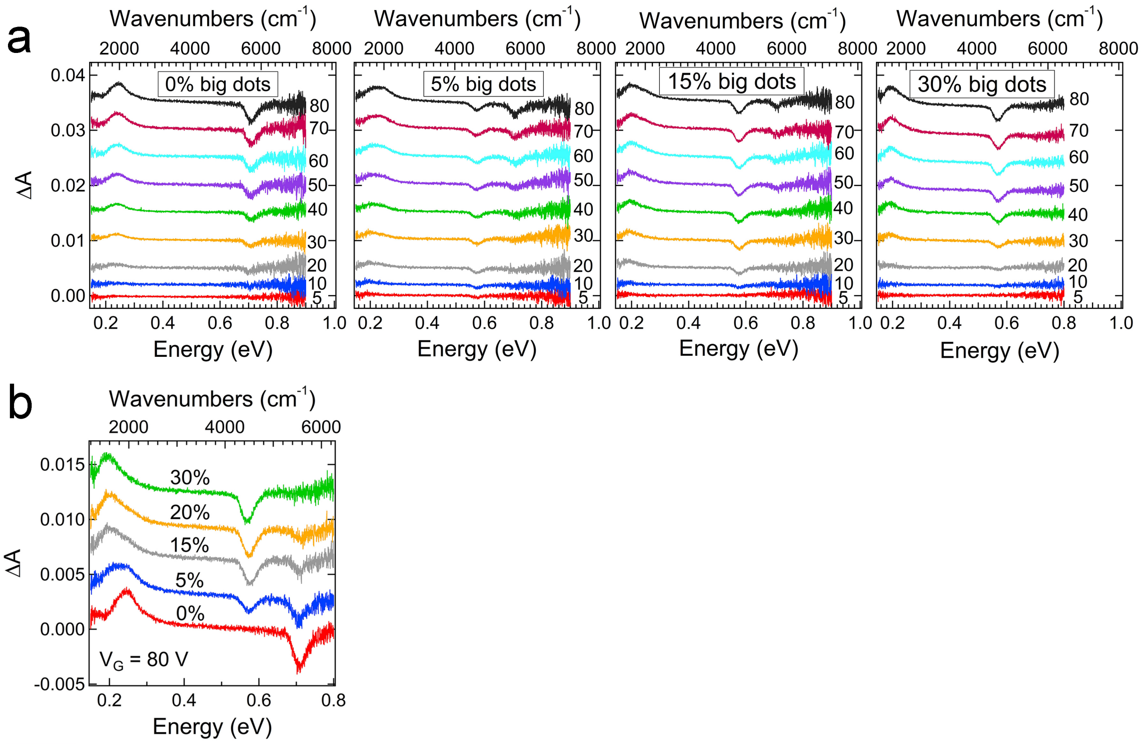

**Figure 6.10 State filling in mixed QD films.** Difference spectra as a function of gate voltage for PbSe QDs EDT-treated and alumina infilled from solution of 5.6 nm QDs containing 0%, 5%, 15%, and 30% 6.5 nm QDs by number. (b) Comparison of mixed films loaded at $V_G = 80$ V.

In order to remove artifacts from the transients, all measurements were done at 80 K. It is clear in figure 6.10 that the injected electrons first fill the large QDs and occupies only the large QDS for loadings greater than 25-30%. We note that this data was taken under no applied electric field (i.e. $V_{SD} = 0$ V), which implies that on average, statistically the injected carriers still diffuse and redistribute themselves preferably on larger dots. To connect percolation theory to this experiment, we assumed that the energetic disorder in these mixed films is large enough that charge carriers would energetically prefer carriers lower in energy (“localized” states). Similar to the classical percolation problem, initially we have a small cluster of large dots that is randomly distributed throughout the film. This cluster is small enough and is below the critical probability that a percolation pathway made up of only larger dots is possible. As we continue to load the film with more large dots up to 30%, we find that the injected electrons only occupy the large dots. This critical threshold is comparable to those values quotes for a randomly packed hard spheres with six nearest neighbors.[37]

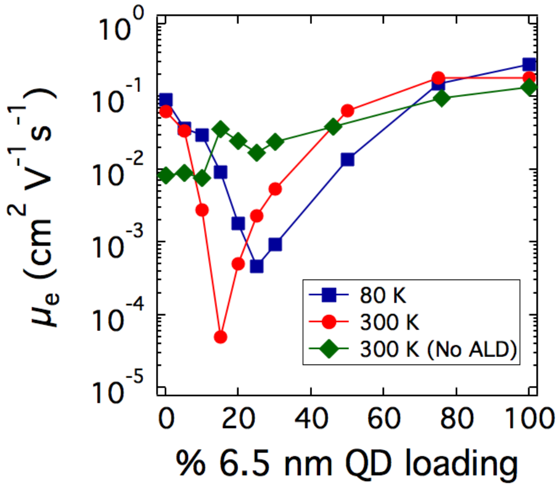

**Figure 6.11 Mobility for mixed QD films.** Films without ALD do not show the expected percolation data. See later discussion in text.

We also postulated that if a percolation network of large dots do exist and that these large dots act as *localized states*, then carriers falling into these *dead ends* would result in lower current and hence lower mobility because based on the formalism for hopping based on percolation theory, current is extracted based on states that are able to hop to available empty sites around the Fermi level. As we can see in figure 6.11 above, as we continue to increase the number loading of large dots, the mobility continues to drop orders of magnitude, consistent with this percolation pathway. Eventually, there is a demarcation and the mobility starts to increase again at an about 15% at 80K and 25% at 300K. The shift in the critical point can easily be understand if we look at equation 6.3. At lower temperatures, for a hopping conduction mechanism in disordered semiconductors, the probability for a carrier to hop to a distance $r_{ij}$ that is farther will occur because it is energetically more favorable. For a randomly packed film of mixed dots this more favorable dot has to be resonant in energy and could possibly be the next nearest neighbor dot. As such, the threshold shifts because amount of next nearest neighbors may not be large enough for a critical pathway to form. On the contrary, at higher temperatures, the probability for hopping is not limited to the next nearest neighbor, which can shift the critical threshold to smaller values because it is easier to find a carrier (or site) and is lower an energy. This phenomenon is described as *variable-range hopping* which was derived in the context of percolation theory. We also note that this behavior is slightly different from the classical theory of percolation with respect to conductivity. In this classical theory, it assumes zero probability for $p < p_C$, therefore one should expect zero conductivity, and "*zero*" mobility. In figure 6.11, we have a finite probability of hopping as it is related to equation 6.3 for $p < p_c$.

In the discussion above, we assumed that our films were randomly packed and that domains of one size dot did not exist. If it did, our interpretation would be incorrect. In order to confirm the morphology of our mixed films, we analyzed monolayers of films for different mixtures of 5.4 nm PbSe dots containing 10%, 20%, 30%, and 50% 6.4 nm dots. Note that during the time of this data collection, the solution of dots used were not the same as those data collected for the state-filling and mobility experiments (see appendix A for mobility plot of mixtures with known percentages based on SEM images) Although, the data collected from the SEM and SAXS experiment represent dots that are < 5% of the size distribution.

Using FIJI, an image analysis software, we can generate and analyze the SEM images of the binary mixtures of QDs to determine the distribution of large dots. A color replicator scheme was scripted to assign a green color scheme to small dots and a blue color scheme for larger dots. This color scheme is also consistent with the SAXS data in figure 6.9. The following procedure is used to analyze the dots and generate a histogram to determine the distribution of large dots in a matrix of small dots:

1) Bandpass Fast-Fourier Transform Filter – used to filter pixels larger and smaller than the pixel size of the region of interest; this reduces the amount of noise and normalizes the intensity of the entire image
2) Convert filtered image into a binary image (0 and 255; black and white)
3) From the binary image, based on the surrounding areas, watersheds or segments the particles
4) Analyze the particles to determine the area
5) Using color replicator of green and blue, assign analyzed particles to green for small dots and blue for large dots

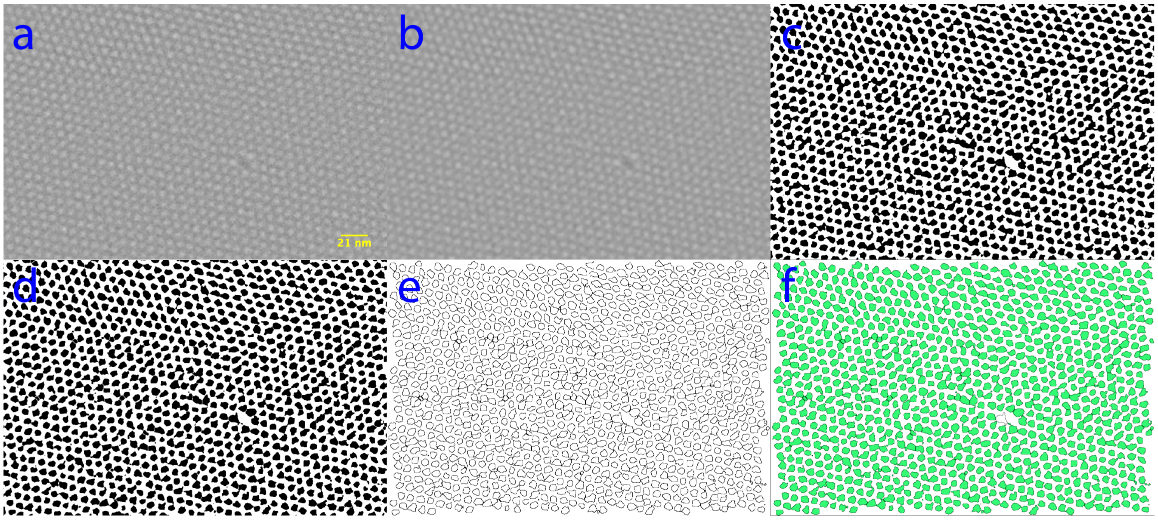

**Figure 6.12 Image analysis of 0% PbSe (1570 nm 1st exciton)** (a) raw image (b) bandpass fast Fourier transform filter (c) binary conversion (d) watershed (e) analyze particles (f) color code

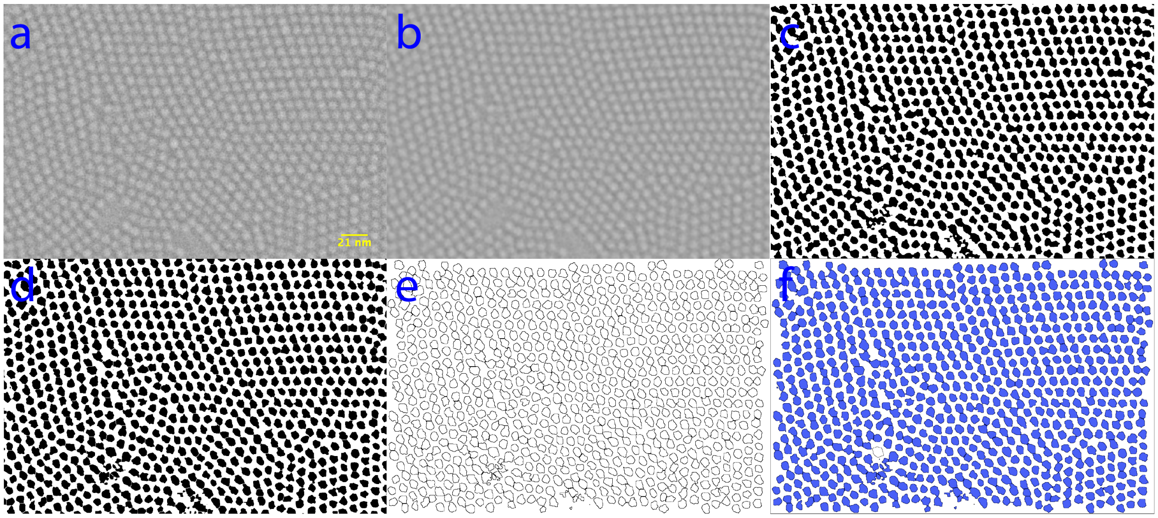

**Figure 6.13 Image analysis of 100% PbSe (1944 nm 1st exciton)** (a) raw image (b) bandpass fast Fourier transform filter (c) binary conversion (d) watershed (e) analyze particles (f) color code

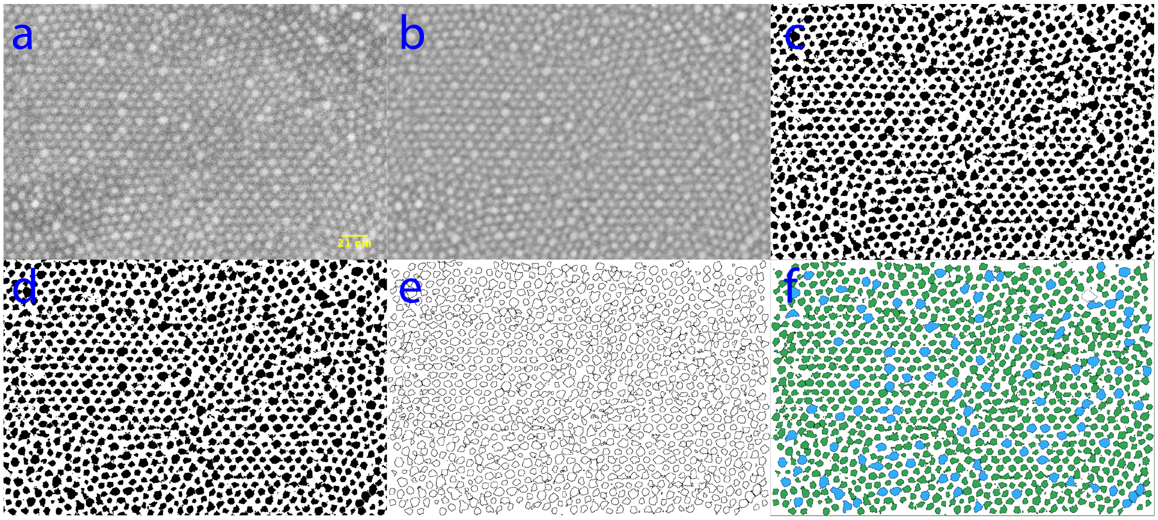

**Figure 6.14 Image analysis of 10% 1944 nm PbSe QDs** (a) raw image (b) bandpass fast Fourier transform filter (c) binary conversion (d) watershed (e) analyze particles (f) color code

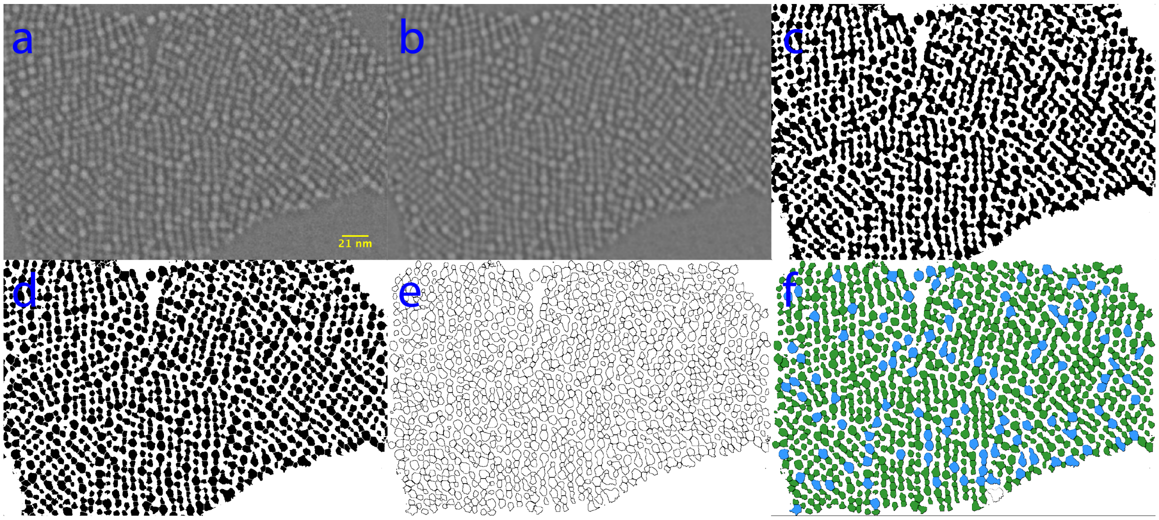

**Figure 6.15 Image analysis of 20% 1944 nm PbSe QDs** (a) raw image (b) bandpass fast Fourier transform filter (c) binary conversion (d) watershed (e) analyze particles (f) color code

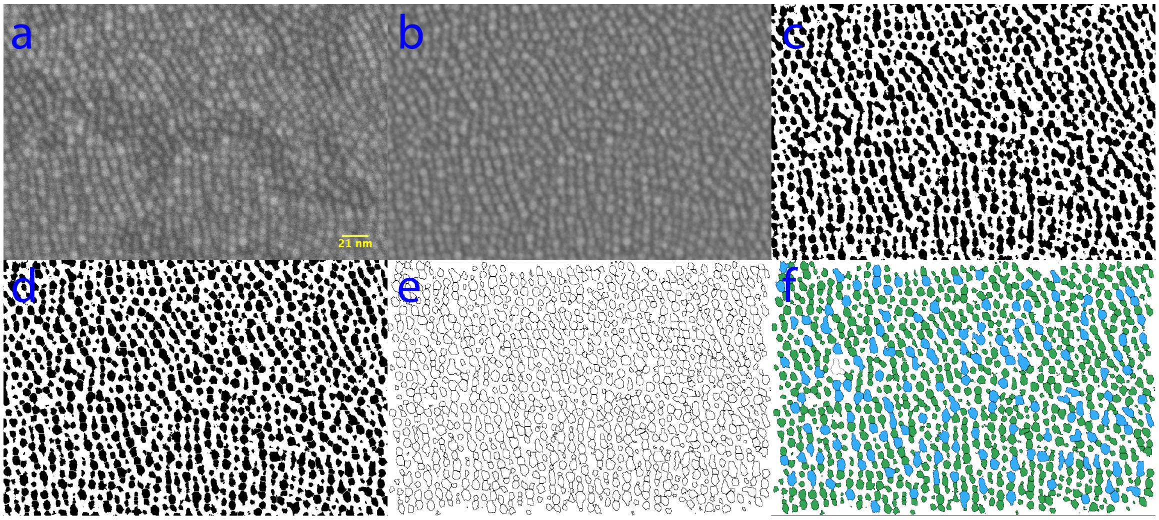

**Figure 6.16 Image analysis of 30% 1944 nm PbSe QDs** (a) raw image (b) bandpass fast Fourier transform filter (c) binary conversion (d) watershed (e) analyze particles (f) color code

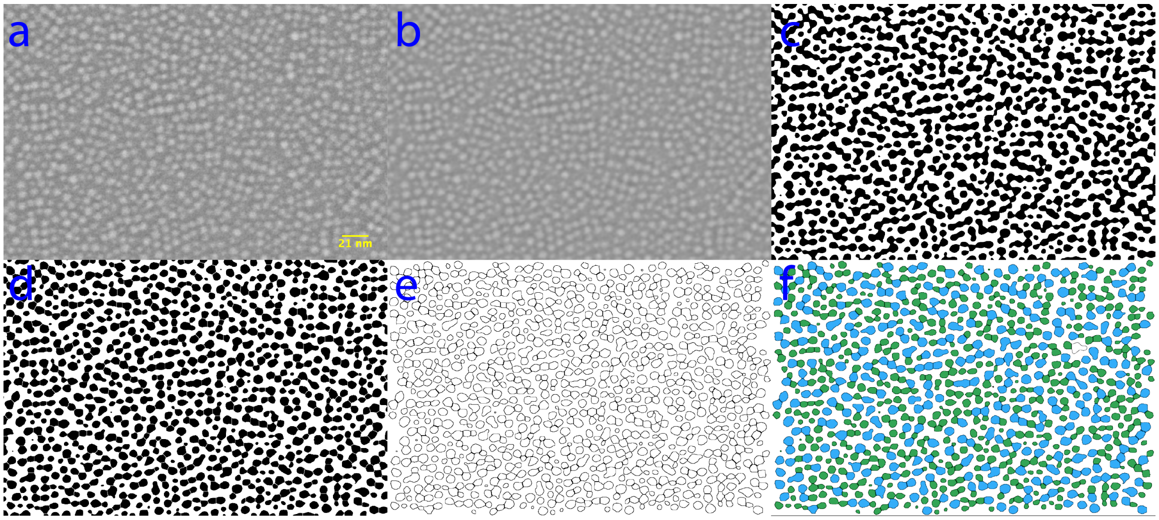

**Figure 6.17 Image analysis of 50% 1944 nm PbSe QDs** (a) raw image (b) bandpass fast Fourier transform filter (c) binary conversion (d) watershed (e) analyze particles (f) color code

Upon close inspection of figures 6.12-6.17, we find that this analysis is accurate to a certain extent with respect to picking up particles and correctly sizing the particles. We note that imaging the same STEM and TEM did the same image analysis. We find that measured dot size is within 0.2 nm of each other, which further qualifies this technique to measure particle size.

As a result of these analyzed particles, similar to SAXS, we can generate a histogram and determine the loading percentage of large dots and compare how accurate our techniques are in terms of analyzing particle distributions.

| **Intended** | **SAXS** | **SEM** |
|---|---|---|
| 0% | 0% | 0% |
| 10% | 12% | 15% |
| 20% | 23% | 22.8% |
| 30% | 33% | 32.7% |
| 50% | 60% | 51.2% |
| 100% | 100% | 100% |

**Table 6.1: Summary of analysis for numerical percentage of large dots in a matrix of small dots.** SAXS(solution). SEM(monolayer films)

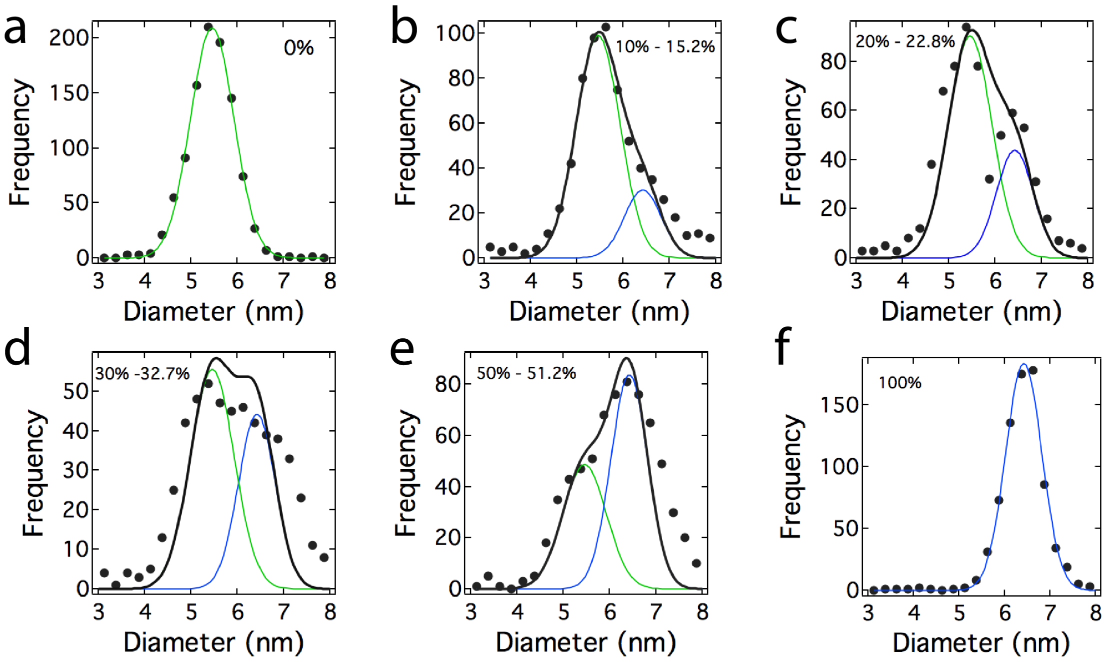

**Figure 6.18 SEM Histograms generated from image analysis** (a) 1570 nm 1st exciton; 0% measured; 5.4789 nm (b) 10% mixture by number; 15.2% measured (c) 20% mixture by number; 22.8% measured (d) 30% mixture by number; 32.7% measured (e) 50% mixture by number; 51.2% measured (f) 1940 nm 1st exciton; 100% measured; 6.4233 nm. Fits to histograms are color-coded appropriately based on the image analysis. Green (5.4789 nm). Blue (6.4233 nm)

From these analyzed figures, we can see that our mixed films are indeed random. Moreover, we can see that at loadings less than what we believe is the threshold of 25%-30%, we have clusters of the large (blue) dots that again act as *localized states*. It is only until we are near this threshold that we see a percolating network (see figure 6.17) of large (blue) dots.

We now discuss the differences in the data presented in this thesis versus that collected within the group in 2010. In figure 6.11, we see that we can easily reproduce the data presented in the paper, [27] where the authors found that regardless of the energetic disorder, the mobility is invariant. For films without ALD infilling, we also find that this is data is consistent. After the ALD infilling, we find that we see this percolating behavior at all temperatures. One explanation could be due to the temperature in which the experiment was performed. Under the variable-range hopping formalism in disordered semiconductors, current is extracted when there is a percolating network. In reference to equation 6.3 or 6.5, the probability for a carrier to hop at room temperature (we are only concerned at room temperature since the data in the publication was taken only at ambient temperatures) depends on the spatial disorder ($\propto \exp(-\frac{2r_{ij}}{\alpha})$ and energetic disorder ($\propto \exp(-\frac{\epsilon_j - \epsilon_i + |\epsilon_i - \epsilon_F| + |\epsilon_j - \epsilon_F|}{2kT})$. At high temperatures, carriers prefer to hop spatially to nearest neighbors (NNH). As such, the second term in equation 6.3 and 6.5 is not important (the energetic disorder) and only spatial distances determine the rates. This resistance as it relates to spatial distances can be expressed as $R(r) = R_0 \exp(-\frac{2r}{\alpha})$ where $R_0$ is a preexponential factor that depends on the relative position of the energy level ascribed to the isoenergetic sites with respect to the Fermi level. For films without ALD, spatially, a carrier has no preference where to hop because it is at high temperature and it can easily hop its nearest neighbor regardless of the energy barrier. To test this idea, further experiments at low temperature is needed to show that if the temperature of the film is lowered, the injected electrons will now *energetically* find and occupy sites that are more energetically favorable (larger dots).

A second comment about the differences between films with and without ALD is that suppose now we have to consider correlation effects where the spatial position of sites and energetic occupation of sites matter. This condition is met when $kT$ is smaller than the energy scale of DOS (or the width of the DOS, σ) and the distribution of site energies and its dependence on concentration.[34,45,46] For this condition to be met, we see that if $kT$ is small, the distribution of energies in which a carrier can hop matters. For transistors, the injected electron moves about the Fermi level and its movement depends on the magnitude of the applied gate bias. In light of extending percolation theory to transport within the tail DOS for QDs, the transport properties are determined by the tail of density of (localized) states. Under the condition that these tail states are small or the temperature is low, one can use the Miller-Abrahams hopping expression to describe activation of carriers from deep energy states to a particular energy level (typically called the *transport edge* where carriers hop upward in energy ($\varepsilon_i$, $\varepsilon_j$ > $\varepsilon_F$) and participate in conduction. In an empty system where charge carriers will dive in energy to unoccupied states (within the tail), most carriers will be distributed in time and temperature. As a function of time, this distribution of carriers will move lower in energy making it more difficult for carriers to be thermally activated to the transport edge, thus lowering the values for the measured mobility.

With this in mind one can rationalize that perhaps during the ALD process, we have reduced the width of the exponential tail of the DOS because of the typically observed improvement in mobility. By reducing the density of tail states (the width), we satisfy the assumption developed for hopping between localized states based on percolation theory.[41,47] This can only be achieved by trap passivation or barrier lowering which increases wavefunction overlap and increases probability for hopping.[48]

A third possibility is that in the previous study, the system size was too small such that the energy regions for various physical effects are statistically not present in the system because of its too small size. While these are only speculations, further experiments, especially at lower temperatures for films without ALD are needed to understand the separate roles of spatial disorder and energetic disorder on the percolation behavior in QD films. Regardless of the explanation, we find that once we achieve better surface trap passivation (through our ALD), polydispersity will become important towards developing high performing devices.

## REFERENCES

(1) Shockley, W.; Queisser, H. J. *Journal of Applied Physics*. 1961, p 510.

(2) Semonin, O. E.; Luther, J. M.; Choi, S.; Chen, H. Y.; Gao, J.; Nozik, A. J.; Beard, M. C. *Science*. American Association for the Advancement of Science December 15, 2011, pp 1530–1533.

(3) Zhang, J.; Gao, J.; Miller, E. M.; Luther, J. M.; Beard, M. C. *ACS Nano*. American Chemical Society 2013.

(4) Weidman, M. C.; Beck, M. E.; Hoffman, R. S.; Prins, F.; Tisdale, W. A. *ACS Nano*. American Chemical Society June 24, 2014, pp 6363–6371.

(5) Kim, J. Y.; Chou, K. W.; Amassian, A.; Sargent, E. H. *Adv. Mater.* 2014, pp 3513–3519.

(6) Levina, L.; Comin, R.; Voznyy, O.; Sargent, E. H. *Adv. Mater.* 2015, pp 3325–3330.

(7) Crisp, R. W.; Kroupa, D. M.; Marshall, A. R.; Miller, E. M.; Zhang, J.; Beard, M. C.; Luther, J. M. *Scientific Reports*. Nature Publishing Group April 24, 2015, pp 9945–.

(8) Oh, S. J.; Berry, N. E.; Choi, J.-H.; Gaulding, E. A.; Lin, H.; Paik, T.; Diroll, B. T.; Muramoto, S.; Murray, C. B.; Kagan, C. R. *Nano Letters*. American Chemical Society 2014, pp 1559–1566.

(9) Nagpal, P.; Klimov, V. I. *Nature Communications*. September 27, 2011, p 486.

(10) Diaconescu, B.; Padilha, L. A.; Nagpal, P. *Physical Review Letters*. 2013, p 127406.

(11) Tang, J.; Kemp, K. W.; Hoogland, S.; Jeong, K. S.; Liu, H.; Levina, L.; Furukawa,

M.; Wang, X.; Debnath, R.; Cha, D.; Chou, K. W.; Fischer, A.; Amassian, A.; Asbury, J. B.; Sargent, E. H. *Nature Materials*. Nature Publishing Group September 18, 2011, pp 765–771.

(12) Erslev, P. T.; Chen, H.-Y.; Gao, J.; Beard, M. C.; Frank, A. J.; van de Lagemaat, J.; Johnson, J. C.; Luther, J. M. *Physical Review B*. October 17, 2012, p 155313.

(13) Bozyigit, D.; Jakob, M.; Yarema, O.; Wood, V. *ACS Applied Materials and Interfaces*. American Chemical Society 2013, pp 2915–2919.

(14) Zhang, Y.; Zherebetskyy, D.; Bronstein, N. D.; Barja, S.; Lichtenstein, L.; Schuppisser, D.; Wang, L.-W.; Alivisatos, A. P.; Salmeron, M. *Nano Letters*. May 13, 2015, pp 3249–3253.

(15) Chuang, C.-H. M.; Brown, P. R.; Bulović, V.; Bawendi, M. G. *Nature Materials*. Nature Publishing Group August 1, 2014, pp 796–801.

(16) Brown, P. R.; Kim, D.; Lunt, R. R.; Zhao, N.; Bawendi, M. G.; Grossman, J. C.; Bulović, V. *ACS Nano*. American Chemical Society 2014, pp 5863–5872.

(17) Santra, P. K.; Palmstrom, A. F.; Tanskanen, J. T. *The Journal of Physical Chemistry C*. 2015, pp 2996–3005.

(18) Jean, J.; Buonassisi, T.; Bulović, V.; Bawendi, M. G. *Nano Letters*. 2015, pp 3286–3294.

(19) Gao, J.; Zhang, J.; van de Lagemaat, J.; Johnson, J. C.; Beard, M. C. *ACS Nano*. American Chemical Society December 23, 2014, pp 12814–12825.

(20) Bozyigit, D.; Lin, W. M. M.; Yazdani, N.; Yarema, O.; Wood, V. *Nature Communications*. Nature Publishing Group January 27, 2015, pp 6180–.

(21) Wehrenberg, B. L.; Yu, D.; Ma, J.; Guyot-Sionnest, P. *The Journal of Physical Chemistry B*. November 2005, pp 20192–20199.

(22) Wehrenberg, B. L.; Guyot-Sionnest, P. *Journal of the American Chemical Society*. July 2003, pp 7806–7807.

(23) Shim, M.; Guyot-Sionnest, P. *Nature*. Nature Publishing Group October 26, 2000, pp 981–983.

(24) Yu, D.; Wang, C.; Guyot-Sionnest, P. *Science*. 2003, p 1277.

(25) Erwin, S. C. *Physical Review B*. November 2010.

(26) Zarghami, M. H.; Liu, Y.; Gibbs, M.; Gebremichael, E.; Webster, C.; Law, M. *ACS Nano*. American Chemical Society 2010, pp 2475–2485.

(27) Liu, Y.; Gibbs, M.; Puthussery, J.; Gaik, S.; Ihly, R.; Hillhouse, H. W.; Law, M. *Nano Letters*. American Chemical Society 2010, pp 1960–1969.

(28) Gao, Y.; Sandeep, C. S. S.; Schins, J. M.; Houtepen, A. J.; Siebbeles, L. D. A. *Nature Communications*. September 13, 2013, p 2329.

(29) Akselrod, G. M.; Prins, F.; Poulikakos, L. V.; Lee, E. M. Y.; Weidman, M. C.; Mork, A. J.; Willard, A. P.; Bulović, V.; Tisdale, W. A. *Nano Letters*. American Chemical Society June 11, 2014, pp 3556–3562.

(30) Lee, E. M. Y.; Tisdale, W. A.; Willard, A. P. *The Journal of Physical Chemistry B*. American Chemical Society July 9, 2015, p 150709124556007.

(31) Poulikakos, L. V.; Prins, F.; Tisdale, W. A. *The Journal of Physical Chemistry C*. April 17, 2014, pp 7894–7900.

(32) Guyot-Sionnest, P. *The Journal of Physical Chemistry Letters*. American Chemical

Society 2012, pp 1169–1175.

(33) Coehoorn, R.; Pasveer, W. F.; Bobbert, P. A.; Michels, M. *Physical Review B*. 2005, p 155206.

(34) Baranovskii, S. D.; Faber, T.; Hensel, F.; Thomas, P. *Journal of Physics: Condensed Matter*. IOP Publishing January 1, 1999, pp 2699–2706.

(35) Coropceanu, V.; Cornil, J.; da Silva Filho, D. A. *Chem. Rev.* 2007.

(36) Miller, A.; Abrahams, E. *Physical Review*. November 1, 1960, pp 745–755.

(37) Fitzpatrick, J. P.; Malt, R. B.; Spaepen, F. *Physics Letters A*. March 1974, pp 207–208.

(38) Powell, M. J. *Physical Review B*. November 15, 1979, pp 4194–4198.

(39) Ambegaokar, V.; Halperin, B. I.; Langer, J. S. *Physical Review B*. October 15, 1971, pp 2612–2620.

(40) Roelofs, W. S. C.; Mathijssen, S. G. J.; Janssen, R. A. J.; de Leeuw, D. M.; Kemerink, M. *Physical Review B*. February 7, 2012, pp 085202–085206.

(41) Vissenberg, M. C. J. M.; Matters, M. *Physical Review B*. May 15, 1998, pp 12964–12967.

(42) K D Benkstein; N Kopidakis; J van de Lagemaat, A.; Frank, A. J. *Influence of the Percolation Network Geometry on Electron Transport in Dye-Sensitized Titanium Dioxide Solar Cells*; American Chemical Society, 2003.

(43) Shklovskii, B. I.; Efros, A. L. *Electronic Properties of Doped Semiconductors*; Springer Science & Business Media: Berlin, Heidelberg, 2013; Vol. 45.

(44) Pollak, M.; Pike, G. E. *Physical Review Letters*. May 29, 1972, pp 1449–1451.

(45) Baranovskii, S. D.; Zvyagin, I. P.; Cordes, H.; Yamasaki, S.; Thomas, P. *physica status solidi (b)*. WILEY-VCH Verlag Berlin GmbH March 1, 2002, pp 281–288.

(46) Baranovskii, S. D. *Physica Status Solidi B-Basic Solid State Physics*. March 2014, pp 487–525.

(47) Grünewald, M.; Thomas, P. *physica status solidi (b)*. WILEY-VCH Verlag July 1, 1979, pp 125–133.

(48) Pautmeier, L.; Ries, B.; Richert, R.; Bässler, H. *Chemical Physics Letters*. January 1988, pp 459–462.

# CHAPTER 7

# SUMMARY AND OUTLOOK

## 7.1. Thesis findings and scientific contributions

This thesis focused on the development of an understanding on charge transport in colloidal quantum dot films using field-effect transistors with special emphasis on translating gained outcomes to applications in solar cell devices. In chapter 4, the field-effect mobility was improved by an order magnitude to about 7 cm$^2$ V$^{-1}$ s$^{-1}$ which at the time was the highest mobility for PbSe. This was accomplished in two steps: 1) using a small, compact ligand such as sodium sulfide to increase the electronic coupling and 2) trap passivation using $Al_2O_3$ infilling at 75°C. These films processed in this behavior yielded devices that were air-stable for more than a year and maintained the high field-effect mobility.

In chapter 5, we eliminated the long-standing operational instability problem with quantum dot field-effect transistors. Achieving transistors that did not suffer from the bias-stress effect was accomplished by leveraging concepts and processing learned in chapter 4. Unlike in chapter 4, sulfur-capped PbSe QDs were achieved by protonating a PbSe QD film treated with a volatile ligand such as 1,2-ethanedithiol (EDT), formic acid (FA), or ammonium thiocyante (SCN). Following protonation with $H_2S$ in the ALD chamber, the films were then infilled with alumina. This somewhat universal processing of $H_2S$ exposure and alumina infilling yield transistors that are operational stable almost indefinitely. Moreover, using higher temperature processing and a ligand that promoted better spatial ordering, FETs that are air stable, operationally stable (bias-stress free), and have high mobility (~13 $cm^2 V^{-1} s^{-1}$) are now attainable. It was discovered that for this process to be effective, a minimum thickness of ~4 nm was required in order to prevent surface proton migration. Through ion-exchange experiments on a partially infilled alumina surface, we were able to improve the current transients, but not completely suppress suggesting multiple mechanisms for the bias-stress effect in QD FETs.

In chapter 6, we investigated how localized states affect transport by developing a novel transistor geometry that allows us to prove electrostatically induced charge carriers in PbSe QD films for different chemical treatments and sizes. By modulating the injected charges, we can determine how carriers are transported and extracted. We find that under low charge injection, carriers find themselves in localized states. Eventually, with large enough currents or large magnitude in the gate voltage, all the traps are filled and occupation of conduction band orbitals of the QDs occurs. We also finally resolve that transport in QD films based on transistor geometries is truly two-dimensional by doing thickness studies and find that a large number of carriers are injected mostly near the QD/dielectric interface. Moreover, we also use this platform to study disorder effects and find that due to size homogeneity, almost always present in a nanocrystal synthesis, large disorder can be introduced, which can greatly affect charge transport properties. In addition, we find that due to the self-heating effects for QD transistors that exhibit high performance and high current levels, one would have to consider engineering better device architectures to dissipate heat.

## 7.2. Outlook and future work

Having established such a great platform to determine how carriers are moving, the large-area electroabsorption FET devices can offers a wealth of experiments that combine transport studies and density of states. Initial measurements and fitting data demonstrated that this platform could easily be used to test current transport models, photoconductivity, and trap passivation with the new library of processing techniques involving metal cations and halides. Moreover, using the density of states extracted from field-effect conductivity, one can determine the position of the Fermi level and transport edge as a function of carrier density. This transport edge, for transport in disordered semiconductors, determines equilibrium and nonequilibrium, transient and steady state transport phenomenon. For hopping transport within band-tails, a single shopping event occurs in the vicinity of the Fermi level and this transport edge. It is this transport energy that maximizes the hopping rate as a final electron hop, independent of its initial energy (i.e. an electron will hop to sites with energy greater than its initial energy (a.k.a. variable range hopping; when $kT < \varepsilon$). By knowing this information, further information regarding the temperature dependence on the intensity of the bleach can be correlated to establish and confirm hopping transport within quantum dot solids.

From the percolation experiments, we can also encourage future work towards improving the monodispersity of quantum dots through refined size selection such as chromatography techniques. If transport is truly dictated by these sub assemblies of large quantum dots (energetically more favorable), work towards improving this energetic disorder will enable higher performing devices.

Furthermore, this thesis outlines a new processing technique to develop high mobility FETs that are bias-stress free. Future work can begin looking at things such as photoconductivity, carrier concentration, and minority carrier diffusion lengths to determine the usefulness of this process towards enabling higher performing solar cells based on quantum dot solids.

# APPENDIX A

## SEM IMAGE ANALYSIS/HISTOGRAM AND MOBILITY FOR A DIFFERENT BATCH OF QUANTUM DOTS

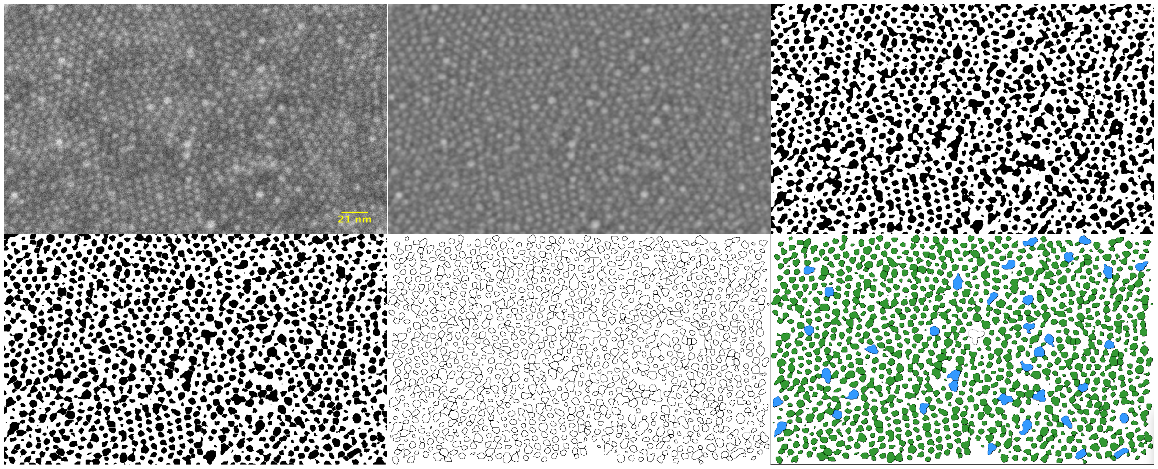

**A.1 10.8%**

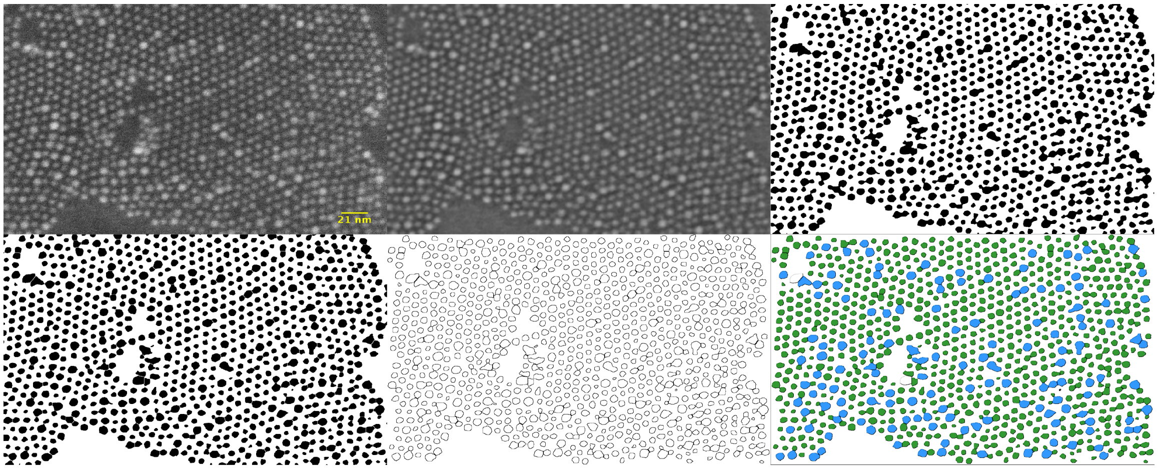

**A.2 13.5%**

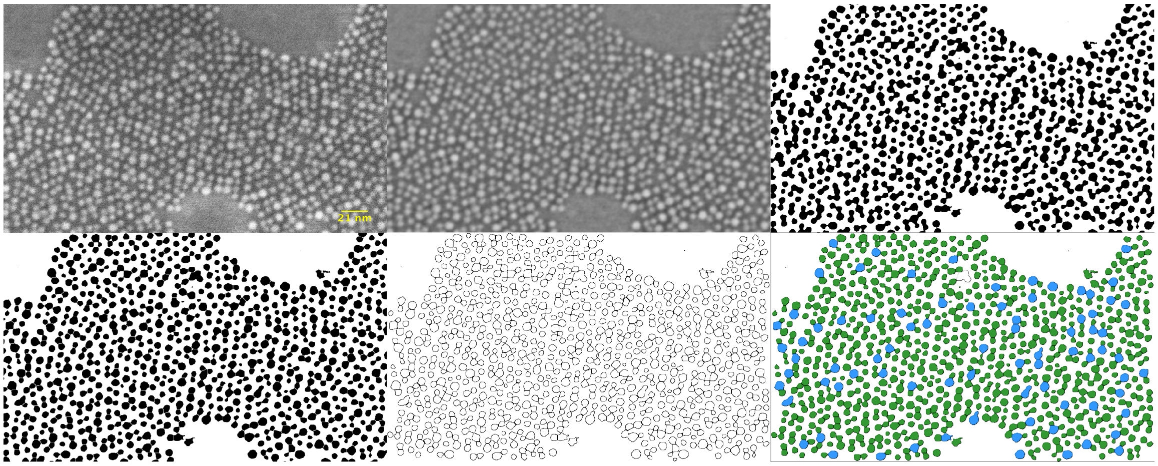

**A.3 18.39%**

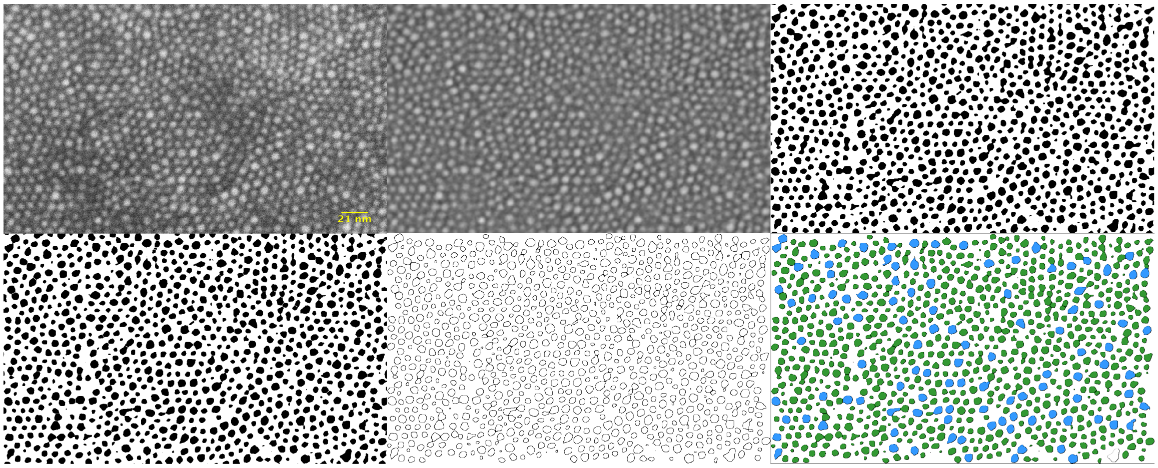

**A.4 22.8%**

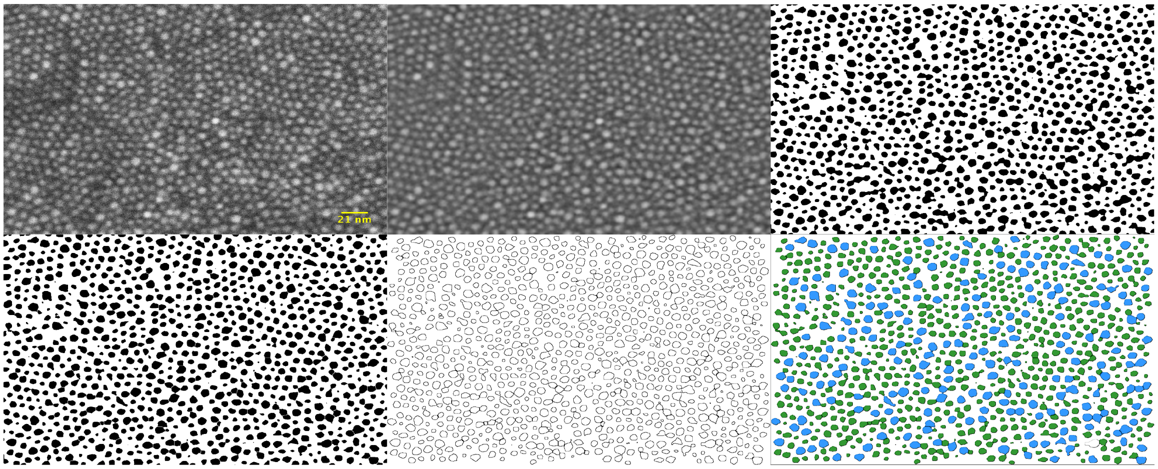

**A.5 28.2%**

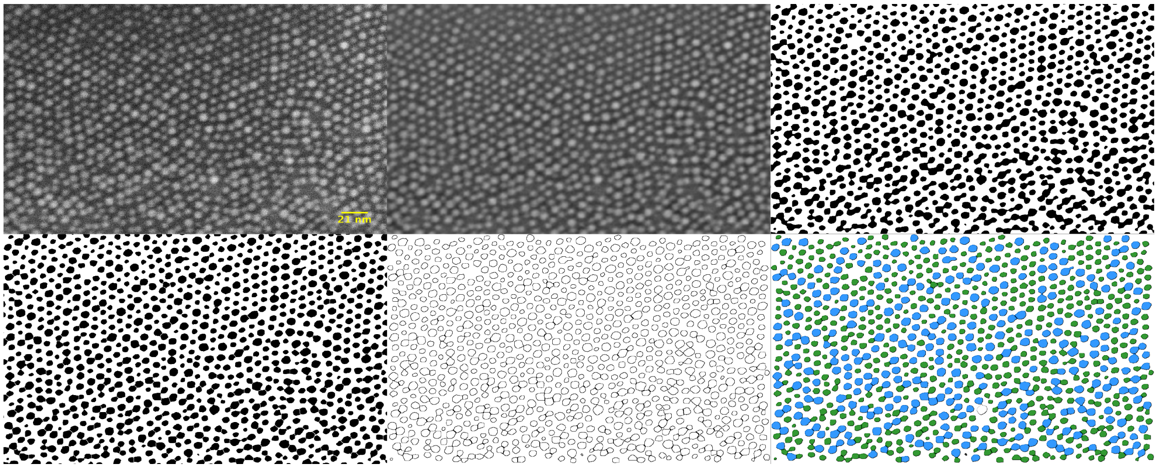

**A.6 39.8%**

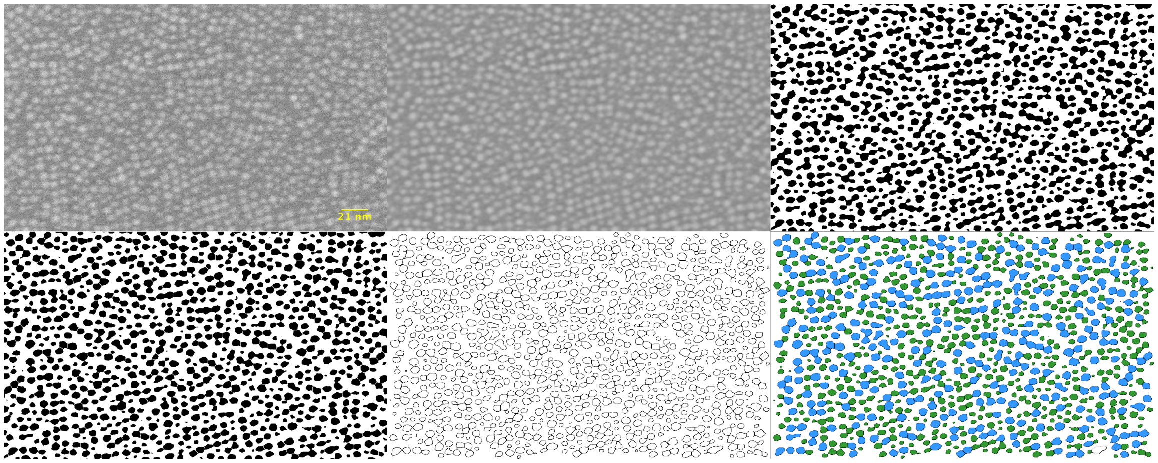

**A.7 42%**

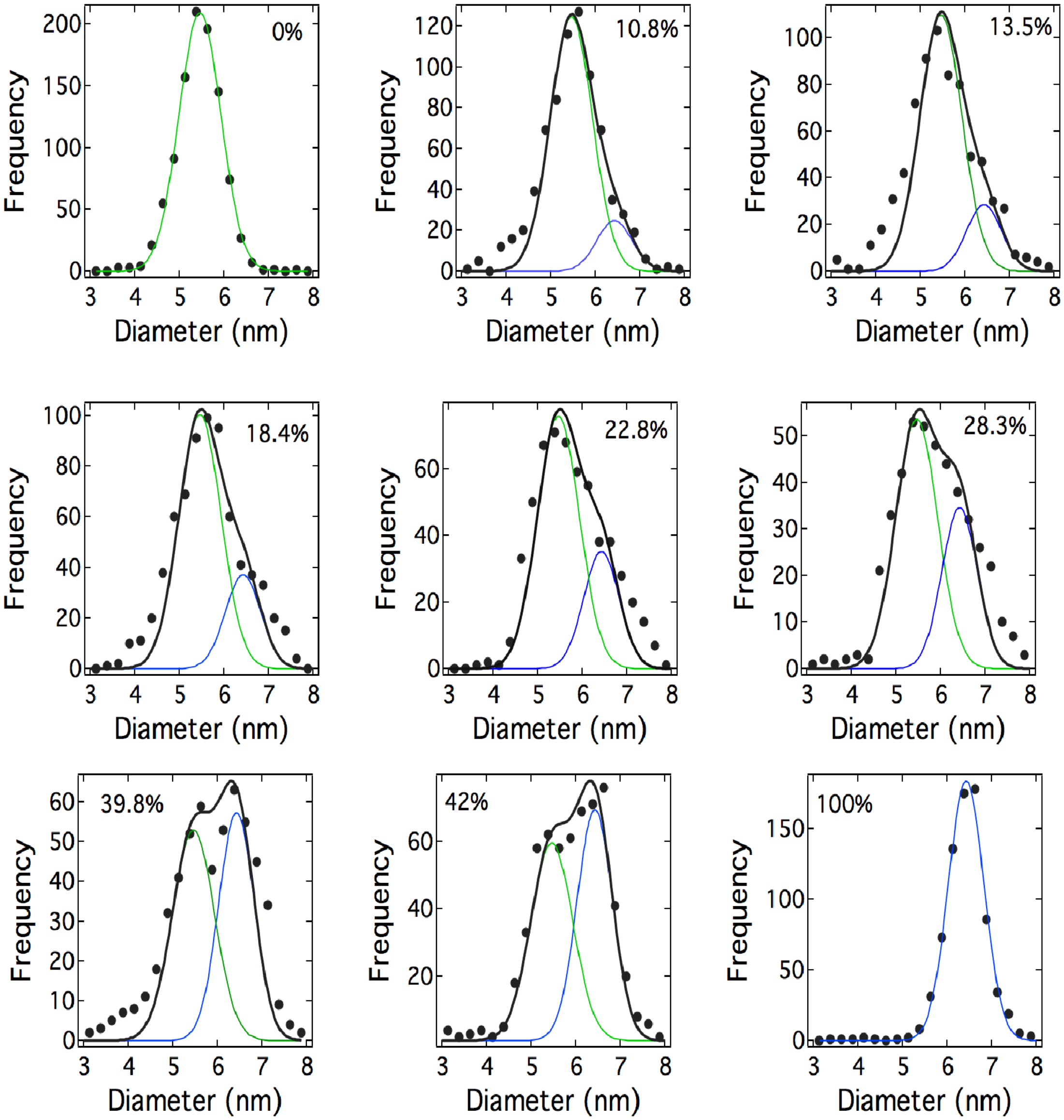

A.8 SEM Histograms generated through image analysis in images A.1-A.7

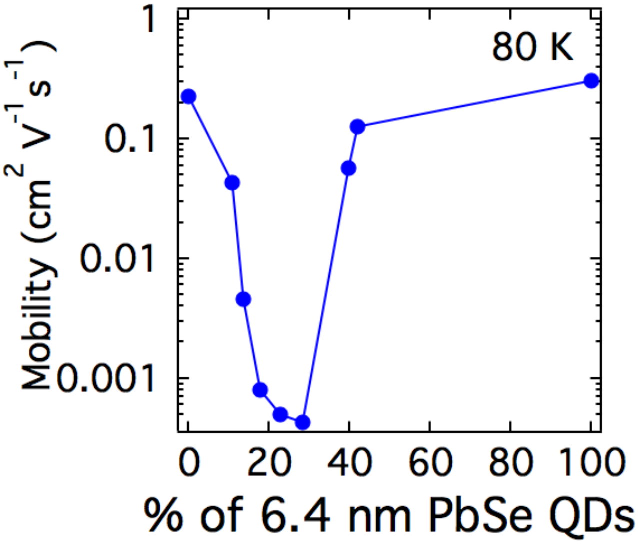

**A.9 Mobility as a function of 6.4 nm PbSe QD loading**. T = 80K. Loading percentages are based on the generated histograms in A.8